1-29-2009

Electromagnetic modeling of hot-wire detonators using analytical and numerical methods with comparison to experiment

Michael Lambrecht

Michael Lambrecht
Candidate

Electrical and Computer Engineering
Department

This dissertation is approved, and it is acceptable in quality and form for publication on microfilm:

Approved by the Dissertation Committee:

, Chairperson

Accepted:

Dean, Graduate School

NOV 17 2008

Date

ELECTROMAGNETIC MODELING OF HOT-WIRE DETONATORS USING ANALYTICAL AND NUMERICAL METHODS WITH COMPARISON TO EXPERIMENT

BY

MICHAEL LAMBRECHT

B.S., Electrical Engineering, University of Nevada Reno, 2003
M.S., Electrical Engineering, University of Nevada Reno, 2005

DISSERTATION

Submitted in Partial Fulfillment of the
Requirements for the Degree of

Doctor of Philosophy in Engineering

The University of New Mexico
Albuquerque, New Mexico

December, 2008

ACKNOWLEDGEMENTS

Any undertaking of this magnitude is not possible without the support of many wonderful people, and this project is no exception. I would first like to thank my advisor and committee chair Dr. Edl Schamiloglu for accepting me into his research group and providing valuable advice and mentoring throughout my time at the University of New Mexico (UNM). Dr. Schamiloglu provided inspiration and instilled confidence through our many meetings and discussions.

My other primary mentor throughout this project was Dr. Keith Cartwright at the Air Force Research Laboratory (AFRL). Keith provided almost daily support during my research, giving me direction and advice for making this project successful not only for myself and UNM, but also for the Air Force and AFRL. I must thank Keith for all of this and for bringing me into his group and helping me start my career.

Several other extremely intelligent folks were involved with this project and the completion of my degree. Dr. Carl Baum provided his renowned electromagnetic insight for the analytical modeling portion of this work. In addition, Dr. Mark Rader at NRL and Dr. Richard St. John of KTech were instrumental in providing me with the experimental data used for this project. Dr.'s Mark Gilmore and Christos Christodoulou were not only excellent instructors, but also honor me by being a part of my dissertation committee and lending me some of their very valuable time. I would like to thank Dr. Alexander Stone of the Department of Mathematics and Statistics at UNM for rounding out my committee.

I would also like to recognize the members of the Computational Physics team at AFRL's Directed Energy Directorate at Kirtland AFB for welcoming me to the group and showing me the ropes of ICEPIC and AFRL operating procedures while I worked on this

degree. Special thanks go to Elmyra Grelle of the Electrical and Computer Engineering Department at UNM and Candace Shirley at the UNM branch of the Defense Threat Reduction Agency (DTRA). Elmyra has done so much to help me with the impressive amount of paperwork and other requirements that come along with completing a Ph.D. degree at UNM. She has also been instrumental in keeping me funded and my tuition paid by making sure my contracts were done correctly and in time. Candace was the one who signed these contracts, and thanks to her diligent work with DTRA, has kept the program going that has funded me for three years.

Finally, none of my accomplishments would have been possible without the love and support of my family. Everything I am I owe to my parents, sister, and grandparents who have been there for me through it all. My wife and daughter have provided daily support at home, allowing me to forget about research and work related problems. The completion of this work is dedicated to both of them.

The research reported in this dissertation was also supported, in part, by a grant from the Office of Naval Research, ONR Grant N00014-06-1-0476.

ELECTROMAGNETIC MODELING OF HOT-WIRE DETONATORS USING ANALYTICAL AND NUMERICAL METHODS WITH COMPARISON TO EXPERIMENT

BY

MICHAEL LAMBRECHT

ABSTRACT OF DISSERTATION

Submitted in Partial Fulfillment of the
Requirements for the Degree of

Doctor of Philosophy in Engineering

The University of New Mexico
Albuquerque, New Mexico

December, 2008

ELECTROMAGNETIC MODELING OF HOT-WIRE DETONATORS USING ANALYTICAL AND NUMERICAL METHODS WITH COMPARISON TO EXPERIMENT

by

Michael Lambrecht

B.S., Electrical Engineering, University of Nevada Reno, 2003
M.S., Electrical Engineering, University of Nevada Reno, 2005

Doctor of Philosophy in Engineering

ABSTRACT

The electromagnetic (EM) characteristics of hot-wire detonators are determined in order to quantify more precisely their response to EM illumination. The analyses include a comprehensive study of detonators' physical characteristics, which is then used to model detonators using transmission line theory. The theoretical analysis treats the detonator as a cascaded transmission line incorporating several different dielectrics, and examines both differential and common mode excitation for a generic detonator model. This 1-D analytical model is implemented in MatLAB and used to determine the input impedance of the detonator for a frequency range spanning DC to 9 GHz. This program can then quickly investigate similar hot-wire detonators by varying their parameters.

The generic model of the detonator is also simulated using ICEPIC, a 3-D finite-difference-time-domain (FDTD) full wave numerical EM solver. The ICEPIC simulations are performed at several frequencies for both differential and common mode

excitations, and are used to determine EM properties of the detonator. The results of these simulations are compared with the analytical predictions. Both the analytical and numerical techniques are then used to improve the MatLAB program's ability to accurately predict the detonator's EM characteristics. This is accomplished by including additional elements in the 1-D model accounting for detonator properties revealed in the 3-D EM simulation results.

Finally, the analytical model is used to predict the input impedance for state-of-the-art blasting cap. These predictions are then compared with data from experimental measurements performed on 108 live devices.

TABLE OF CONTENTS

LIST OF FIGURES

Chapter 2 – Description of Detonators

Chapter 3 – Formulation of the Detonator Electromagnetic Model

Chapter 4 – Numerical Model Formulation and Analytical Model Modification

Chapter 5 – Simulation Results and Comparison to Analytic Predictions

Chapter 6 – Investigations into Model Improvement

Chapter 7 – Modeling the State-of-the-Art Blasting Cap and Comparison to Experimental Measurements

LIST OF TABLES

Chapter 2 – Description of Detonators

Chapter 3 – Formulation of the Detonator Electromagnetic Model

Chapter 5 – Simulation Results and Comparison to Analytic Predictions

Chapter 6 – Investigations into Model Improvement

Chapter 7 – Modeling the State-of-the-Art Blasting Cap and Comparison to Experimental Measurements

Chapter 1 – Introduction

The goal of this project is to comprehensively model, simulate, and characterize the electromagnetic (EM) properties of hot-wire detonators. To accomplish this task, the physical dimensions and material components of detonators will be examined to create a generic representation of a hot-wire detonator. Using this information, the generic detonator will be modeled analytically as a cascaded transmission line utilizing both differential and common mode excitation. In addition, the entire generic detonator geometry will be modeled numerically and simulated electromagnetically using the finite-difference-time-domain (FDTD) method. The results from each of these analyses will be directly compared in order to validate the one-dimensional (1-D) analytical model with the three-dimensional (3-D) EM simulation. The fast-running analytical model can then be used to predict the EM characteristics of any similarly constructed detonator by merely changing the input dimensions from those of the generic model to any specific type being investigated. This will be done for a state-of-the-art blasting cap (SABC), and the modeling results will be compared with experimental measurements.

The long-term goal of this research is the establishment of accurate safety measures to prevent accidental detonation of detonators in an electromagnetically rich environment by determining which frequency ranges pose the greatest safety hazard to these devices.

Hypothesis

A detonator has certain EM characteristics across a frequency range of DC-9 GHz. Within this spectrum, there are frequency ranges which may cause the detonator to

dud or explode. These properties must be well understood if the long term objectives of the project are to be met.

Detonator Excitation

As shall be described in greater detail later, two types of EM detonator excitation will be investigated: differential mode, and common mode excitation. Due to the nature of these excitations, the differential mode variety is far more likely to cause detonation since EM energy coupled in this manner induces current flow in the bridge wire, which could potentially detonate the device. Common mode coupling must cause a dielectric breakdown in the vicinity of the bridge wire to detonate the device. This method of ignition requires considerably more energy being deposited onto the detonator as compared to the differential mode, making common mode detonation less likely. However, as common mode excitation is still possible, it will be thoroughly investigated.

Related Experiments Appearing in the Literature

To our knowledge, there have been only two investigations in the open literature with similarities to the work performed for this project. Both of these studies [1, 2] focus on experimentally measuring the amount of energy deposited into the bridge wire of a detonator and modeling the detonator as a transmission line. The modeling of the detonator is treated very simply and is used as a mechanism to aid in the construction of a connection network between the detonator and a source. The work presented here deals nearly exclusively with accurate modeling of the detonator, with a small amount of experimental data presented for comparison.

Typical research in this area involves using an infrared sensor to detect the amount of energy deposited into the bridge wire by sensing the temperature increase of the bridge wire [1, 3]. This is done at different pulse lengths and power levels to determine which excitation conditions are most likely to detonate a device. This project works in the other direction by first accurately modeling the detonator to then determine which types of experiments will yield the most pertinent information about the detonator.

Dissertation Summary

This dissertation is organized as follows. A discussion of detonators and their physical properties is presented in Chapter 2. The analytical model of the detonator is developed based on generic detonator dimensions for both differential and common mode excitations in Chapter 3. Chapter 4 will discuss how a 3-D model of the generic detonator is created for FDTD simulation, along with appropriate additions made to the analytical model described in Chapter 3 to allow for a direct comparison between analytical predictions and simulated results. Results of both methods are compared in Chapter 5. Chapter 6 describes investigations into several detonator variations using both EM simulation and analytical modeling to improve the model's robustness and accuracy. The models are then used to analyze a SABC in Chapter 7, and the analytical and simulated results are compared with experimental measurements taken on 108 SABCs. Finally, conclusions will be drawn in Chapter 8 about the success of modeling results to date, as well as a description of future work to be performed towards attaining the long term project goals.

Chapter 2 – Description of Detonators

Some general aspects of detonators will now be discussed along with their use and some available types. From these descriptions, a generic representation of a detonator will be developed for use in subsequent modeling efforts. Also, a SABC will be described in detail.

Detonator Usage

A detonator, also called a blasting cap, is a small explosive device that is used to initiate a larger explosive charge. A photograph of typical detonators is shown as Figure 1. Detonators are used in a wide variety of applications including the initiation of explosives used in mining, lumbering, and tunneling [4]. Smaller detonators, called squibs, are used in pyrotechnics and special effects in movies.

Figure 1: Photograph of typical detonators [4].

Types of Detonators and Their Models

There are many different types of detonators, all of which have several properties in common. In general, a detonator is composed of a metallic case and two lead-in wires. Housed inside the case are up to two types of explosive, along with a seal that keeps them compressed within the case. The two types of explosives are referred to as the primary and the secondary.

The primary explosive is composed of a volatile material (lead-azide, lead-styphnate, silver fulminate, among others) and is extremely sensitive to heat, impact, or friction and can therefore be initiated in a variety of ways. The secondary explosive has greater explosive yield than the primary explosive, but is more stable and requires a larger amount of energy to initiate. Typically, pentaerythritol tetranitrate (PETN) or cyclotrimethylene-trinitramine (RDX) are used as a secondary explosive in detonators [5]-[7].

While these features are typical to detonators in general, the manner in which they are initiated yields several different kinds of detonators. Some detonators can be initiated mechanically, but most are set off using an electric current. These types of detonators are also referred to as Electro Explosive Devices (EED). Several types of EEDs include a pyrotechnic fuse (squib), hot-wire, match type, exploding bridge wire (EBW), and slapper type (improved EBW) [4]. Of these detonators, the hot-wire and EBW are most prevalent, and will be discussed here [5, 6].

Hot-Wire Detonators

A hot-wire detonator consists of a primary and secondary explosive, along with a seal, inside a metallic case. An illustration of the cross-section of a hot-wire detonator is

shown in Figure 2. The lead-in wires outside the metallic case extend to the power source that delivers the initiating current to the detonator. The seal, a waterproof sealing material, is used to hold the lead-in wires in place as well as the explosives inside the metallic case. The seal is followed by an ignition charge and primer charge, which are both primary explosives. Following the primer charge is the base charge, which is a secondary explosive. The detonator is initiated by a current flowing through the lead-in wires and into the bridge wire. The current heats up the bridge wire, which is a very thin wire made of a highly resistive material. When the bridge wire reaches approximately 300^{o}C, the heat initiates the primary explosive which surrounds the bridge wire. This begins the explosive chain that continues through the primary explosive making up the primer charge. Finally, after the first two sections have been ignited, the explosive chain has acquired sufficient energy to initiate the secondary explosive in the base charge, completing the detonation of the device. The presence of primary explosives in hot-wire detonators makes them susceptible to accidental detonation from extreme heat changes, impact from being dropped, static electric discharge, or electromagnetic energy [5]-[7]. Also, since the bridge wire must first heat up to a critical temperature, and then heat a small portion of the surrounding primary explosive to this critical temperature, the firing time for hot-wire detonators is milliseconds.

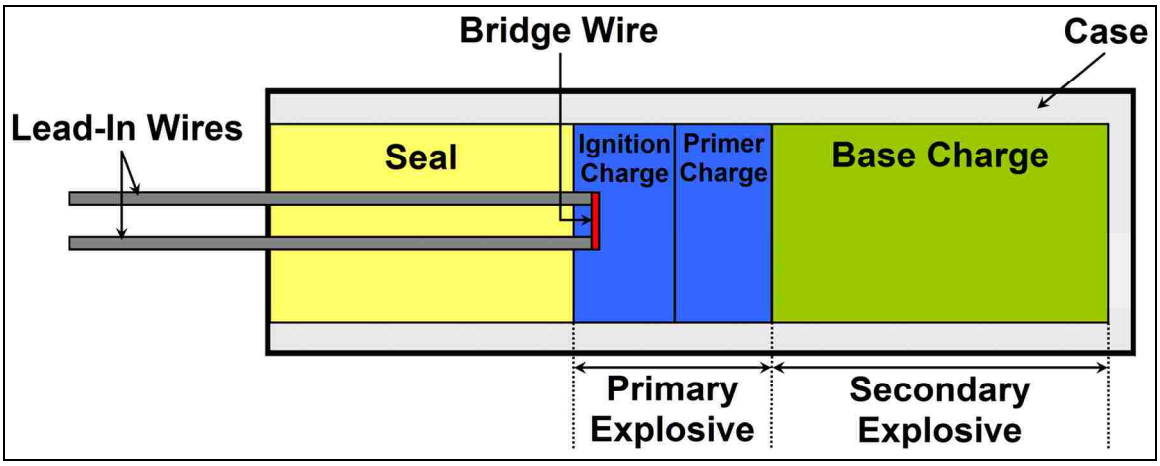

Figure 2: Illustration of a hot-wire detonator.

EBW Detonators

An EBW detonator consists of a secondary explosive and a header (seal) within a metallic case. An illustration of the cross section of an EBW is shown in Figure 3. Since an EBW does not contain primary explosive, it is a much safer detonator for handling and is used in many commercial applications [4, 5, 7]. However, since the secondary explosive requires more energy for detonation, an EBW requires a large amount of current to be initiated. The EBW is set off when the bridge wire, embedded in the secondary explosive, vaporizes. To vaporize the bridge wire, a very high current must be delivered to the detonator very rapidly (~200 A/μs). If the current delivered to the detonator is insufficient, the detonator will dud because the bridge wire is partially melted or broken without igniting the secondary explosive, and be unusable [5, 7]. The detonation sequence follows from the ignition charge (PETN) to the booster charge (RDX), which are both secondary explosives. Also, due to the nature of the ignition mechanism, which occurs with bridge wire vaporization, detonation occurs almost instantly in an EBW detonator [7].

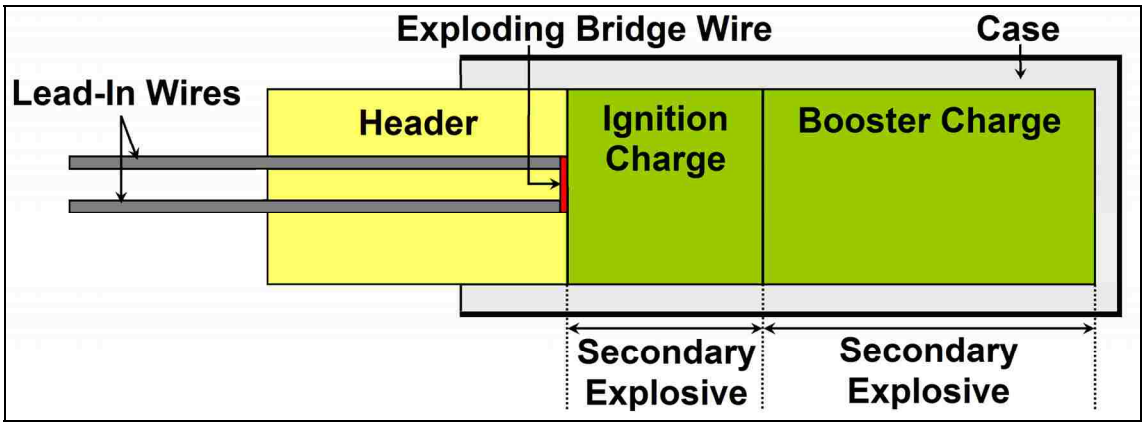

Figure 3: Illustration of an EBW detonator.

Creating a Generic Detonator Representation

Based on the detonation requirements for both of these detonators, the hot-wire detonator could potentially be set off by radio frequency (RF) and microwave (MW) radiation coupling into the detonator. The amount of current and timescales required for an EBW preclude it from being accidentally set off by an impinging electric field. From this point forward, the hot-wire detonator will be the focus of all modeling and characterization efforts.

In order to electromagnetically model a hot-wire detonator, a generic physical model must be created and the properties of all included materials must be understood. Since hot-wire detonators are manufactured by many companies [8]-[11], the model must be representative of hot-wire detonators in general. This can be done since the detonators are all of similar construction, and only the dimensions vary between different manufacturers. For this generic representation, the ignition and primer charges will become one coherent section within the detonator since both sections are composed of primary explosive. Values found in [5] determine the detonator length (32.25 mm) and diameter (7 mm). Relative lengths of the seal (10.67 mm), primary (7.87 mm), and

secondary (13.21 mm) sections within the detonator are also found from [5], along with the distance of the bridge wire from the seal-primary boundary (1.27 mm). To determine the distance between the lead-in wires, the typical length of the bridge wire (1.5 mm) from [6] is used such that each end of the bridge wire coincides with an outer edge of a lead-in wire. The diameter of the lead-in wires (0.25 mm) is approximated based on a reasonable wire diameter for being attached to a source. This diameter yields a center-to-center spacing of 1.25 mm for the lead-in wires. The radius of the bridge wire (25 μm) is also taken from [6]. The thickness of the case (0.5 mm) is approximated based on a reasonable value for such an application. Lastly, since the length of the lead-in wires outside the detonator can be any arbitrary value, 5.25 mm was chosen through numerical modeling described in Chapter 4. Figure 4 is a representation of the generic detonator dimensions.

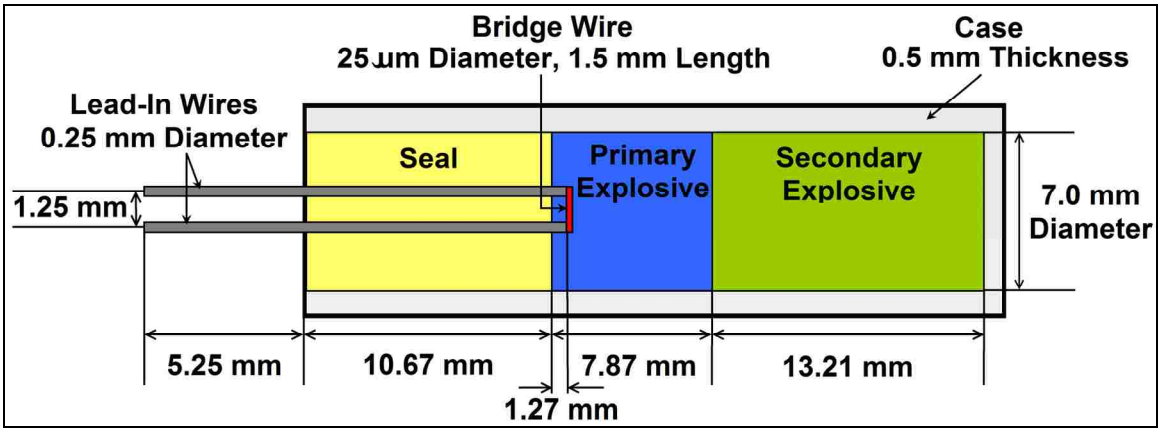

Figure 4: Illustration of generic model dimensions for a hot-wire detonator.

With the dimensions of the generic hot-wire detonator model determined, the EM properties of the constituent parts of the detonator must be found. Beginning with the metal in the system, [10] was used to determine that the lead-in wires are made of copper while the case is made of aluminum. The high resistance bridge wire is generally an alloy of platinum or gold and has a nominal DC resistance of approximately 1 Ω [5]-[7].

Within the detonator, the seal is made of a waterproof sealing material such as rubber or diallyl phthalate (DAP) [7]. For this model, DAP will be selected as the seal material, which has an approximate dielectric constant of 4.0 [12, 13]. The primary explosive generally used in hot-wire detonators is lead-azide, which has an approximate dielectric constant of 17.0 [14]. Lastly, the secondary explosive most commonly used in hot-wire detonators is PETN, which has an approximate dielectric constant of 3.0 [11]. Table 1 summarizes the constitutive parts of the detonator and their corresponding properties. Note that the dielectric constants for the detonator materials are approximated as being constant across the entire frequency range, since detailed and broad frequency spectrum dielectric data for these materials has not been published in the literature. Figure 5 is an illustration of the final generic model, indicating all dimensions and properties. This final representation is what will be used when modeling the detonator both analytically and numerically in Chapters 3 through 6.

Table 1: Material properties for the generic model of a hot-wire detonator.

Detonator Part	Material	Dielectric Permittivity (ε_r)	Dielectric Permeability (μ_r)	Conductivity (σ)
Lead-In Wires	Copper	-	-	$5.8*10^7$ [12]
Case	Aluminum	-	-	$3.82*10^7$ [12]
Bridge Wire	Alloy	-	-	Effective
Seal	DAP	4.0	1.0	0
Primary Explosive	Lead-Azide	17.0	1.0	0
Secondary Explosive	PETN	3.0	1.0	0

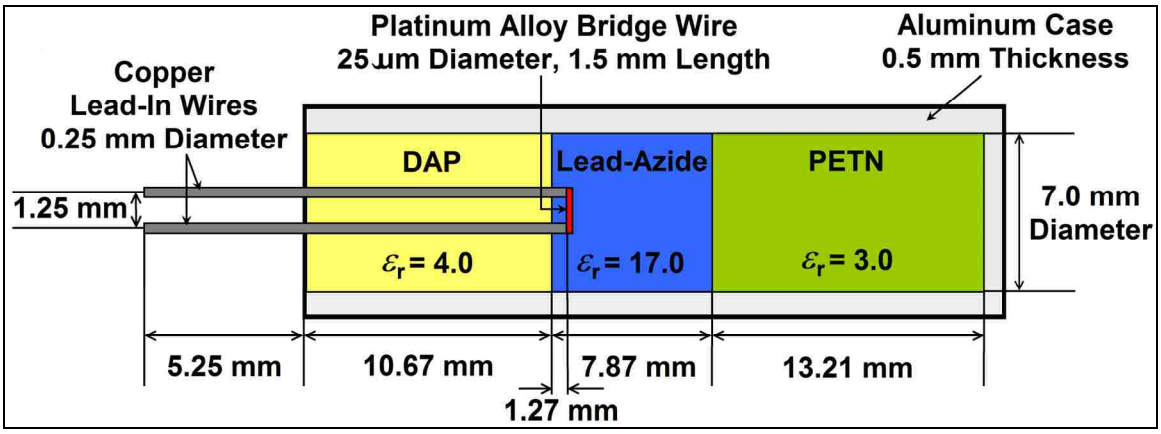

Figure 5: Illustration of the generic detonator geometry dimensions and EM properties.

The State-of-the-Art Blasting Cap

The SABC is manufactured under strict guidelines [16] and while the generic model previously presented is to be representative of hot-wire detonators in general, the prevalence of the SABC warrants additional examination. Based upon the dimensions of the SABC given in [10], along with direct measurements taken of live SABCs at Ktech Inc. [Albuquerque, NM, USA][1], the model of the SABC is given as Figure 6. Some dimensions of the SABC are conjecture due to proprietary information regarding their manufacture, but represent an educated guess based on both observation and the measurements taken.

In addition to the physical dimension changes illustrated in Figure 6, the SABC has a few other features which deviate from the generic detonator model. First, the bridge wire is longer (3.175 mm) and is bent into a U-shape within the primary explosive. This additional length increases the bridge wire's nominal DC resistance to 1.6 Ω [10]. Also, the seal is rubber with a dielectric constant of 3.0 [15], and the secondary explosive

[1]Ktech Corporation
10800 Gibson Blvd. S.E.
Albuquerque, NM 87123
(505)998-5830

is RDX with a dielectric constant of 3.14 [14]. Table 2 lists the constitutive parts of the SABC and their corresponding properties. Also, the firing characteristics of the SABC detonator are given in Table 3 [10].

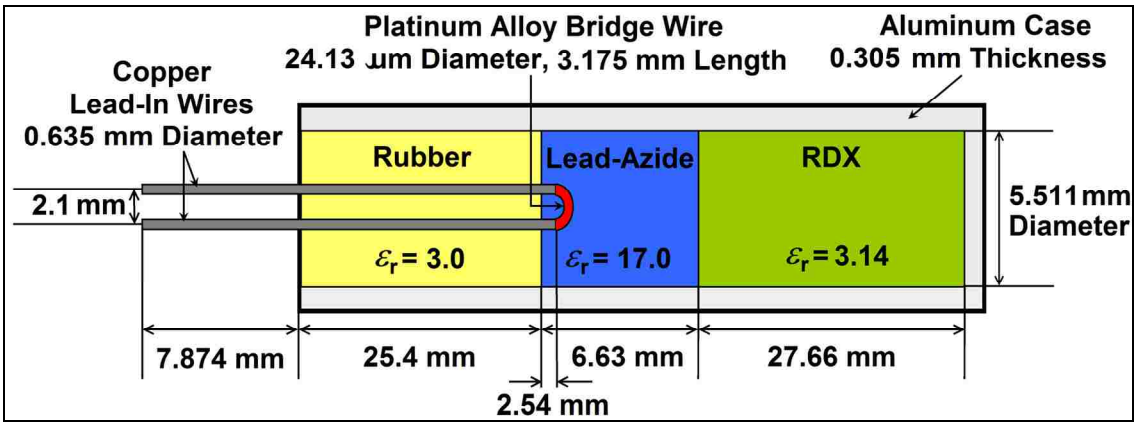

Figure 6: Illustration of the SABC geometry dimensions and EM properties.

Table 2: Material properties for the SABC model.

Detonator Part	Material	Dielectric Permittivity (ε_r)	Dielectric Permeability (μ_r)	Conductivity (σ)
Lead-In Wires	Copper	-	-	$5.8*10^7$
Case	Aluminum	-	-	$3.82*10^7$
Bridge Wire	Alloy	-	-	Effective
Seal	Rubber	3.0	1.0	0
Primary Explosive	Lead-Azide	17.0	1.0	0
Secondary Explosive	RDX	3.14	1.0	0

Table 3: Firing characteristics for the SABC [10].

Input Current DC (A)	Firing Time (ms)
0.7	9.0
1.0	6.5
1.5	5.0
2.0	4.6
5.0	2.0

Chapter Summary

A detonator is an explosive device used to initiate a much larger explosive charge. Detonators have a variety of applications, and are manufactured in several different styles. For purposes of research into the RF/MW initiation of detonators, only the hot-wire detonator is of interest. A generic representation of a hot-wire detonator has been developed, which describes both the physical dimensions of the detonator and the EM properties of its constituent parts. This information will be used to create a hot-wire detonator model for analyzing its EM characteristics when excited by an RF/MW source. Also, due to its prevalence, a similar representation has been developed for the SABC which will also be used to create an SABC model.

Chapter 3 – Formulation of the Detonator Electromagnetic Model

To investigate the input impedance characteristics of detonators, an analytical EM model is required that is representative of the physical parameters of the detonator. This approach is important for several reasons. First, different detonators can be quickly investigated by changing the dimensions inputted to the model. Since most hot-wire detonators are similarly constructed, a single EM methodology can be utilized while using specific dimensions of the detonator being investigated. Second, the results of the analytical model can be directly compared to those found through numerical modeling of the detonator geometry using computational methods (Chapter 5). Lastly, the purpose of the model is to determine specific detonator characteristics, such as input impedance and bridge wire current, across a frequency range of DC-9 GHz. This data will help determine resonances and EM properties at specific frequencies based on the physical dimensions of the particular detonator being investigated. Initially, the model will be based on the representative detonator characteristics given in Chapter 2.

When an EM field impinges upon a detonator, the energy must be coupled into the detonator to cause detonation. This investigation into detonator EM characteristics will assume that this coupling has already taken place, and that a certain voltage or current has been deposited onto the detonator. The detonator geometry can be excited by incident EM fields via either differential or common mode coupling of energy. In each case, the detonator will be modeled as a transmission line consisting of different sections connected in series. A model will be developed for each mode of excitation.

Detonator Transmission Line Model – Differential Mode

Differential Mode Excitation

Differential mode excitation occurs when incident EM energy is coupled across the two lead-in wires outside the detonator case. This develops a voltage across the two lead-in wires, causing a current to flow through the bridge wire. This is typically how a detonator is ignited in practice, as described in detail in Chapter 2. A diagram showing differential mode excitation is seen below as Figure 1, where the bridge wire is depicted as a load impedance at the end of the transmission line.

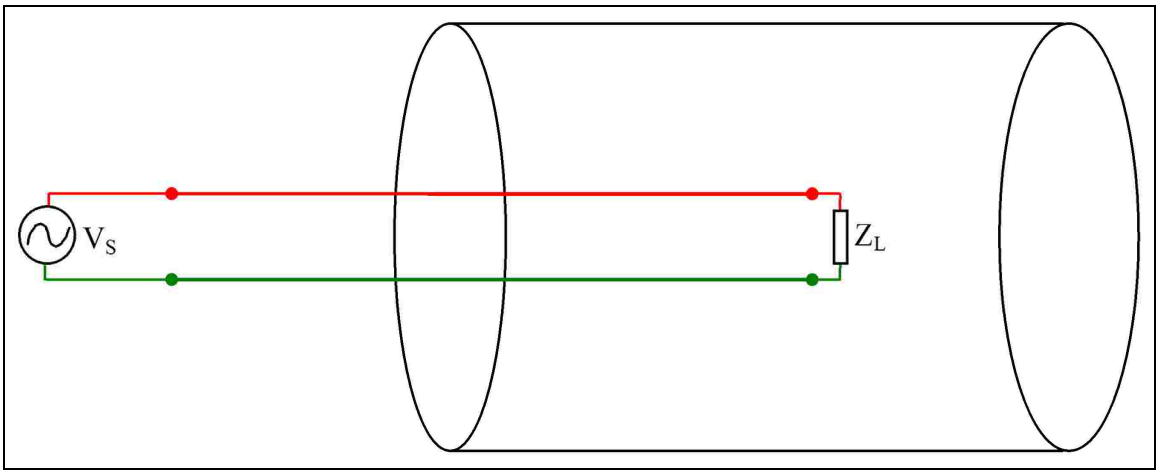

Figure 1: Drawing of detonator differential mode excitation.

In this mode of excitation, the detonator consists of two different types of transmission line, a two-wire line and a twinaxial line, connected in series and terminated in a load impedance. The two-wire section is simply the lead-in wires in air. The twinaxial section is located within the detonator geometry and consists of two wires encompassed within a cylindrical sheath of metal. Figure 2 illustrates how parts of the detonator are represented by each transmission line type. Using this representation, the detonator's material properties can be used with transmission line equations for each transmission line type to determine the constituent parameters for developing an analytical EM model.

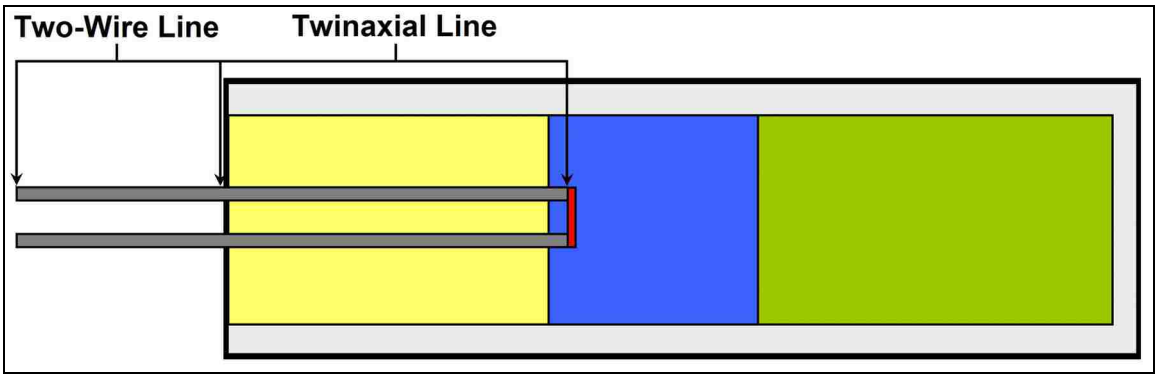

Figure 2: Illustration of transmission line sections of a detonator for differential mode excitation.

Transmission Line Characteristics - Two-Wire Line

Each portion of the transmission line model consists of its own set of EM characteristics. These characteristics can be calculated based on the transmission line type and dielectric properties for each section of the detonator. For reference the detonator dimension diagram from Chapter 2 is reproduced here as Figure 3. The two-wire portion of the detonator has a cross-section as given in Figure 4, indicating lead-in wire diameter (d) and spacing (s).

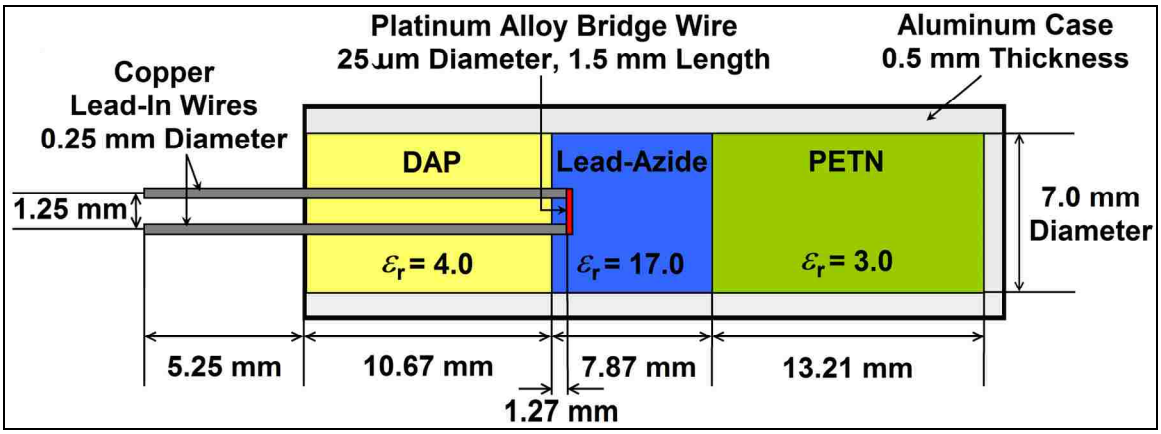

Figure 3: Illustration of the generic detonator geometry dimensions and EM properties.

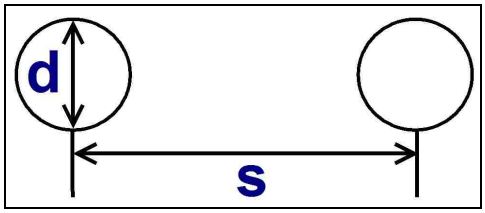

Figure 4: Illustration of the two-tire transmission line portion of a detonator.

The parameters of the two-wire line per-unit length are well understood and can be easily calculated [17]. The subscript 'a' will be used to denote properties of the two-wire transmission line in air.

$$P = \frac{s}{d} = 5 \quad , \tag{1}$$

$$L_a = \frac{\mu_r \mu_0}{\pi} \cosh^{-1}\left(P\right) = 0.917 \frac{\mu H}{m} \quad \text{, and} \tag{2}$$

$$C_a = \frac{\pi \varepsilon_r \varepsilon_0}{\cosh^{-1}\left(P\right)} = 12.13 \frac{pF}{m} \quad . \tag{3}$$

Alternatively, the transmission line parameters can be found using the characteristic impedance and the wave impedance [17]. Here, the ratio of the characteristic impedance to the wave impedance is used with the permittivity and permeability to determine the transmission line per-unit inductance and capacitance.

$$\begin{aligned} Z_{oa} &= 120 \cosh^{-1}(P) \quad , \\ &= 120 \cosh^{-1}(5) \\ &= 275.10\ \Omega \end{aligned} \tag{4}$$

$$Z_{wa} = \sqrt{\frac{\mu_0}{\varepsilon_0}} = 376.734 \Omega \quad , \tag{5}$$

$$f_{ga} = \frac{Z_{oa}}{Z_{wa}} = \frac{275.09}{376.734} = 0.730 \quad , \tag{6}$$

$$L_a = \mu_0 f_{ga} = 0.917 \frac{\mu H}{m} \quad \text{, and} \tag{7}$$

$$C_a = \frac{\varepsilon_0}{f_{ga}} = 12.13 \frac{pF}{m} \quad (8)$$

The wave impedance method produces the same results as using separate equations for the inductance and capacitance. Since this method is slightly simpler and will be needed for subsequent twinaxial sections, the wave impedance method will be used for consistency and ease of programming.

Transmission Line Characteristics - Twinaxial Line

The twinaxial portion of the detonator has a cross-section as given in Figure 5, indicating the lead-in wire diameter (d) and spacing (s) along with the inner diameter of the outer case (D). The input impedance of the twinaxial line in differential mode is given in [18, 19] and its approximate inductance can be found in [20]. Since exact equations for the capacitance of a twinaxial line could not be found, it is desirable to use the wave impedance method to calculate both the inductance and capacitance of this transmission line.

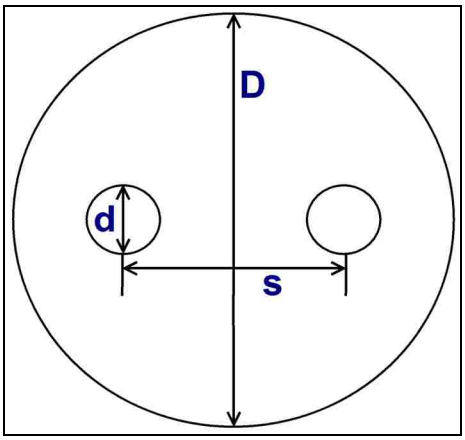

Figure 5: Illustration of the twinaxial transmission line portion of a detonator.

To validate this approach, the inductance calculated directly will be compared with that found using the wave impedance method. The subscript 's' will be used to denote

properties of the twinaxial transmission line within the seal portion of the detonator. From [20], the DC inductance of a two-wire line consisting of a signal on one wire, and a return on the other is given as:

$$L_{DC} = 4 \cdot 10^{-7} \left[\ln\left(\frac{2s}{d} \right) + \frac{1}{4} \right] . \tag{9}$$

This equation will be used to approximate the inductance of the twinaxial line, as the sheath is not in close proximity to the wires (D >> s). The approximate inductance per-unit length of this line can be found by substituting its dimensions into (9):

$$L_{DC} = 4 \cdot 10^{-7} \left[\ln\left(\frac{2\left(1.25 * 10^{-3}\right)}{0.25 * 10^{-3}} \right) + \frac{1}{4} \right]$$

$$= 1.021 \frac{\mu H}{m} .$$

From [18, 19] the characteristic impedance of the seal section of the twinaxial line and subsequently the inductance per-unit length via the wave impedance method can be found by:

$$Z_{os} = \frac{1}{\pi} \sqrt{\frac{\mu}{\varepsilon}} \left(\ln\left[2P \left(\frac{1 - Q^2}{1 + Q^2} \right) \right] - \left[\frac{1 + 4P^2}{16P^4} \right] \cdot \left[1 - 4Q^2 \right] \right) , \tag{10}$$

$$Q = \frac{s}{D} = 0.179 , \tag{11}$$

$$Z_{os} = \frac{1}{\pi} \sqrt{\frac{\mu_0}{(4.0)\varepsilon_0}} \left(\ln\left[2(5) \left(\frac{1 - 0.179^2}{1 + 0.179^2} \right) \right] - \left[\frac{1 + 4(5)^2}{16(5)^4} \right] \cdot \left[1 - 4(0.179)^2 \right] \right)$$

$$= 133.69\Omega ,$$

$$Z_{ws} = \sqrt{\frac{\mu_0}{(4.0)\varepsilon_0}} = 188.37\Omega \quad , \tag{12}$$

$$f_{gs} = \frac{Z_{os}}{Z_{ws}} = \frac{133.69}{188.37} = 0.7097 \quad \text{, and} \tag{13}$$

$$L_s = \mu_0 f_{gs} = 0.892 \frac{\mu H}{m} \quad . \tag{14}$$

The difference between these two approaches is 12.6%, and is explained by the fact that the inductance formula does not take into account the sheath encompassing the two wires. However, since the detonator model will be used across a frequency range of DC-9 GHz, the inductance will change as the frequency increases, and so the frequency dependence of the inductance of the transmission line must be investigated.

The earlier equation used to calculate the inductance is modified to include a high frequency correction factor [20],

$$L_{HF} = 4 \cdot 10^{-7} \left[\ln\left(\frac{2s}{d}\right) + \frac{T}{4} \right] \quad . \tag{15}$$

Here, the value of the correction factor T is determined based on the value of X in (16) and is found from Table 52 [20]. The lead-in wires are made of copper, and assuming a conductivity at 20^0 C ($\sigma = 5.8*10^7$ S/m) the value of T can be found which corresponds to the calculated value of X. Finally, the frequency-corrected inductance can be found at 900 MHz.

$$X = 1.406*10^{-3} d\sqrt{f\sigma} = 80.325 \quad , \tag{16}$$

$$T = 0.0354 \quad \text{, and}$$

$$L_{HF} = 4 \cdot 10^{-7} \left[\ln\left(\frac{2(1.25)}{0.25} \right) + \frac{0.0354}{4} \right]$$

$$= 0.925 \frac{\mu H}{m} .$$

Comparing this frequency-corrected value of the inductance to that calculated earlier using the wave impedance method:

$$\Delta = \left(\frac{9.246 * 10^{-7} - 8.9187 * 10^{-7}}{9.246 * 10^{-7}} \right) * 100\% = 3.54\% .$$

With the frequency correction, the inductance calculation is within 4% of that calculated with the wave impedance method. Since the model is to be used from DC-9 GHz, the frequency-corrected inductance at 9 GHz will also be calculated and compared to the wave impedance inductance, which is constant across the entire frequency range. As the frequency and calculated value of X increase, the value of T decreases in Table 52, and above a certain value of X, the value of T becomes 0 [20]. At 9 GHz, T = 0, and the inductance can be found as:

$$L_{HF} = 4 \cdot 10^{-7} \left[\ln\left(\frac{2s}{d} \right) \right] \tag{17}$$

$$= 0.921 \frac{\mu H}{m} .$$

This is a decrease in inductance from the value calculated at 900 MHz of:

$$\Delta = \left(\frac{9.246 * 10^{-7} - 9.210 * 10^{-7}}{9.246 * 10^{-7}} \right) * 100\% = 0.39\% .$$

Also, the inductance at 9 GHz differs from the wave impedance value by:

$$\Delta = \left(\frac{9.210 * 10^{-7} - 8.9187 * 10^{-7}}{9.210 * 10^{-7}} \right) * 100\% = 3.16\% .$$

These results indicate that the wave impedance method, though constant across the frequency range, can be used for the entire frequency range without incurring a large error, based on frequency-dependent values calculated for the inductance. The largest error (12.6%) occurs at DC, which is of little importance when considering the investigation is primarily concerned with the high frequency characteristics of detonators.

Lastly, since it has been shown that the wave impedance method is a valid way to find the inductance per-unit length of the detonator twinaxial line in differential mode, it follows that the capacitance per-unit length can also be found in this way. The capacitance per-unit length of the seal section of the twinaxial line is calculated as:

$$C_s = \frac{(4.0)\varepsilon_0}{f_{gs}} = 49.90\frac{pF}{m}\ . \tag{18}$$

The second section of the twinaxial line is in the lead-azide portion of the detonator, so the per-unit length properties will be different. These values are again found using the wave impedance method along with the characteristic impedance (10-14, 18), and denoted with the subscript 'l'.

$$Z_{ol} = \frac{1}{\pi}\sqrt{\frac{\mu_0}{(17.0)\varepsilon_0}}\left(\ln\left[2(5)\left(\frac{1-0.179^2}{1+0.179^2}\right)\right]-\left[\frac{1+4(5)^2}{16(5)^4}\right]\cdot\left[1-4(0.179)^2\right]\right)$$
$$= 64.85\Omega\ ,$$

$$Z_{wl} = \sqrt{\frac{\mu_0}{(17.0)\varepsilon_0}} = 91.37\Omega\ ,$$

$$f_{gl} = \frac{Z_{ol}}{Z_{wl}} = \frac{64.85}{91.37} = 0.7097\ ,$$

$$L_l = \mu_0 f_{gl} = 0.892 \frac{\mu H}{m} \text{ , and}$$

$$C_l = \frac{(17.0)\varepsilon_0}{f_{gl}} = 212.07 \frac{pF}{m} \text{ .}$$

Transmission Line Characteristics - Including Loss

Since the lead-in wires within the differential mode detonator geometry are composed of copper, they have a finite conductivity, and thus dissipate a small amount of energy as current flows through them. This loss can easily be calculated, and will also be frequency-dependent [17]. As the frequency increases, the skin depth (δ) of the copper wires will decrease, effectively reducing the cross-sectional area of the wires on which current flows. This reduction in area will increase the amount of loss in the wires as the current becomes more confined, and is illustrated in Figure 6.

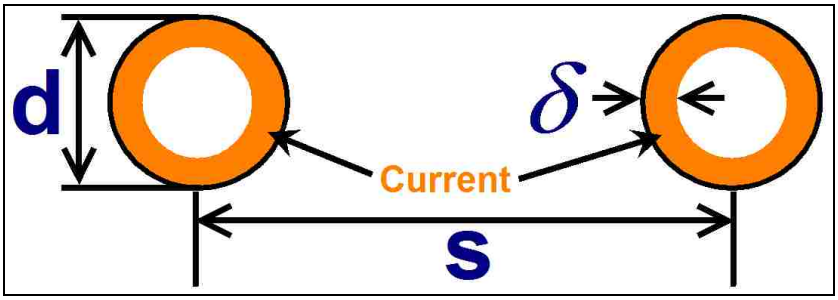

Figure 6: Illustration of current distribution along detonator during high frequency differential mode excitation.

In general, the characteristic impedance of a transmission line is found by [17]:

$$Z_0 = \sqrt{\frac{R + j\omega L}{G + j\omega C}} \text{ .} \qquad (19)$$

Since the dielectric regions of the detonator do not have a finite conductivity, G = 0 S/m and the characteristic impedance becomes

$$Z_0 = \sqrt{\frac{R + j\omega L}{j\omega C}} \quad . \tag{20}$$

For the calculation of the characteristic impedance in the preceding sections, the line was assumed to be lossless, and the wave impedance method was used to find the per-unit length inductance and capacitance. The assumed lossless characteristic impedance equation becomes

$$Z_0 = \sqrt{\frac{L}{C}} \quad . \tag{21}$$

In order to use the wave impedance to extract the inductance and capacitance from the characteristic impedance, which does not include the loss term, it must be shown that the resistive term does not contribute significantly to the characteristic impedance. For a low-loss line R << ωL with loss term (α) the characteristic impedance becomes [17]

$$\alpha = \frac{1}{2} R\left(\sqrt{\frac{C}{L}}\right) = \frac{R}{2Z_0} \Rightarrow Z_0 = \sqrt{\frac{L}{C}} \quad . \tag{22}$$

If the detonator transmission line is shown to be a low-loss line, then the resistive term can be separated from the characteristic impedance, and the lossless characteristic impedance can continue to be calculated as before to determine the inductance and capacitance of the line. At 900 MHz, using the conductivity of copper lead-in wires at 20^0 C, each wire has a resistance calculated based upon the annular ring on which the current resides due to the skin depth [17]

$$\delta = \sqrt{\frac{2}{\omega\mu\sigma}} \tag{23}$$

$$= 503.292\sqrt{\frac{1}{(900*10^{6})(5.8*10^{7})}}$$

$$= 2.20\ \mu\text{m}\ ,$$

$$A = \pi r^{2} = \pi\left[\left(\frac{0.25*10^{-3}}{2}\right)^{2} - \left(\frac{0.25*10^{-3}}{2} - 2.20*10^{-6}\right)^{2}\right]$$

$$= 1.715*10^{-9}\,m^{2}\ \text{, and}$$

$$R = \frac{1}{\sigma A} = \frac{1}{(5.8*10^{7})(1.715*10^{-9})} \tag{24}$$

$$= 10.05\ \frac{\Omega}{m}\ .$$

This resistance is for one lead-in wire and since the detonator has two such wires, the resistance term for the transmission line is

$$R = 20.10\ \frac{\Omega}{m}\ .$$

To check whether the transmission line is a low-loss line, the lowest inductance value along the line, found along the twinaxial portions of the detonator, is used:

$$R << \omega L = 2\pi(900*10^{6})(8.9187*10^{-7})$$

$$20.10 << 5043.41\ .$$

Since this statement is true at 900 MHz it will also be true at higher frequencies as the quantity ωL will increase much faster with frequency than will R. Therefore, the detonator transmission line in differential mode is a low-loss line and the resistance term can be separated from the characteristic impedance. Also, since the resistance term is based on current through two wires and is not dependent on dielectric properties, it is the

same for both portions of the twinaxial line as well as the two-wire line in air. However, this resistance term is not constant across frequency. The above calculation was performed at 900 MHz and, as mentioned previously, the resistance will increase with frequency. Figure 7 is a MatLAB [Version 7.0.1 (R14), The MathWorks Inc., Natick, MA, U.S.A.] plot of the resistance term across the frequency range of DC-9 GHz. Table 1 is a summary of the transmission line characteristics for each portion of the detonator under differential mode excitation.

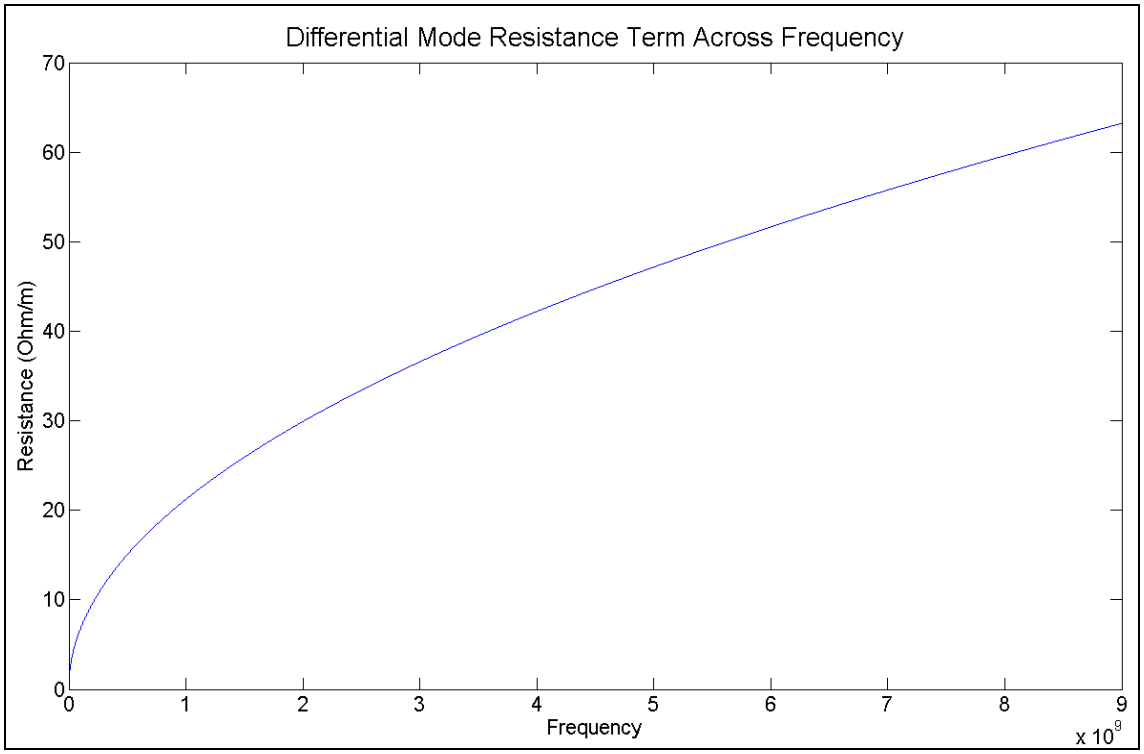

Figure 7: MatLAB plot of the detonator differential mode resistance term across the frequency range DC-9 GHz.

Table 1: Characteristics of each portion of the detonator transmission line in differential mode.

Property	Two-Wire Line	Twinaxial Line – Seal Section	Twinaxial Line – Lead-Azide Section
ε_r	1	4	17
μ_r	1	1	1
Z_o (Ω)	275.10	133.69	64.85
Z_w (Ω)	376.73	188.37	91.37
L (μH/m)	0.918	0.892	0.892
C (pF/m)	12.13	49.90	212.07
G (S/m)	0	0	0
R (900 MHz) (Ω/m)	20.10	20.10	20.10
R (9 GHz) (Ω/m)	63.20	63.20	63.20

Transmission Line Characteristics - Modeling the Bridge Wire as a Load Impedance

The lead-in wires are connected to the bridge wire within the lead-azide portion of the detonator. From a modeling perspective, this is analogous to terminating the detonator transmission line in a load impedance, Z_L. This was illustrated previously in Figure 1. To complete the determination of the transmission line characteristics the bridge wire load impedance must be determined.

The first property of the bridge wire which must be found is conductivity, as this facilitates the calculation of the bridge wire resistance at high frequencies. From the generic detonator characteristics described in Chapter 2, the bridge wire is 25 μm in diameter and 1.5 mm in length, with a nominal DC resistance of 1 Ω [6, 7]. Since the bridge wire is made of a platinum alloy, the generic bridge wire's effective conductivity can be calculated based on assumed characteristics. Given a 1 Ω resistance at DC, the conductivity is calculated as [17]:

$$A = \pi r^2 = \pi \left(\frac{25 * 10^{-6}}{2} \right)^2$$

$$= 4.91*10^{-10}\, m^2 ,$$

$$R = \frac{l}{\sigma A} = \frac{1.5*10^{-3}}{(\sigma_{eff})(4.91*10^{-10})} = 1 \text{ , and} \qquad (25)$$

$$\Rightarrow \sigma_{eff} = 3.056*10^6 \ \frac{S}{m} .$$

Using this effective conductivity, the high frequency resistance of the bridge wire can be found from the skin depth. At a frequency of 900 MHz the area of the annular ring on which the current resides will be calculated, and is analogous to the lead-in wire skin depth illustration in Figure 6. Finally, the resistance of the 1.5 mm bridge wire can be found:

$$\delta = 503.292\sqrt{\frac{1}{(900*10^6)(3.056*10^6)}}$$

$$= 9.60\ \mu\text{m} ,$$

$$A = \pi r^2 = \pi\left[\left(\frac{25*10^{-6}}{2}\right)^2 - \left(\frac{25*10^{-6}}{2} - 9.60*10^{-6}\right)^2\right]$$

$$= 4.644*10^{-10}\, m^2 \text{ , and}$$

$$R = \frac{l}{\sigma A} = \frac{1.5*10^{-3}}{(3.056*10^6)(4.644*10^{-10})}$$

$$= 1.057\ \Omega .$$

This resistance will increase with increasing frequency, as the area through which the current flows decreases. Figure 8 is a MatLAB plot of the bridge wire resistance across the frequency range DC-9 GHz.

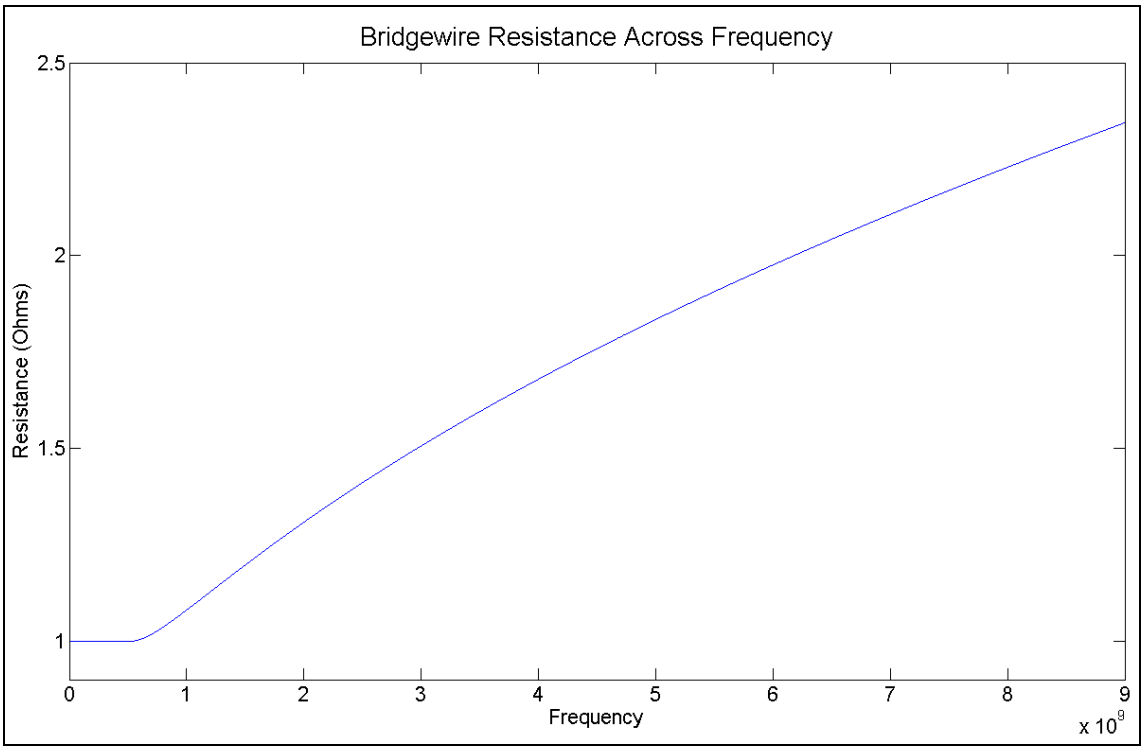

Figure 8: MatLAB plot of bridge wire resistance across the frequency range DC-9 GHz.

In addition to resistance, the bridge wire will also have a self-inductance. This self-inductance is that of an isolated wire at DC, and can be calculated as [20]:

$$L_{DC} = 2\cdot 10^{-7}(l)\left[\ln\left(\frac{4l}{d}\right)-\frac{3}{4}\right] H \tag{26}$$

$$= 2\cdot 10^{-7}\left(1.5*10^{-3}\right)\left[\ln\left(\frac{4\left(1.5*10^{-3}\right)}{25*10^{-6}}\right)-\frac{3}{4}\right]$$

$$= 1.419 \text{ nH} .$$

However, this investigation will include a frequency sweep from DC to 9 GHz. For high frequency excitation, the self-inductance formula includes a frequency-dependent correction factor [20], given as:

$$L_{HF} = 2\cdot 10^{-7}(l)\left[\ln\left(\frac{4l}{d}\right)+\frac{T}{4}-1\right] . \tag{27}$$

Here, the value of T is determined based on the value of X (16) and is found from Table 52 [20]. Using the effective conductivity calculated earlier for the bridge wire ($\sigma = 3.056*10^6$ S/m) the value of T can be found which corresponds to the calculated value of X. Finally, the frequency-corrected inductance can be found.

At 9 GHz:

$X = 5.8$,

$T = 0.4809$, and

$$L_{HF} = 2\cdot 10^{-7}\left(1.5*10^{-3}\right)\left[\ln\left(\frac{4\left(1.5*10^{-3}\right)}{25*10^{-6}}\right)+\frac{0.4809}{4}-1\right]$$

$$= 1.38 \text{ nH} .$$

The self-inductance of the bridge wire does change from DC to 9 GHz, and this change can be quantified as:

$$\Delta = \left(\frac{1.419*10^{-9}-1.38*10^{-9}}{1.38*10^{-9}}\right)*100\% = 2.83\% .$$

The resulting error of less than 3% indicates that the frequency correction in the self-inductance of the bridge wire is negligible, and that the DC self-inductance can be used across the entire frequency range from DC to 9 GHz. The final piece of the differential mode detonator transmission line model is the bridge wire, which is modeled as a frequency-dependent load impedance

$$Z_L(f) = R(f) + j2\pi f \cdot L_{DC}\ \Omega . \tag{28}$$

Figure 9 is a MatLAB plot of the bridge wire reactance across frequency. As expected, since the self-inductance remains constant, the reactance increases linearly with frequency.

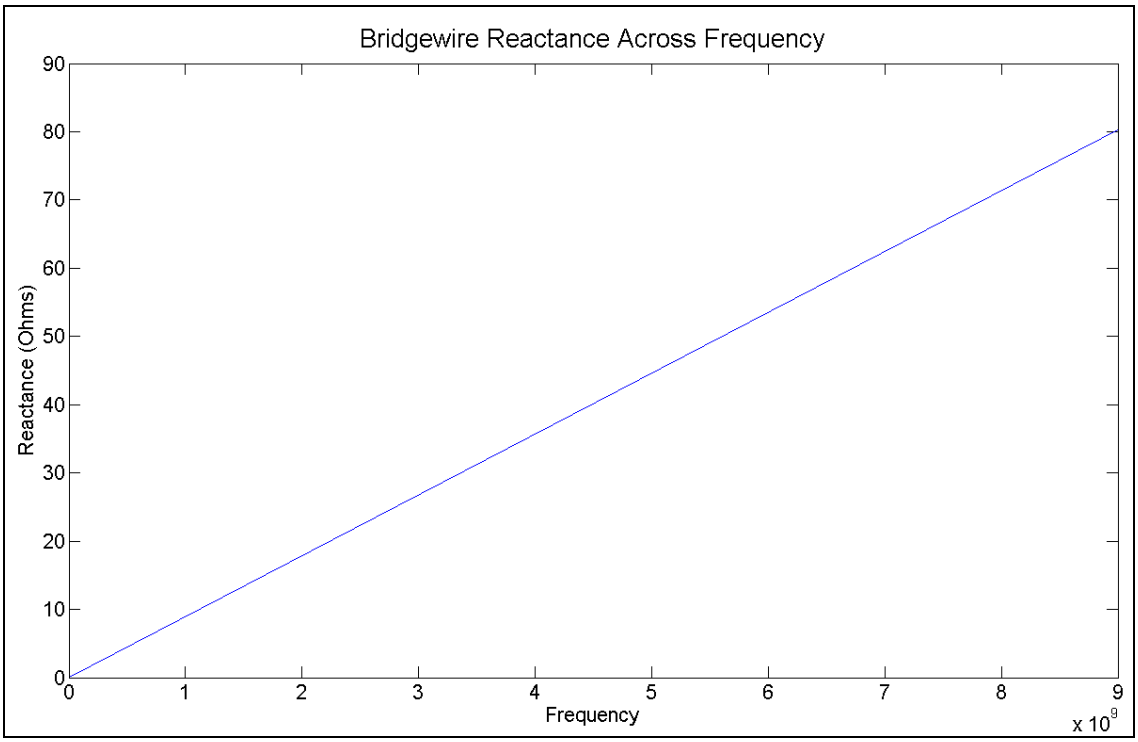

Figure 9: MatLAB plot of bridge wire reactance across the frequency range DC-9 GHz.

Using the Detonator Transmission Line Characteristics in an Electromagnetic Model

With the resistance, inductance, and capacitance calculated for each portion of the detonator transmission line along with the bridge wire load impedance, an analytical model must be developed to use these values for accurately representing the detonator in a mathematical form. In general, the voltage and current along a transmission line in the Z direction can be found using the telegrapher's equations [17]:

$$\frac{dV(z)}{dz} = -\left(R + j\omega L\right) I(z) \text{ , and} \tag{29}$$

$$\frac{dI(z)}{dz} = -\left(G + j\omega C\right) V(z) \text{ .} \tag{30}$$

The telegrapher's equations can be easily expressed in matrix form, while also taking G = 0 S/m for the detonator transmission line:

$$\frac{d}{dz}\begin{bmatrix} V(z) \\ I(z) \end{bmatrix} = -\begin{bmatrix} 0 & R + j\omega L \\ j\omega C & 0 \end{bmatrix} \cdot \begin{bmatrix} V(z) \\ I(z) \end{bmatrix} . \tag{31}$$

To solve the coupled telegrapher's equations in matrix form, the product integral method will be used [21]. This representation simplifies the solution of the coupled differential equations when expressed in matrix form. Below, the telegrapher's equations are solved at an arbitrary point z_2 given the voltage and current at a point z_1. Also, a $'$ has been added to R, L, and C to indicate that these are per-unit length parameters of the transmission line:

$$\frac{d}{\mathrm{dz}}\begin{bmatrix} V(z_2) \\ I(z_2) \end{bmatrix} = -\begin{bmatrix} 0 & R' + j\omega L' \\ j\omega C' & 0 \end{bmatrix} \cdot \begin{bmatrix} V(z_1) \\ I(z_1) \end{bmatrix} , \tag{32}$$

$$\frac{d}{\mathrm{dz}}\begin{bmatrix} V(z_2) \\ I(z_2) \end{bmatrix} = \Gamma \cdot \begin{bmatrix} V(z_1) \\ I(z_1) \end{bmatrix} , \tag{33}$$

$$\begin{bmatrix} V(z_2) \\ I(z_2) \end{bmatrix} = \left[\prod_{z_1}^{z_2} e^{\Gamma dz'} \right] \cdot \begin{bmatrix} V(z_1) \\ I(z_1) \end{bmatrix} \text{ , and} \tag{34}$$

$$\begin{bmatrix} V(z_2) \\ I(z_2) \end{bmatrix} = \begin{bmatrix} e^{\int_{z_1}^{z_2} \Gamma dz'} \end{bmatrix} \cdot \begin{bmatrix} V(z_1) \\ I(z_1) \end{bmatrix} . \tag{35}$$

Using this methodology, each of the three portions of the detonator will have a corresponding matrix solution of the telegrapher's equations, all resulting in a 2x2 matrix. As such, they can form a cascaded transmission line wherein the output voltage at the end

of one section becomes the input voltage to the next section through matrix multiplication. Figure 10 illustrates how the detonator will be divided into sections with corresponding Z locations.[2]

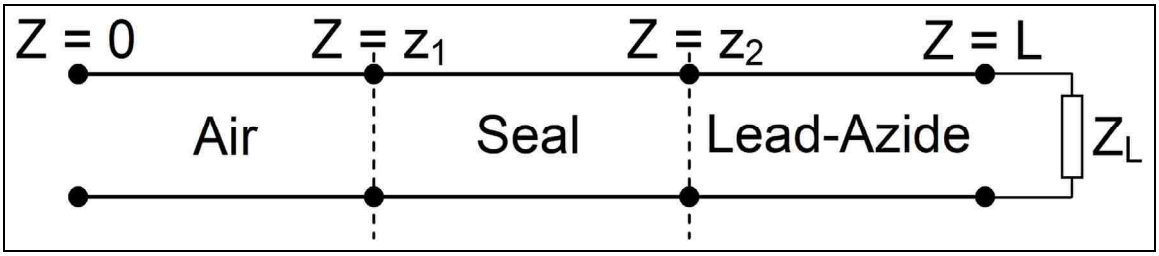

Figure 10: Illustration of dividing the detonator into sections with corresponding Z values.

The mathematical representation of the detonator then becomes as follows, using subscripts as before for each portion transmission line:

$$\begin{bmatrix} V(z_1) \\ I(z_1) \end{bmatrix} = \left[\prod_{0}^{z_1} e^{\Gamma_a dz'} \right] \cdot \begin{bmatrix} V(0) \\ I(0) \end{bmatrix}, \tag{36}$$

$$\begin{bmatrix} V(z_2) \\ I(z_2) \end{bmatrix} = \left[\prod_{z_1}^{z_2} e^{\Gamma_s dz'} \right] \cdot \begin{bmatrix} V(z_1) \\ I(z_1) \end{bmatrix}, \tag{37}$$

$$\begin{bmatrix} V(L) \\ I(L) \end{bmatrix} = \left[\prod_{z_2}^{L} e^{\Gamma_l dz'} \right] \cdot \begin{bmatrix} V(z_2) \\ I(z_2) \end{bmatrix}, \tag{38}$$

$$\begin{bmatrix} V(L) \\ I(L) \end{bmatrix} = \left[\prod_{z_2}^{L} e^{\Gamma_l dz'} \right] \cdot \left[\prod_{z_1}^{z_2} e^{\Gamma_s dz'} \right] \cdot \left[\prod_{0}^{z_1} e^{\Gamma_a dz'} \right] \cdot \begin{bmatrix} V(0) \\ I(0) \end{bmatrix}, \text{ and} \tag{39}$$

$$\begin{bmatrix} V(L) \\ I(L) \end{bmatrix} = \left[U(L,0) \right] \cdot \begin{bmatrix} V(0) \\ I(0) \end{bmatrix}. \tag{40}$$

[2] In this dissertation Z is used to represent both detonator axial position and impedance. The context should clarify which definition is appropriate for each occurrence of Z.

However, in the case of the detonator model, the input voltage V(0) and current I(0) must be solved for to find the overall input impedance of the detonator. In the above configuration, the voltage V(L) and current I(L) at the end of the detonator are the values being calculated. Therefore, the matrix equation must be inverted. This is accomplished by reversing the order of the matrices multiplied to construct [U(L, 0)] [21]:

$$\begin{bmatrix} V(0) \\ I(0) \end{bmatrix} = \left[U(L,0)\right]^{-1} \cdot \begin{bmatrix} V(L) \\ I(L) \end{bmatrix}, \tag{41}$$

$$\begin{bmatrix} V(0) \\ I(0) \end{bmatrix} = \left[U(0,L)\right] \cdot \begin{bmatrix} V(L) \\ I(L) \end{bmatrix}, \text{ and} \tag{42}$$

$$\begin{bmatrix} V(0) \\ I(0) \end{bmatrix} = \left[\prod_{z_1}^{0} e^{\Gamma_a dz'}\right] \cdot \left[\prod_{z_2}^{z_1} e^{\Gamma_s dz'}\right] \cdot \left[\prod_{L}^{z_2} e^{\Gamma_l dz'}\right] \cdot \begin{bmatrix} V(L) \\ I(L) \end{bmatrix}. \tag{43}$$

From Figure 3, the values of Z are as follows:

Z_1 = 5.25 mm
Z_2 = 15.92 mm
L = 17.19 mm.

Using these Z values along with the per-unit length transmission line parameters calculated earlier, the matrix equation can be constructed for a frequency of 900 MHz as follows:

Air Section:

$$\Gamma_a = -\begin{bmatrix} 0 & R + j\omega L_a \\ j\omega C_a & 0 \end{bmatrix} \tag{44}$$

$$= -\begin{bmatrix} 0 & 20.10 + j5191.17 \\ j0.0686 & 0 \end{bmatrix}, \text{ and}$$

$$\prod_{z_1}^{0} e^{\Gamma_a dz'} = \prod_{0.00525}^{0} e^{\Gamma_a dz'} = e^{\int_{0.00525}^{0} \Gamma_a dz'} = e^{\Gamma_a (0-0.00525)}$$

$$= M_a = \begin{bmatrix} 0.995 & 0.105 + j27.20 \\ j0.00036 & 0.995 \end{bmatrix}. \tag{45}$$

Seal Section:

$$\Gamma_s = -\begin{bmatrix} 0 & R + j\omega L_s \\ j\omega C_s & 0 \end{bmatrix} \tag{46}$$

$$= -\begin{bmatrix} 0 & 20.10 + j5043.41 \\ j0.2822 & 0 \end{bmatrix}, \text{ and}$$

$$\prod_{z_2}^{z_1} e^{\Gamma_s dz'} = \prod_{0.01592}^{0.00525} e^{\Gamma_s dz'} = e^{\int_{0.01592}^{0.00525} \Gamma_s dz'} = e^{\Gamma_s (0.00525-0.01592)} \tag{47}$$

$$= M_s = \begin{bmatrix} 0.92 + j0.0003 & 0.23 + j52.38 \\ j0.003 & 0.92 + j0.0003 \end{bmatrix}.$$

Lead-Azide Section:

$$\Gamma_l = -\begin{bmatrix} 0 & R + j\omega L_l \\ j\omega C_l & 0 \end{bmatrix} \tag{48}$$

$$= -\begin{bmatrix} 0 & 20.10 + j5043.41 \\ j1.199 & 0 \end{bmatrix}, \text{ and}$$

$$\prod_{L}^{z_2} e^{\Gamma_l dz'} = \prod_{0.01719}^{0.01592} e^{\Gamma_l dz'} = e^{\int_{0.01719}^{0.01592} \Gamma_l dz'} = e^{\Gamma_l (0.01592-0.01719)} \tag{49}$$

$$= M_l = \begin{bmatrix} 0.995 & 0.026 + j6.39 \\ j0.0015 & 0.995 \end{bmatrix}.$$

The three sections are then multiplied together to form the U[(0, L)] matrix:

$$[U(0,L)] = \left[\prod_{z_1}^{0} e^{\Gamma_a dz'}\right] \cdot \left[\prod_{z_2}^{z_1} e^{\Gamma_s dz'}\right] \cdot \left[\prod_{L}^{z_2} e^{\Gamma_l dz'}\right] \tag{50}$$

$$= [M_a] \cdot [M_s] \cdot [M_l] \tag{51}$$

$$= \begin{bmatrix} 0.715 + j0.0011 & 0.304 + j82.12 \\ j0.0046 & 0.872 + j0.0005 \end{bmatrix}.$$

Finally, the entire matrix equation becomes:

$$\begin{bmatrix} V(0) \\ I(0) \end{bmatrix} = \begin{bmatrix} 0.715 + j0.0011 & 0.304 + j82.12 \\ j0.0046 & 0.872 + j0.0005 \end{bmatrix} \cdot \begin{bmatrix} V(L) \\ I(L) \end{bmatrix} \tag{52}$$

.

This matrix representation of the detonator can be used to determine the input impedance of the detonator at 900 MHz, given the voltage and current at the end of the detonator. However, the voltage and current at the end of the detonator are unknown quantities. Since the detonator transmission line is terminated with the bridge wire load impedance, the voltage and current at the end of the detonator can be written in terms of this impedance:

$$V(L) = Z_L * I(L). \tag{53}$$

This relationship can then be written in matrix form as:

$$\begin{bmatrix} V(L) \\ I(L) \end{bmatrix} = \begin{bmatrix} Z_L \\ 1 \end{bmatrix} I(L). \tag{54}$$

Using the load impedance at 900 MHz results in the following boundary conditions for the bridge wire:

$$\begin{bmatrix} V(L) \\ I(L) \end{bmatrix} = \begin{bmatrix} 1.057 + j8.025 \\ 1 \end{bmatrix} I(L) \quad .$$

These boundary conditions are then applied to the detonator transmission line:

$$\begin{bmatrix} V(0) \\ I(0) \end{bmatrix} = \left[U(0,L) \right] \cdot \begin{bmatrix} Z_L \\ 1 \end{bmatrix} I(L) \tag{55}$$

$$= \left[U(0,L) \right] \cdot \begin{bmatrix} 1.057 + j8.025 \\ 1 \end{bmatrix} I(L) \quad .$$

Then the entire system can be represented at 900 MHz with the following:

$$\begin{bmatrix} V(0) \\ I(0) \end{bmatrix} = \begin{bmatrix} 0.715 + j0.0011 & 0.304 + j82.12 \\ j0.0046 & 0.872 + j0.0005 \end{bmatrix} \cdot \begin{bmatrix} 1.057 + j8.025 \\ 1 \end{bmatrix} I(L)$$

$$= \begin{bmatrix} 1.051 + j87.84 \\ 0.835 + j0.0048 \end{bmatrix} I(L) \quad .$$

Finally, the input impedance of the detonator at 900 MHz can be found by:

$$Z_{in} = \frac{V(0)}{I(0)} \tag{56}$$

$$= \frac{(1.051 + j87.84) I(L)}{(0.835 + j0.0048) I(L)}$$

$$= 1.87 + j105.18 \ \Omega \quad .$$

This process can be repeated to find the detonator input impedance at each frequency in the range DC-9 GHz.

Determining the Detonator Input Impedance Across the Frequency Range DC-9 GHz

Previously, the entire differential mode EM model describing the detonator from input to bridge wire was derived. This model was solved for the detonator input impedance at 900 MHz. In order to investigate the detonator input impedance across the entire frequency range of DC-9 GHz, the model must be programmed into a computer, a process accomplished using MatLAB.

Taking advantage of MatLAB's inherent use of matrices in programming, the model as described above was implemented using native MatLAB programming functionality. The detonator input impedance in differential mode was found with this program, using all given dimensions and characteristics of the generic detonator model. Figures 11 and 12 are plots of the real and imaginary parts of the detonator input impedance, respectively. Figure 13 is a plot of the magnitude of the detonator input impedance, and Figure 14 is a plot of the resistance of the detonator transmission line.

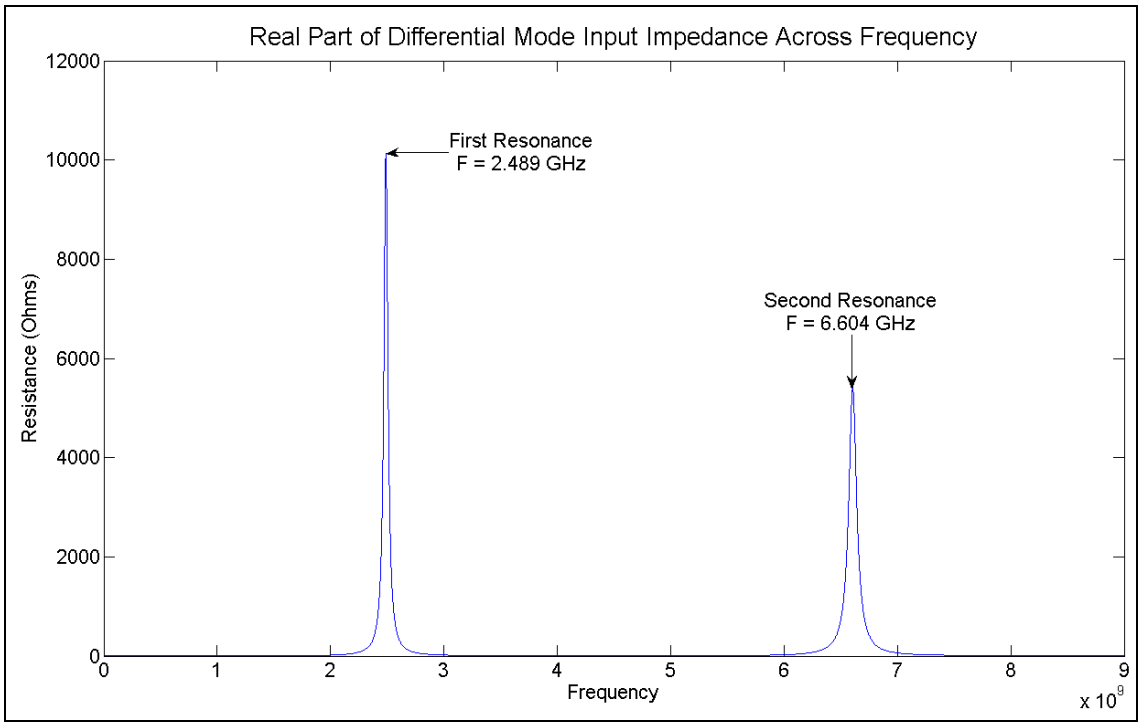

Figure 11: MatLAB plot of the real part of the differential mode detonator input impedance across the frequency range DC-9 GHz.

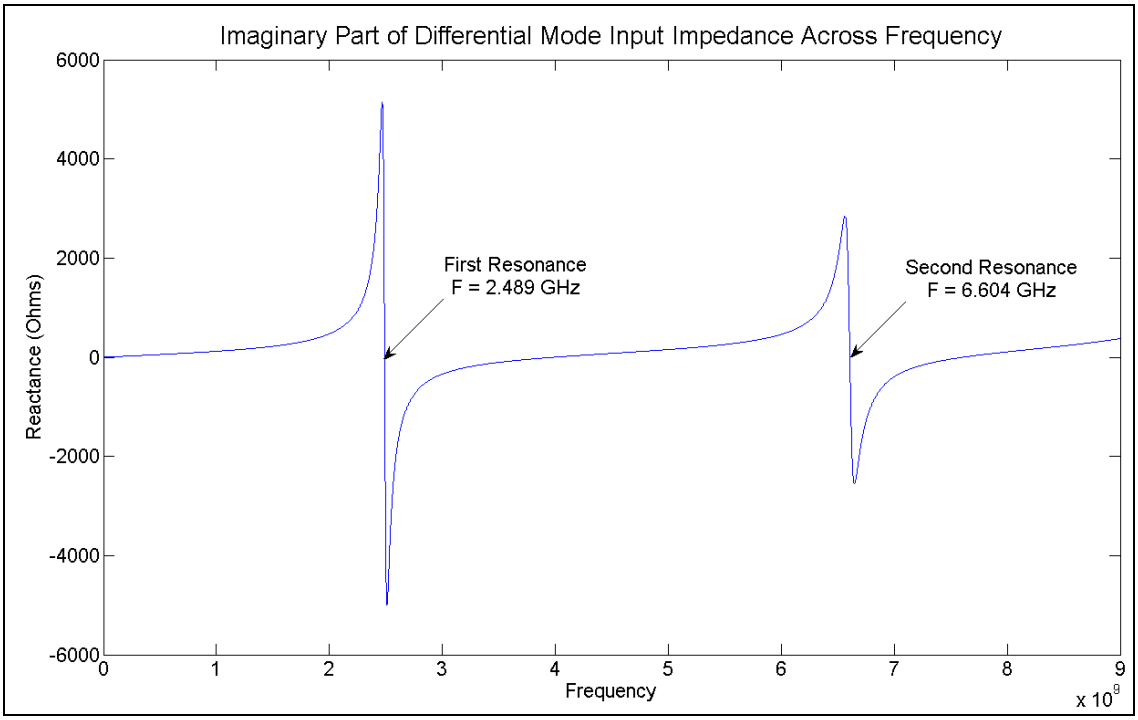

Figure 12: MatLAB plot of the imaginary part of the differential mode detonator input impedance across the frequency range DC-9 GHz.

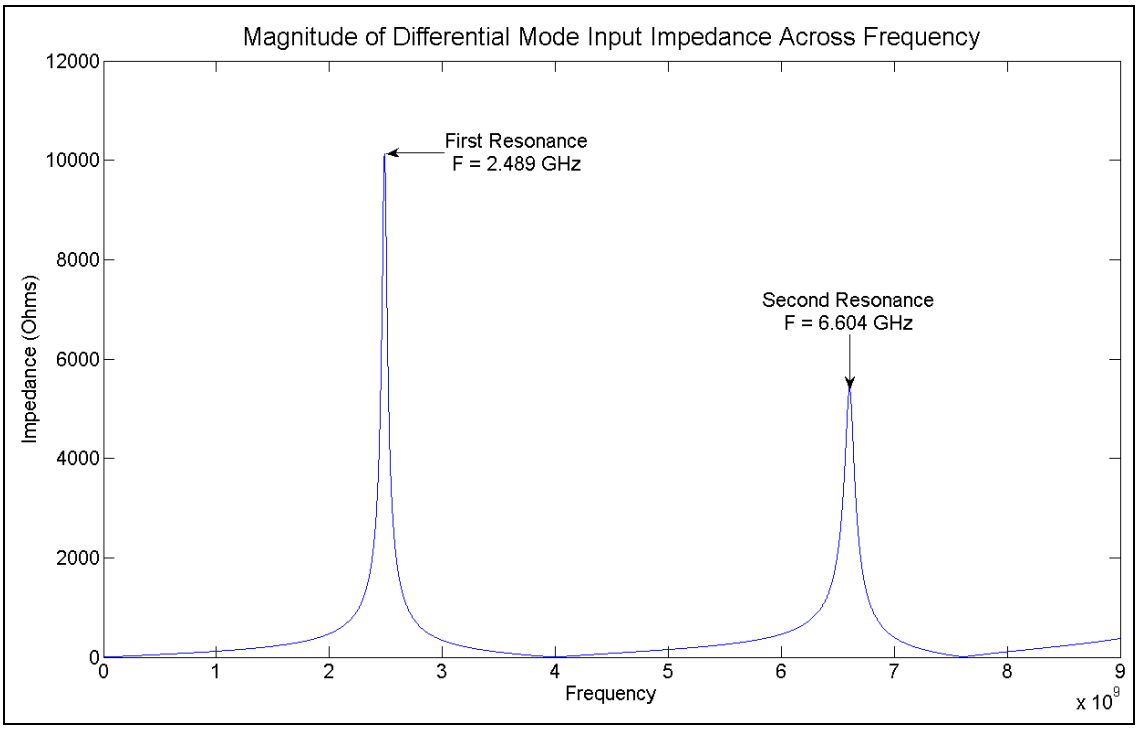

Figure 13: MatLAB plot of the magnitude of the differential mode detonator input impedance across the frequency range DC-9 GHz.

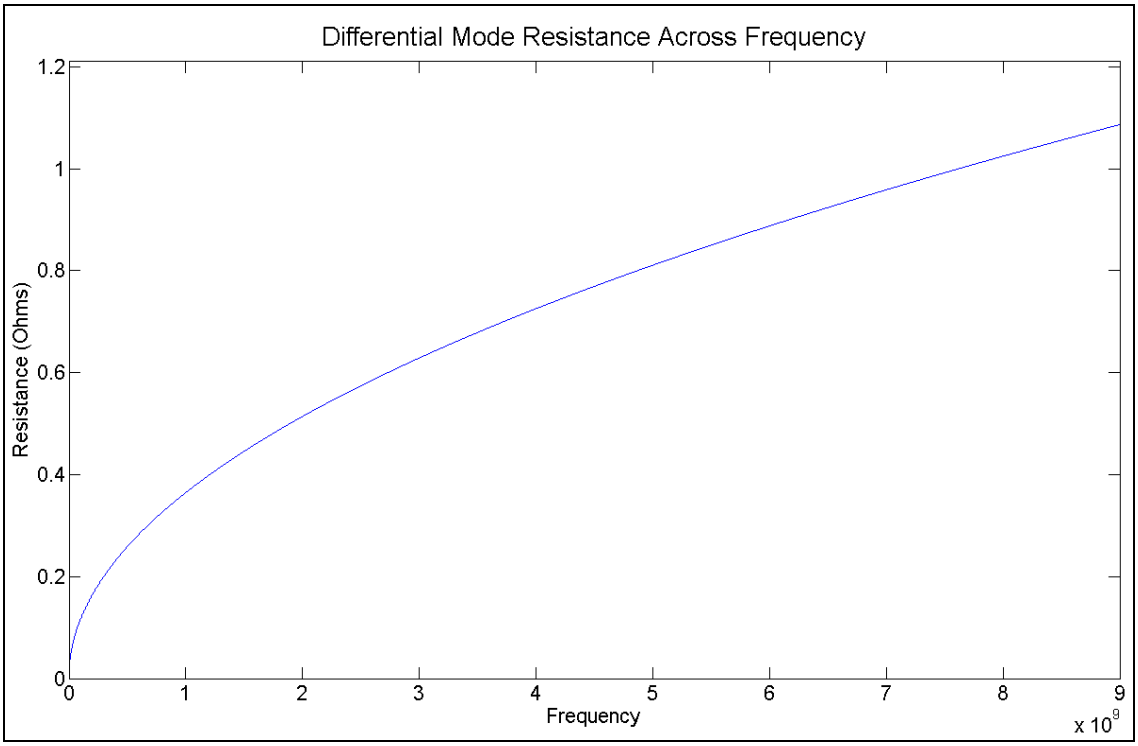

Figure 14: MatLAB plot of the differential mode detonator resistance across the frequency range DC-9 GHz.

From Figures 11-13, it can be seen that the generic detonator geometry resonates at 2.489 and 6.604 GHz, and that both the real and imaginary parts of the input impedance have identical resonant frequencies. Also, since the real part has a much larger value at resonance compared to the imaginary part, the magnitude of the input impedance follows the real part very closely. Lastly, the resistance of the detonator varies from approximately 0 Ω at low frequencies to 1.086 Ω at 9 GHz.

Detonator Transmission Line Model – Common Mode

Common Mode Excitation

Common mode excitation occurs when incident EM energy is coupled onto the edge of the detonator case. This coupling causes the two lead-in wires to be at the same potential relative to the outer sheath of the detonator. Since this potential difference is between the lead-in wires and the case, no current flows through the bridge wire and the detonator transmission line ends in an open. This excitation mode is shown in Figure 15.

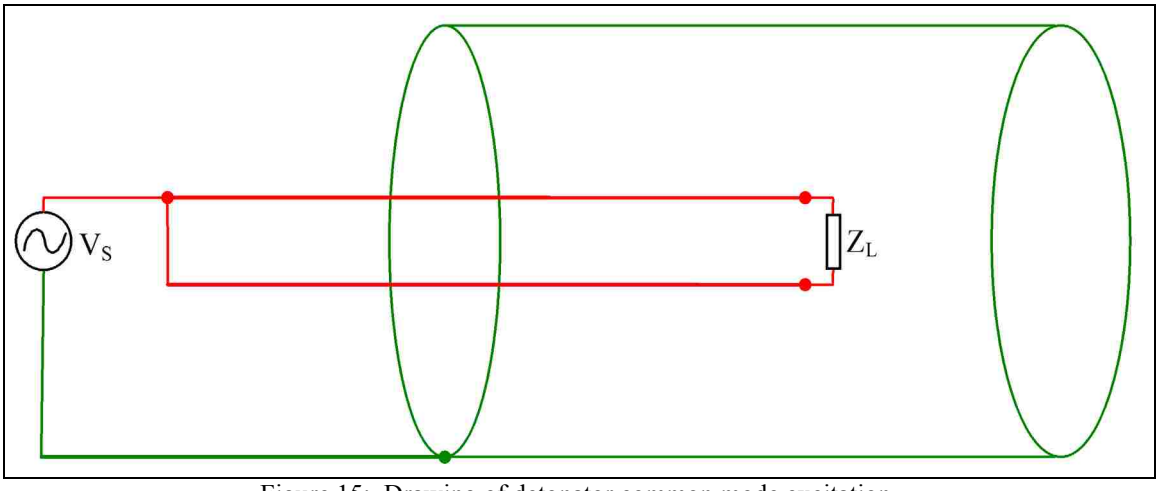

Figure 15: Drawing of detonator common mode excitation.

In this mode of operation, the lead-in wires on the outside of the detonator are not part of the transmission line as they are not surrounded by the detonator sheath. Since the common mode exists solely within the detonator itself, only the twin-axial transmission

line type is required to model the detonator during this excitation. This is shown in Figure 16.

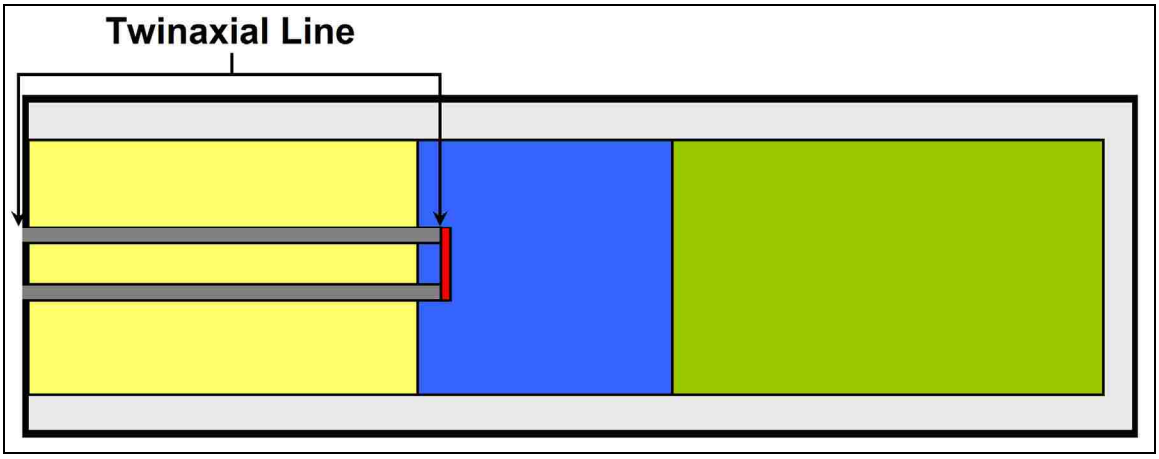

Figure 16: Illustration of transmission line sections of a detonator for common mode excitation.

Using this representation, the detonator's material properties can be used with transmission line equations for twinaxial line to determine the constituent parameters used to develop an analytical EM model.

Transmission Line Characteristics - Twinaxial Line

The common mode detonator transmission line consists of two twinaxial portions, both having a cross-section as given in Figure 17, indicating the lead-in wire diameter (d) and spacing (s) along with the outer (D1) and inner (D2) case diameters. The input impedance of the twinaxial line in common mode is given in [18, 19] and its inductance can be found in [20]. Since expressions for the capacitance of a twinaxial line could not be found, it is desirable to use the wave impedance method to calculate both the inductance and capacitance of this transmission line, as was done earlier for differential mode excitation. Refer back to Figure 3 for the dimensional drawing of the detonator.

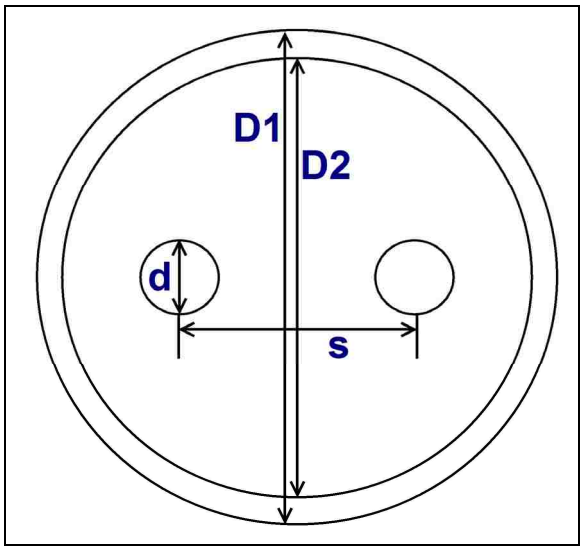

Figure 17: Illustration of the detonator common mode twinaxial transmission line.

To validate this approach, the inductance calculated directly will be compared with that found using the wave impedance method. The subscript 's' will be used to denote properties of the twinaxial transmission line within the seal portion of the detonator. From [20], the DC inductance of a transmission line consisting of a signal on two wires and a return on an encompassing outer sheath is given as:

$$L_{DC} = 2 \cdot 10^{-7} \left[\ln\left(\frac{D_1}{s}\right) + \frac{2\left(\frac{D_2^2}{D_1^2}\right)}{1-\left(\frac{D_2^2}{D_1^2}\right)} \cdot \ln\left(\frac{D_1}{D_2}\right) + \frac{1}{2}\ln\left(\frac{s}{2d}\right) + \ln(\zeta) - \frac{7}{8} \right] . \quad (57)$$

The geometric mean distance correction factor, ln(ζ), can be found from Table 4 in [20] which corresponds to the calculated ratio of D_2/D_1. The inductance per-unit length of this line can be found by using the generic detonator dimensions, and assuming a sheath thickness of 0.5 mm:

$$\frac{D_2}{D_1} = \frac{7}{8} = 0.875 , \quad (58)$$

$\ln\zeta = 0.0416$, and

$$L_{DC} = 2\cdot 10^{-7}\left[\ln\left(\frac{8}{1.25}\right)+\frac{2\left(\frac{7^2}{8^2}\right)}{1-\left(\frac{7^2}{8^2}\right)}\cdot\ln\left(\frac{8}{7}\right)+\frac{1}{2}\ln\left(\frac{1.25}{2(0.25)}\right)+0.0416-\frac{7}{8}\right]$$

$$= 0.471\frac{\mu H}{m}.$$

From [18, 19], the characteristic impedance of the seal section of the twinaxial line and subsequently the inductance per-unit length via the wave impedance method can be found by:

$$Z_{os} = \frac{1}{4\pi}\sqrt{\frac{\mu}{\varepsilon}}\left(\ln\left[\left(\frac{P(1-Q^4)}{2Q^2}\right)\right]-\left[\frac{1+4Q^4}{1+4P^4}\right]\cdot\left[1+4Q^4\left(\frac{5+4P^2}{1+4P^2}\right)\right]\right), \quad (59)$$

$$P = \frac{s}{d} = 5,$$

$$Q = \frac{s}{D} = 0.179,$$

$$Z_{os} = \frac{1}{4\pi}\sqrt{\frac{\mu_0}{(4.0)\varepsilon_0}}\left(\ln\left[\left(\frac{5(1-0.179^4)}{2(0.179)^2}\right)\right]-\left[\frac{1+4(0.179)^4}{1+4(5)^4}\right]\cdot\left[1+4(0.179)^4\left(\frac{5+4(5)^2}{1+4(5)^2}\right)\right]\right)$$

$$= 65.29\ \Omega,$$

$$Z_{ws} = \sqrt{\frac{\mu_0}{(4.0)\varepsilon_0}} = 188.367\ \Omega,$$

$$f_{gs} = \frac{Z_{os}}{Z_{ws}} = \frac{65.29}{188.37} = 0.3466, \text{ and}$$

$$L_s = \mu_0 f_{gs} = 0.436\frac{\mu H}{m}.$$

The difference between these two approaches is 7.46%. However, since this model will be used across a frequency range of DC-9 GHz, the inductance will change as

the frequency increases, and so the frequency dependence of the inductance of the transmission line must be investigated. The earlier equation used to calculate the inductance can be modified to include a high frequency correction factor [20]:

$$L_{HF} = 2\cdot 10^{-7}\left[\ln\left(\frac{D_1}{s}\right)+\frac{2\left(\frac{D_2^2}{D_1^2}\right)}{1-\left(\frac{D_2^2}{D_1^2}\right)}\cdot\ln\left(\frac{D_1}{D_2}\right)+\frac{1}{2}\ln\left(\frac{s}{2d}\right)+\ln(\zeta)+\frac{T}{8}-1\right] \quad (60)$$

Here, the value of T is determined based on the value of X (16) and is found from Table 52 in [20]. Using the values of X and T found earlier for the differential mode, the frequency-corrected inductance can be calculated.

At 900 MHz:

$X = 80.325$,

$T = 0.0354$, and

$$L_{HF} = 2\cdot 10^{-7}\left[\ln\left(\frac{8}{1.25}\right)+\frac{2\left(\frac{7^2}{8^2}\right)}{1-\left(\frac{7^2}{8^2}\right)}\cdot\ln\left(\frac{8}{7}\right)+\frac{1}{2}\ln\left(\frac{1.25}{2(0.25)}\right)+0.0416+\frac{0.0354}{8}-1\right]$$

$$= 0.447\frac{\mu H}{m}.$$

Comparing this frequency-corrected value of the inductance to that calculated earlier using the wave impedance method:

$$\Delta = \left(\frac{4.466*10^{-7}-4.356*10^{-7}}{4.466*10^{-7}}\right)*100\% = 2.46\% .$$

With the frequency correction, the inductance calculation is within 3% of that calculated with the wave impedance method. Since the model is to be used from DC-9 GHz, the

frequency-corrected inductance at 9 GHz will also be calculated and compared to the wave impedance inductance, which is constant across the entire frequency range. As the frequency and calculated value of X increase, the value of T decreases in Table 52, and above a certain value of X, the value of T becomes 0. At 9 GHz, T = 0, and the inductance can be found as:

$$L_{HF} = 2\cdot 10^{-7}\left[\ln\left(\frac{8}{1.25}\right)+\frac{2\left(\frac{7^2}{8^2}\right)}{1-\left(\frac{7^2}{8^2}\right)}\cdot\ln\left(\frac{8}{7}\right)+\frac{1}{2}\ln\left(\frac{1.25}{2(0.25)}\right)+0.0416-1\right]$$
$$= 0.446\frac{\mu H}{m}.$$

This is a decrease in inductance from the value calculated at 900 MHz of

$$\Delta = \left(\frac{4.466*10^{-7}-4.457*10^{-7}}{4.466*10^{-7}}\right)*100\% = 0.20\%.$$

Also, the inductance at 9 GHz differs from the wave impedance value by:

$$\Delta = \left(\frac{4.457*10^{-7}-4.356*10^{-7}}{4.457*10^{-7}}\right)*100\% = 2.27\%.$$

These results indicate that the wave impedance method, though constant across frequency, can be used across the entire frequency range without incurring a large error, based on frequency-dependent values calculated for the inductance. The largest error (7.46%) occurs at DC, which is of little importance when considering the investigation is primarily concerned with the high frequency characteristics of detonators.

Lastly, since it has been shown that the wave impedance method is a valid way to find the inductance per-unit length of the detonator twinaxial line in common mode, it

follows that the capacitance per-unit length can also be found in this way. The capacitance per-unit length of the seal section of the twinaxial line is calculated as:

$$C_s = \frac{(4.0)\varepsilon_0}{f_{gs}} = 102.18\frac{pF}{m} .$$

The second section of the twinaxial line is in the lead-azide portion of the detonator, and the per-unit length properties will be different. These values are again found using the wave impedance method along with the characteristic impedance, and denoted with the subscript 'l'.

$$Z_{ol} = \frac{1}{4\pi}\sqrt{\frac{\mu_0}{(17.0)\varepsilon_0}}\left(\ln\left[\left(\frac{5(1-0.179^4)}{2(0.179)^2}\right)\right] - \left[\frac{1+4(0.179)^4}{1+4(5)^4}\right]\cdot\left[1+4(0.179)^4\left(\frac{5+4(5)^2}{1+4(5)^2}\right)\right]\right)$$
$$= 31.67\ \Omega ,$$

$$Z_{wl} = \sqrt{\frac{\mu_0}{(17.0)\varepsilon_0}} = 91.37\Omega ,$$

$$f_{gl} = \frac{Z_{ol}}{Z_{wl}} = \frac{31.67}{91.37} = 0.3466 ,$$

$$L_l = \mu_0 f_{gl} = 0.436\frac{\mu H}{m} , \text{ and}$$

$$C_l = \frac{(17.0)\varepsilon_0}{f_{gl}} = 434.27\frac{pF}{m} .$$

Transmission Line Characteristics - Including Loss

Since the lead-in wires and outer sheath within the common mode detonator geometry are composed of copper and aluminum, respectively, they have a finite conductivity and thus dissipate a small amount of energy as current flows through them.

This loss can easily be calculated, and will also be frequency-dependent [17]. As the frequency increases, the skin depth of the copper wires (δ_1) and aluminum sheath (δ_2) will decrease, effectively reducing the cross-sectional area of the wires on which current flows. This reduction in area will increase the amount of loss in the wires and sheath as the current becomes more confined. An illustration of the current distribution within the detonator geometry is shown in Figure 18.

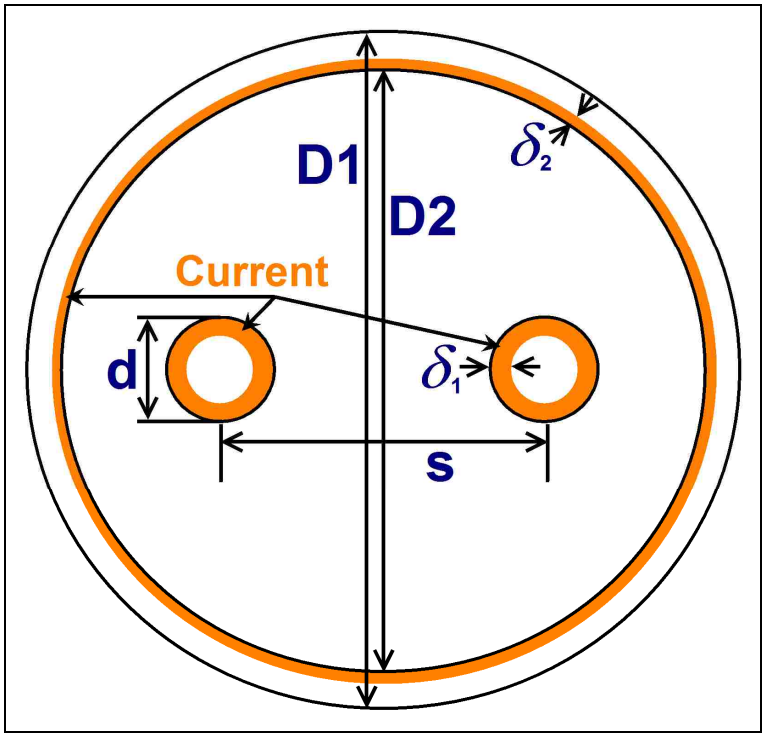

Figure 18: Illustration of current distribution along detonator during high frequency common mode excitation.

In general, the characteristic impedance of a transmission line is found by [17]:

$$Z_0 = \sqrt{\frac{R + j\omega L}{G + j\omega C}}$$

Since the dielectric regions of the detonator do not have a finite conductivity, G = 0 S/m, and the characteristic impedance becomes:

$$Z_0 = \sqrt{\frac{R + j\omega L}{j\omega C}} \quad .$$

In the calculation of the characteristic impedance in the preceding sections, the line was assumed to be lossless, and the wave impedance method was used to find the per-unit length inductance and capacitance. The assumed lossless characteristic impedance equation becomes:

$$Z_0 = \sqrt{\frac{L}{C}} \quad .$$

In order to use the wave impedance to extract the inductance and capacitance from the characteristic impedance which does not include the loss term, it must be shown that the resistive term does not contribute significantly to the characteristic impedance. For a low-loss line R << ωL with loss term (α) the characteristic impedance becomes [17]:

$$\alpha = \frac{1}{2} R\left(\sqrt{\frac{C}{L}}\right) = \frac{R}{2Z_0} \Rightarrow Z_0 = \sqrt{\frac{L}{C}} \quad .$$

If the detonator transmission line is shown to be a low-loss line, then the resistive term can be separated from the characteristic impedance, and the lossless characteristic impedance can continue to be calculated as before to determine the inductance and capacitance of the line. The conductivity of copper and aluminum at 20^0 C are used to find the resistance of the lead-in wires and sheath at 900 MHz. Each wire has a resistance as calculated earlier for the differential mode, based upon the annular ring on which the current resides due to the skin depth [17]. A similar calculation can be performed for the outer sheath.

$$\delta_2 = \sqrt{\frac{2}{\omega\mu\sigma}}$$

$$= 503.292\sqrt{\frac{1}{(900*10^6)(3.82*10^7)}}$$

$$= 2.71\ \mu\text{m},$$

$$A = \pi r^2 = \pi\left[\left(\frac{7*10^{-3}}{2} + 2.71*10^{-6}\right)^2 - \left(\frac{7*10^{-3}}{2}\right)^2\right]$$

$$= 5.972*10^{-8}\,m^2, \text{ and}$$

$$R = \frac{1}{\sigma A} = \frac{1}{(3.82*10^7)(5.972*10^{-8})}$$

$$= 0.438\ \frac{\Omega}{m}.$$

This resistance is for the outer sheath and since the detonator in common mode contains this along with both lead-in wires, the resistance term for the transmission line is:

$$R = 20.10 + 0.438$$

$$= 20.538\ \frac{\Omega}{m}.$$

To check if the transmission line is a low-loss line:

$$R << \omega L = 2\pi(900*10^6)(4.356*10^{-7})$$

$$20.538 << 2463.26.$$

Since this statement is true at 900 MHz it will also be true at higher frequencies as the quantity ωL will increase much faster with frequency than will R. Therefore, the detonator transmission line in common mode is a low-loss line and the resistance term can be separated from the characteristic impedance. Also, since the resistance term is

based on current through the two lead-in wires and sheath it is not dependent on dielectric properties, and is thus the same for both portions of the twinaxial line. However, this resistance term is not constant across frequency. The above calculation was performed at 900 MHz, and as mentioned previously, the resistance will increase with frequency. Figure 19 is a MatLAB plot of the common mode resistance term across the frequency range of DC-9 GHz. Table 2 is a summary of the transmission line characteristics for each section of the detonator under common mode excitation.

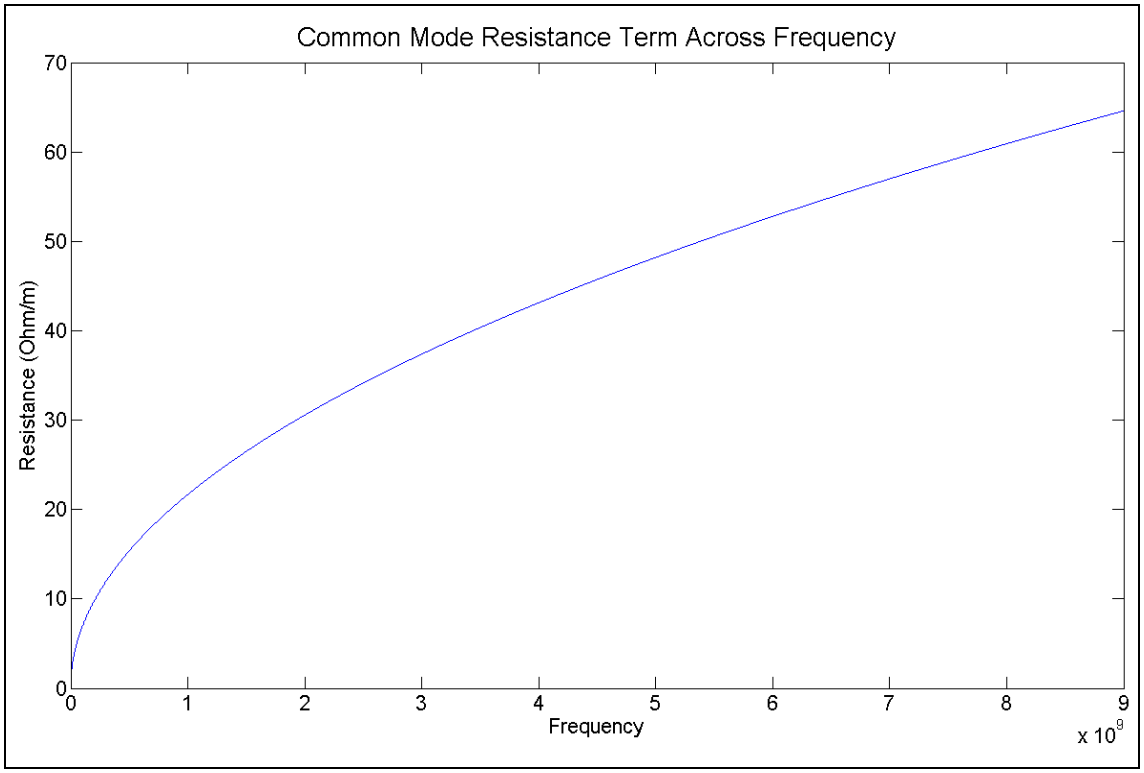

Figure 19: MatLAB plot of the detonator common mode resistance term across the frequency range DC-9 GHz.

Table 2: Characteristics of each portion of the detonator transmission line in common mode.

Property	Twinaxial Line – Seal Section	Twinaxial Line – Lead-Azide Section
ε_r	4	17
μ_r	1	1
Z_o (Ω)	65.29	31.67
Z_w (Ω)	188.37	91.37
L (μH/m)	0.436	0.436
C (pF/m)	102.18	434.27
G (S/m)	0	0
R (900 MHz) (Ω/m)	20.538	20.538
R (9 GHz) (Ω/m)	64.59	64.59

Using the Detonator Transmission Line Characteristics in an Electromagnetic Model

With the resistance, inductance, and capacitance calculated for each portion of the detonator transmission line, the analytical model must be developed to use these values for accurately representing the detonator in a mathematical form. Similarly to what was done for the differential mode model, the telegrapher's equations for each section will be solved using the product integral method, and each resulting matrix will be multiplied together forming a cascaded transmission line [21]. As the derivation of this model using matrix multiplication is identical to the differential mode case, it will not be repeated. Figure 20 illustrates how the detonator will be divided into sections with corresponding Z locations for the common mode model.

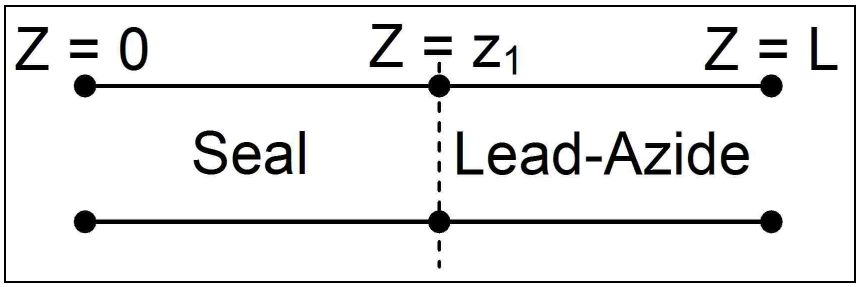

Figure 20: Illustration of dividing the detonator into sections with corresponding Z values for common mode excitation.

The mathematical representation of the detonator then becomes

$$\begin{bmatrix} V(0) \\ I(0) \end{bmatrix} = \left[\prod_{z_1}^{0} e^{\Gamma_s dz'} \right] \cdot \left[\prod_{L}^{z_1} e^{\Gamma_l dz'} \right] \cdot \begin{bmatrix} V(L) \\ I(L) \end{bmatrix}. \tag{61}$$

From Figure 3, the values of Z are as follows:

Z_1 = 10.67 mm
L = 11.94 mm.

Using these Z values along with the per-unit length transmission line parameters calculated earlier, the matrix equation can be constructed for a frequency of 900 MHz.

Seal Section:

$$\Gamma_s = -\begin{bmatrix} 0 & R + j\omega L_s \\ j\omega C_s & 0 \end{bmatrix}$$

$$= -\begin{bmatrix} 0 & 20.538 + j2465.52 \\ j0.578 & 0 \end{bmatrix}, \text{ and}$$

$$\prod_{z_1}^{0} e^{\Gamma_s dz'} = \prod_{0.01067}^{0} e^{\Gamma_s dz'} = e^{\int_{0.01067}^{0} \Gamma_s dz'} = e^{\Gamma_s (0 - 0.01067)}$$

$$= M_s = \begin{bmatrix} 0.92 + j0.0007 & 0.208 + j25.605 \\ j0.006 & 0.92 + j0.0007 \end{bmatrix}.$$

Lead-Azide Section:

$$\Gamma_l = -\begin{bmatrix} 0 & R + j\omega L_l \\ j\omega C_l & 0 \end{bmatrix}$$

$$= -\begin{bmatrix} 0 & 20.538 + j2465.52 \\ j2.456 & 0 \end{bmatrix}, \text{ and}$$

$$\prod_{L}^{z_1} e^{\Gamma_l dz'} = \prod_{0.01194}^{0.01067} e^{\Gamma_l dz'} = e^{\int_{0.01194}^{0.01067} \Gamma_l dz'} = e^{\Gamma_l (0.01067 - 0.01194)}$$

$$= M_l = \begin{bmatrix} 0.995 & 0.026 + j3.13 \\ j0.0031 & 0.995 \end{bmatrix}.$$

The two sections are then multiplied together to form the U[(0, L)] matrix.

$$[U(0,L)] = \left[\prod_{z_1}^{0} e^{\Gamma_s dz'}\right] \cdot \left[\prod_{L}^{z_1} e^{\Gamma_l dz'}\right] \tag{62}$$

$$= [M_s] \cdot [M_l] \tag{63}$$

$$= \begin{bmatrix} 0.836 + j0.0013 & 0.227 + j28.357 \\ j0.0088 & 0.897 + j0.0008 \end{bmatrix}.$$

Finally, the entire matrix equation becomes:

$$\begin{bmatrix} V(0) \\ I(0) \end{bmatrix} = \begin{bmatrix} 0.836 + j0.0013 & 0.227 + j28.357 \\ j0.0088 & 0.897 + j0.0008 \end{bmatrix} \cdot \begin{bmatrix} V(L) \\ I(L) \end{bmatrix}.$$

This matrix representation of the detonator can be used to determine the input impedance of the detonator at 900 MHz, given the voltage and current at the end of the detonator. However, the voltage and current at the end of the detonator are unknown quantities. Under common mode excitation, the detonator transmission line terminates in an open. The voltage and current at the end of the detonator in an open condition are [17]:

$$V(L) = 2 * V(L) \text{ , and} \tag{64}$$

$$I(L) = 0 \text{ .} \tag{65}$$

This can be written in matrix form as:

$$\begin{bmatrix} V(L) \\ I(L) \end{bmatrix} = \begin{bmatrix} 2 \\ 0 \end{bmatrix} V(L) \quad . \tag{66}$$

These boundary conditions are then applied to the detonator transmission line:

$$\begin{bmatrix} V(0) \\ I(0) \end{bmatrix} = \left[U(0,L) \right] \cdot \begin{bmatrix} 2 \\ 0 \end{bmatrix} V(L) \quad . \tag{67}$$

Then the entire system can be represented at 900 MHz with the following:

$$\begin{bmatrix} V(0) \\ I(0) \end{bmatrix} = \begin{bmatrix} 0.836 + j0.0013 & 0.227 + j28.357 \\ j0.0088 & 0.897 + j0.0008 \end{bmatrix} \cdot \begin{bmatrix} 2 \\ 0 \end{bmatrix} V(l)$$

$$= \begin{bmatrix} 1.672 + j0.003 \\ j0.0177 \end{bmatrix} V(l) \quad .$$

Finally, the input impedance of the detonator at 900 MHz can be found by:

$$Z_{in} = \frac{V(0)}{I(0)}$$

$$= \frac{(1.672 + j0.003)V(L)}{(j0.0177)V(L)}$$

$$= 0.112 - j94.716\ \Omega \quad .$$

This process can be repeated to find the detonator input impedance at each frequency in the range DC-9 GHz.

Determining the Detonator Input Impedance Across the Frequency Range DC-9 GHz

Previously, the entire common mode EM model describing the detonator from input to open was derived. This model was solved for the detonator input impedance at 900 MHz. In order to investigate the detonator input impedance across the entire frequency range of DC-9 GHz, the model must be programmed into a computer. This was accomplished using MatLAB, as was done for the differential mode.

Taking advantage of MatLAB's inherent use of matrices in programming, the model as described above was implemented using native MatLAB programming functionality. The detonator input impedance in common mode was found with this program, using all given dimensions and characteristics of the generic detonator model. Figures 21 and 22 are plots of the real and imaginary parts of the detonator input impedance, respectively. Figure 23 is a plot of the magnitude of the detonator input impedance, and Figure 24 is a plot of the resistance of the detonator transmission line.

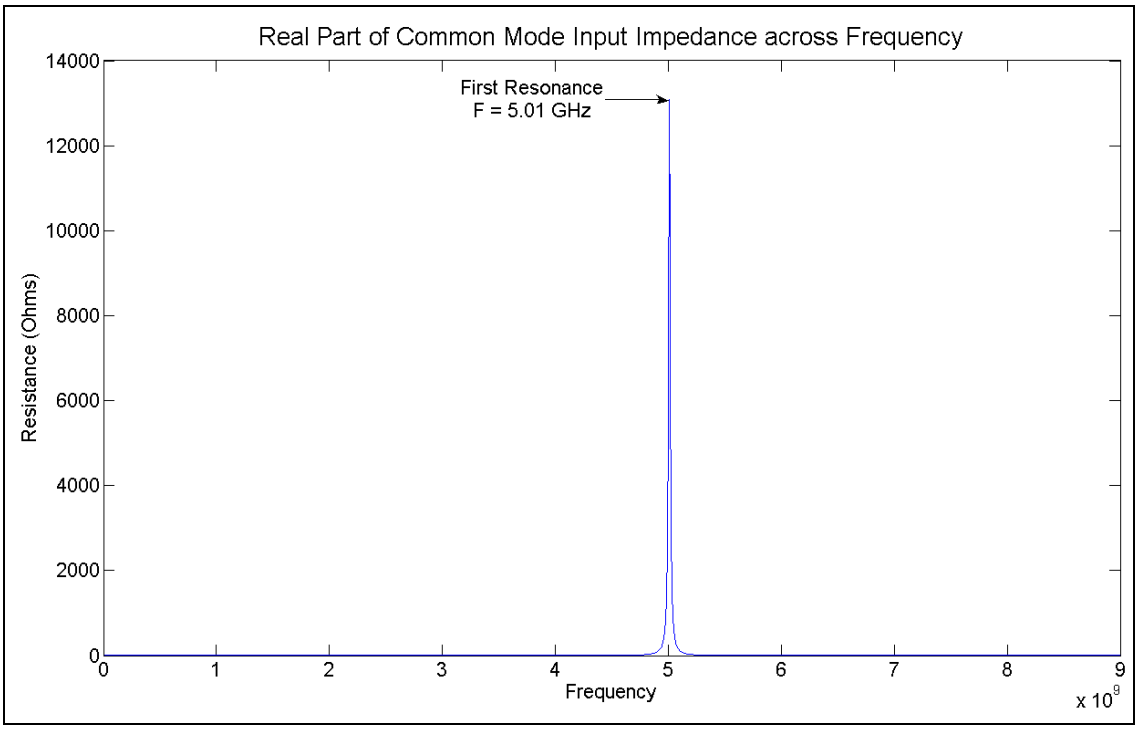

Figure 21: MatLAB plot of the real part of the common mode detonator input impedance across the frequency range DC-9 GHz.

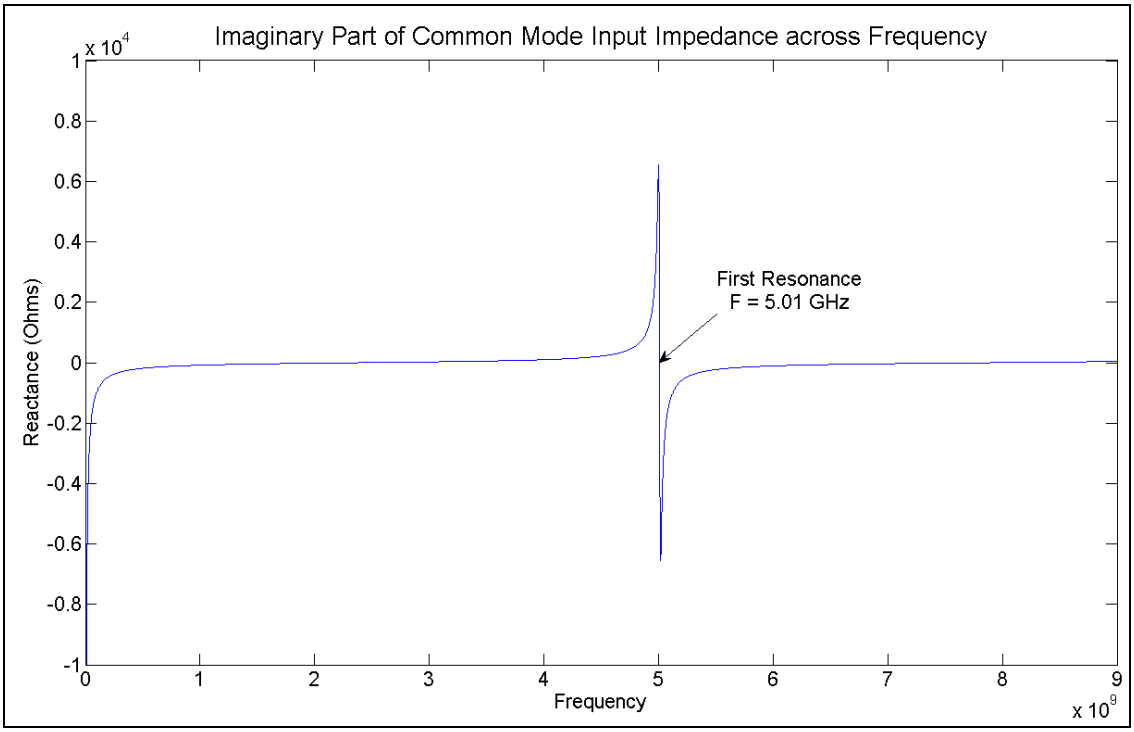

Figure 22: MatLAB plot of the imaginary part of the common mode detonator input impedance across the frequency range DC-9 GHz.

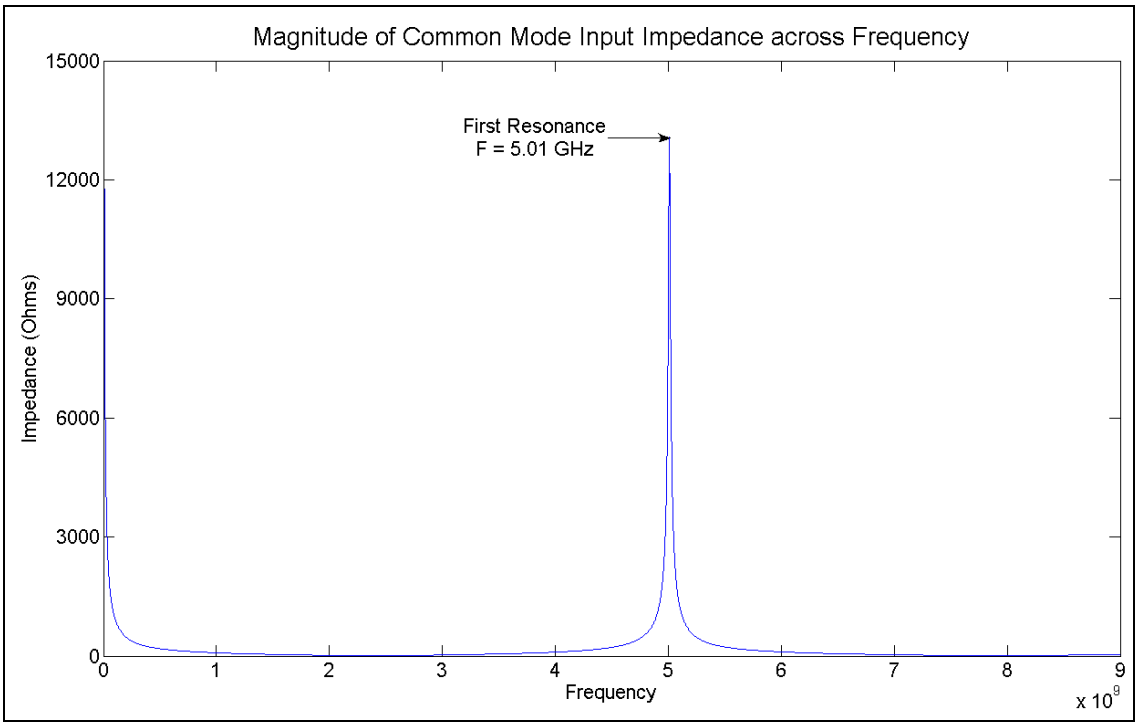

Figure 23: MatLAB plot of the magnitude of the common mode detonator input impedance across the frequency range DC-9 GHz.

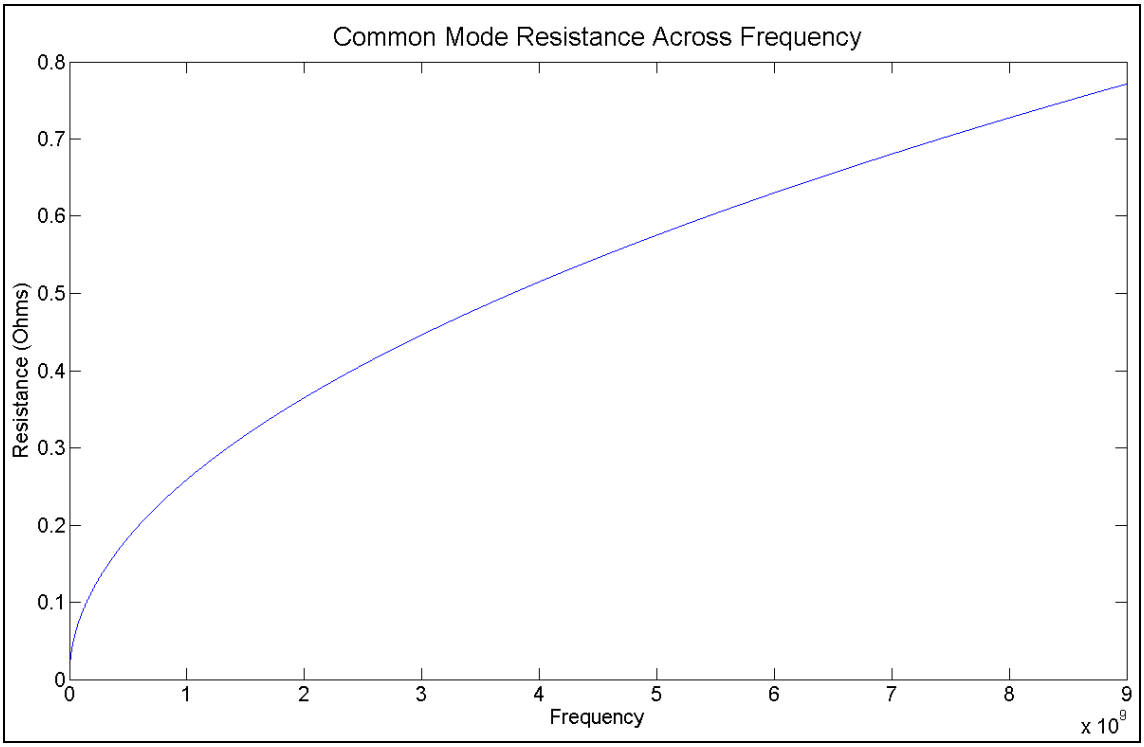

Figure 24: MatLAB plot of the common mode detonator resistance across the frequency range DC-9 GHz.

From Figures 21-23, it can be seen that the generic detonator geometry resonates at 5.01 GHz, and that both the real and imaginary parts of the input impedance have identical resonant frequencies. Also, since the real part has a value at resonance twice that of the imaginary part, the magnitude of the input impedance follows the real part very closely. Lastly, the resistance of the detonator varies from approximately 0 Ω at low frequencies to 0.771 Ω at 9 GHz.

Chapter Summary

In this chapter, an analytical EM model was developed and derived for the generic detonator geometry described in Chapter 2 for both differential and common mode excitation conditions. Using telegrapher's equations, product integral method, and matrix multiplication, the detonator was represented mathematically. The input impedance was found at 900 MHz for illustrative purposes, and then MatLAB was used to reproduce the calculations for the frequency range of DC-9 GHz.

Chapter 4 – Numerical Model Formulation and Analytical Model Modification

In the previous chapter, a 1-D analytical EM model for differential and common mode excitation of a generic detonator geometry was developed. Predictions were then made for the detonator input impedance across a frequency range of DC-9 GHz. In this chapter the 3-D numerical modeling set-up for simulating and determining detonator characteristics will be described. Also, several modifications will be made to the analytical model so that the predictions can be directly compared to these simulated results.

Description of ICEPIC

The simulations will be carried out using ICEPIC (Improved Concurrent Electromagnetic Particle In Cell), a powerful, parallelized, FDTD EM solver.[3] Due to its parallel architecture, EM simulations with very fine gridding can be performed using ICEPIC in a short period of time using the DoD MSRC (Department of Defense Major Shared Resource Center), a collection of state-of-the-art supercomputers.

Rendering the Detonator Geometry

The generic geometry, shown here again as Figure 1, can be re-created using ICEPIC in 3-D, and is excited with current source(s) at the beginning of the lead-in wires. This excitation represents the EM energy that has been assumed to have already coupled onto the detonator from some external source. These exciting source(s) can be set to any desired frequency with an amplitude that is ramped linearly from 0 to the desired value

[3] The particle simulating capability of ICEPIC will not be utilized during the course of this investigation.

over the course of three full cycles. Figures 2 through 4 are images of the ICEPIC rendering of the generic detonator geometry for differential mode excitation. Figure 2 is a perspective view of the detonator geometry and shows all of the detonator components, including the placement of the exciting current source that is connected across the lead-in wires to create a potential difference between them. Figure 3 is a top view of the geometry with the outer case removed. Figure 4 is a close-up view of the bridge wire with associated dimensions. To ensure a connection between the lead-in wires and the bridge wire, the lead-in wires were extended an additional 50 μm into the bridge wire. Also, the bridge wire in ICEPIC has a diameter of 150 μm instead of the prescribed 25 μm from Figure 1.

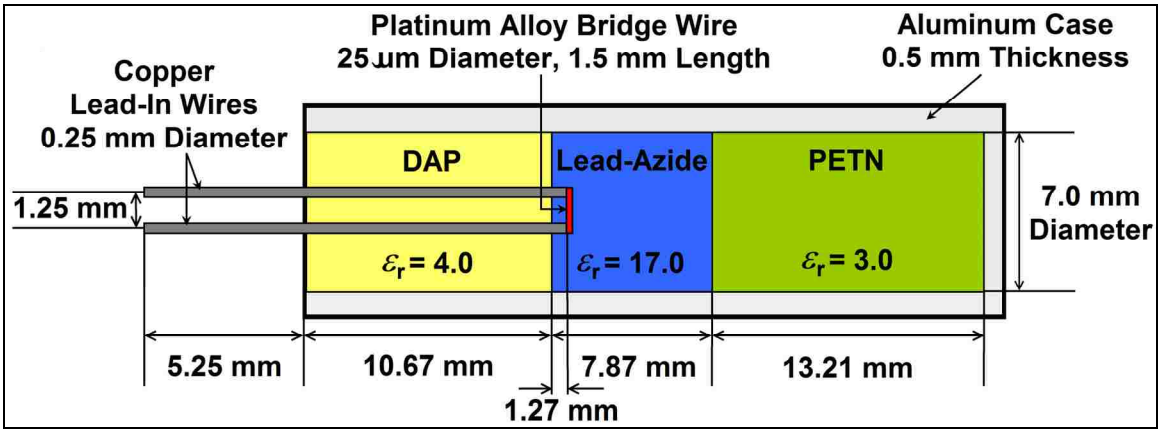

Figure 1: Illustration of the generic detonator geometry dimensions and EM properties.

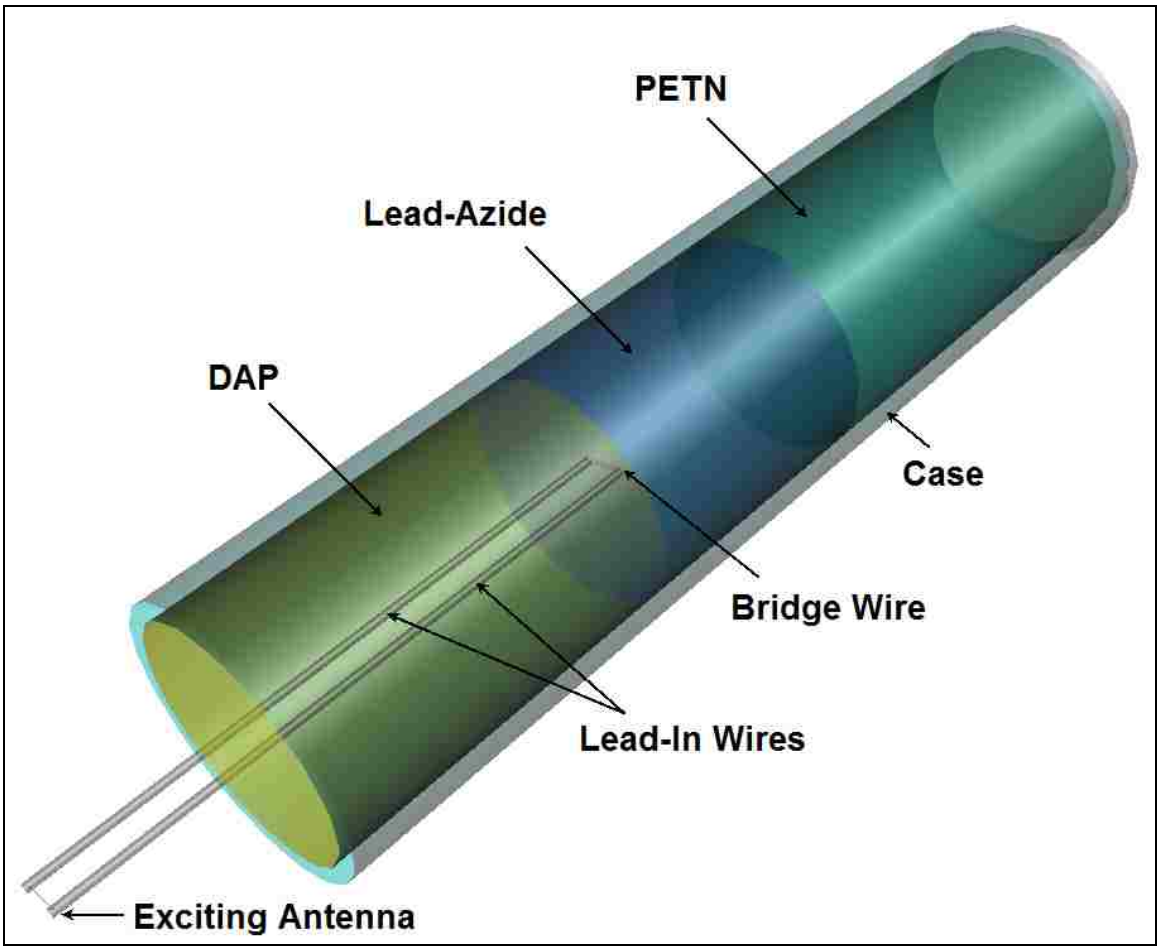

Figure 2: Perspective view of the ICEPIC rendering of the generic detonator geometry for differential mode excitation indicating detonator components and exciting antenna current source.

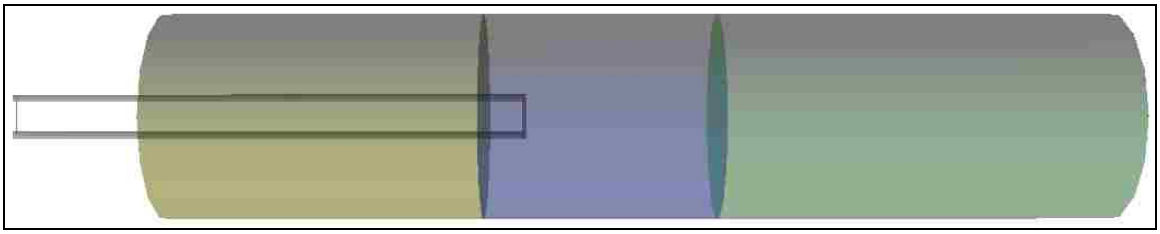

Figure 3: Top view of the ICEPIC rendering of the generic detonator geometry for differential mode excitation.

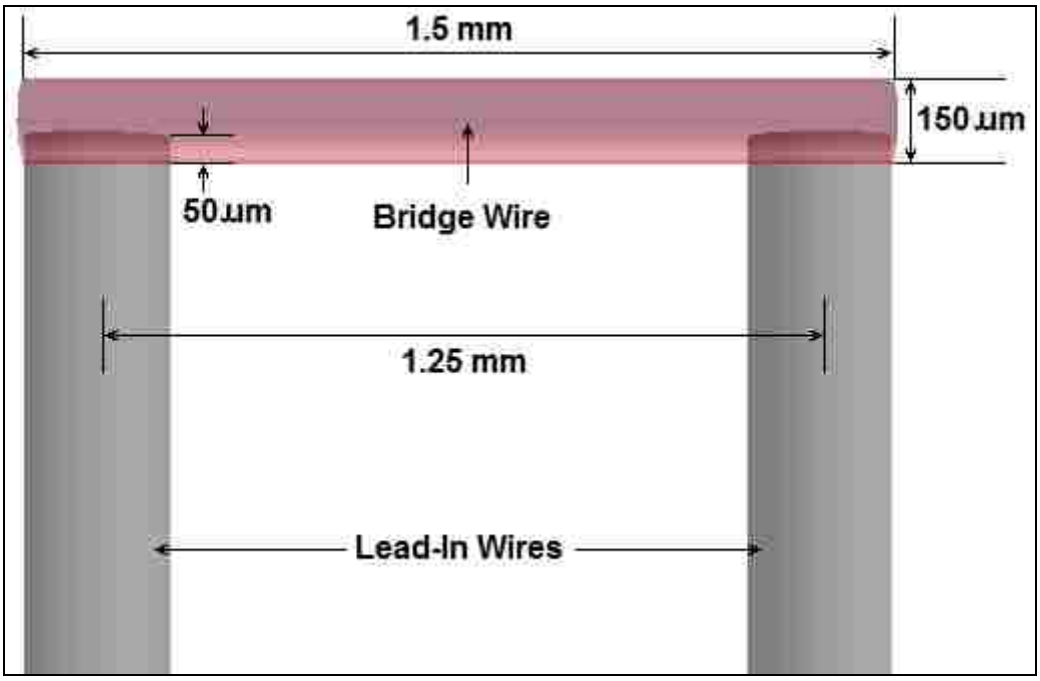

Figure 4: Close-up view of the bridge wire and its connection to the lead-in wires.

Figures 5 and 6 are images of the ICEPIC rendering of the generic detonator geometry for common mode excitation. Figure 5 is a perspective view of the detonator geometry, and shows the placement of the exciting current sources. Here there are no lead-in wires outside the case. Also, in order to excite the common mode, two current sources are used, one connected to each lead-in wire. This configuration forces the lead-in wires to be at the same potential relative to the outer case since their excitations are identical. The two antennas are made very long so that the opposite ends are sufficiently far from the geometry so as to not excite the detonator with additional radiated EM energy. Figure 6 is a top view of the geometry with the outer case removed. The bridge wire and its connection to the lead-in wires is identical to what was shown in Figure 4 for differential mode excitation.

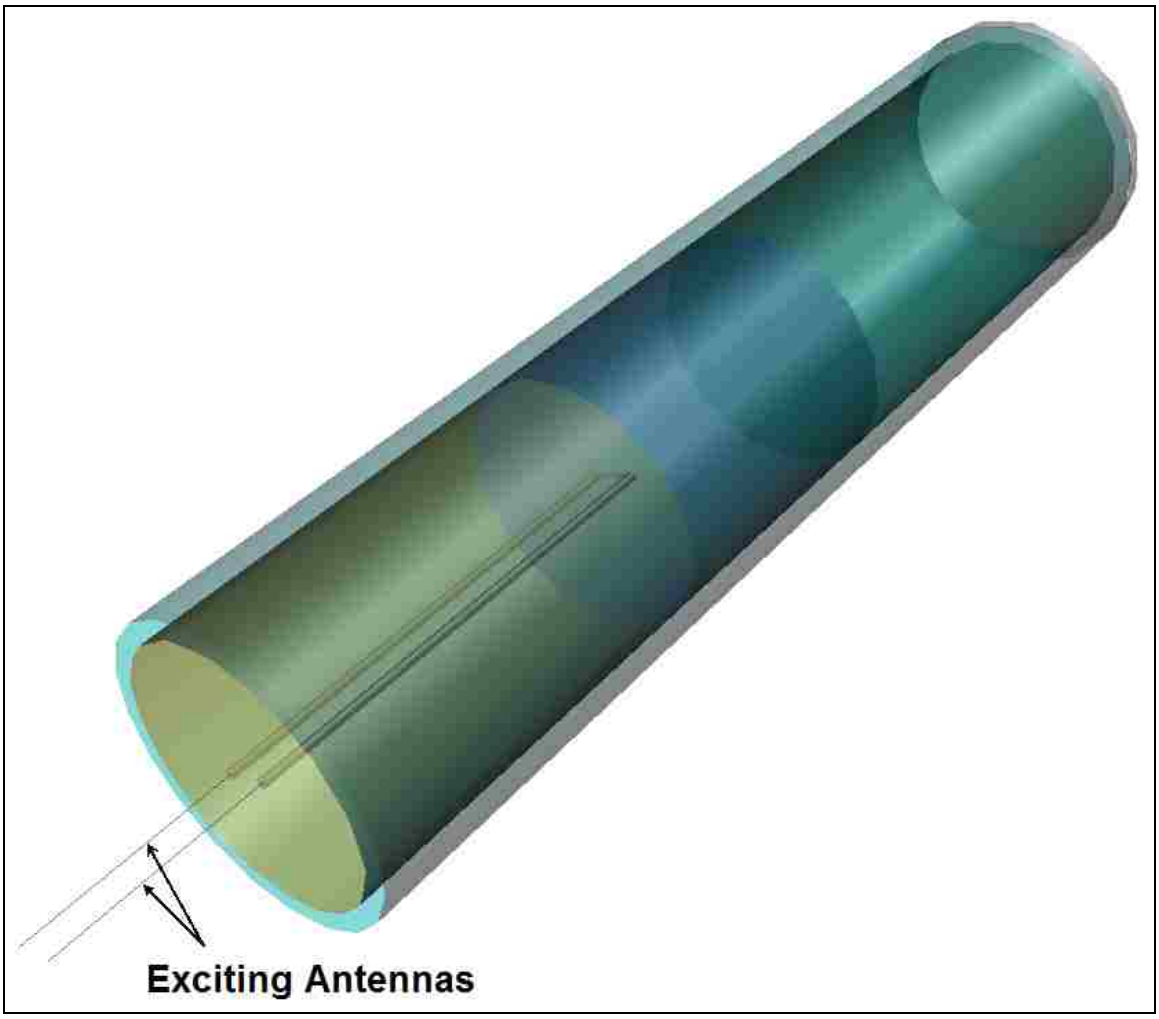

Figure 5: Perspective view of the ICEPIC rendering of the generic detonator geometry for common mode excitation indicating the exciting antenna current sources.

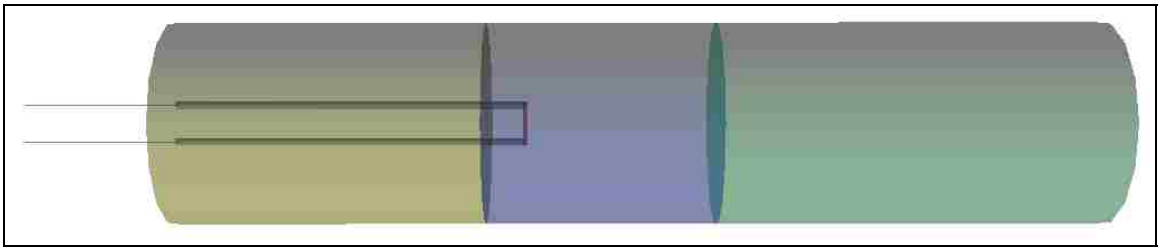

Figure 6: Side view of the ICEPIC rendering of the generic detonator geometry for differential mode excitation showing the length of the exciting antenna current sources.

Creating the Simulation Space and Gridding the Geometry

The rendered geometry shown in the previous section was then placed into a simulation space surrounded by perfect electric conductor (PEC). Figures 7 and 8

illustrate how the simulation space is defined for differential and common mode excitation, respectively. The PEC boundary signifies the end of the simulation space and no field calculations are performed there.

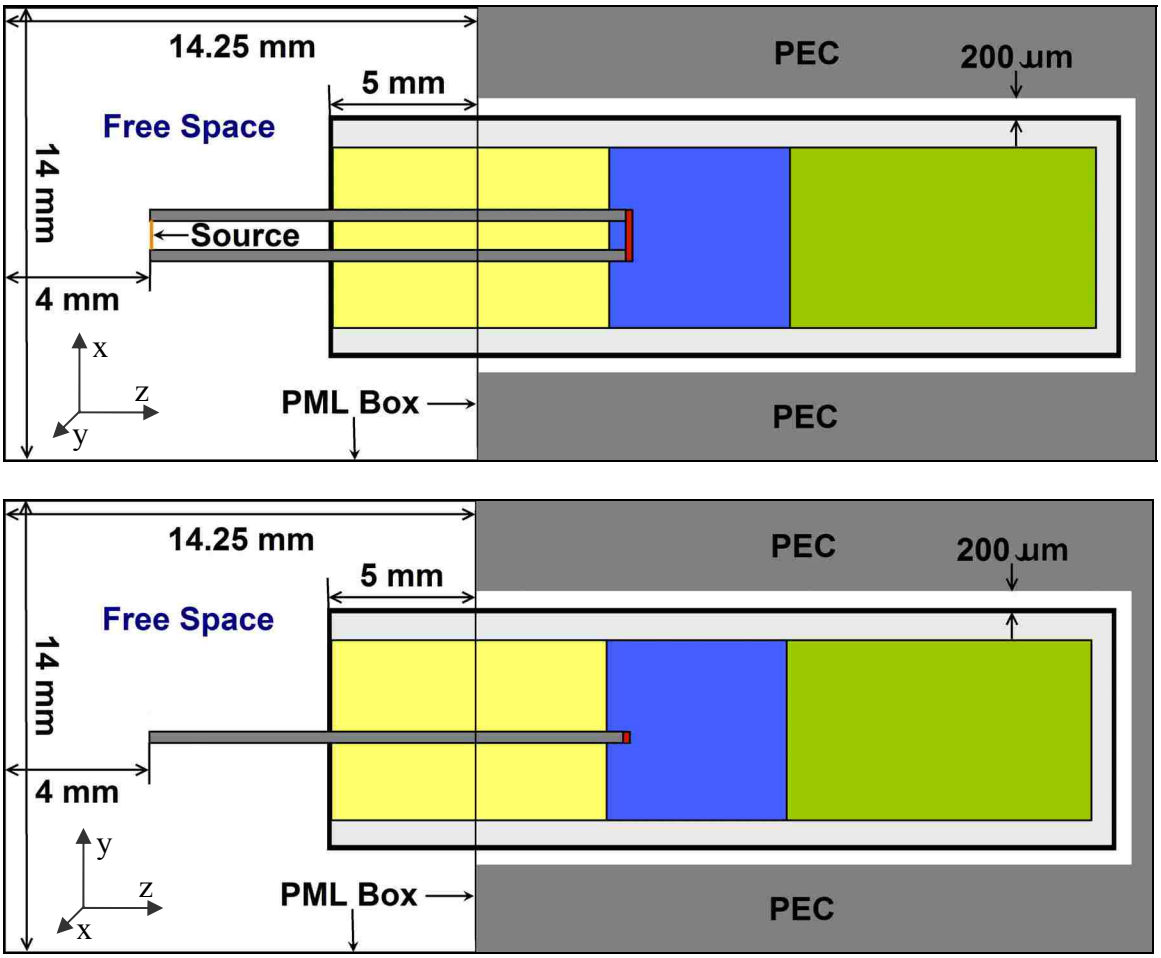

Figure 7: Illustration of the differential mode simulation space set-up from both a top view (top), and side view (bottom), indicating regions of PEC and free space, along with the placement and dimensions of the PML box encompassing the excitation source.

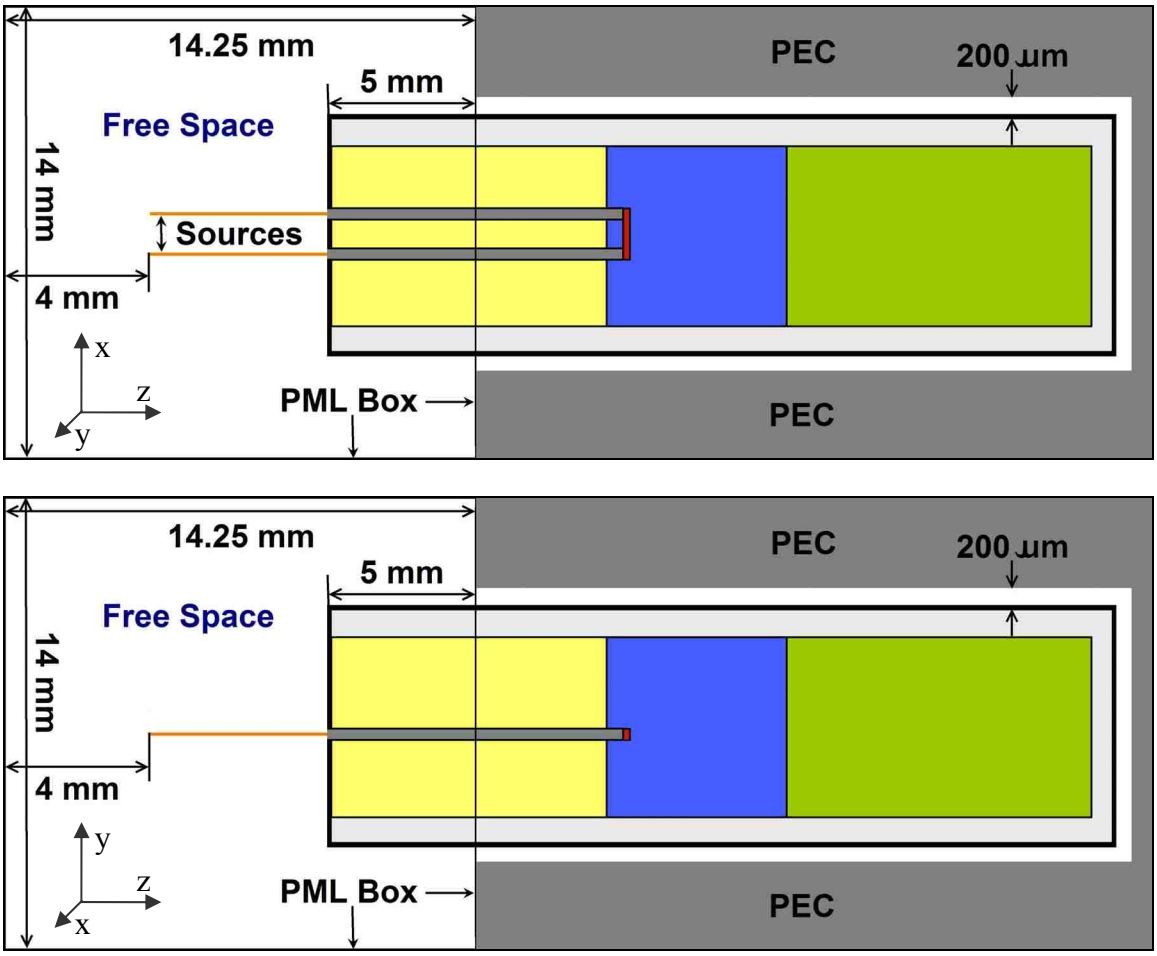

Figure 8: Illustration of the common mode simulation space set-up from both a top view (top), and side view (bottom), indicating regions of PEC and free space, along with the placement and dimensions of the PML box encompassing the excitation sources.

Since the antennas for both the differential and common mode excitations will radiate, appropriate spacing and boundary conditions must be in place to prevent these stray electric fields from reflecting off of the PEC and providing additional out of phase excitation to the geometry. This will be accomplished by placing a box around the geometry composed of free space. In the Z (axial) direction, the end of the simulation space is placed 4 mm from the ends of the antennas for each excitation. For the differential mode excitation case this boundary is 4 mm from the beginning of the lead-in wires, and for the common mode excitation case it is 4 mm from the opposite ends of the antennas connected to the lead-in wires. Reflections in the Z direction within the

detonator are not as important since the fields within the geometry will remain there due to the surrounding aluminum case. Because of this requirement the geometry does not have to be completely encapsulated within a free space box. Limiting the amount of space surrounding the geometry will significantly reduce computation time. Therefore, the free space box will be limited to 5 mm past the beginning of the detonator case. Also, there must be sufficient space above and below the excitation antennas to allow the radiated fields to travel and in both the X and Y directions. A box whose side is twice the detonator outer radius (14 mm) was chosen for both the X and Y directions. These box dimensions ensure that the radiated fields will not immediately reflect off the PEC boundary and return to the simulation region. However, if sufficient simulated time has passed, these fields will eventually reach the PEC boundary, reflect from it, and return to the geometry. To prevent this, the boundary condition for the box is changed to a perfectly matched layer (PML). This boundary condition absorbs incoming fields by creating a series of layers along the boundary with increasing conductivities, and will eliminate reflections back into the simulation space so that only the primary drive current enters the system.

For the remainder of the cylindrical detonator geometry not encompassed by the large PML box, there must be an additional outer air region. Since the outer case is aluminum, it has a finite conductivity. As such, it must be physically separated from the PEC boundary surrounding it. However, since the amount of EM energy radiating outward from this aluminum sheath is extremely small, it does not need as large a free space volume as did the excitation antennas. To accomplish this, a small cylindrical air region was created extending an additional 200 μm in both the radial and axial directions

from the outer sheath. Figures 9 and 10 are 3-D illustrations of the ICEPIC rendering of the excitation end of the simulation space for differential and common mode excitation, respectively. The entire white area surrounding the geometry is a PEC.

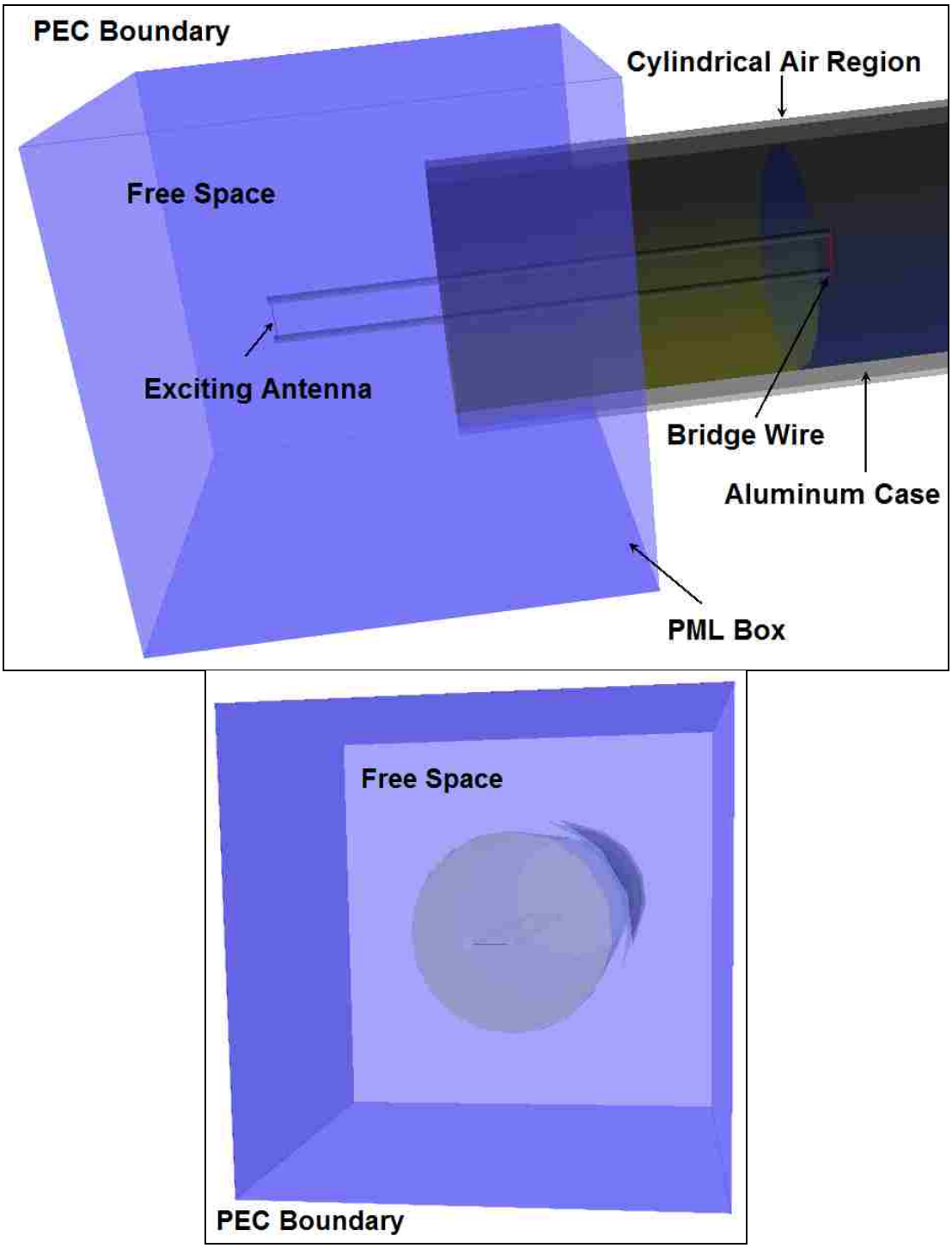

Figure 9: Illustration of the 3-D ICEPIC rendering of the differential mode excitation space from a perspective top-view (top), and a perspective rear-view (bottom).

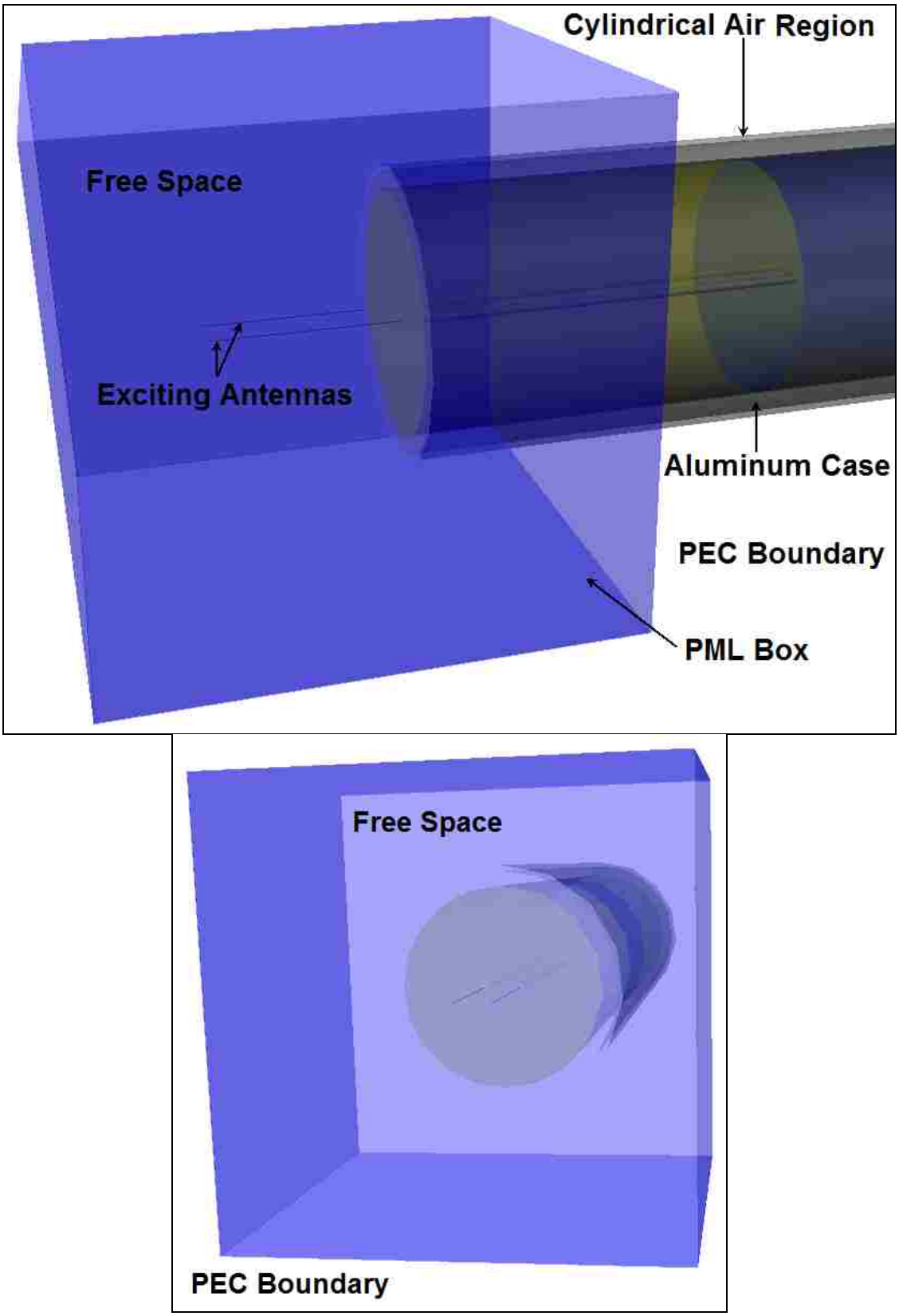

Figure 10: Illustration of the 3-D ICEPIC rendering of the common mode excitation space from a perspective side-view (top), and a perspective rear-view (bottom).

Given the above simulation space, a grid size was chosen to both accurately represent the geometry and be solved with a reasonable computation time. As the grid size becomes smaller, the geometry becomes better resolved, and the simulation results become more accurate. However, with a smaller grid size comes a much larger number of cells in which the EM field must be solved for each time step, greatly increasing the amount of time ICEPIC takes to complete the simulation. Based on the size of the simulation space, a grid size of 50 μm was chosen, as that would be able to accurately model the lead-in wires (250 μm diameter). This grid size resulted in a simulation space composed of $6.57*10^7$ cells. However, since many of these cells to the right of the PML box and outside the cylindrical air cushion are PEC, there are $3.45*10^7$ cells requiring computation each time step. This is still a very large number of cells, but terminating the PML box 5 mm from the beginning of the detonator case instead of surrounding the entire geometry in free space reduced the number of cells by a factor 1.90.

While this set-up will still require a large amount of computation time, utilizing ICEPIC's parallel architecture renders the simulation feasible. The fine grid size ensures accurate results, but it also makes the choice of simulated time important. Based on observations made for the first few simulations, a simulation time of 50 ns was sufficient to allow the system to reach steady state and provide sufficient data to extract required frequency information from the results. Also, the courant condition [22] was used to determine the time step for the simulations, and was found to be $9.534*10^{-14}$ sec. With this time step, each simulation ran for 524,459 steps to reach 50 ns.

Bridge Wire Scaling

A grid size of 50 μm, while extremely small and more than adequate for resolving the detonator geometry, is not small enough to accurately represent the bridge wire of 25 μm in diameter. To resolve the bridge wire a grid size of 5 μm or less is needed, requiring a prohibitively long computation time. Since this cannot be done, the bridge wire must be appropriately scaled so that a 50 μm grid size can adequately resolve it. From Chapter 3, the effective conductivity of a 1.5 mm long, 25 μm diameter bridge wire with a 1 Ω DC resistance was found to be $3.056*10^6$ S/m. To input this bridge wire into ICEPIC, the bridge wire diameter must be appropriately increased. However, in order to maintain a 1 Ω DC resistance, the conductivity of the bridge wire must also be modified. An accurate representation of the bridge wire is accomplished when the skin depth of the bridge wire at 900 MHz is equal to or less than the grid spacing of 50 μm. From Chapter 3 the skin depth of the bridge wire at 900 MHz is 9.60 μm, and so a scaled skin depth of 6*9.60 μm = 57.58 μm > 50 μm can be accurately represented by a 50 μm grid spacing. Using this new skin depth, the conductivity of the scaled bridge wire can be found (68), and then this conductivity is used to find the new radius (69):

$$57.58*10^{-6} = 503.292\sqrt{\frac{1}{(900*10^6)(\sigma_{new})}} \tag{68}$$

$$\Rightarrow \sigma_{new} = 84882.6\frac{S}{m} \ \left(36x \text{ Decrease!}\right) \text{, and}$$

$$1 = \frac{0.0015}{(84882.6)(\pi r^2)}$$

$$\Rightarrow r_{new} = 75\ \mu m \ \left(6x \text{ Increase!}\right). \tag{69}$$

The bridge wire input into ICEPIC has the properties described above, and is accurately represented using a 50 μm grid spacing.

ICEPIC Diagnostics

ICEPIC can implement a number of diagnostics for measuring EM quantities during a simulation. The three primary diagnostics used in this investigation are to measure the voltage between two points, determine the current flow within a circular region, and find the EM fields across the entire simulation space.

The magnitude of the voltage between two points is found by integrating the electric field values within cells from one specified point to another [23]:

$$V_{AB} = -\int_A^B \vec{E} \cdot d\vec{l} \quad . \tag{70}$$

This diagnostic will be used to determine the voltage between the two lead-in wires at different points along the detonator geometry in differential mode, and between one of the lead-in wires and the case in common mode. This diagnostic will be referred to as an EDL. Figures 11 and 12 illustrate where the EDLs are placed along the detonator geometry for differential and common mode excitation, respectively. In differential mode, the bridge wire voltage EDL is intentionally placed 50 μm (one grid length) from the end of the lead-in wires to ensure that the diagnostic is not in contact with the bridge wire. This additional spacing is not necessary in common mode, as the diagnostic is above the bridge wire, so it is placed right at the end of the lead-in wires.

The current through a circular region is found by integrating the magnetic field values within cells along a closed path [23]:

$$I_{enc} = \oint \vec{H} \cdot d\vec{l} \quad . \tag{71}$$

This diagnostic will be used to determine the magnitude of the current flowing through the bridge wire for differential mode excitation. During common mode excitation, this same diagnostic will be used to verify that no current flows through the bridge wire, indicating that both lead-in wires are indeed at the same potential. For these cases the specified closed path will be a circle whose radius is twice that of the scaled bridge wire to ensure the entire region is accounted for in the calculation. This type of diagnostic will be referred to as a CUR_CIR, and Figures 11 and 12 indicate the location of the CUR_CIR for both differential and common mode excitation, respectively.

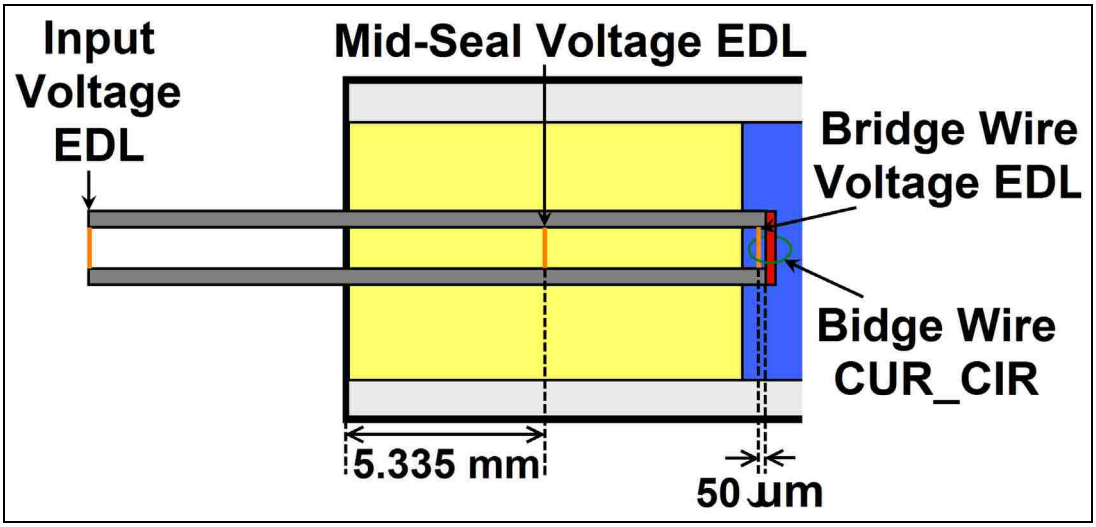

Figure 11: Illustration of EDL and CUR_CIR diagnostic locations for differential mode excitation.

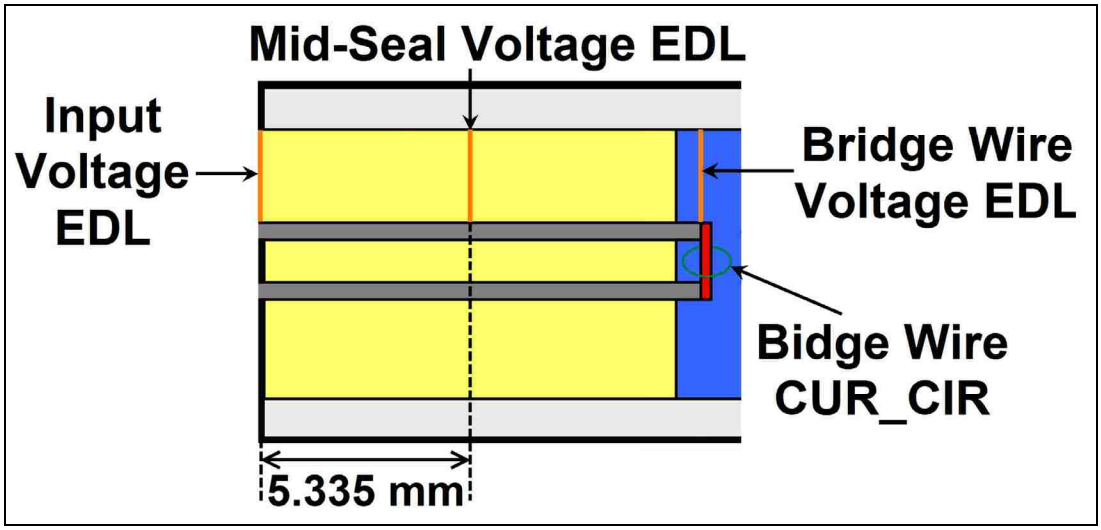

Figure 12: Illustration of EDL and CUR_CIR diagnostic locations for common mode excitation.

Finally, the electric and magnetic fields calculated by ICEPIC can be displayed for certain planes throughout the geometry for specified time steps. During both modes of excitation four primary planes will be examined and these are indicated in Figures 13 and 14.

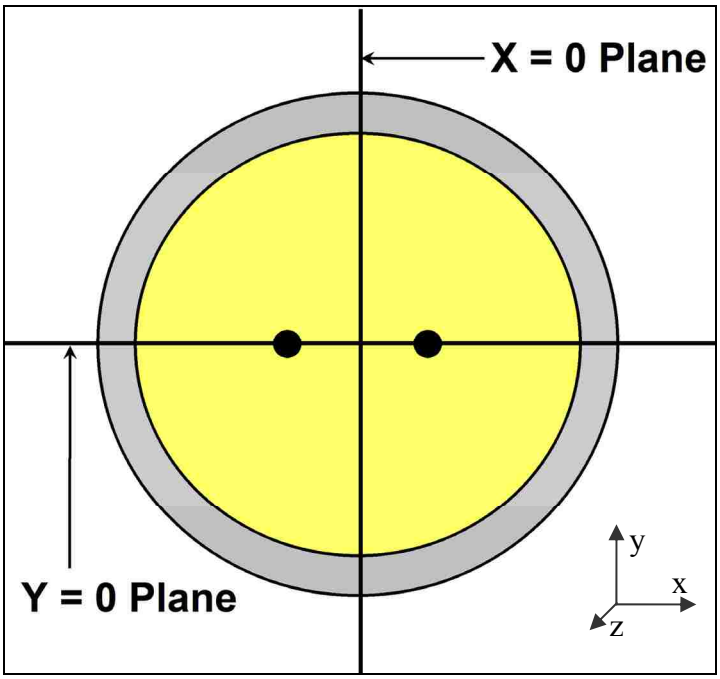

Figure 13: Illustration of X = 0 and Y = 0 planes, two EM field diagnostic planes used during both common and differential mode excitation.

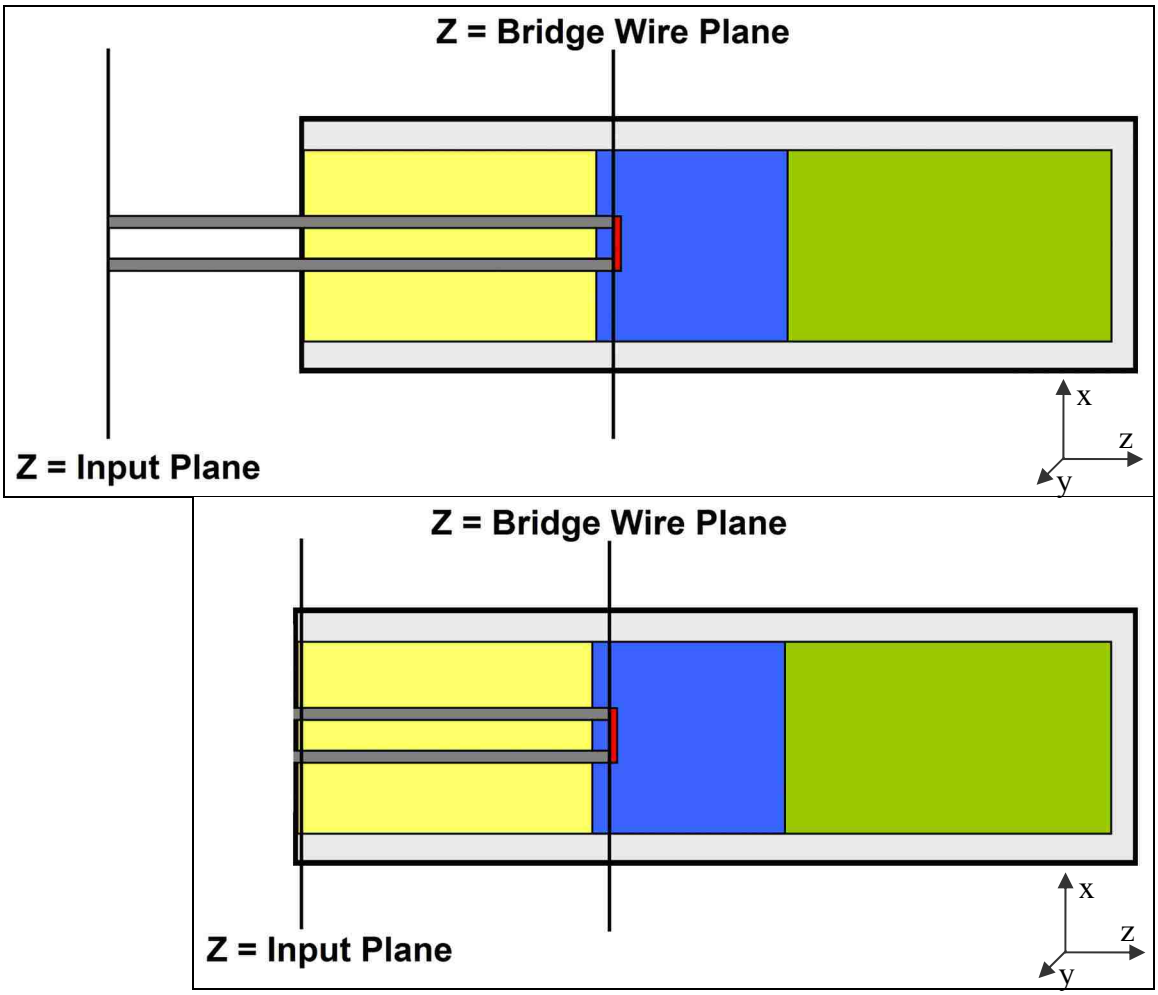

Figure 14: Illustration of input and bridge wire planes, two EM field diagnostic planes used during differential (top) and common (bottom) mode excitation.

Using the Analytical Model to Determine Detonator Voltage and Current

In Chapter 3 an analytical model was developed to determine the real and imaginary parts of the detonator input impedance as well as the magnitude for both differential and common mode excitation. However, from the above description, ICEPIC will not be calculating input impedance but the input voltage magnitude. Also, the voltage magnitude will be calculated not only for the input to the detonator, but in the middle of the seal section as well as near the bridge wire. Lastly, the current through the

bridge wire will also be found. In order to use the analytical model to compare predicted values to ICEPIC results, additional calculations must be made by the model.

Input Voltage

Using the analytical model to find the magnitude of the input voltage requires the use of the impedance as calculated in Chapter 3. Since the current source in ICEPIC can be set at any arbitrary magnitude, a value of 1 A was chosen for all simulations to simplify the voltage calculations. Given the input impedance, the input voltage is found using Ohm's law [23] with the assumed input current. The magnitude of the resulting voltage can then be found. Using the differential mode input impedance at 900 MHz (Chapter 3), the input voltage can be found by:

$$Z_{in} = 1.87 + j105.18\ \Omega\ , \tag{72}$$

$$V_{in} = I_{in} Z_{in} \tag{73}$$

$$= \left(1.87 + j105.18\right)\left(1\right) = 1.87 + j105.18\ \text{, and}$$

$$\left|V_{in}\right| = 105.20\ V\ . \tag{74}$$

This voltage magnitude can now be directly compared to the input voltage EDL value given by ICEPIC for a differential mode excitation frequency of 900 MHz. While this example was for differential mode excitation, the calculation for common mode input voltage is performed the same way, and can likewise be compared to ICEPIC results. This functionality has been added to the MatLAB program for predicting detonator EM characteristics and is computed across the entire frequency range. Figures 15 and 16 are MatLAB plots of the detonator input voltage across frequency for differential and common mode excitation, respectively. The plots are identical to those seen for the input

impedance magnitude in Chapter 3 (Figures 13 and 23). This is expected due to the way the voltage is calculated (72-74), and the choice of a 1 A input current.

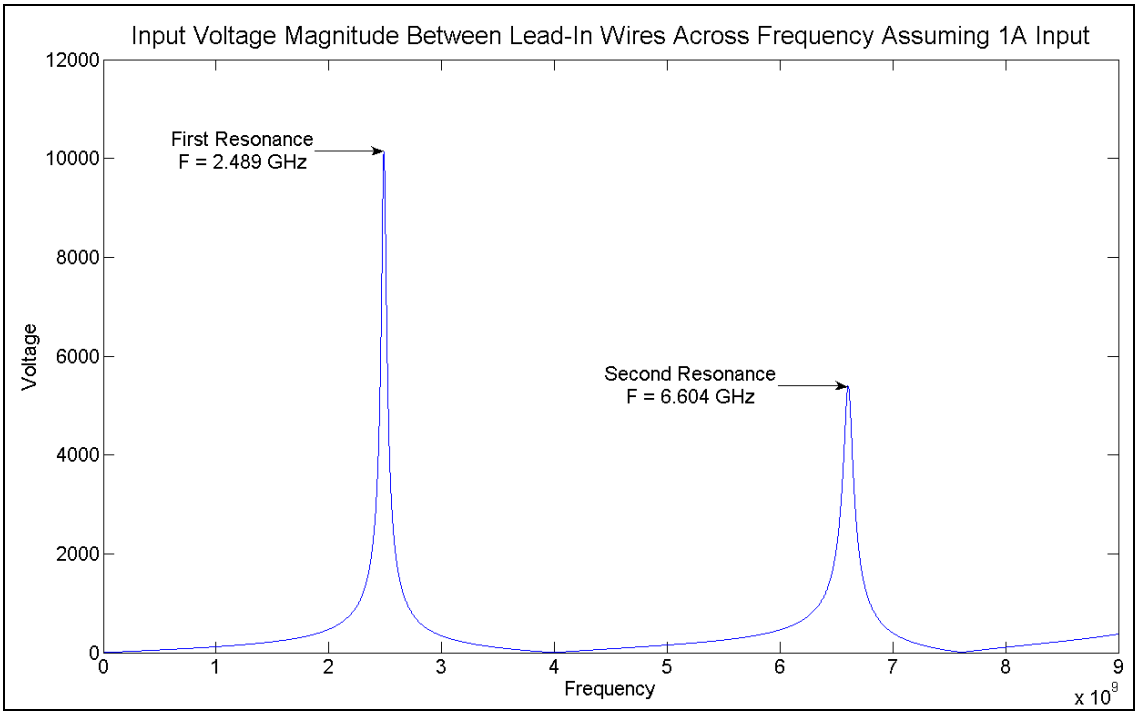

Figure 15: MatLAB plot of the magnitude of the differential mode detonator input voltage across the frequency range DC-9 GHz.

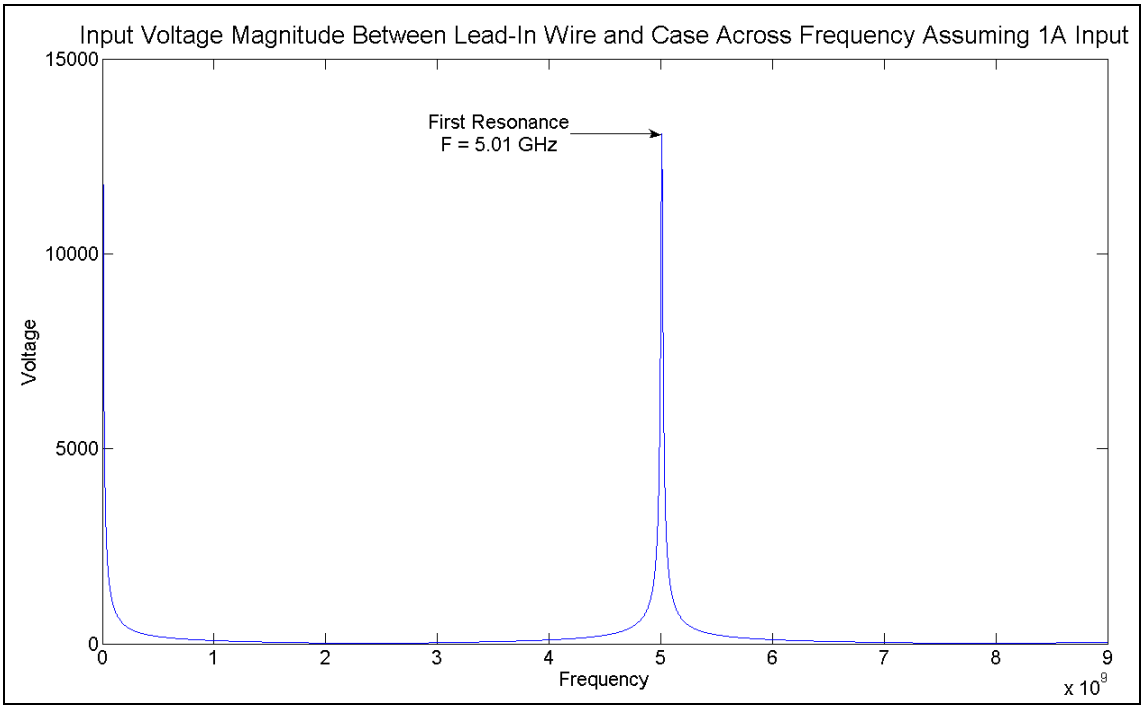

Figure 16: MatLAB plot of the magnitude of the common mode detonator input voltage across the frequency range DC-9 GHz.

Mid-Seal Voltage – Differential Mode

Given the detonator input parameters as calculated in (73), the mid-seal voltage between lead-in wires can be found using a transmission matrix, as described in Chapter 3. First, the input parameters for differential mode excitation at 900 MHz are:

$$\begin{bmatrix} V_{in} \\ I_{in} \end{bmatrix} = \begin{bmatrix} 1.87 + j105.18 \\ 1 \end{bmatrix}. \tag{75}$$

The next step requires the formation of a transmission matrix, which will determine the voltage and current at the mid-point of the seal based on the input parameters. A diagram of the transmission line being modeled is shown as Figure 17.

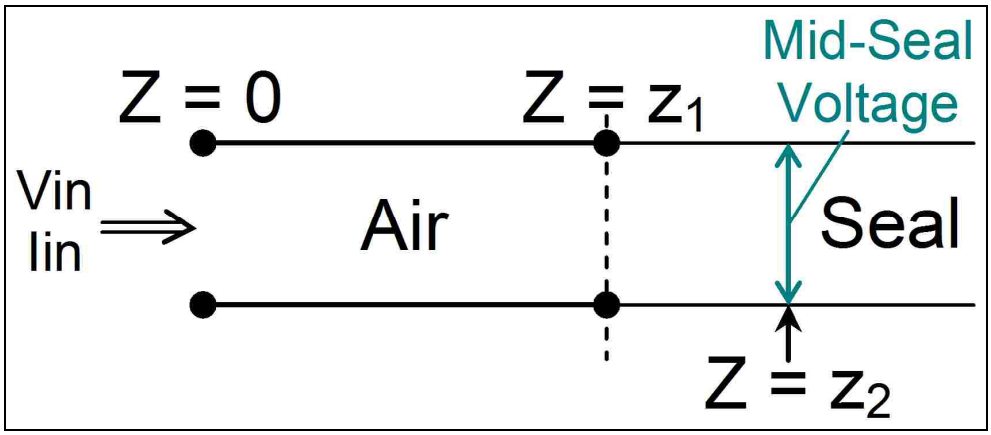

Figure 17: Illustration of dividing the detonator into sections for determining the mid-seal voltage during differential mode excitation.

The transmission matrix is then formed using the properties found in Chapter 3 (Table 1) to solve the telegrapher's equations [17] for each section using the product integral method [21]:

$$\begin{bmatrix} V(z_1) \\ I(z_1) \end{bmatrix} = \left[\prod_0^{z_1} e^{\Gamma_a dz'} \right] \cdot \begin{bmatrix} V(0) \\ I(0) \end{bmatrix}, \tag{76}$$

$$\begin{bmatrix} V(z_2) \\ I(z_2) \end{bmatrix} = \left[\prod_{z_1}^{z_2} e^{\Gamma_s dz'} \right] \cdot \begin{bmatrix} V(z_1) \\ I(z_1) \end{bmatrix}, \tag{77}$$

$$\begin{bmatrix} V(z_2) \\ I(z_2) \end{bmatrix} = \left[\prod_{z_1}^{z_2} e^{\Gamma_s dz'} \right] \cdot \left[\prod_{0}^{z_1} e^{\Gamma_a dz'} \right] \cdot \begin{bmatrix} V(0) \\ I(0) \end{bmatrix}, \text{ and} \tag{78}$$

$$\begin{bmatrix} V(z_2) \\ I(z_2) \end{bmatrix} = \left[U(z_2, 0) \right] \cdot \begin{bmatrix} V(0) \\ I(0) \end{bmatrix}. \tag{79}$$

Since the goal is to find the voltage at $Z = Z_2$ due to the input parameters at $Z = 0$, the $[U(Z_2, 0)]$ matrix does not need to be inverted. From Figures 1 and 11, the values of Z are as follows:

$Z_1 = 5.25$ mm
$Z_2 = 10.585$ mm.

The transmission matrix for the air section is the inverse of that calculated in Chapter 3, as the limits have been reversed:

$$M_{a-rev} = \left(M_a \right)^{-1} = \begin{bmatrix} 0.995 & -0.105 - j27.20 \\ -j0.00036 & 0.995 \end{bmatrix}. \tag{80}$$

For the smaller seal section, the transmission matrix is calculated as:

$$\prod_{z_1}^{z_2} e^{\Gamma_s dz'} = \prod_{0.00525}^{0.010585} e^{\Gamma_s dz'} = e^{\int_{0.00525}^{0.010585} \Gamma_s dz'} = e^{\Gamma_s (0.010585 - 0.00525)} \tag{81}$$

$$= M_{s-half} = \begin{bmatrix} 0.98 + j0.0001 & -0.106 - j26.73 \\ -j0.0015 & 0.98 + j0.0001 \end{bmatrix}, \text{ and}$$

$$\left[U(z_2, 0) \right] = \left[\prod_{z_1}^{z_2} e^{\Gamma_s dz'} \right] \cdot \left[\prod_{0}^{z_1} e^{\Gamma_a dz'} \right] \tag{82}$$

$$= \left[M_{s-half} \right] \cdot \left[M_{a-rev} \right] \tag{83}$$

$$= \begin{bmatrix} 0.965 + j0.0001 & -0.206 - j53.246 \\ -j0.0018 & 0.934 \end{bmatrix}.$$

Finally, the entire matrix equation becomes:

$$\begin{bmatrix} V(z_2) \\ I(z_2) \end{bmatrix} = \begin{bmatrix} 0.965 + j0.0001 & -0.206 - j53.246 \\ -j0.0018 & 0.934 + j0.0003 \end{bmatrix} . \begin{bmatrix} V(0) \\ I(0) \end{bmatrix} \quad (84)$$

After substituting the input voltage and current from (75), the magnitude of the voltage at mid-seal is calculated as:

$$\begin{bmatrix} V(z_2) \\ I(z_2) \end{bmatrix} = \begin{bmatrix} 0.965 + j0.0001 & -0.206 - j53.246 \\ -j0.0018 & 0.934 + j0.0003 \end{bmatrix} . \begin{bmatrix} 1.87 + j105.18 \\ 1 \end{bmatrix}$$

$$\begin{bmatrix} V(z_2) \\ I(z_2) \end{bmatrix} = \begin{bmatrix} 1.65 + j48.34 \\ 1.13 - j0.003 \end{bmatrix}$$

$$V\left(\text{Mid-Seal}\right) = \left|1.65 + j48.34\right| = 48.373 \ V .$$

This voltage magnitude can now be directly compared to the mid-seal voltage EDL value given by ICEPIC for a differential mode excitation frequency of 900 MHz. This functionality has been added to the MatLAB program and is computed across the entire frequency range. Figure 18 is a MatLAB plot of the mid-seal voltage as a function of frequency for differential mode excitation. The overall shape of the plot is similar to Figure 15, with resonances at 2.489 and 6.604 GHz. This is expected since the resonant frequencies are determined by the geometry and will be the same at any point along the transmission line.

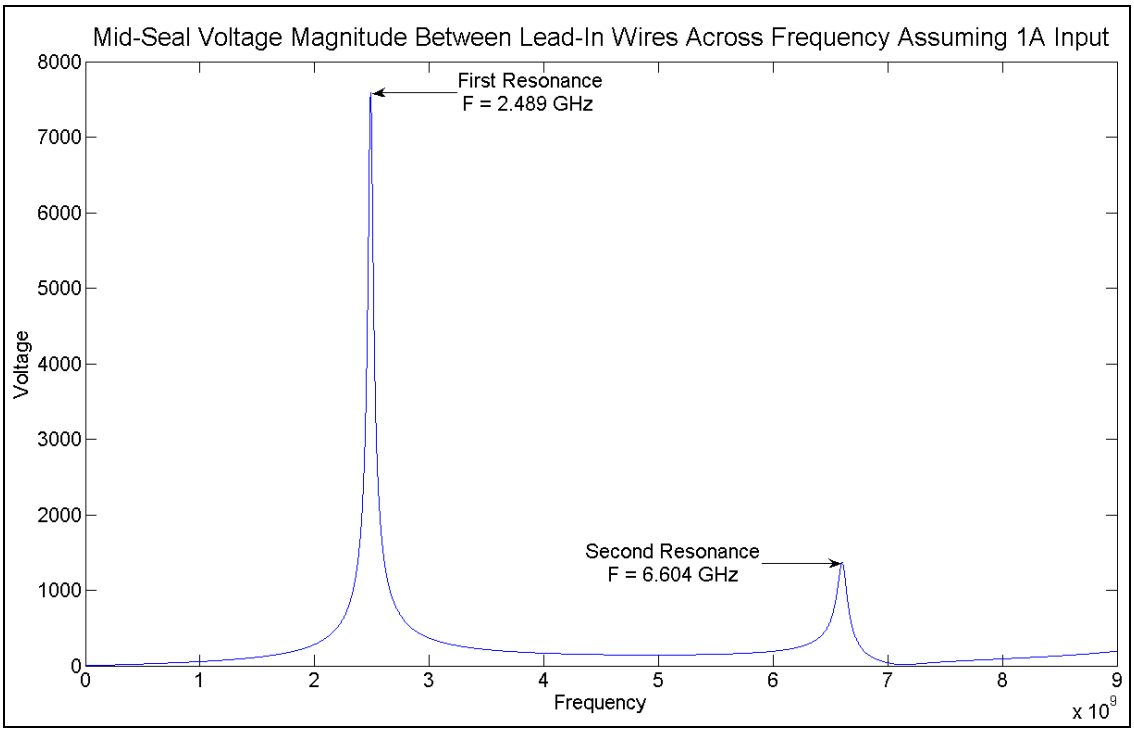

Figure 18: MatLAB plot of the magnitude of the differential mode mid-seal voltage across the frequency range DC-9 GHz.

Mid-Seal Voltage – Common Mode

The voltage between the case and lead-in wires at the midpoint of the seal is found in a similar way, requiring the common mode input parameters and a transmission matrix. Using (73) and the input impedance given in Chapter 3, the common mode input parameters at 900 MHz are:

$$\begin{bmatrix} V_{in} \\ I_{in} \end{bmatrix} = \begin{bmatrix} 0.112 - j94.716 \\ 1 \end{bmatrix}. \tag{85}$$

Now the transmission matrix will be constructed to determine the voltage and current at the mid-point of the seal based on the input parameters. A diagram of the transmission line being modeled is shown in Figure 19.

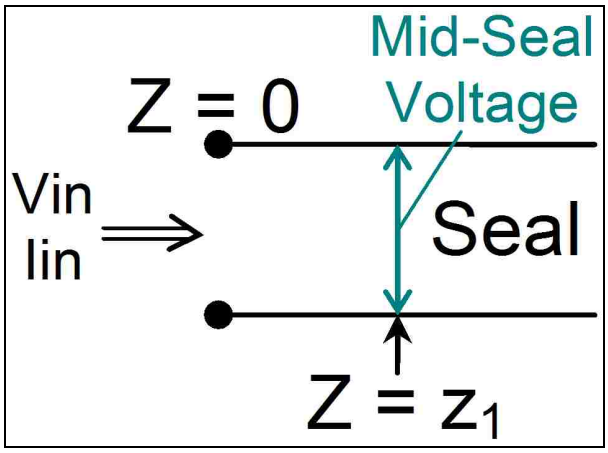

Figure 19: Illustration of dividing the detonator into sections for determining the mid-seal voltage during common mode excitation.

The transmission matrix is simple and composed of a single section, and can be formed using the properties found in Chapter 3 (Table 2) to solve the telegrapher's equations for the section using the product integral method:

$$\begin{bmatrix} V(z_1) \\ I(z_1) \end{bmatrix} = \left[\prod_0^{z_1} e^{\Gamma_s dz'} \right] \cdot \begin{bmatrix} V(0) \\ I(0) \end{bmatrix}. \tag{86}$$

From Figure 12, the value of Z is:

Z_1 = 5.335 mm.

For the single seal section, the transmission matrix is calculated as:

$$\prod_0^{z_1} e^{\Gamma_s dz'} = \prod_0^{0.005335} e^{\Gamma_s dz'} = e^{\int_0^{0.005335} \Gamma_s dz'} = e^{\Gamma_s (0.005335-0)} \tag{87}$$

$$= M_{s-half} = \begin{bmatrix} 0.98 + j0.0002 & -0.108 - j13.066 \\ -j0.0031 & 0.98 + j0.0002 \end{bmatrix}.$$

Finally, the entire matrix equation becomes:

$$\begin{bmatrix} V(z_1) \\ I(z_1) \end{bmatrix} = \begin{bmatrix} 0.98 + j0.0002 & -0.108 - j13.066 \\ -j0.0031 & 0.98 + j0.0002 \end{bmatrix} \cdot \begin{bmatrix} V(0) \\ I(0) \end{bmatrix}. \tag{88}$$

After substituting the input voltage and current from (85), the magnitude of the voltage between the lead-in wires and case at mid-seal is calculated as:

$$\begin{bmatrix} V(z_1) \\ I(z_1) \end{bmatrix} = \begin{bmatrix} 0.98 + j0.0002 & -0.108 - j13.066 \\ -j0.0031 & 0.98 + j0.0002 \end{bmatrix} \cdot \begin{bmatrix} 0.112 - j94.716 \\ 1 \end{bmatrix}$$

$$\begin{bmatrix} V(z_1) \\ I(z_1) \end{bmatrix} = \begin{bmatrix} 0.017 - j105.87 \\ 0.69 - j0.0002 \end{bmatrix}$$

$$V\left(\text{Mid-Seal}\right) = \left|0.017 - j105.87\right| = 105.87 \ V \ .$$

This voltage magnitude can now be directly compared to the mid-seal voltage EDL value given by ICEPIC for a common mode excitation frequency of 900 MHz. This functionality has been added to the MatLAB program, and is computed across the entire frequency range. Figure 20 is a MatLAB plot of the mid-seal voltage across frequency for common mode excitation. The overall shape of the plot is very similar to Figure 16, with a resonance at 5.01 GHz. As with the differential mode mid-seal voltage, this is expected since the resonant frequencies are determined by the geometry and will be the same at any point along the transmission line.

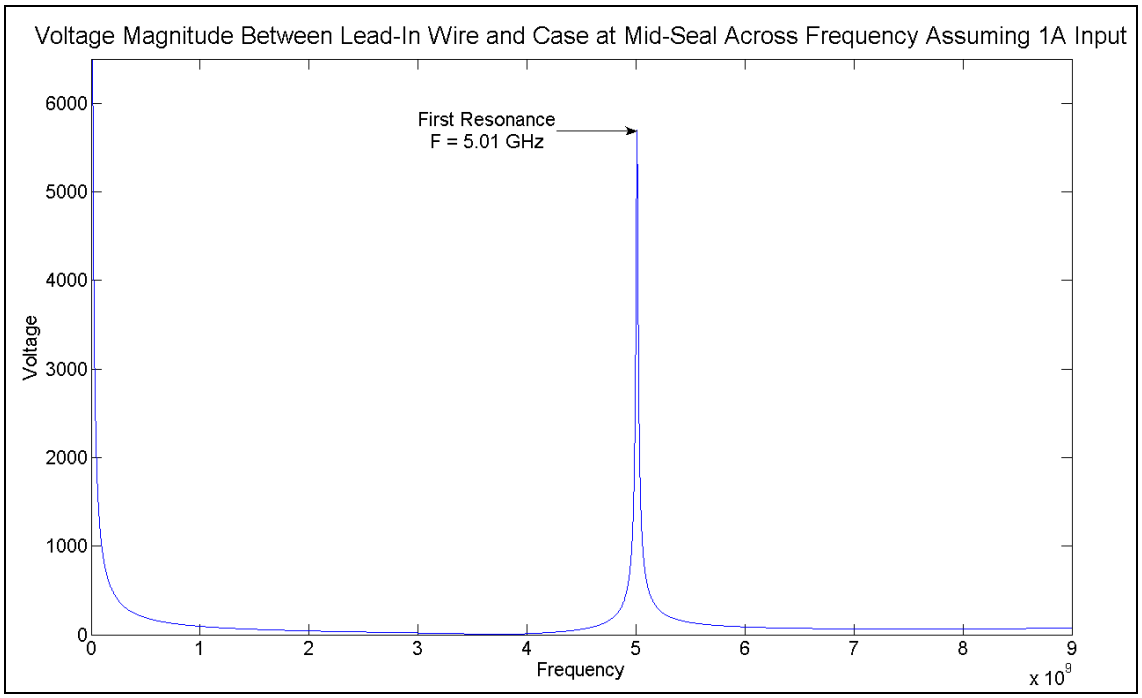

Figure 20: MatLAB plot of the magnitude of the common mode mid-seal voltage across the frequency range DC-9 GHz.

Bridge Wire Voltage – Differential Mode

In a manner similar to finding the mid-seal voltage, the voltage between the lead-in wires near the bridge wire can also be computed. Figure 11 shows the voltage diagnostic at 50 μm from the end of the lead-wires and their connection to the bridge wire. This modification will require the computation of a new transmission matrix for the truncated lead-azide section. For differential mode excitation at 900 MHz the input parameters are as given in (75). A diagram of the transmission line being modeled is shown as Figure 21.

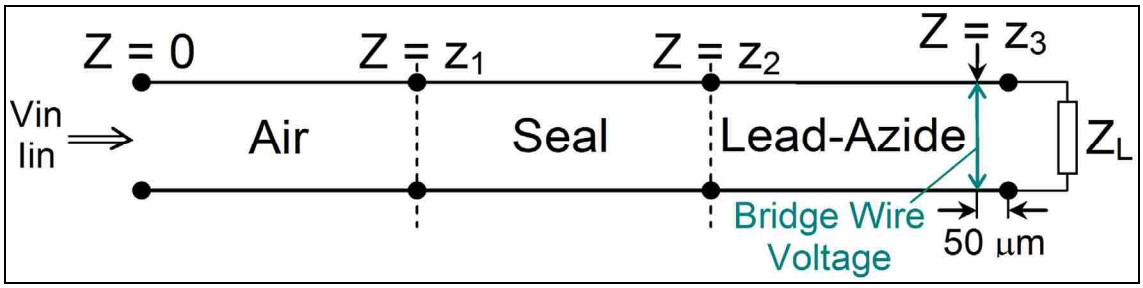

Figure 21: Illustration of dividing the detonator into sections for determining the bridge wire voltage during differential mode excitation.

The transmission matrix is then formed using the properties found in Chapter 3 (Table 1) to solve the telegrapher's equations for each section using the product integral method. Using (76) and (77) for the air and seal sections, the transmission matrix can be written as:

$$\begin{bmatrix} V(z_3) \\ I(z_3) \end{bmatrix} = \left[\prod_{z_2}^{z_3} e^{\Gamma_l dz'} \right] \cdot \begin{bmatrix} V(z_2) \\ I(z_2) \end{bmatrix} , \tag{89}$$

$$\begin{bmatrix} V(z_3) \\ I(z_3) \end{bmatrix} = \left[\prod_{z_2}^{z_3} e^{\Gamma_l dz'} \right] \cdot \left[\prod_{z_1}^{z_2} e^{\Gamma_s dz'} \right] \cdot \left[\prod_{0}^{z_1} e^{\Gamma_a dz'} \right] \cdot \begin{bmatrix} V(0) \\ I(0) \end{bmatrix} \tag{90}$$

, and

$$\begin{bmatrix} V(z_3) \\ I(z_3) \end{bmatrix} = [U(z_3, 0)] \cdot \begin{bmatrix} V(0) \\ I(0) \end{bmatrix} . \tag{91}$$

Since the goal is to find the voltage at $Z = Z_3$ due to the input parameters at $Z = 0$, the $[U(z_3, 0)]$ matrix does not need to be inverted. From Figures 1 and 11, the values of Z are as follows:

$Z_1 = 5.25$ mm
$Z_2 = 15.92$ mm
$Z_3 = 17.14$ mm.

The transmission matrix for the air section is given as (80), and the transmission matrix for the seal section is the inverse of that calculated in Chapter 3, as the limits have been reversed:

$$M_{s-rev} = \left(M_s\right)^{-1} = \begin{bmatrix} 0.92 + j0.0003 & -0.23 - j52.38 \\ -j0.003 & 0.92 + j0.0003 \end{bmatrix}. \quad (92)$$

For the truncated lead-azide section, the transmission matrix is calculated as:

$$\prod_{z_2}^{z_3} e^{\Gamma_s dz'} = \prod_{0.01592}^{0.01714} e^{\Gamma_s dz'} = e^{\int_{0.01592}^{0.01714} \Gamma_s dz'} = e^{\Gamma_s (0.01714 - 0.01592)} \quad (93)$$

$$= M_{l-trunc} = \begin{bmatrix} 1.0 + j0.00002 & -0.024 - j6.144 \\ -j0.0015 & 1.0 + j0.00002 \end{bmatrix}, \text{ and}$$

$$\left[U(z_3, 0)\right] = \left[\prod_{z_2}^{z_3} e^{\Gamma_l dz'}\right] \cdot \left[\prod_{z_1}^{z_2} e^{\Gamma_s dz'}\right] \cdot \left[\prod_{0}^{z_1} e^{\Gamma_a dz'}\right] \quad (94)$$

$$= \left[M_{l-trunc}\right] \cdot \left[M_{s-rev}\right] \cdot \left[M_{a-rev}\right] \quad (95)$$

$$= \begin{bmatrix} 0.873 + j0.0005 & -0.303 - j81.934 \\ -j0.0045 & 0.719 + j0.0011 \end{bmatrix}.$$

Finally, the entire matrix equation becomes:

$$\begin{bmatrix} V(z_3) \\ I(z_3) \end{bmatrix} = \begin{bmatrix} 0.873 + j0.0005 & -0.303 - j81.934 \\ -j0.0045 & 0.719 + j0.0011 \end{bmatrix} \cdot \begin{bmatrix} V(0) \\ I(0) \end{bmatrix}. \quad (96)$$

After substituting the input voltage and current from (75), the magnitude of the voltage near the bridge wire is calculated as:

$$\begin{bmatrix} V(z_3) \\ I(z_3) \end{bmatrix} = \begin{bmatrix} 0.873 + j0.0005 & -0.303 - j81.934 \\ -j0.0045 & 0.719 + j0.0011 \end{bmatrix} \cdot \begin{bmatrix} 1.87 + j105.18 \\ 1 \end{bmatrix}$$

$$\begin{bmatrix} V(z_3) \\ I(z_3) \end{bmatrix} = \begin{bmatrix} 1.331 + j9.908 \\ 1.197 - j0.008 \end{bmatrix}$$

$$V\left(\text{Bridge Wire}\right) = \left|1.331 + j9.908\right| = 9.997 \ V$$

This voltage magnitude can now be directly compared to the bridge wire voltage EDL value given by ICEPIC for a differential mode excitation frequency of 900 MHz. This functionality has been added to the MatLAB program, and is computed across the entire frequency range. Figure 22 is a MatLAB plot of the bridge wire voltage across frequency for differential mode excitation. The plot is very similar to Figures 15 and 18, with resonances at 2.489 and 6.604 GHz, again due to the resonances being geometry specific. However, in Figure 22, the magnitude of the first resonance is smaller than that of the second resonance. In Figures 15 and 18, the opposite is true. The reason for this is due to the large mismatch between the lead-azide section of the transmission line and the load impedance of the bridge wire. A large reflection occurs at this boundary and increases the voltage 50 μm away. This effect is more pronounced at higher frequencies due to the decreasing wavelength of the reflected wave.

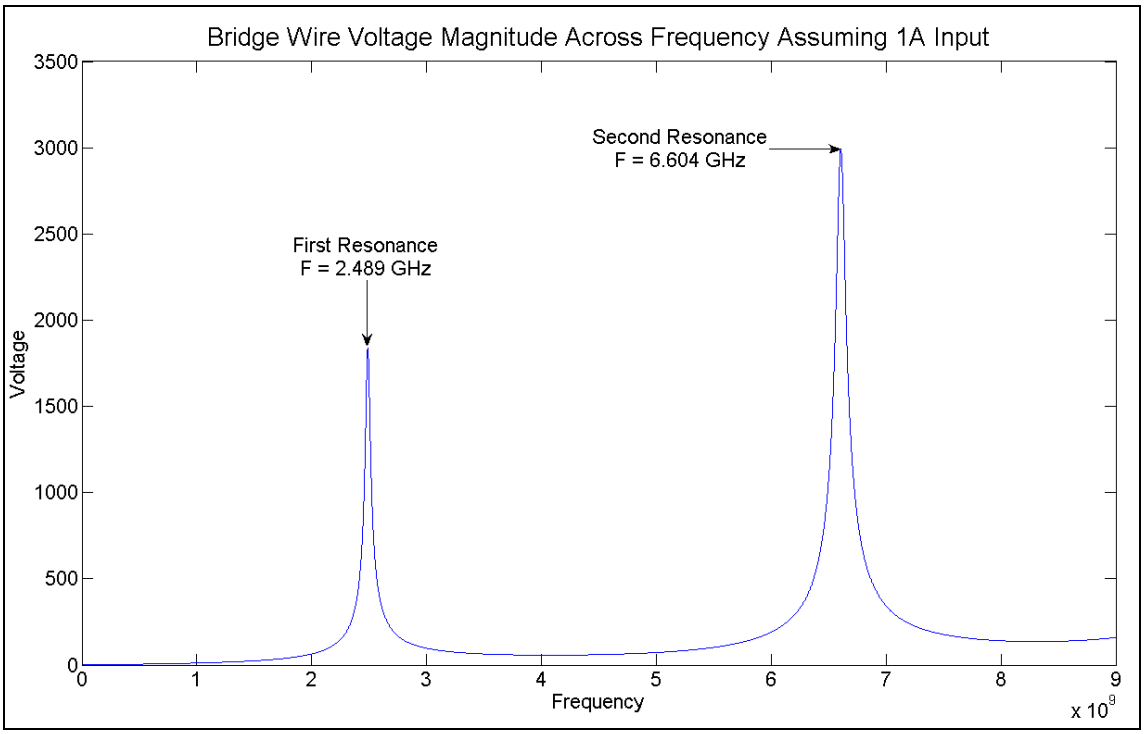

Figure 22: MatLAB plot of the magnitude of the differential mode bridge wire voltage across the frequency range DC-9 GHz.

Bridge Wire Voltage – Common Mode

Unlike for the differential mode excitation case, the bridge wire voltage EDL for common mode excitation is located exactly at the end of the lead-in wires (Figure 12). To find the voltage between the lead-in wires and case at this location the common mode input parameters given in (85) will again be used with a transmission matrix. A diagram of the transmission line being modeled is shown in Figure 23.

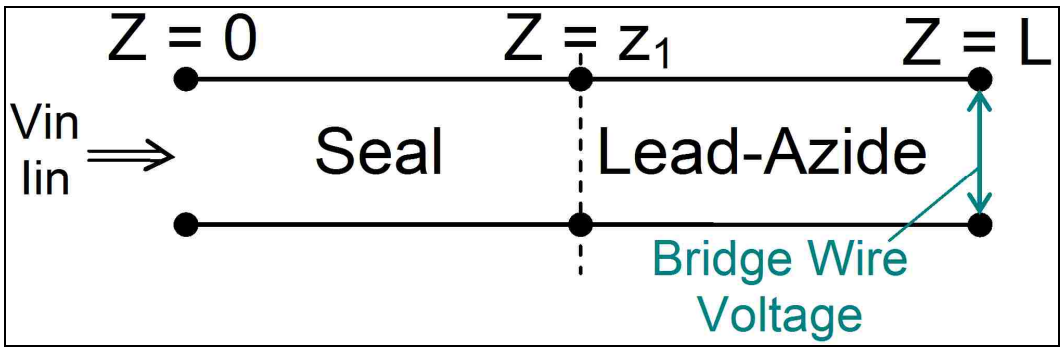

Figure 23: Illustration of dividing the detonator into sections for determining the bridge wire voltage during common mode excitation.

The calculation of the transmission matrix could proceed as in the previous section, where the limits of integration are re-defined, and the matrices for the seal and lead-azide sections are multiplied together. However, while this was necessary in the differential mode case, there is a simpler approach for common mode excitation. Since the location of the bridge wire voltage is at the end of the lead-in wires, the length of the common mode transmission line is unchanged and the transmission matrix calculated in Chapter 3 for a 900 MHz common mode input [U(0, L)] is viable. However, as was observed in previous sections, this transmission matrix needs to be inverted because the limits have been reversed:

$$\begin{bmatrix} V(L) \\ I(L) \end{bmatrix} = \left[\prod_{z_1}^{L} e^{\Gamma_l dz'} \right] \cdot \left[\prod_{0}^{z_1} e^{\Gamma_s dz'} \right] \cdot \begin{bmatrix} V(0) \\ I(0) \end{bmatrix}, \tag{97}$$

$$\begin{bmatrix} V(L) \\ I(L) \end{bmatrix} = \left[U(L,0) \right] \cdot \begin{bmatrix} V(0) \\ I(0) \end{bmatrix} \text{, and} \tag{98}$$

$$\left[U(L,0) \right] = \left[U(0,L) \right]^{-1} \tag{99}$$

$$= \left[M_l \right] \cdot \left[M_s \right] \tag{100}$$

$$= \begin{bmatrix} 0.897 + j0.0008 & -0.227 - j28.357 \\ -j0.0088 & 0.836 + j0.0013 \end{bmatrix}.$$

Finally, the entire matrix equation becomes:

$$\begin{bmatrix} V(L) \\ I(L) \end{bmatrix} = \begin{bmatrix} 0.897 + j0.0008 & -0.227 - j28.357 \\ -j0.0088 & 0.836 + j0.0013 \end{bmatrix} \cdot \begin{bmatrix} V(0) \\ I(0) \end{bmatrix}. \tag{101}$$

After substituting the input voltage and current from (85) the magnitude of the voltage near the bridge wire is calculated as:

$$\begin{bmatrix} V(L) \\ I(L) \end{bmatrix} = \begin{bmatrix} 0.897 + j0.0008 & -0.227 - j28.357 \\ -j0.0088 & 0.836 + j0.0013 \end{bmatrix} \cdot \begin{bmatrix} 0.112 - j94.716 \\ 1 \end{bmatrix}$$

$$\begin{bmatrix} V(L) \\ I(L) \end{bmatrix} = \begin{bmatrix} -0.047 - j113.303 \\ 0 \end{bmatrix}$$

$$V\left(\text{Bridge Wire}\right) = \left|-0.047 - j113.303\right| = 113.303\ V\ .$$

This voltage magnitude can now be directly compared to the bridge wire voltage EDL value given by ICEPIC for a common mode excitation frequency of 900 MHz. This functionality has been added to the MatLAB program, and is computed across the entire frequency range. Figure 24 is a MatLAB plot of the bridge wire voltage across frequency for common mode excitation. The plot is very similar to Figures 16 and 20, with a resonance at 5.01 GHz due to the resonances being determined by the detonator geometry.

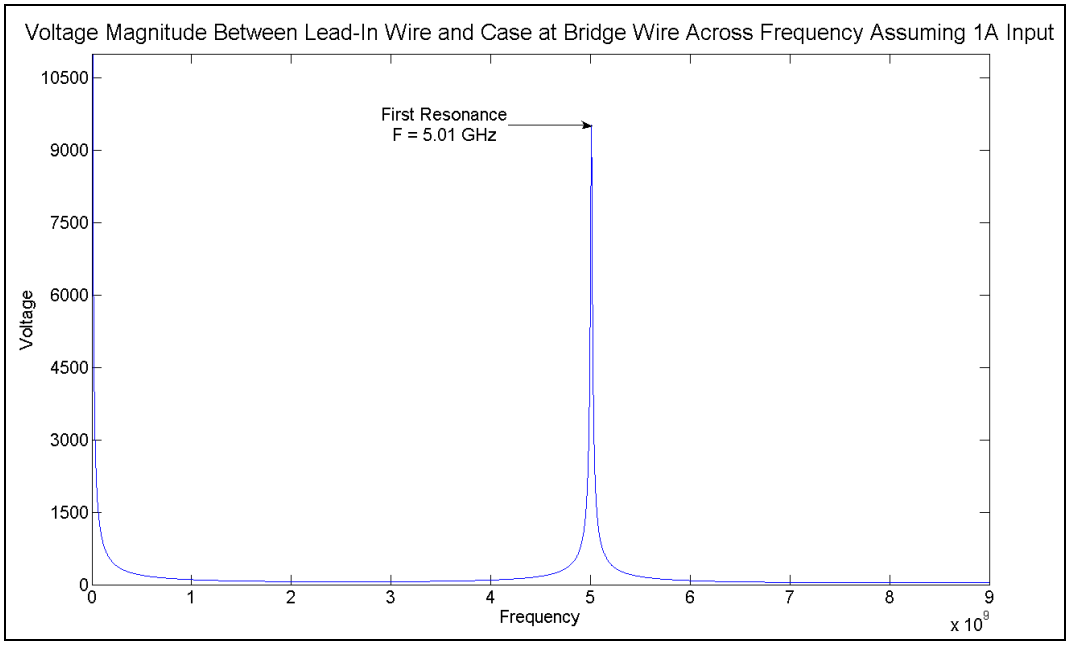

Figure 24: MatLAB plot of the magnitude of the common mode bridge wire voltage across the frequency range DC-9 GHz.

Bridge Wire Current

The bridge wire current is only calculated for differential mode excitation and this computation is performed in the same way as the common mode bridge wire voltage. The current that enters the bridge wire is equal to the current flowing at the end of the lead-in wires, an illustration of which is shown in Figure 25.

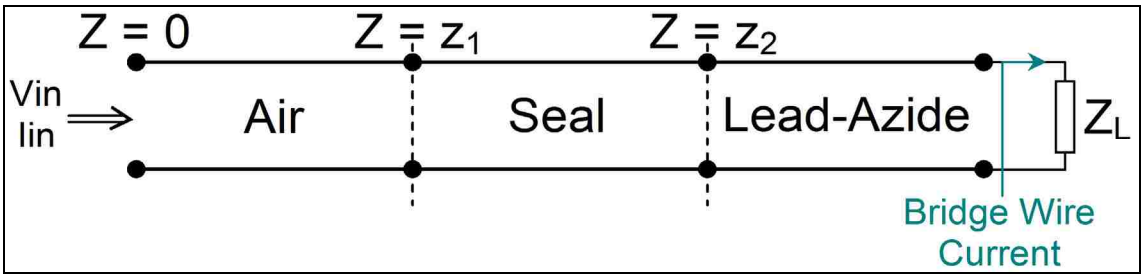

Figure 25: Illustration of dividing the detonator into sections for determining the bridge wire current during differential mode excitation.

Since the transmission line model is identical to what was used in Chapter 3 (Figure 10), the computed transmission matrix for a 900 MHz differential mode input [U(0, L)] can be utilized again here instead of re-computing each section using reversed limits. The transmission matrix used for finding the bridge wire current is calculated by finding the inverse of [U(0, L)]:

$$\begin{bmatrix} V(L) \\ I(L) \end{bmatrix} = \left[\prod_{z_2}^{L} e^{\Gamma_l dz'} \right] \cdot \left[\prod_{z_1}^{z_2} e^{\Gamma_s dz'} \right] \cdot \left[\prod_{0}^{z_1} e^{\Gamma_a dz'} \right] \cdot \begin{bmatrix} V(0) \\ I(0) \end{bmatrix}, \quad (102)$$

$$\begin{bmatrix} V(L) \\ I(L) \end{bmatrix} = \left[U(L,0) \right] \cdot \begin{bmatrix} V(0) \\ I(0) \end{bmatrix}, \text{ and} \quad (103)$$

$$\left[U(L,0) \right] = \left[U(0,L) \right]^{-1} \quad (104)$$

$$= \left[M_l \right] \cdot \left[M_s \right] \cdot \left[M_a \right] \quad (105)$$

$$= \begin{bmatrix} 0.872 + j0.0005 & -0.304 - j82.12 \\ -j0.0046 & 0.715 + j0.0011 \end{bmatrix}.$$

Finally, the entire matrix equation becomes:

$$\begin{bmatrix} V(L) \\ I(L) \end{bmatrix} = \begin{bmatrix} 0.872 + j0.0005 & -0.304 - j82.12 \\ -j0.0046 & 0.715 + j0.0011 \end{bmatrix} . \begin{bmatrix} V(0) \\ I(0) \end{bmatrix} \quad (106)$$

After substituting the input voltage and current from (75) the magnitude of the current through the bridge wire is calculated as:

$$\begin{bmatrix} V(L) \\ I(L) \end{bmatrix} = \begin{bmatrix} 0.872 + j0.0005 & -0.304 - j82.12 \\ -j0.0046 & 0.715 + j0.0011 \end{bmatrix} . \begin{bmatrix} 1.87 + j105.18 \\ 1 \end{bmatrix}$$

$$\begin{bmatrix} V(L) \\ I(L) \end{bmatrix} = \begin{bmatrix} 1.33 - j9.606 \\ 1.198 - j0.008 \end{bmatrix}$$

$$I\left(\text{Bridge Wire}\right) = \left|1.198 - j0.008\right| = 1.198 \text{ A} .$$

This current magnitude can now be directly compared to the bridge wire CUR_CIR value given by ICEPIC for a differential mode excitation frequency of 900 MHz. This functionality has been added to the MatLAB program, and is computed across the entire frequency range. Figure 26 is a MatLAB plot of the bridge wire current across frequency for differential mode excitation. The plot is very similar to Figures 15 and 18 with resonances at 2.489 and 6.604 GHz due to the resonances being determined by the detonator geometry.

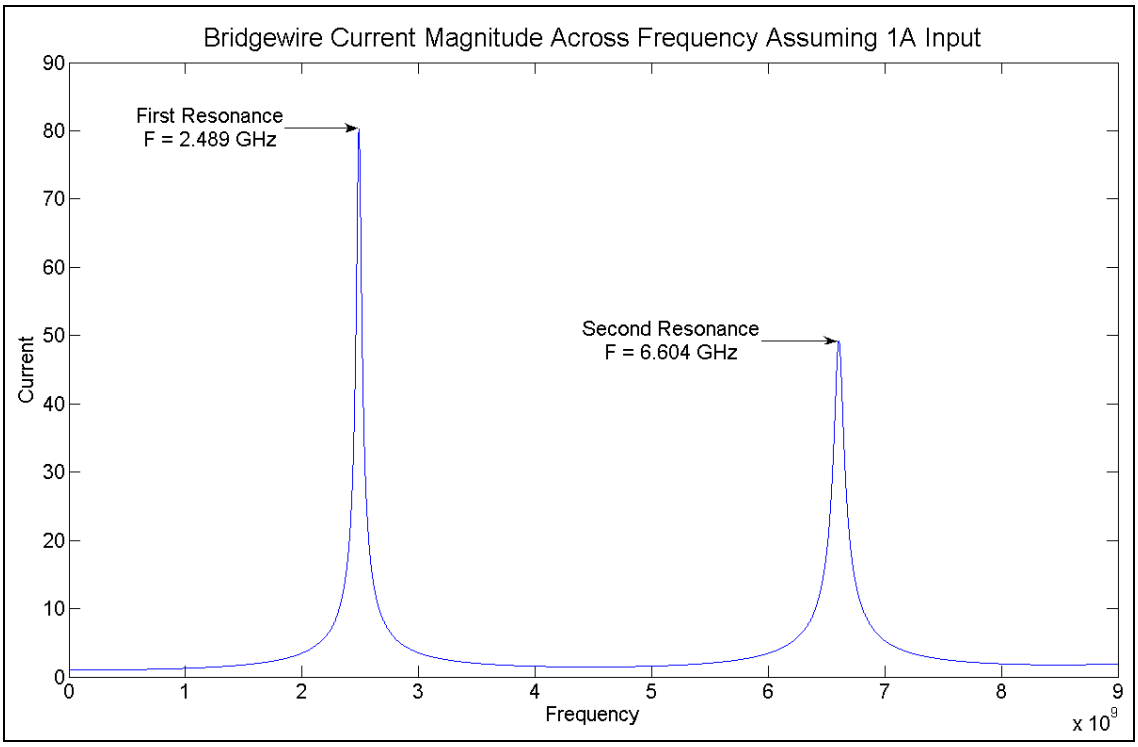

Figure 26: MatLAB plot of the magnitude of the differential mode bridge wire current across the frequency range DC-9 GHz.

Chapter Summary

In this chapter, the process of implementing the generic detonator geometry in the simulation space of ICEPIC was described. This included the dimensions of a PML box enclosing the excitation source(s), the grid size, simulation time, time step, and scaled bridge wire. Also, some ICEPIC diagnostics were described along with where they are to be used within the generic detonator geometry. Then, the analytical model described in Chapter 3 was modified with additional calculations in order to predict voltage and current magnitudes for both differential and common mode excitation for direct comparison with ICEPIC results.

Chapter 5 – Simulation Results and Comparison to Analytic Predictions

Using the numerical model described in Chapter 4 along with the modified analytical model, direct comparisons can now be made between 3-D EM simulations and 1-D transmission line model predictions.

Initial ICEPIC Simulation Results and Data Analysis

The detonator geometry described in Chapter 4 was simulated in ICEPIC for 50 ns with excitation frequencies of 900 MHz and 4 GHz for differential mode excitation and 900 MHz and 6 GHz for common mode excitation. These frequencies were initially chosen as they are near the beginning and middle of the frequency range of interest. The preliminary analysis was performed at only two frequencies to ascertain the model behavior before many frequencies were simulated.

Data Analysis Tools and Procedures

The data analysis involved several different programs. Paraview [Version 3.2.1] and Draw [Version 14.0] were used to visualize the electric ($\vec{E}$) fields within the detonator. The EDL and CUR_CIR results were viewed using XMGrace [Version 5.1.22]. Within XMGrace, several features were utilized. For the 900 MHz simulations, the magnitude and resonant frequency were found using non-linear curve-fitting techniques. First, the drive frequency of 900 MHz was subtracted from the waveform. The resulting signal was then fitted for frequency, which was determined to be the resonant frequency. For all other excitation frequencies greater than 900 MHz, multiple resonant frequencies are excited, making it nearly impossible to discern the drive

frequency magnitude from the given waveform. Under these circumstances, XMGrace was used to perform a discrete Fourier transform (DFT) on the data, separating the drive and resonant frequencies, and determining the magnitude of each. To eliminate any possible effect on the results of the input current amplitude ramping from 0 to 1 A over three cycles, the first 2 ns were chopped from each data set prior to performing the DFT. Lastly, the magnitudes and frequencies found using these DFTs were found by simply placing the mouse as close as possible to the point of interest, and reading off the data value given for that point by XMGrace. These processes will be illustrated in later figures.

The accurate determination of resonant frequencies is important because the detonator has a very high impedance at these frequencies, resulting in a high input voltage into the detonator. The high input voltage produces a high bridge wire current during differential mode excitation and a high case-to-bridge wire voltage during common mode excitation, both conditions potentially causing detonator ignition.

Full Detonator Differential Mode Results

The full detonator model was excited in differential mode as described in Chapter 4, utilizing all the field planes, EDL's and CUR_CIR diagnostics shown in Figures 11, 13, and 14 of Chapter 4. Figures 1 through 4 indicate the E_x field distribution in the Z = input plane, X = 0 plane, Y = 0 plane, and Z = bridge wire plane for 900 MHz and 4 GHz excitation at t = 40.73 ns, or just over 81% of the way through the total simulation time to ensure the system had reached a steady-state condition. Examination of the E_y and E_z field distributions yielded no useable data, and will not be shown. This is expected since

the exciting current source is oriented in the X direction. The red box in Figures 2 and 3 indicates the boundary of the simulation space.

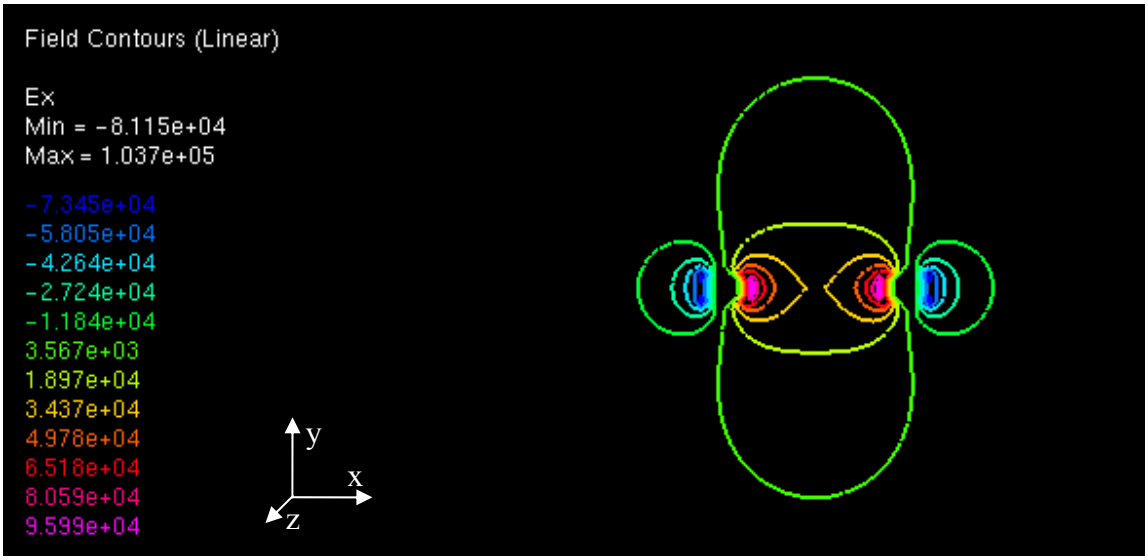

(a)

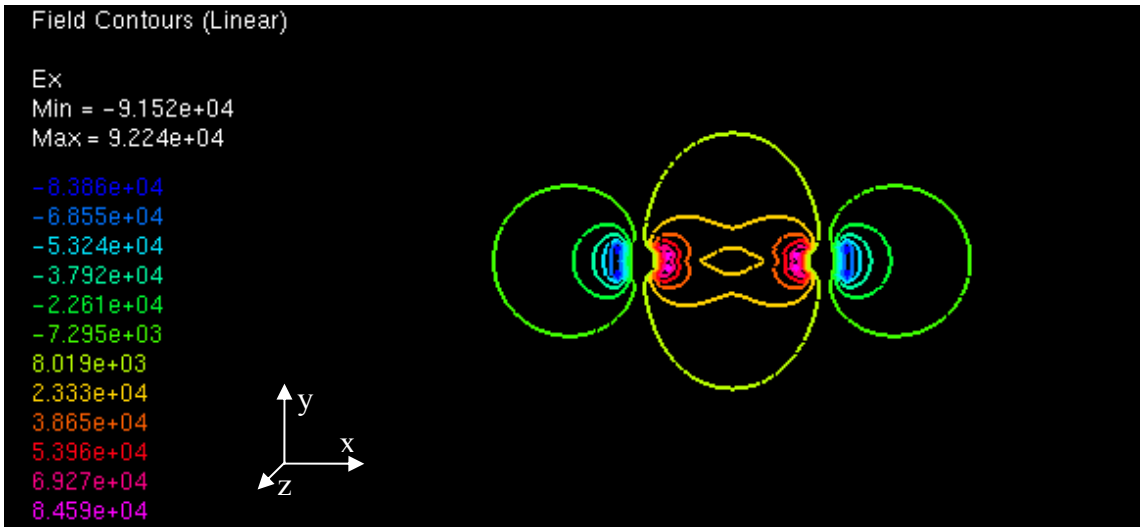

(b)

Figure 1: Contour plot of E_x field distribution in the Z = input plane for 900 MHz (a) and 4 GHz (b) differential mode excitation.

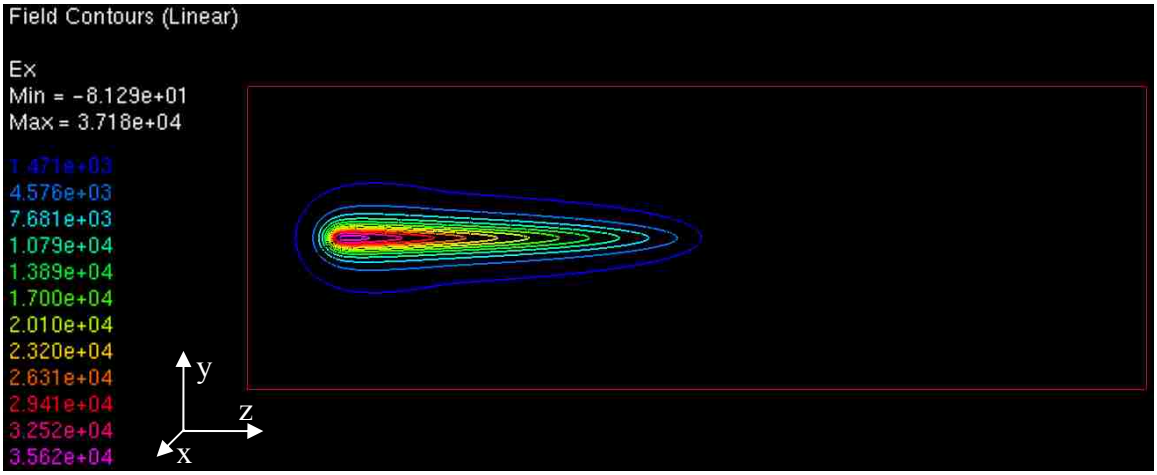

(a)

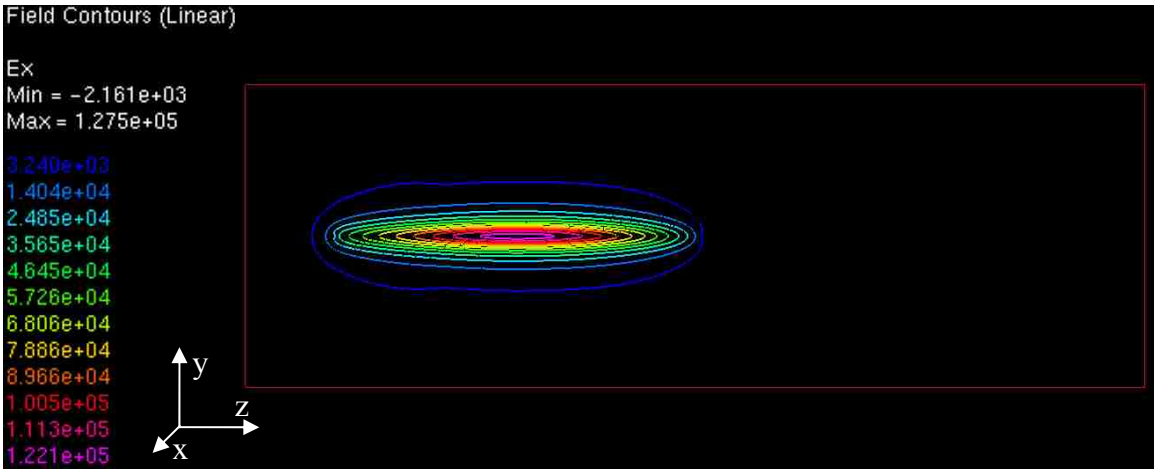

(b)

Figure 2: Contour plot of E_x field distribution in the X = 0 plane for 900 MHz (a) and 4 GHz (b) differential mode excitation.

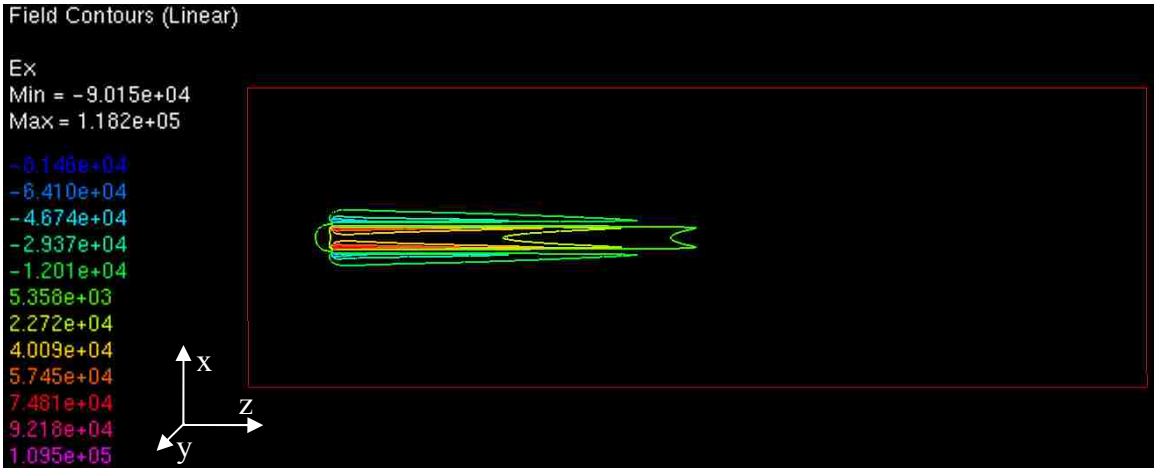

(a)

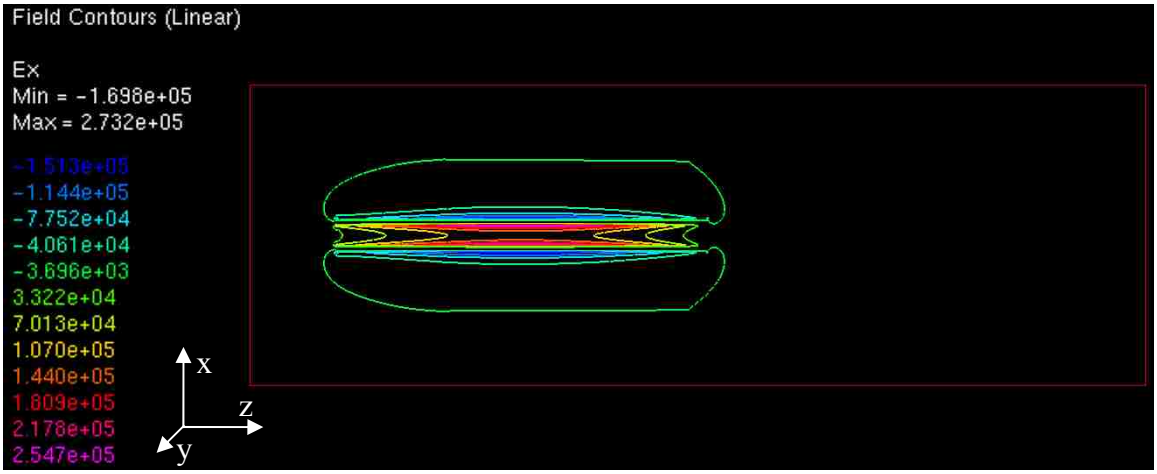

(b)

Figure 3: Contour plot of E_x field distribution in the Y = 0 plane for 900 MHz (a) and 4 GHz (b) differential mode excitation.

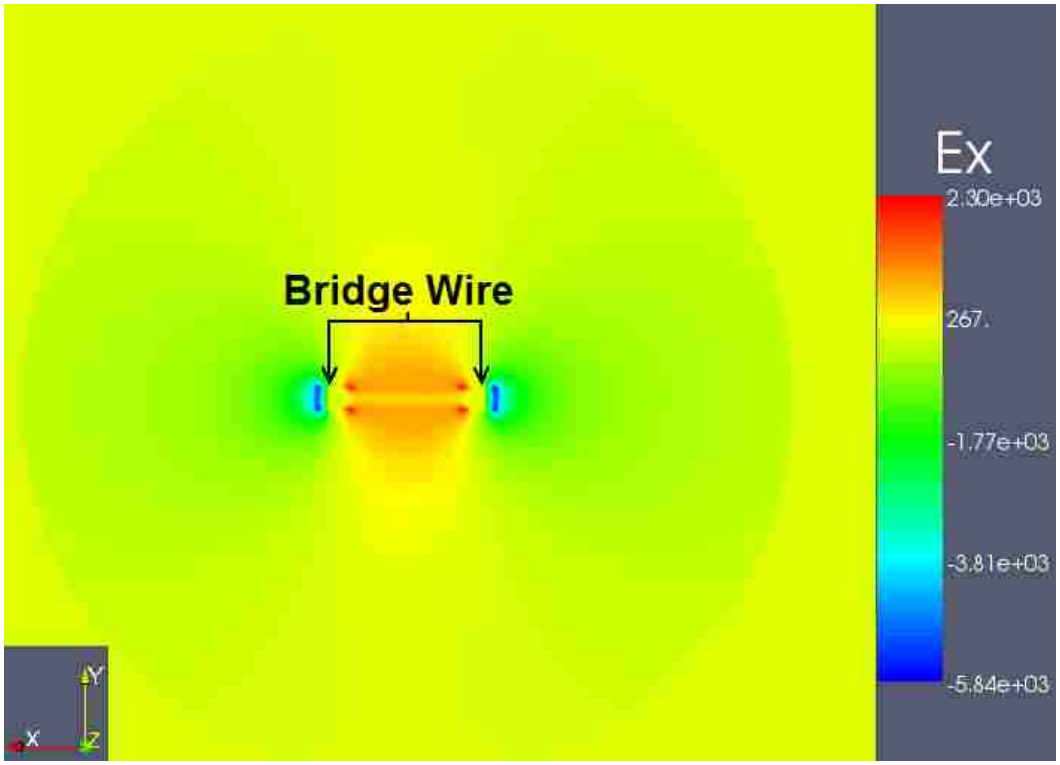

(a)

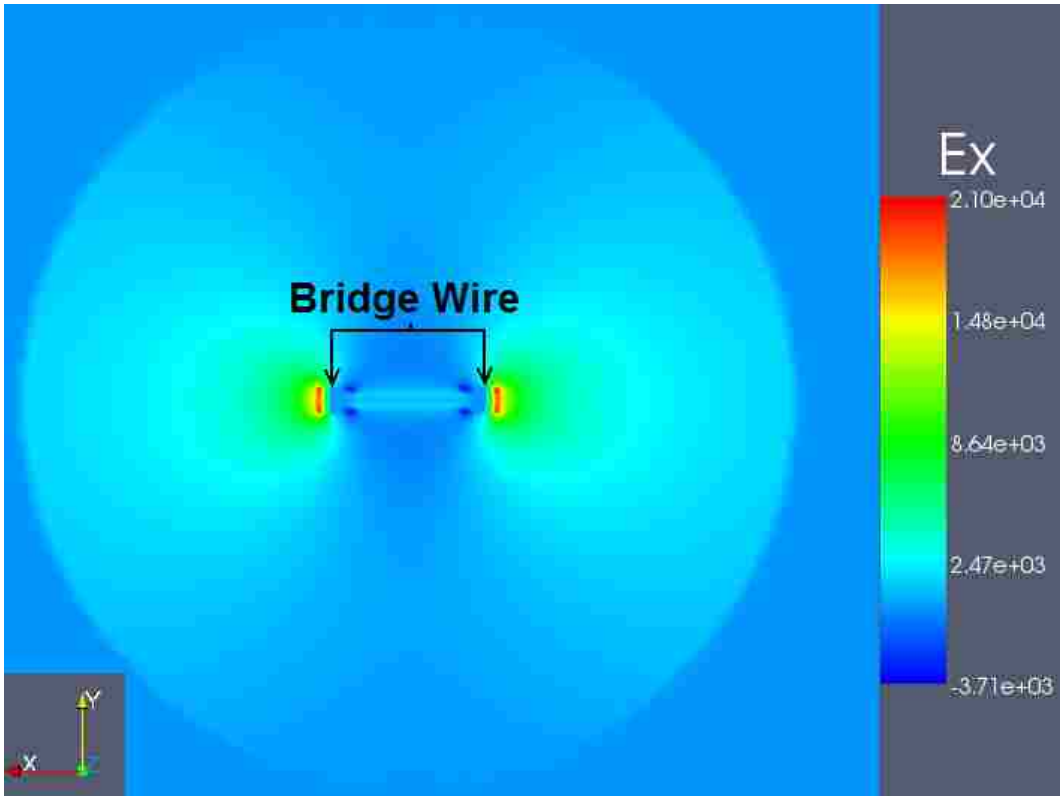

(b)

Figure 4: Contour plot of E_x field distribution in the Z = bridge wire plane for 900 MHz (a) and 4 GHz (b) differential mode excitation.

Figures 1 through 4 indicate similar, though not exact, E_x field distributions among the different detonator planes for both frequencies while the minimum and maximum values differ. Figures 2 and 3 indicate a shift in maximum field intensity for the 900 MHz and 4 GHz E_x field distributions from end to end of the detonator. In general, the 900 MHz distributions indicate a maximum field intensity near the beginning of the lead-in wires while at 4 GHz this maximum occurs just inside the seal portion of the detonator. This shift in maximum location is due to the development of a standing wave pattern at 4 GHz, which creates a higher maximum E_x field value away from the excitation location at the beginning of the lead-in wires. However, the E_x field values at the beginning of the lead-in wires are comparable at both frequencies. For the X = 0 plane, the 900 MHz E_x field value at the lead-in wires is approximately $3.562*10^4$ V/m while at 4 GHz it is approximately $3.565*10^4$ V/m. At 900 MHz this is a maximum value, but at 4 GHz it is not. For the Y = 0 plane, the 900 MHz E_x field value at the lead-in wires is approximately $7.481*10^4$ V/m while at 4 GHz it is approximately $7.013*10^4$ V/m. In Figure 4, the E_x field radiates away from the bridge wire at both edges where it connects to the lead-in wires. This leakage field at the corners is expected due to the 90^0 bend in the wires. This abrupt change in direction causes the E_x field to radiate out from the bend, and this occurs prominently at both frequencies.

While the E_x field distributions are illustrative and indicate what is happening inside the detonator, it is primarily the EDL and CUR_CIR values that need to be analyzed. This is because the purpose of this project is to determine the detonator's EM characteristics such as input impedance and bridge wire current under different RF/MW excitation conditions. The E_x field distributions do not clearly illustrate these

characteristics, and so will not be examined in much more detail then has already been described. Figures 5 through 7 present the input, mid-seal, and bridge wire voltage waveforms respectively at 900 MHz and 4 GHz, while Figure 8 is the bridge wire current waveform at 900 MHz and 4 GHz. A general observation of Figures 5 through 8 is that the voltage waveforms at different places along the detonator as well as that of the bridge wire current waveform are all similar in appearance and behavior across time for each frequency, with the primary difference being the maximum value of the waveform amplitudes. The initial voltage values for the first few nanoseconds of simulation indicate transient values due to the ramping of the excitation current magnitude from 0 to 1 A across three complete cycles, as described in Chapter 4. Also, the 900 MHz waveform reaches steady-state very quickly, and is a relatively flat and simple waveform pattern. The 4 GHz waveforms are more complicated, indicating the excitation of multiple resonant frequencies. The 4 GHz waveforms also take longer to reach steady-state, as the effect of higher order resonances initially excited at the beginning of the simulation decrease over time.

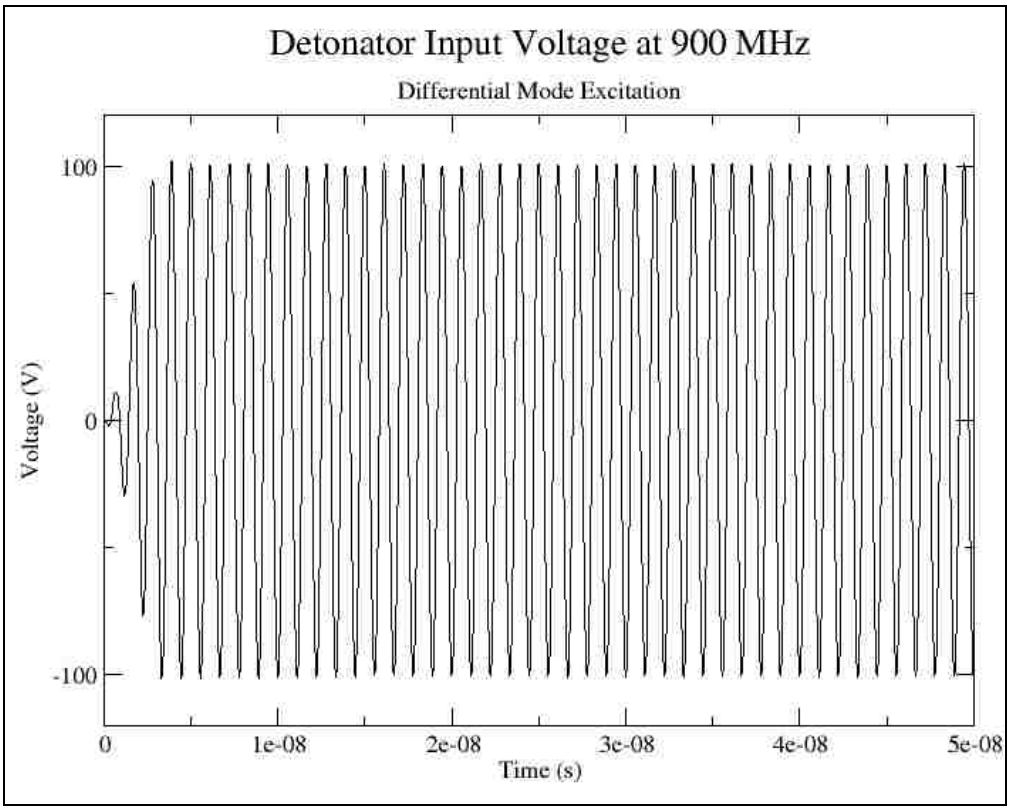

(a)

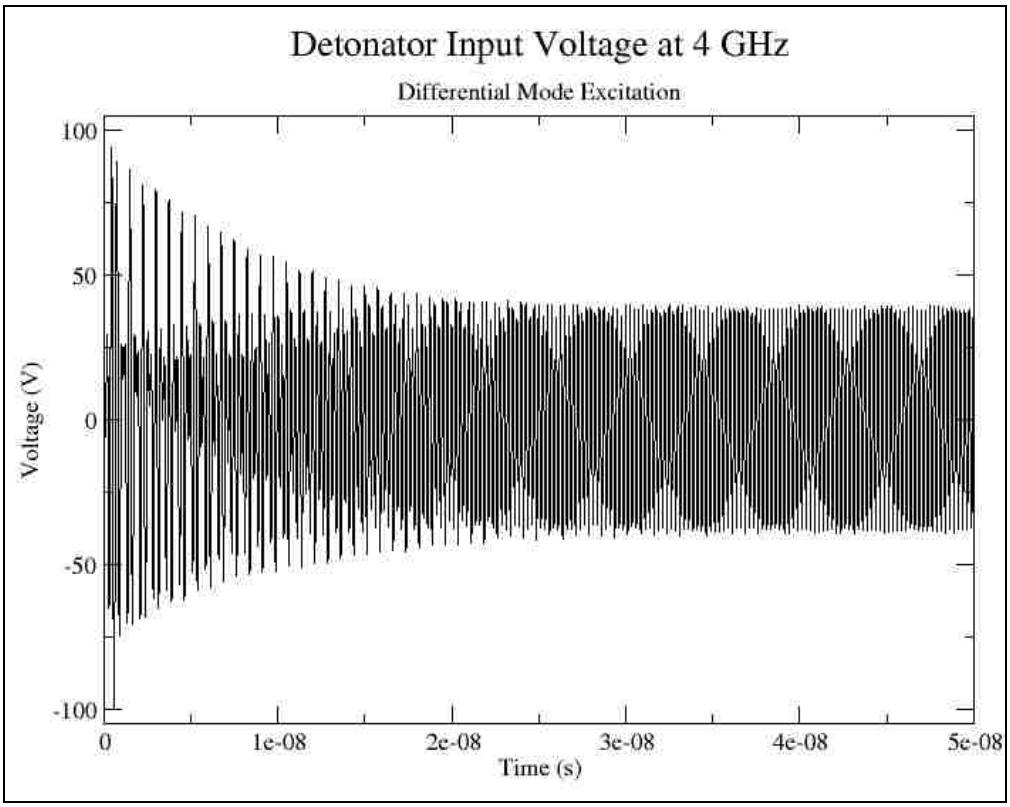

(b)

Figure 5: Detonator input voltage at 900 MHz (a) and 4 GHz (b) during differential mode excitation.

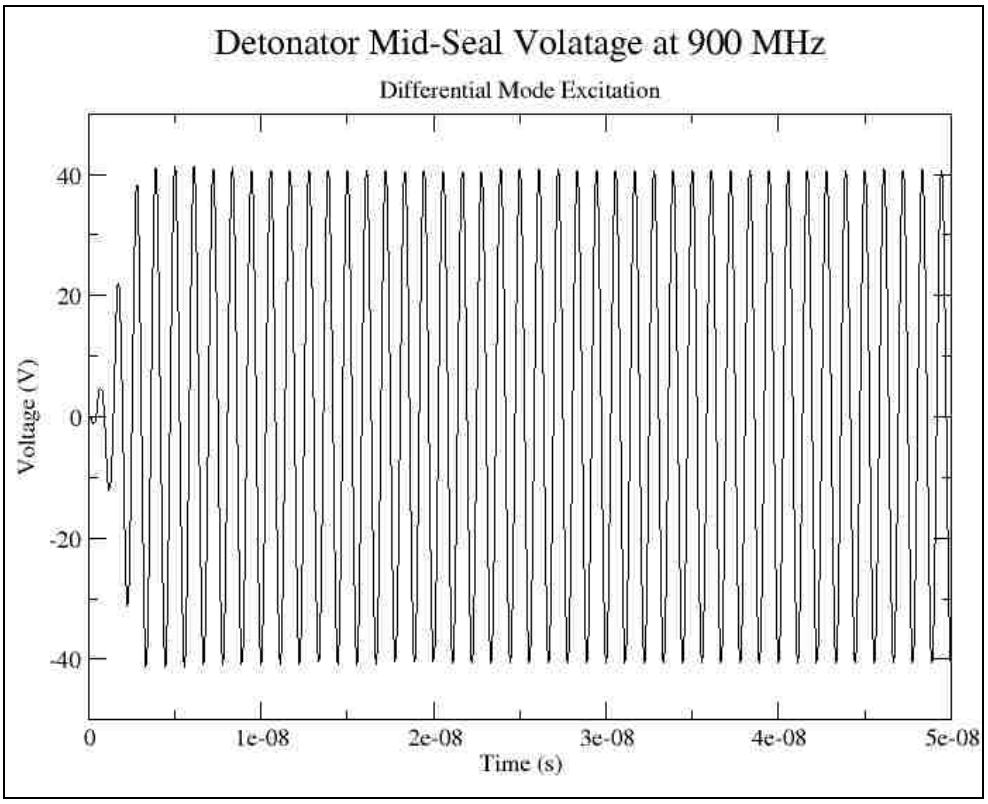

(a)

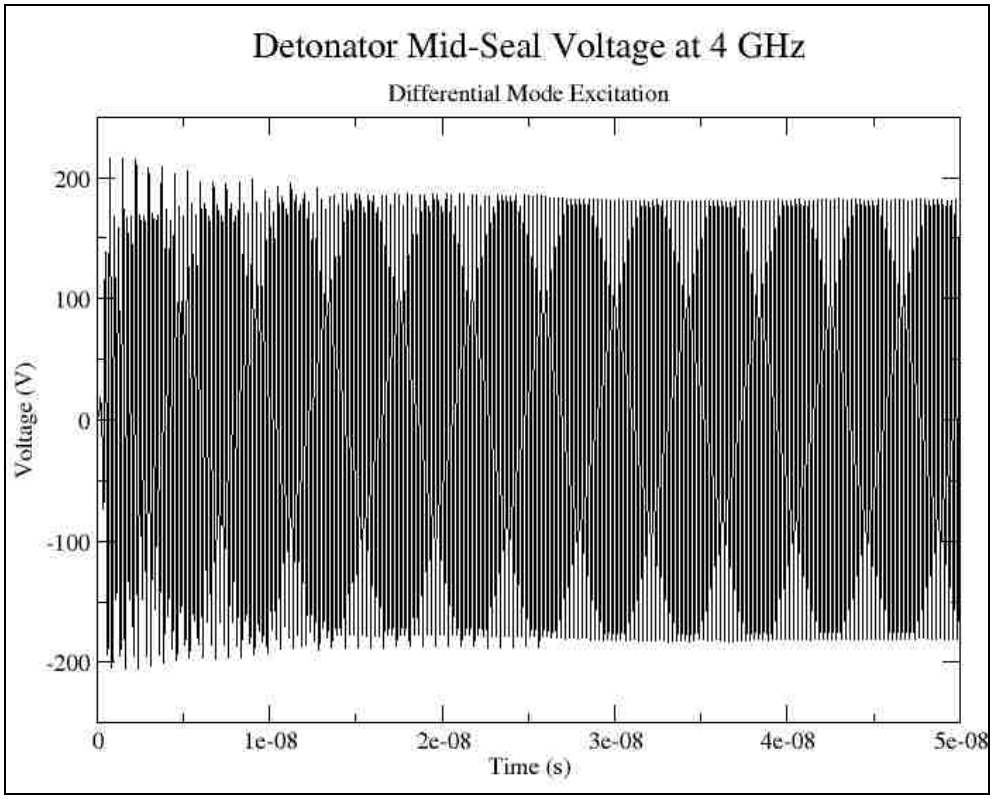

(b)

Figure 6: Detonator mid-seal voltage at 900 MHz (a) and 4 GHz (b) during differential mode excitation.

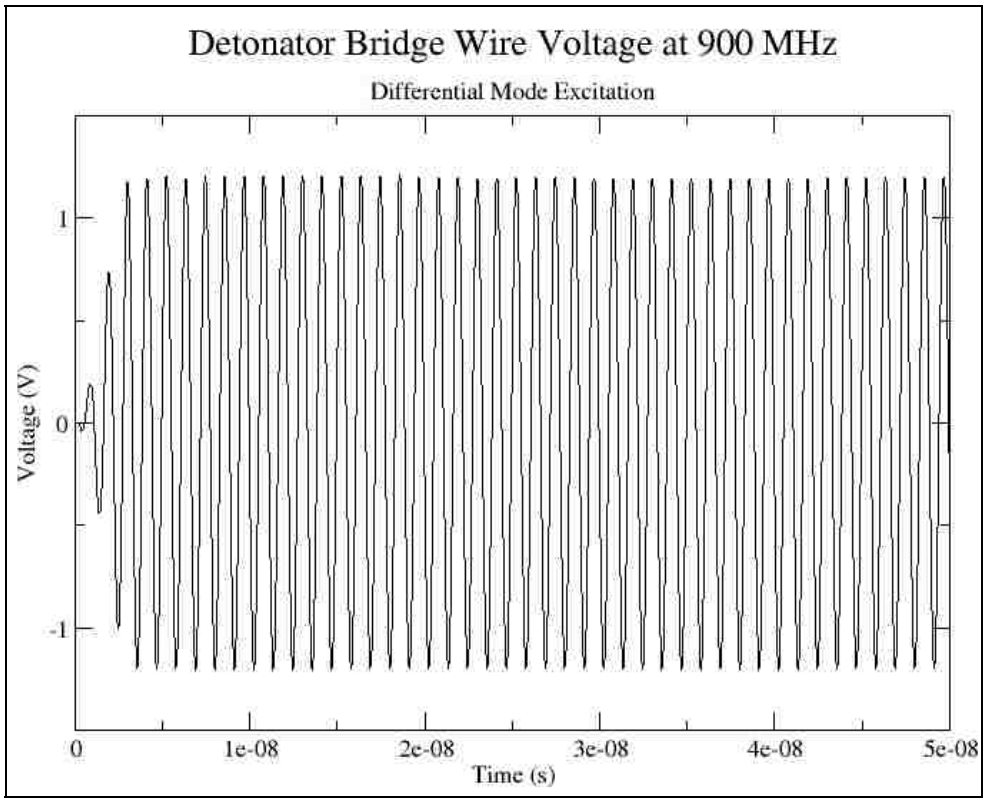

(a)

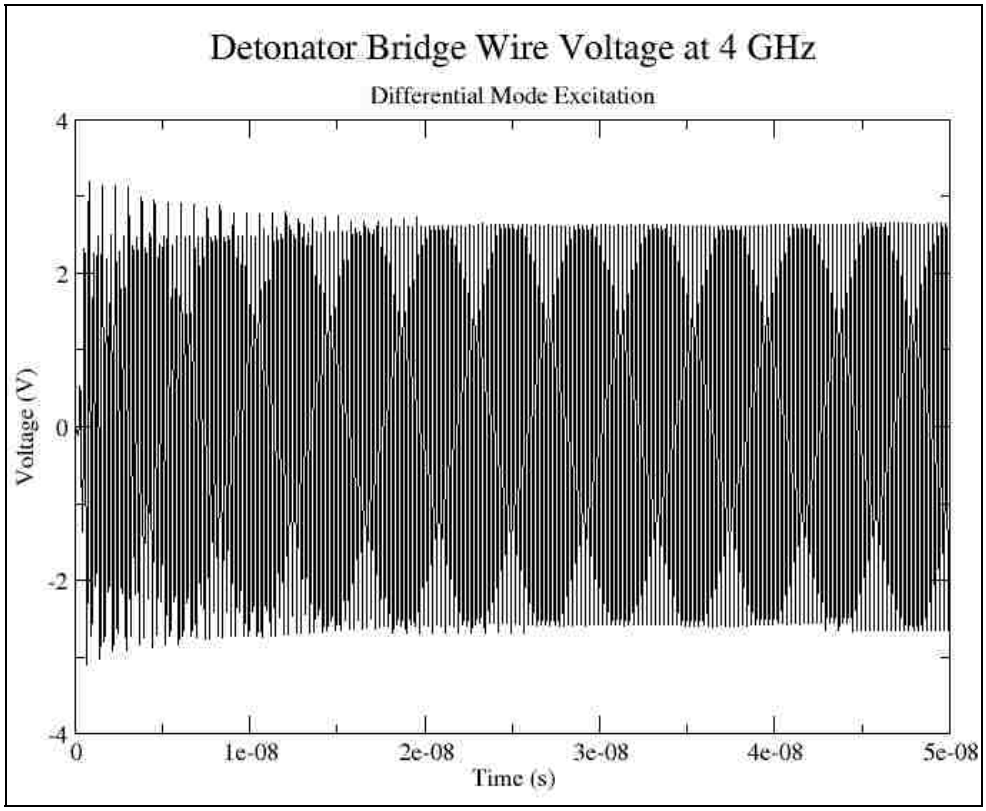

(b)

Figure 7: Detonator bridge wire voltage at 900 MHz (a) and 4 GHz (b) during differential mode excitation.

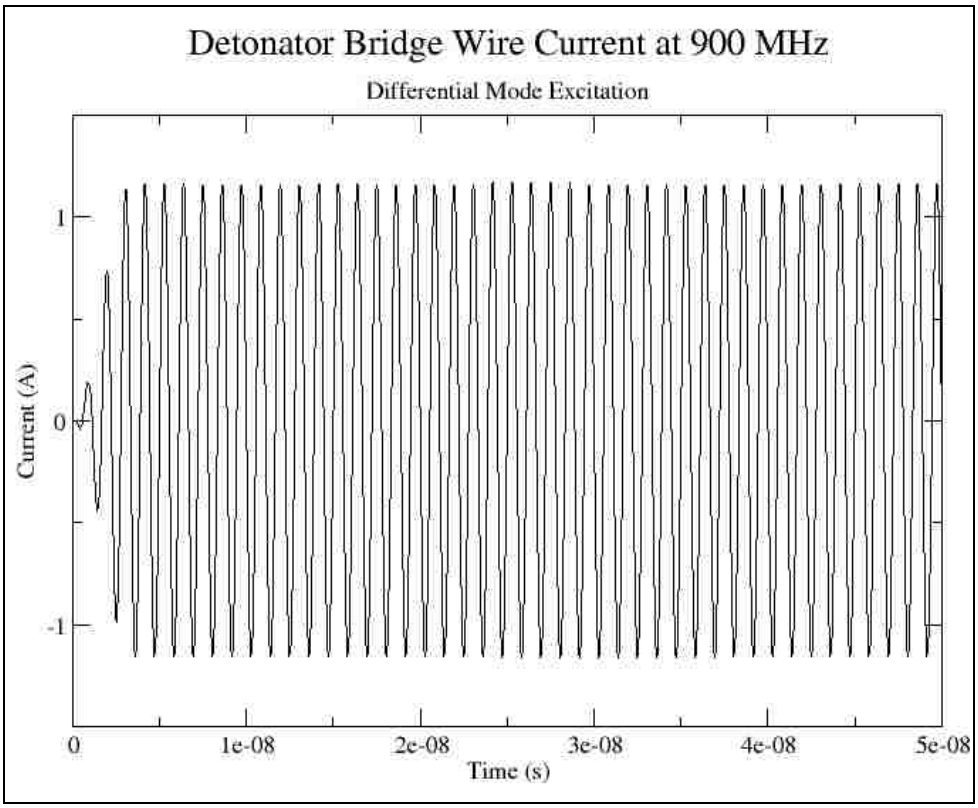

(a)

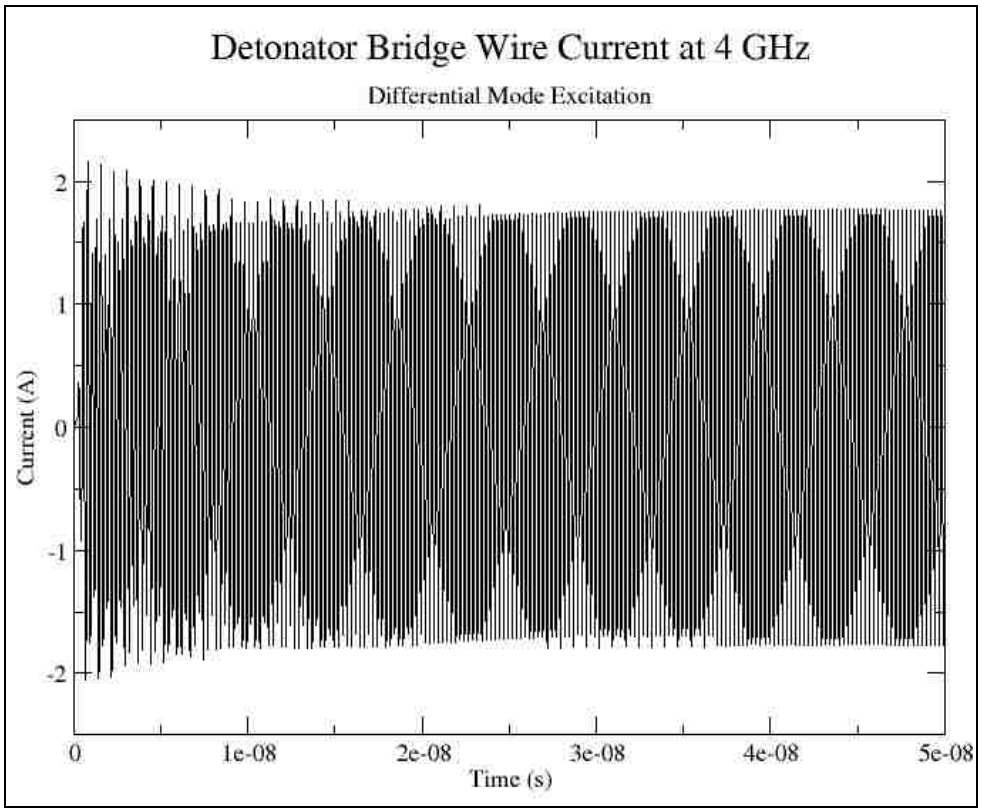

(b)

Figure 8: Detonator bridge wire current at 900 MHz (a) and 4 GHz (b) during differential mode excitation.

Curve-fitting techniques are used to help determine the magnitude of the drive frequency of the input voltage at 900 MHz (Figure 5a), and this curve fit resulted in a drive frequency magnitude of 100.99 V, which represents the input voltage into the detonator given a 1 A 900 MHz differential mode input. A zoomed view of Figure 5a with the curve fit overlaid in red is shown in Figure 9. When this fitted drive frequency waveform is subtracted from the input voltage waveform, the result is the residual voltage shown in Figure 10.

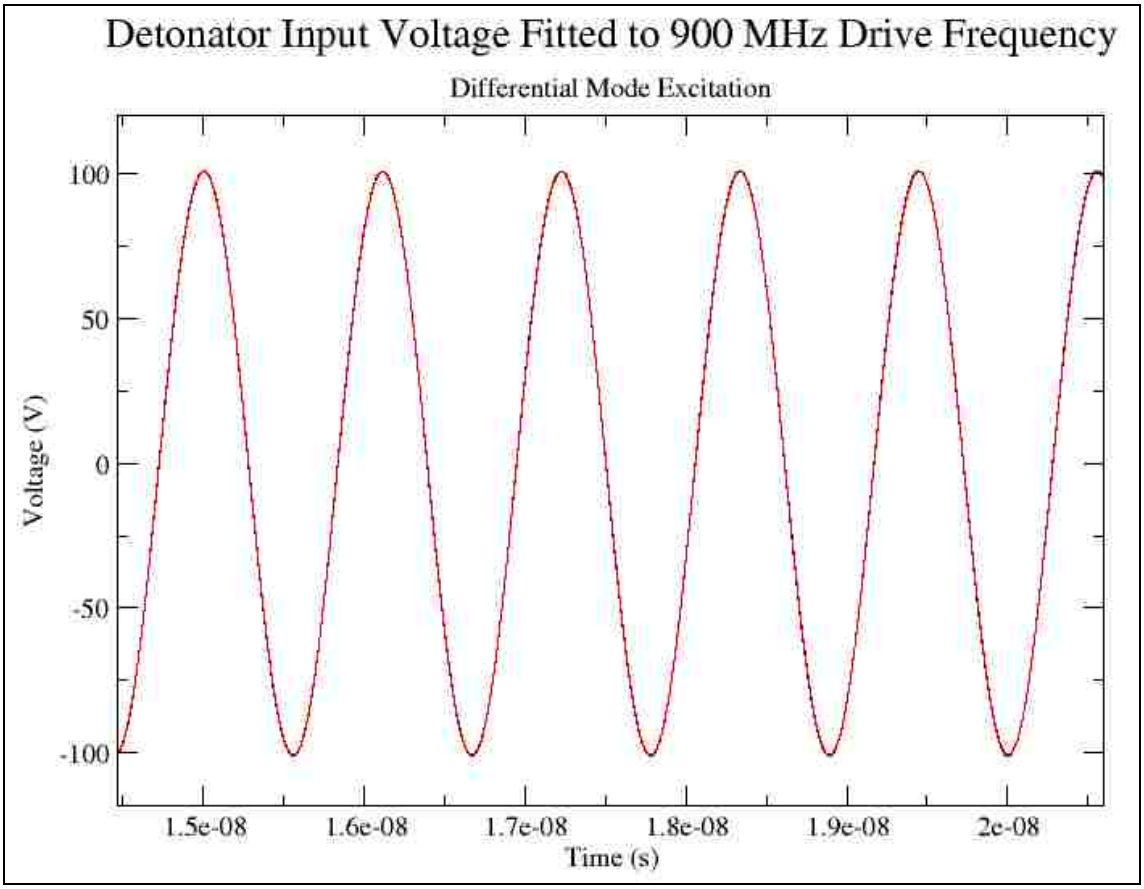

Figure 9: Fitted 900 MHz drive frequency waveform overlaid on the original input voltage waveform shown in Figure 5a.

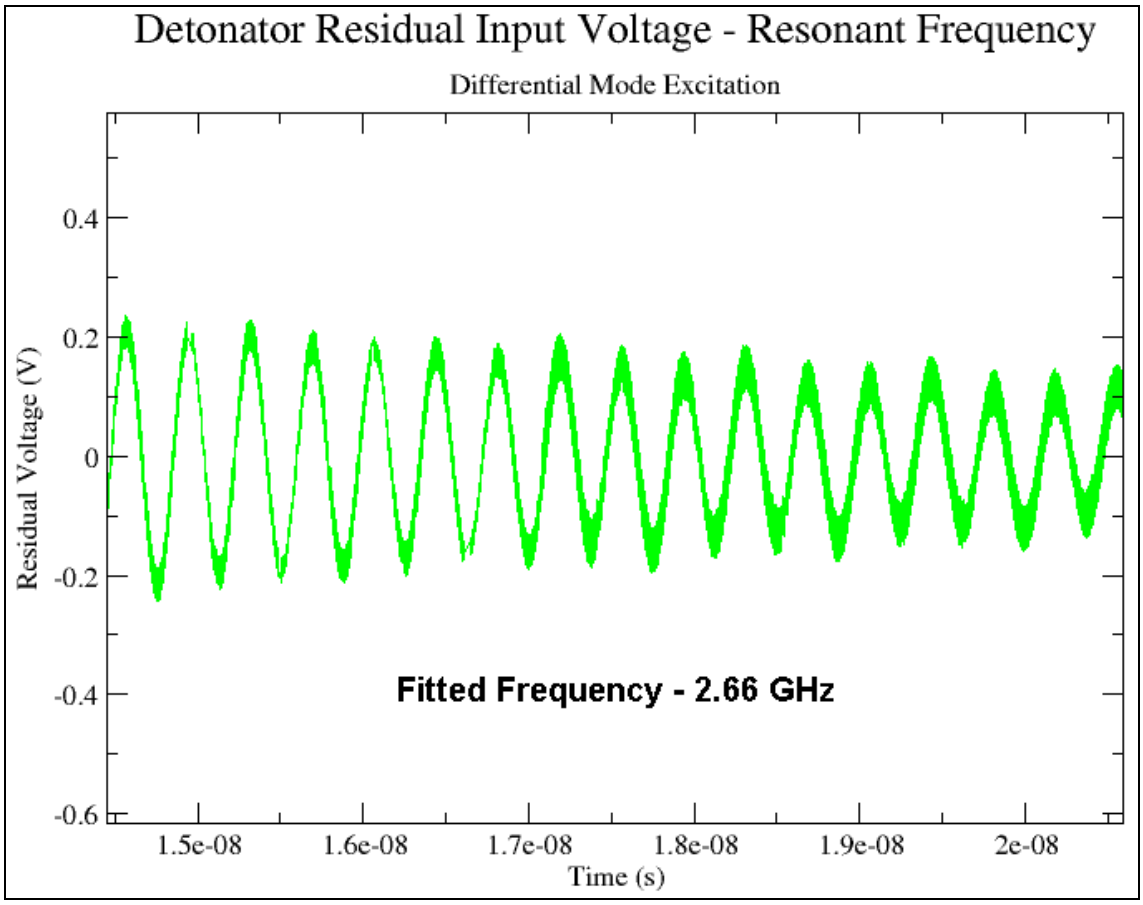

Figure 10: Residual voltage after subtracting the fitted drive frequency from the input voltage waveform.

When curve-fitting is again used on this residual waveform, it is found to have a frequency of 2.66 GHz, which is deemed to be the first resonant frequency of the detonator. Subsequent waveform subtractions did not yield any additional resonant frequencies, indicating that a 900 MHz input is only capable of exciting the first resonant frequency while higher order resonances are not excited. Drive frequency magnitudes and resonant frequencies were found in a similar manner for the mid-seal and bridge wire voltages, as well as the bridge wire current. It was discovered that all four diagnostics revealed the same resonant frequency (2.66 GHz), and as such it is not necessary to show the residual voltage waveforms for each since Figure 10 is representative of all four diagnostic residuals. The results of these analyses are listed in Tables 1 and 2.

The voltage waveforms at 4 GHz are analyzed using a DFT to find the drive frequency magnitude, as well as the resonant frequencies. Figure 11 is the DFT of the 4 GHz input voltage shown in Figure 5b, and Figure 12 is a zoomed view of the DFT to show higher order resonances.

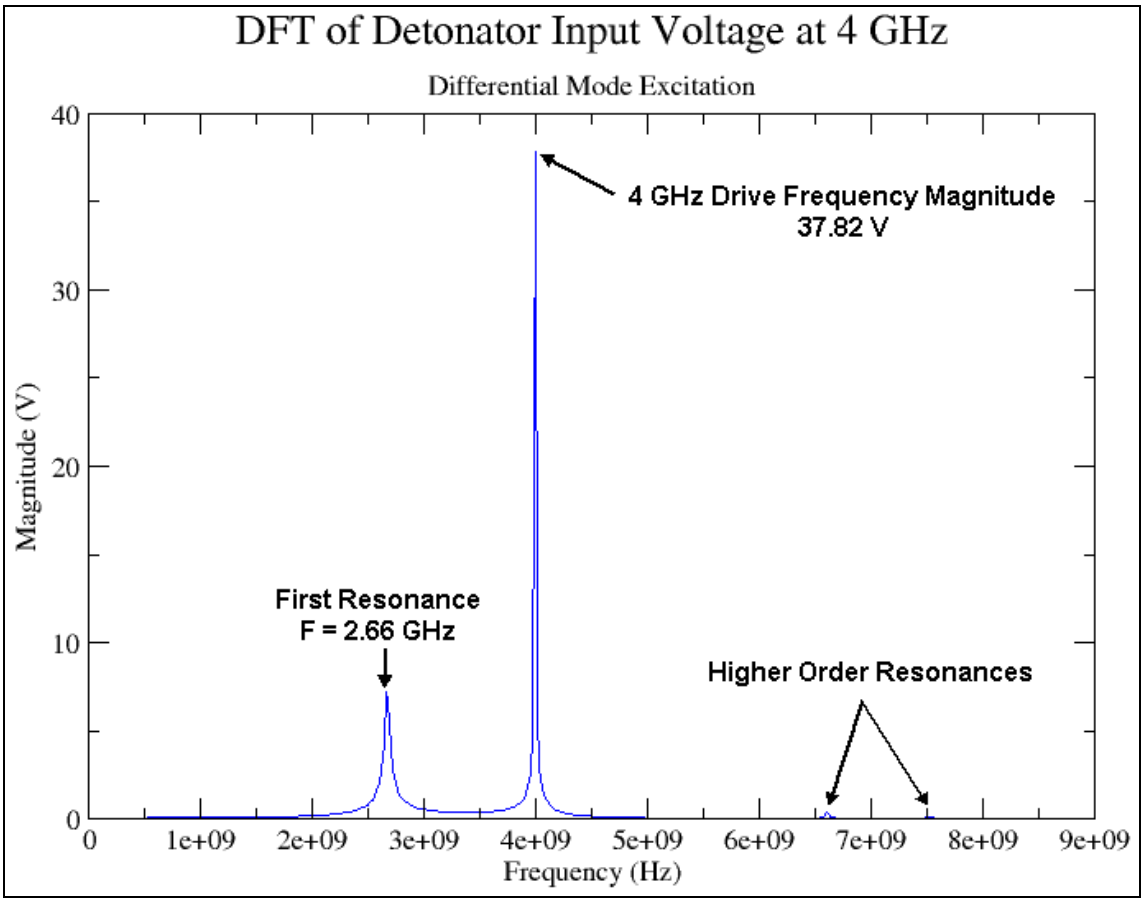

Figure 11: DFT of the detonator input voltage at 4 GHz shown in Figure 5b.

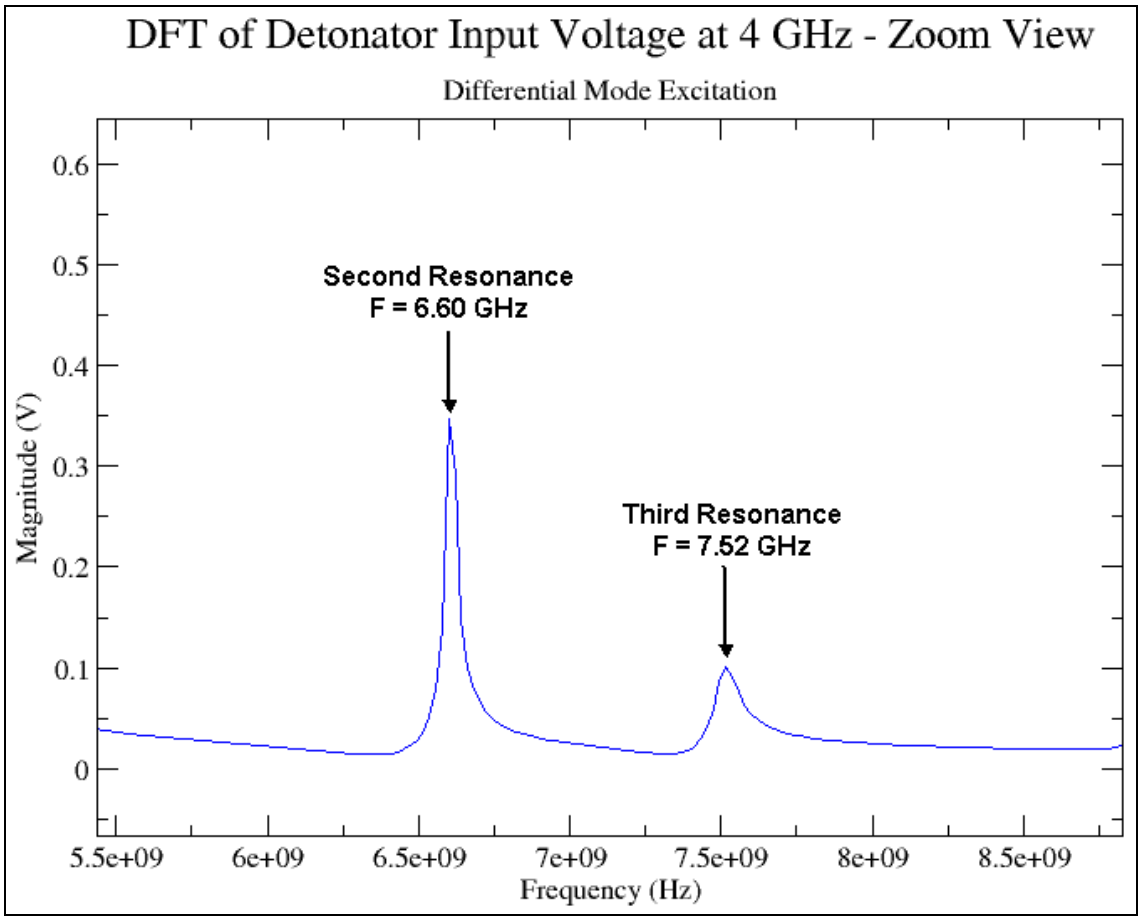

Figure 12: Zoomed view of the DFT to show higher order resonances.

This DFT determines a drive frequency magnitude of 37.82 V, and resonant frequencies of 2.66, 6.60, and 7.52 GHz. This data indicates that a differential mode input signal at 4 GHz and 1 A will result in a 37.82 V input into the detonator. Also the 4 GHz signal was able to excite not only the first resonant frequency of 2.66 GHz found previously with curve-fitting techniques for the 900 MHz waveforms, but also higher order second and third resonant frequencies. This same type of DFT analysis was performed on the mid-seal and bridge wire voltage waveforms as well as the bridge wire current waveform. It was found that all four waveforms indicated the same three resonant frequencies. As such, the DFT results will not be repeated since Figure 10 is representative of all four. The results from these analyses are listed in Tables 1 and 2.

Table 1: Detonator differential mode voltage and current magnitudes.

Frequency	Input Voltage	Mid-Seal Voltage	Bridge Wire Voltage	Bridge Wire Current
900 MHz	100.99	40.89	1.21	1.17
4 GHz	37.82	180.65	2.57	1.73

Table 2: Detonator differential mode resonances.

Frequency	First Resonance	Second Resonance	Third Resonance
900 MHz	2.66 GHz	N/A	N/A
4 GHz	2.66 GHz	6.60 GHz	7.52 GHz

The resonance frequencies shown in Figures 11 and 12 appear on the DFT of the voltage waveforms as additional lower amplitude peaks in the plot compared to that of the drive frequency. To verify that these peaks do in fact represent resonant frequencies, the detonator geometry was simulated with differential mode excitation at the three frequencies found to be resonant. A plot of the resulting input voltage waveform for an excitation frequency of 2.66 GHz is shown in Figure 13. The voltage increases exponentially to an extremely large value of over 10,000 V in just under 20 ns, and levels off at that value for the remaining simulated time of 10 ns. This clearly indicates that a 2.66 GHz differential mode excitation causes resonant behavior within the detonator. The waveforms for differential mode input frequencies of 6.6 and 7.52 GHz illustrated the same behavior, and are well represented by Figure 13. These additional simulations verified that all three resonant frequencies found using the DFT are valid.

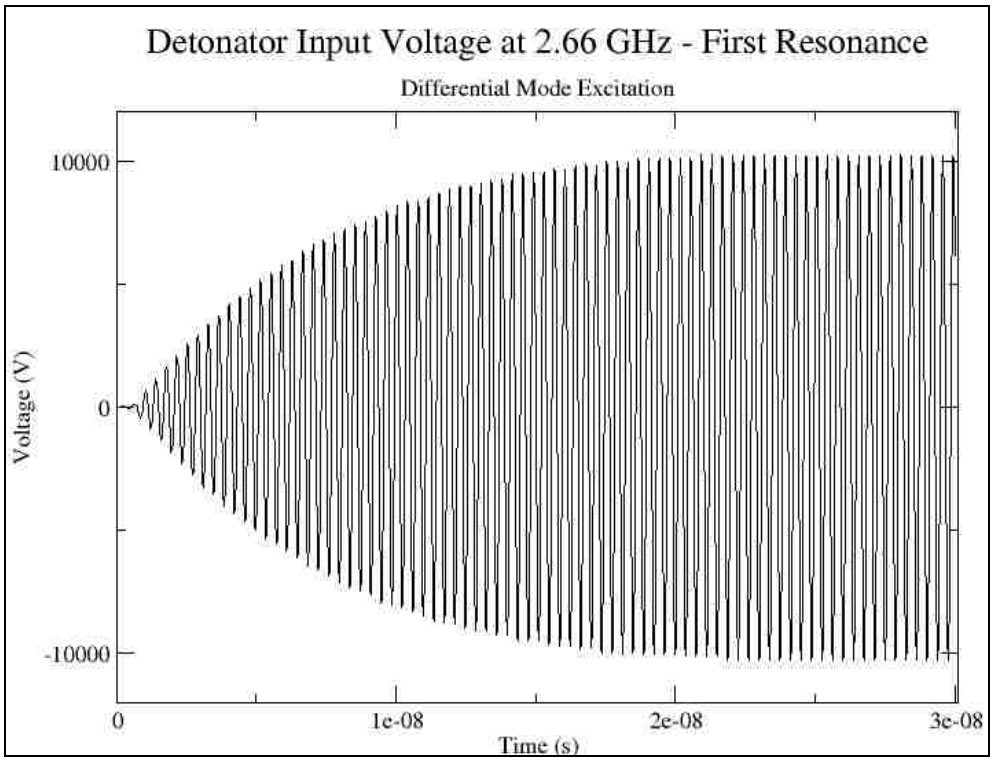

Figure 13: Detonator input voltage at 2.66 GHz during differential mode excitation of the first resonance.

Full Detonator Common Mode Results

The full detonator model also was excited in common mode as described in Chapter 4, utilizing all the field planes, EDL's and CUR_CIR diagnostics shown in Figures 12 through 14 of Chapter 4. Unlike differential mode excitation, the X = 0 and Y = 0 planes contain very little $\vec{E}$ field. This is caused by the method of excitation. During common mode excitation both lead-in wires are at the same potential. Under this condition, an appreciable $\vec{E}$ field distribution is not created between the lead-in wires, where the X and Y = 0 planes are set up. Because of this, these two fields will not be shown. Figures 14 and 15 indicate the E_x field distribution in the Z = input plane and Z = bridge wire plane for 900 MHz and 6 GHz excitation at t = 25 ns, or 50% of the way through the total simulation time. Examination of the E_y and E_z field distributions

yielded no useable data, and will not be shown. The red box in Figures 14 and 15 again indicates the boundary of the simulation space.

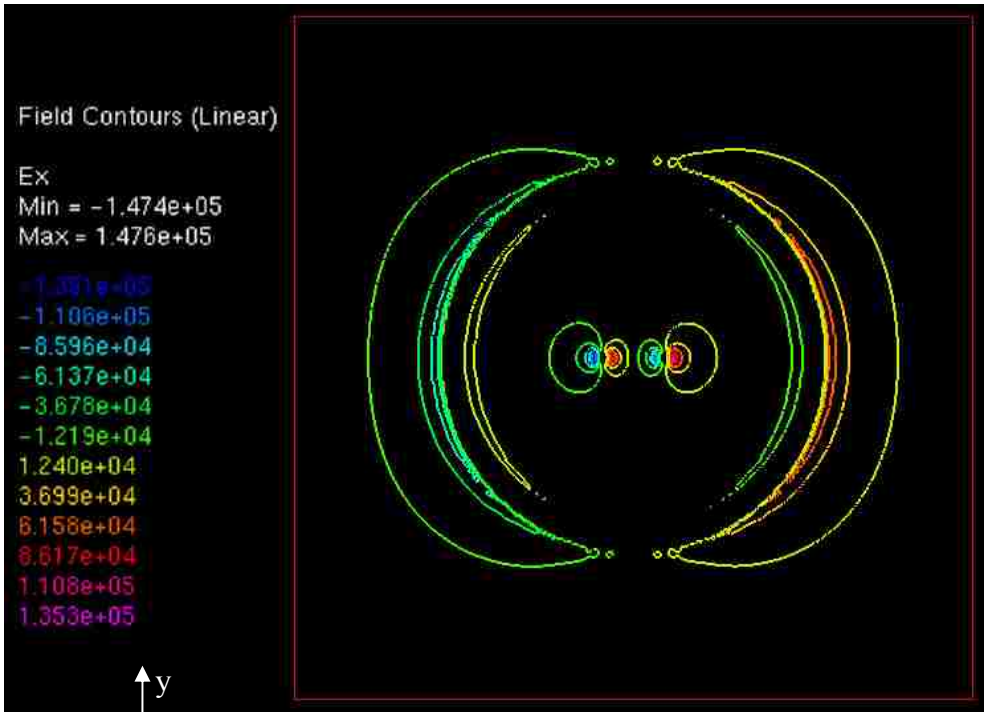

(a)

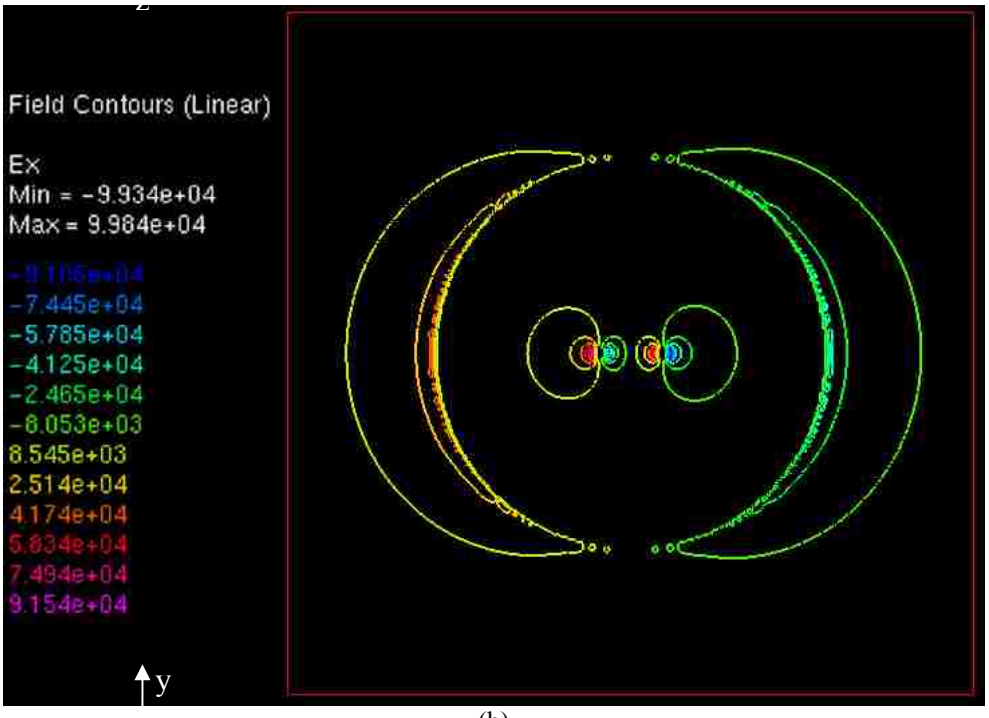

(b)

Figure 14: Contour plot of E_x field distribution in the Z = input plane for 900 MHz (a) and 6 GHz (b) common mode excitation.

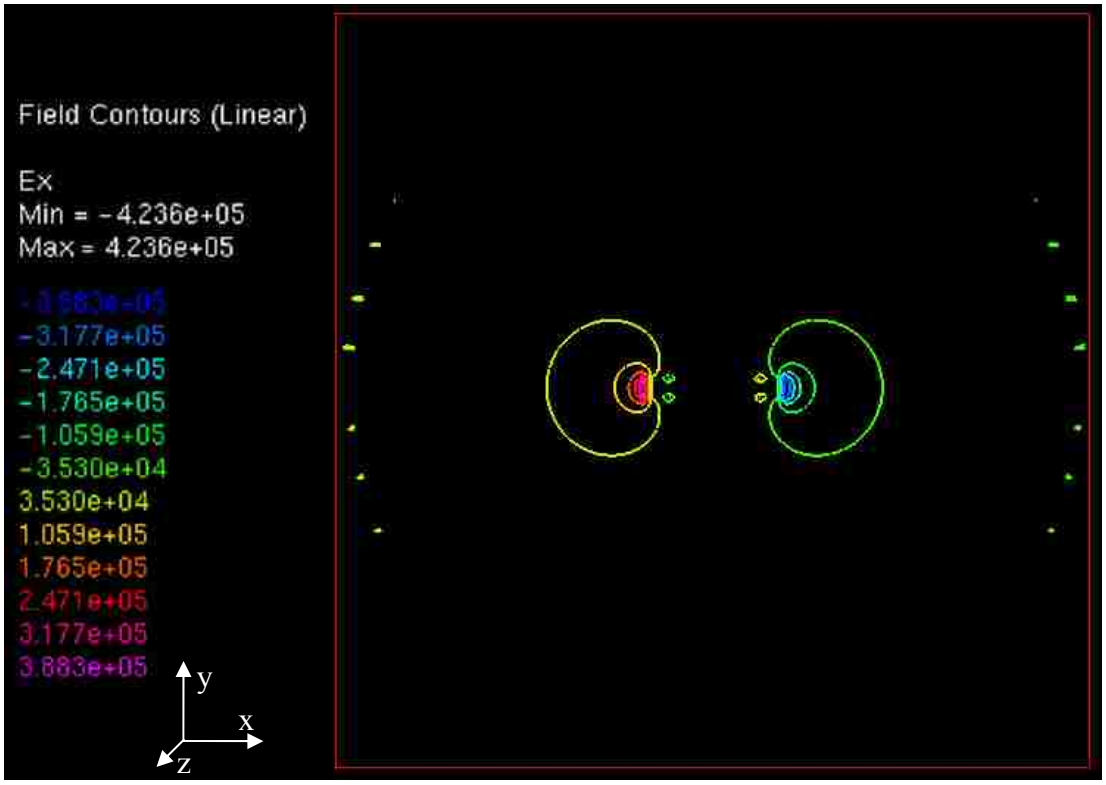

(a)

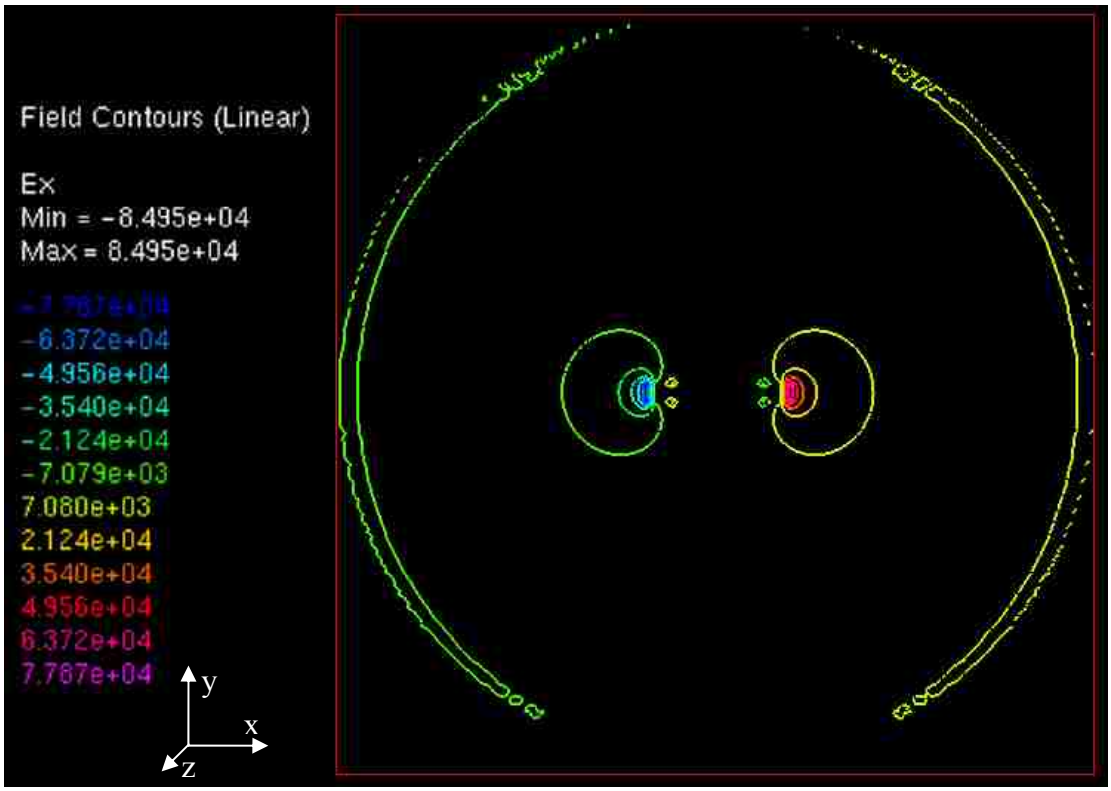

(b)

Figure 15: Contour plot of E_x field distribution in the Z = bridge wire plane for 900 MHz (a) and 6 GHz (b) common mode excitation.

From Figures 14 and 15 the E_x field distribution clearly extends from the lead-in wires to the outer aluminum sheath of the detonator for both frequencies. However Figure 15 indicates that further down the detonator, in the plane of the bridge wire, the E_x field distribution does not reside as predominantly on the sheath as at the input (Figure 14). This is because of the proximity of the exciting sources. At the input plane, the E_x field coupling to the sheath is greater than farther away from the source. At the bridge wire plane, the E_x field that had been propagating along the sheath is radiating away from the sheath, as indicated by the position of the outer E_x field in Figure 15.

As mentioned previously, the E_x field distributions are illustrative and do indicate what is happening inside the detonator, but it is primarily the EDL and CUR_CIR values that need to be analyzed. Figures 16 through 18 are the input, mid-seal, and bridge wire voltage waveforms respectively at 900 MHz and 6 GHz, while Figure 19 is the bridge wire current waveform at 900 MHz and 6 GHz. The plots for the 900 MHz diagnostics have been truncated to 25 ns since the additional 25 ns adds no additional information, as was seen for the differential mode results above. A general observation of Figures 16 through 19 is that the voltage waveforms at different places along the detonator as well as that of the bridge wire current waveform are all similar in appearance and behavior across time for each frequency, with the primary difference being the maximum value of the waveform amplitudes. While this observation was also seen earlier for the differential mode waveforms, the common mode waveforms contain much less magnitude variation. Also, the initial voltage values for the first few nanoseconds of simulation again indicate transient values due to the ramping of the excitation current

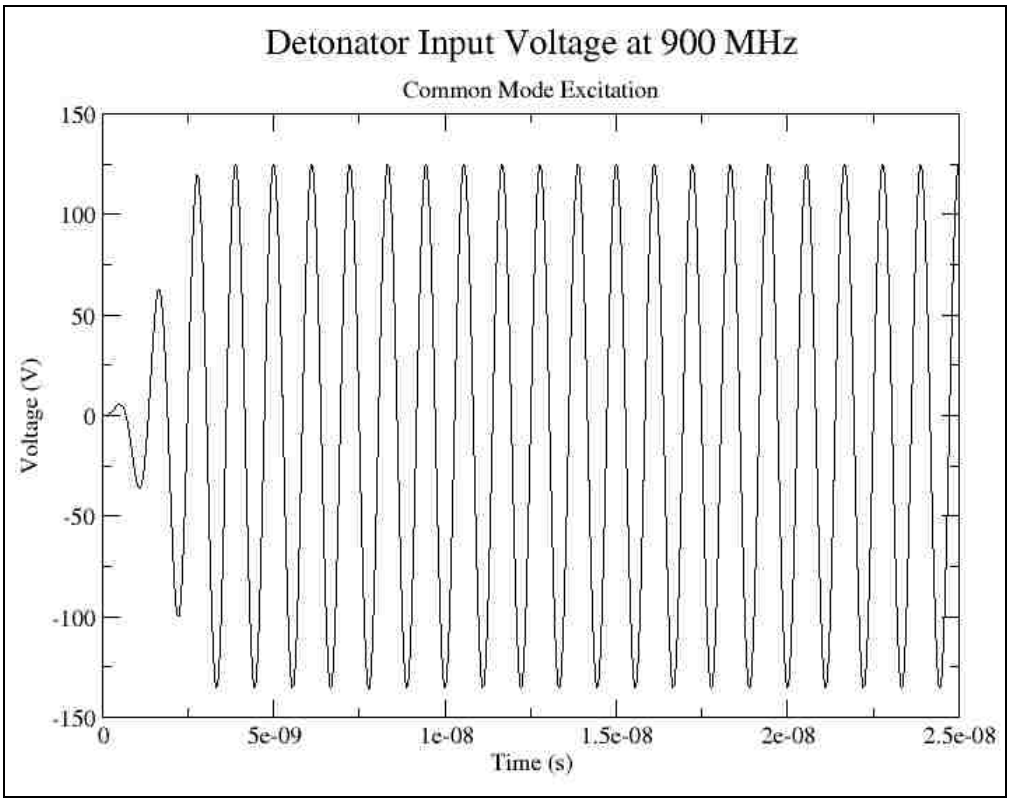

(a)

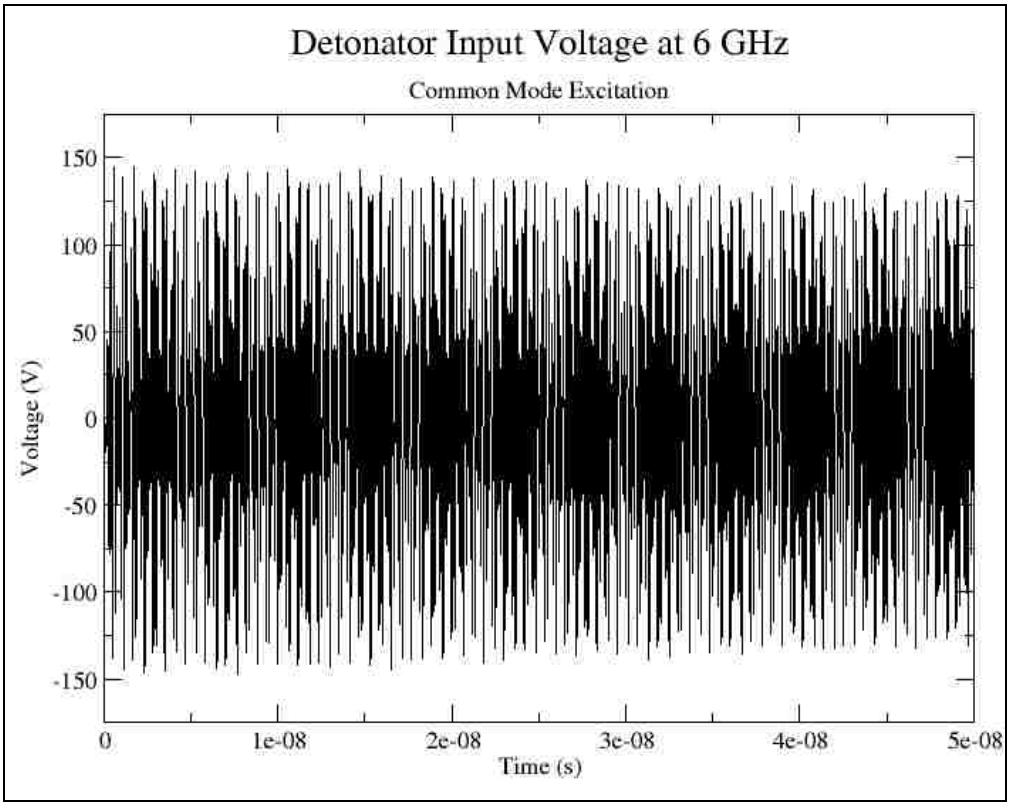

(b)

Figure 16: Detonator input voltage at 900 MHz (a) and 6 GHz (b) during common mode excitation.

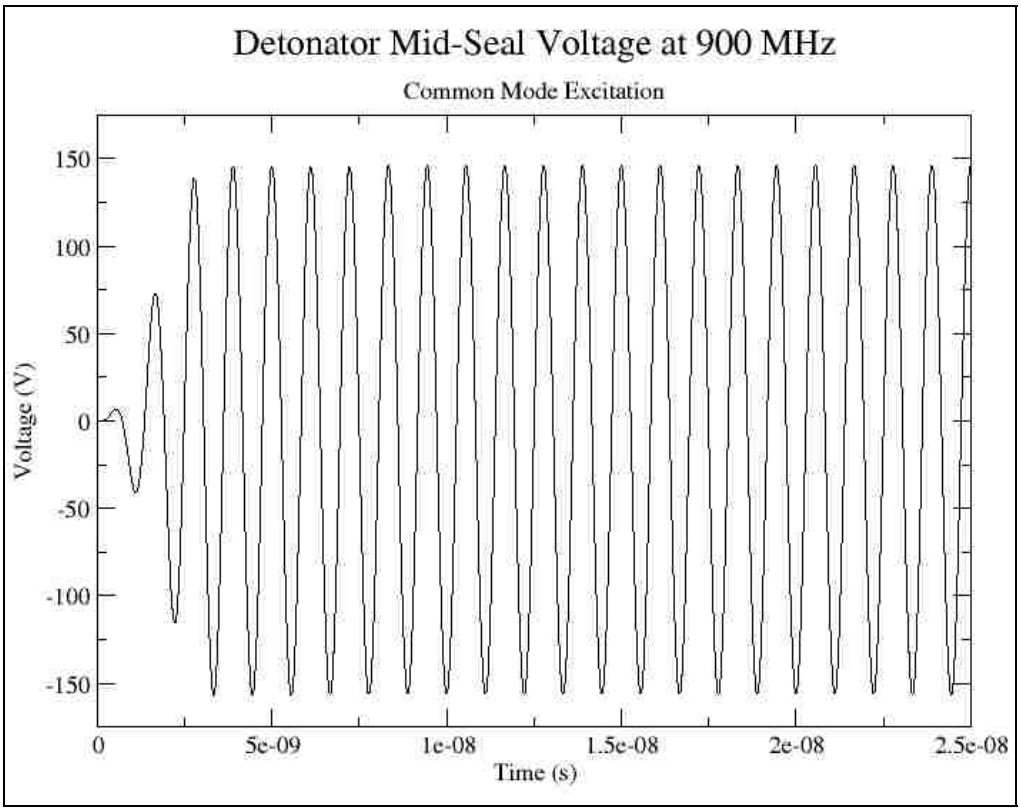

(a)

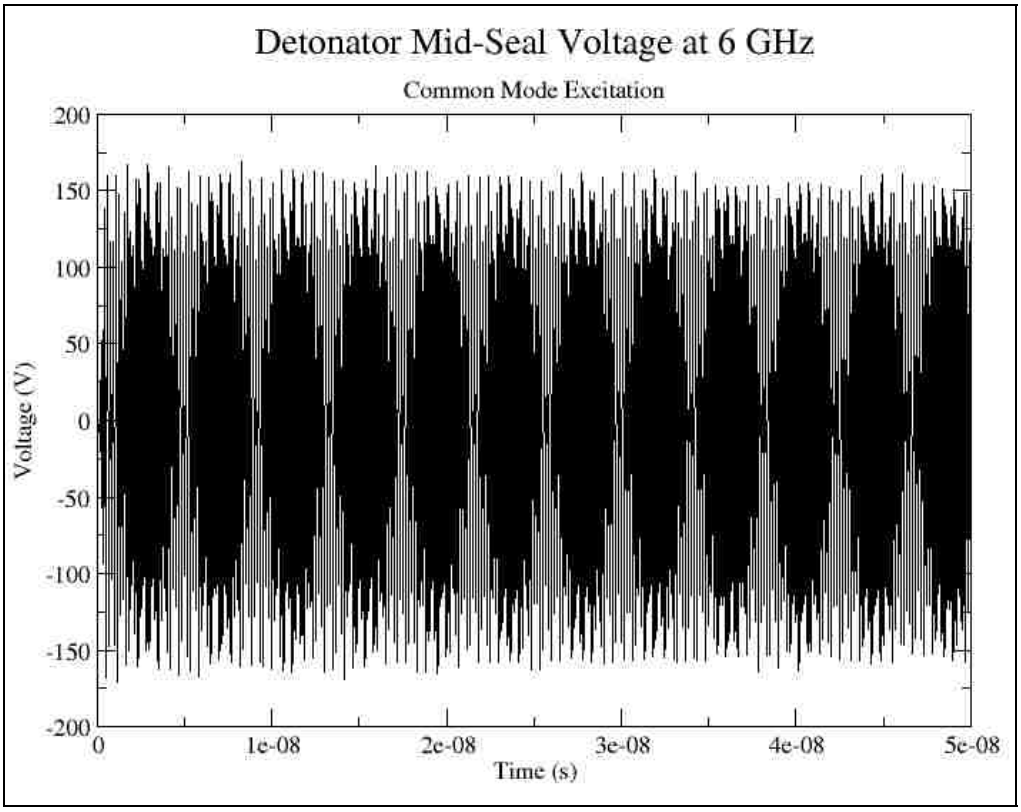

(b)

Figure 17: Detonator mid-seal voltage at 900 MHz (a) and 6 GHz (b) during common mode excitation.

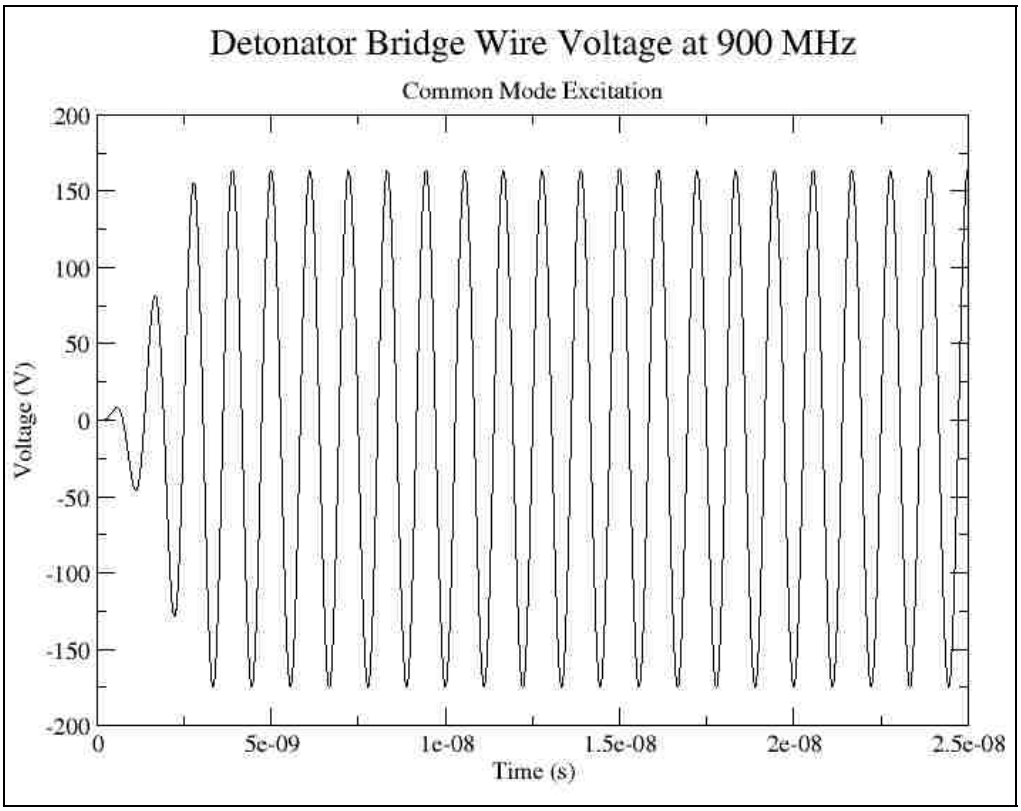

(a)

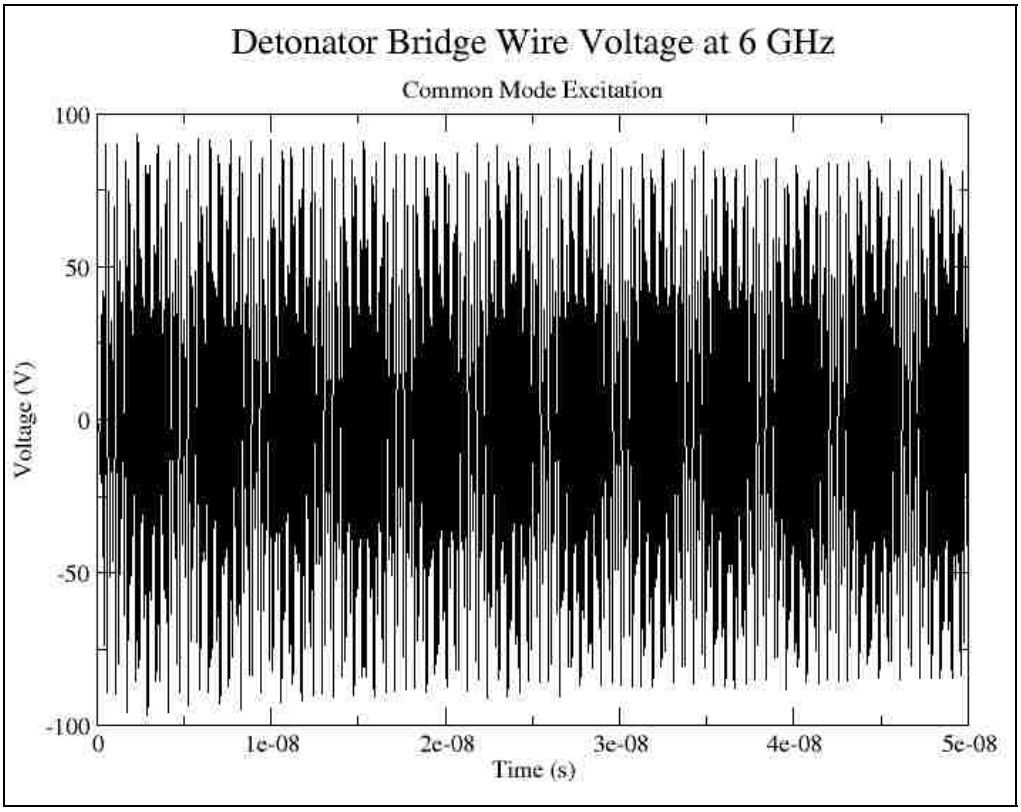

(b)

Figure 18: Detonator bridge wire voltage at 900 MHz (a) and 6 GHz (b) during common mode excitation.

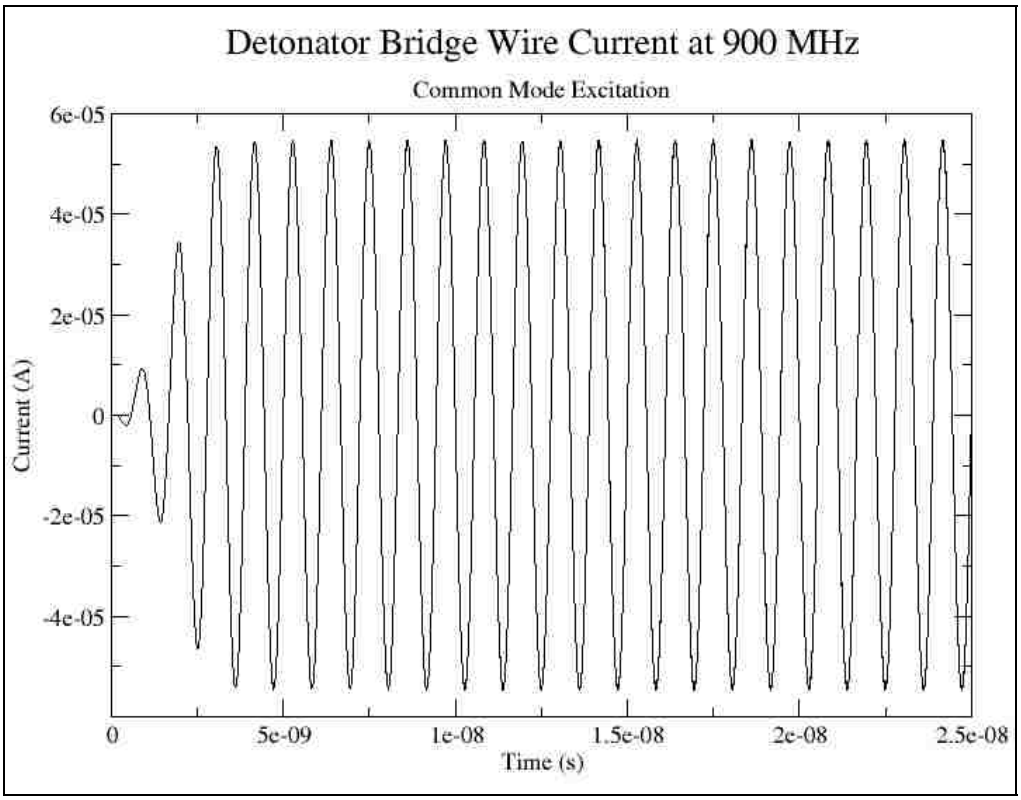

(a)

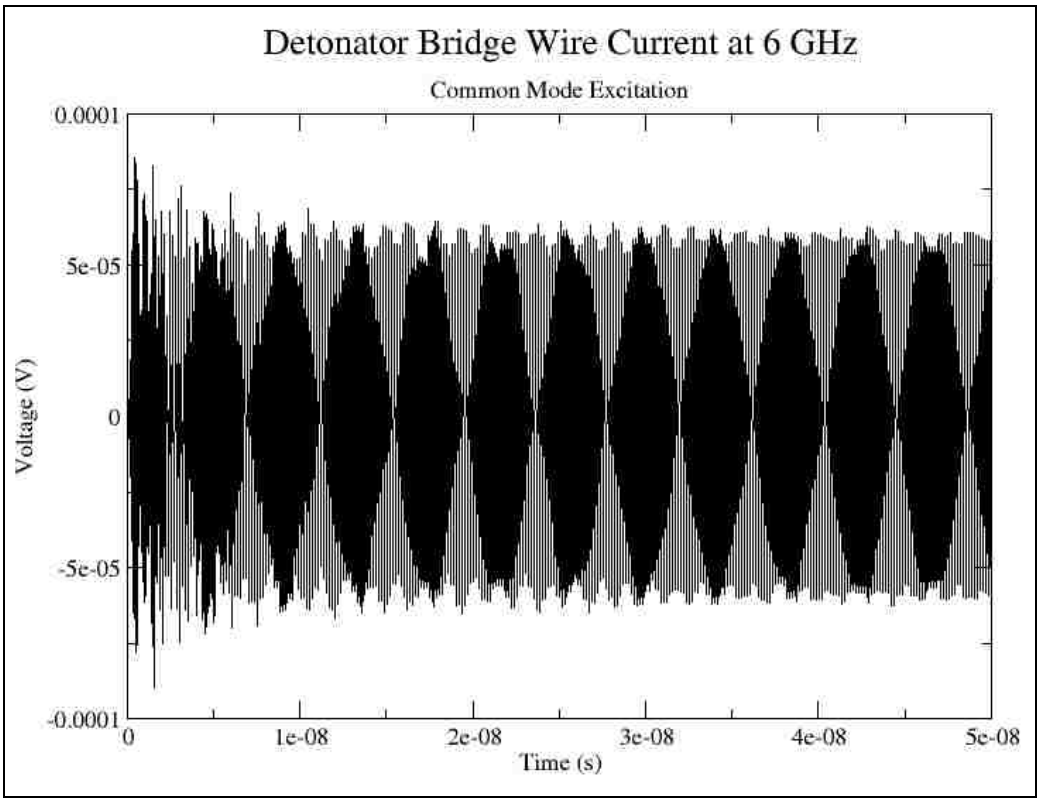

(b)

Figure 19: Detonator bridge wire current at 900 MHz (a) and 6 GHz (b) during common mode excitation.

magnitude from 0 to 1 A across three complete cycles, as described in Chapter 4. Both the 900 MHz and 6 GHz waveforms reach steady-state very quickly. While the 900 MHz waveforms are relatively flat and simple, the 6 GHz waveforms are more complicated, indicating the excitation of resonant frequencies. Finally, the bridge wire current for both frequencies are extremely small, on the order of micro-amps. This is an expected and positive result. Since the lead-in wires are at the same potential, no current should flow through the bridge wire. The small amount that does is potentially due to E_x field radiation and reflection at the ends of the lead-in wires.

The same curve-fitting techniques are used to help determine the magnitude of the drive frequency of the input voltage at 900 MHz (Figure 16a), and this curve fit resulted in a drive frequency magnitude of 125.07 V, which represents the input voltage into the detonator given a 1 A 900 MHz common mode input. A representation of this curve fit was shown previously in Figure 9. However, when this fitted drive frequency waveform is subtracted from the input voltage, a clear resonant frequency waveform pattern is not found. This is caused by the drive signal at 900 MHz being to far away in frequency from the first resonance to excite it. Similar curve-fitting was used to find the magnitudes of the mid-seal and bridge wire voltage waveforms, which also did not produce a resonant frequency. Again, Figure 9 is representative of all four of these curve-fits, and so the others will not be shown. The results of these analyses are listed in Tables 3 and 4. Lastly, the input current was shown to be approximately 0, as expected, and further analysis of this waveform is not required.

The voltage waveforms at 6 GHz are analyzed using a DFT to find the drive frequency magnitude, as well as the resonant frequencies. Figure 20 is the DFT of the 6

GHz input voltage shown in Figure 16b, and Figure 21 is a zoomed view of the DFT to show a higher order resonance.

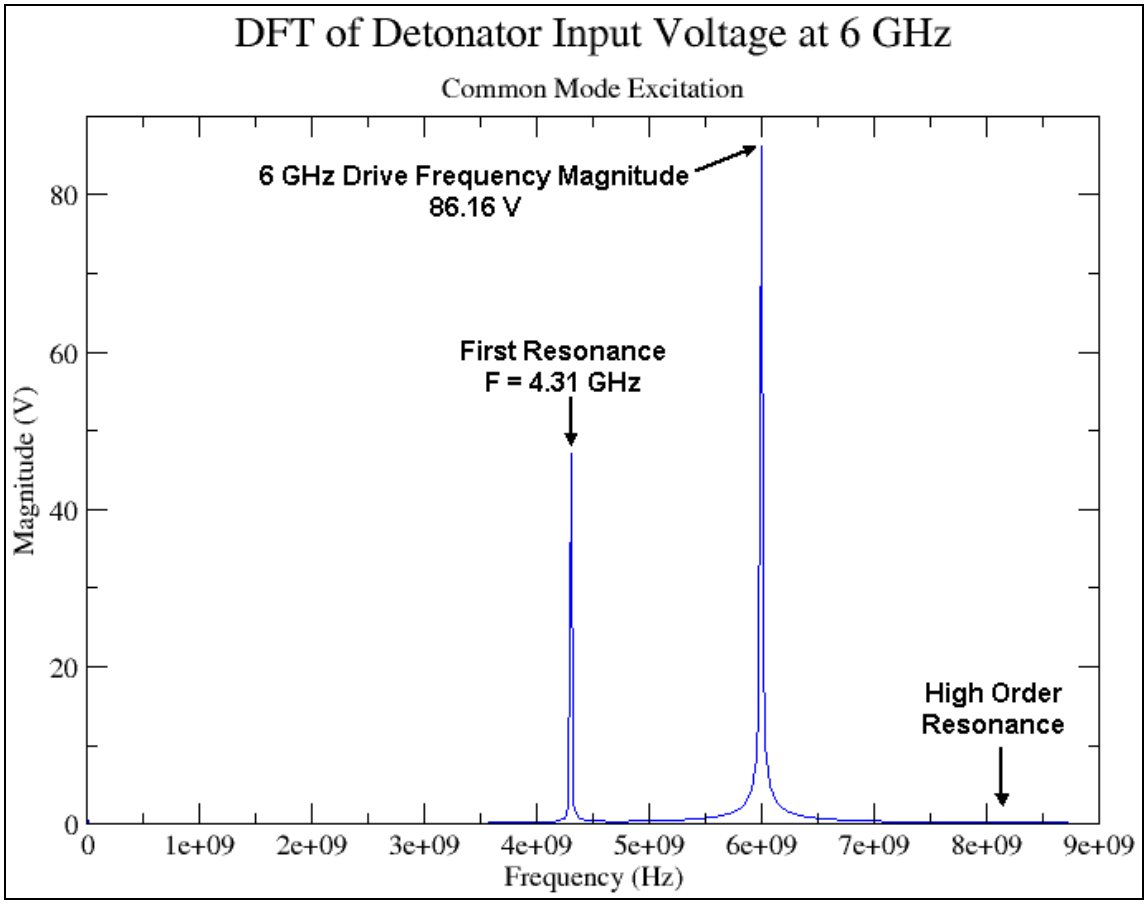

Figure 20: DFT of the detonator input voltage at 6 GHz shown in Figure 15b.

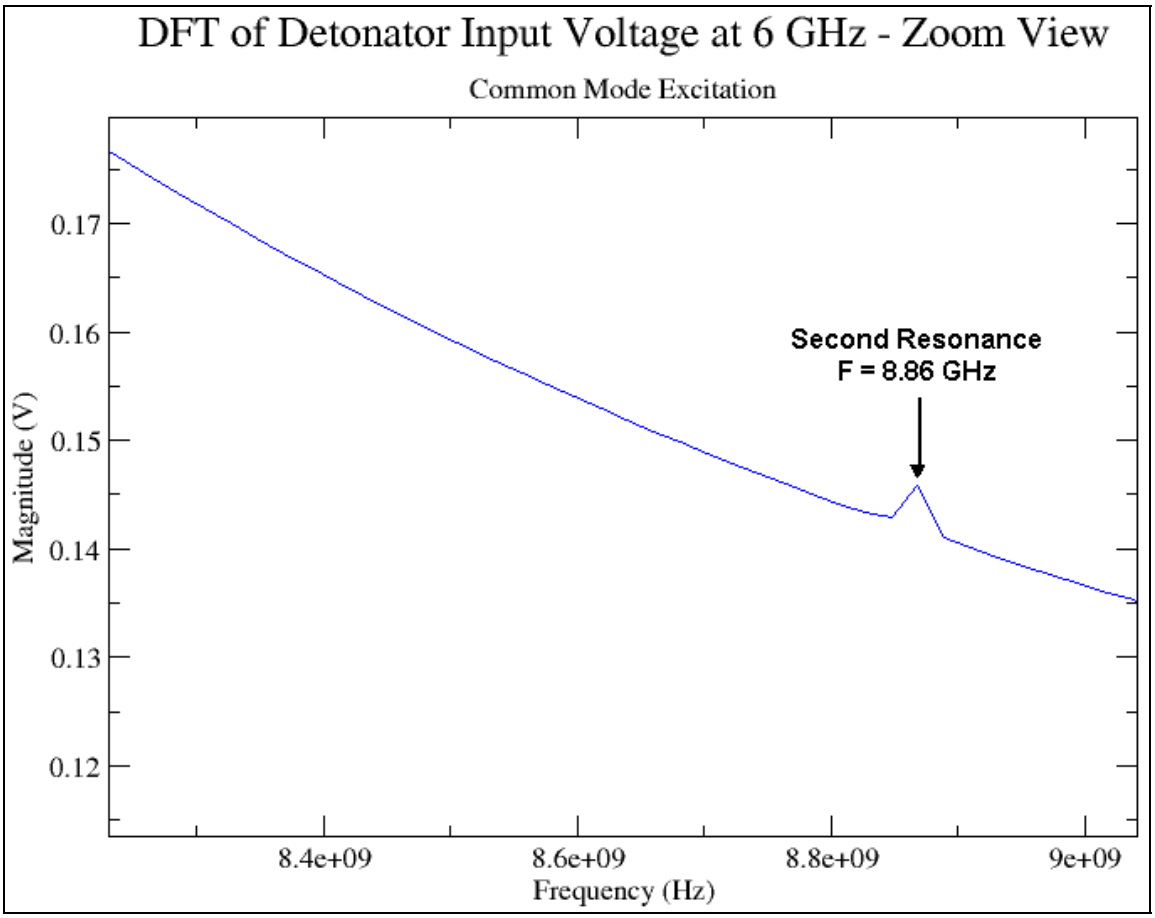

Figure 21: Zoomed view of the DFT to show a higher order resonance.

This DFT determines a drive frequency magnitude of 86.16 V, and resonant frequencies of 4.31 and 8.86 GHz. This data indicates that a common mode input signal at 6 GHz and 1 A will result in an 86.16 V input into the detonator. Also, the 6 GHz signal was able to excite the first and second resonant frequencies, while the 900 MHz signal did not. This same type of DFT analysis was performed on the mid-seal and bridge wire voltage waveforms and it was found that all three waveforms indicated the same two resonant frequencies. As such, the DFT results will not be repeated since Figure 20 is representative of all three. The results from these analyses are listed in Tables 3 and 4. Again, the bridge wire current was not analyzed as it is deemed to be 0.

Table 3: Detonator common mode voltage magnitudes.

Frequency	Input Voltage	Mid-Seal Voltage	Bridge Wire Voltage
900 MHz	125.07	146.35	164.11
6 GHz	86.16	130.20	60.53

Table 4: Detonator common mode resonances.

Frequency	First Resonance	Second Resonance
900 MHz	N/A	N/A
6 GHz	4.31 GHz	8.86 GHz

Similar to the differential mode, the common mode resonance frequencies shown in Figures 20 and 21 were verified by simulating the detonator with common mode excitation at the two frequencies found to be resonant. A plot of the resulting input voltage waveform for an excitation frequency of 4.31 GHz is shown in Figure 22. The voltage increases exponentially to an extremely large value of over 30,000 V in the simulated time of 30 ns. This clearly indicates that 4.31 GHz common mode excitation causes resonant behavior within the detonator. The waveforms for an 8.86 GHz common mode input frequency illustrated the same behavior, and are well represented by Figure 22. These additional simulations verified that both of the resonant frequencies found using the DFT are valid.

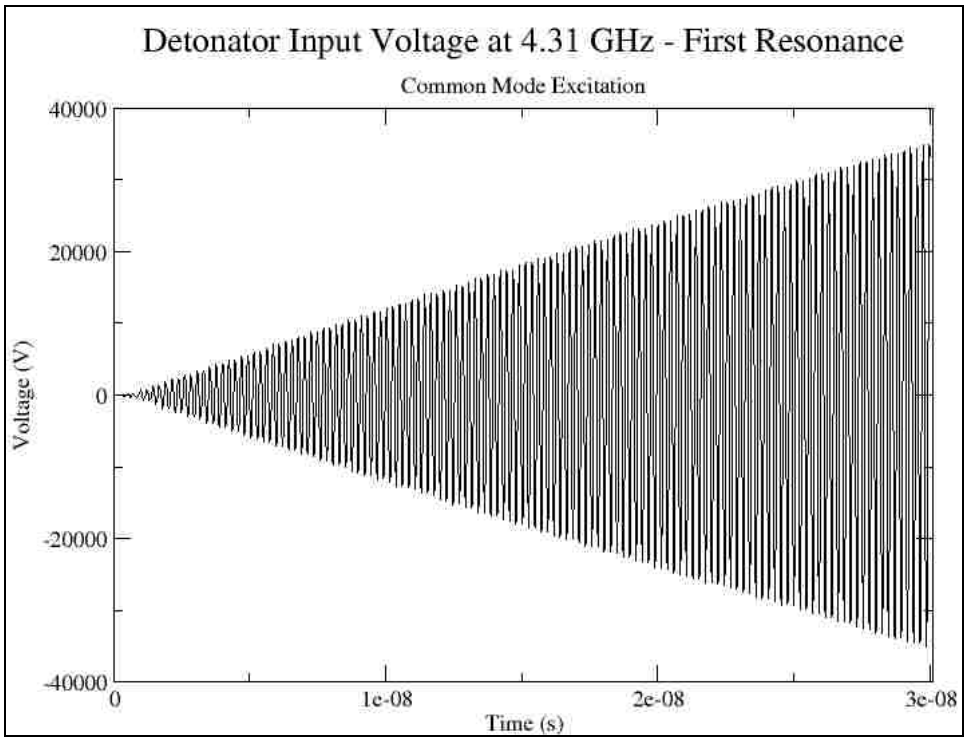

Figure 22: Detonator input voltage at 4.31 GHz during common mode excitation of the first resonance.

Detonator Model Truncation Using ICEPIC Results

In an effort to reduce the required computation resources and time required for each ICEPIC detonator simulation, the results shown in the previous section were carefully examined to determine if a possible reduction in simulation space was possible without affecting the results appreciably. Figure 23 shows the Y = 0 plane E_x field distributions for 900 MHz and 4 GHz from Figure 3 overlaid with the grid of the geometry in that same plane. What can be seen from Figure 23 is that the E_x field distribution ends within the lead-azide portion of the detonator, in the vicinity of the bridge wire. This is expected since the E_x fields radiated from the bridge wire, as illustrated in Figure 4, decrease in magnitude as the square of the distance away from the bridge wire. This causes the radiated fields to drop to a value near 0 very quickly, again illustrated in Figure 23.

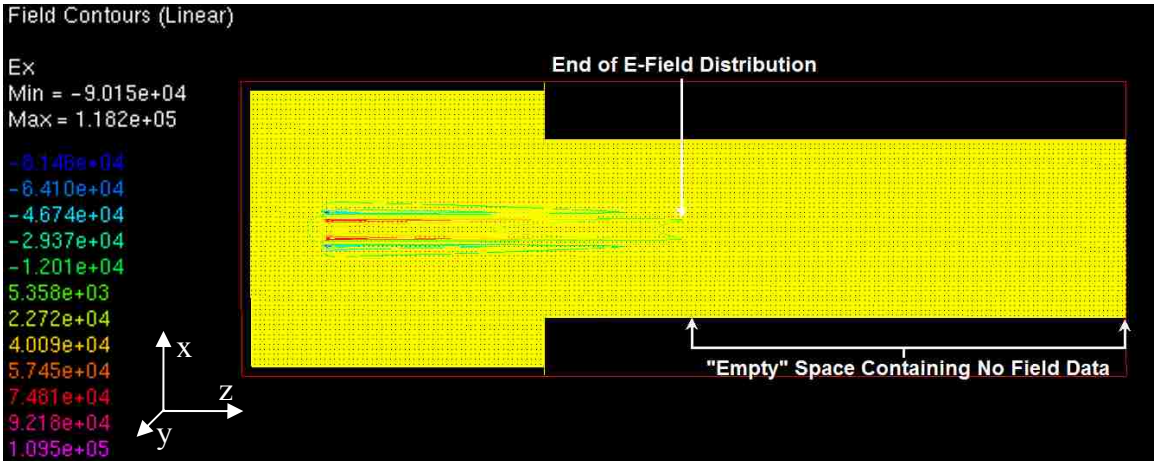

(a)

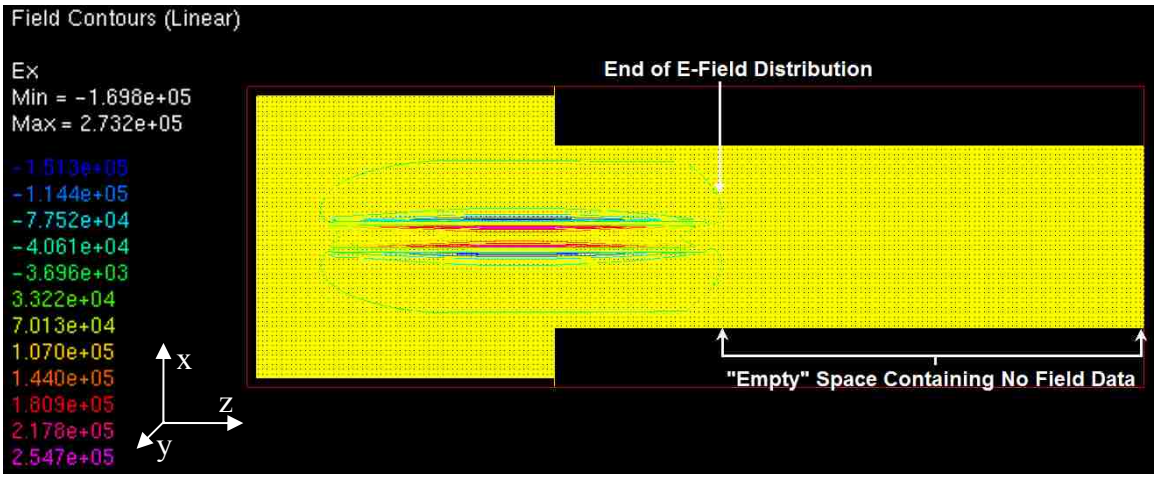

(b)

Figure 23: Contour plot of E_x field distribution in the Y = 0 plane for 900 MHz (a) and 4 GHz (b) differential mode excitation overlaid with the grid of that same plane.

Given the observations from Figure 23, it should be possible to reduce the amount of simulated space by truncating the detonator geometry at the boundary between the lead-azide and the PETN. Since the E_x field only partially penetrates into the lead-azide, leaving the entire lead-azide section intact and truncating the PETN section should ensure that the simulation results are unaffected. This truncation removes a 13.21 mm section of detonator along with the 0.5 mm thick top section of the aluminum sheath, which represents just over half of the simulation space to the right of the PML box. The number of cells requiring computation each time step was reduced to $2.84*10^7$ from $3.45*10^7$, a

17.60% reduction. Beyond this geometry change, the detonator simulation space and excitation conditions are set up in ICEPIC in exactly the same manner as previously described in Chapter 4. Figures 24 and 25 are pictures of the ICEPIC rendering of the truncated detonator geometry for differential and common mode excitation, respectively. Figure 26 is an illustration of the truncated simulation space set-up for both differential and common mode excitation. Also, Figures 27 and 28 are 3-D illustrations of the ICEPIC rendering of the excitation end of the simulation space for differential and common mode excitation, respectively. Again, the entire white area surrounding the geometry is a PEC.

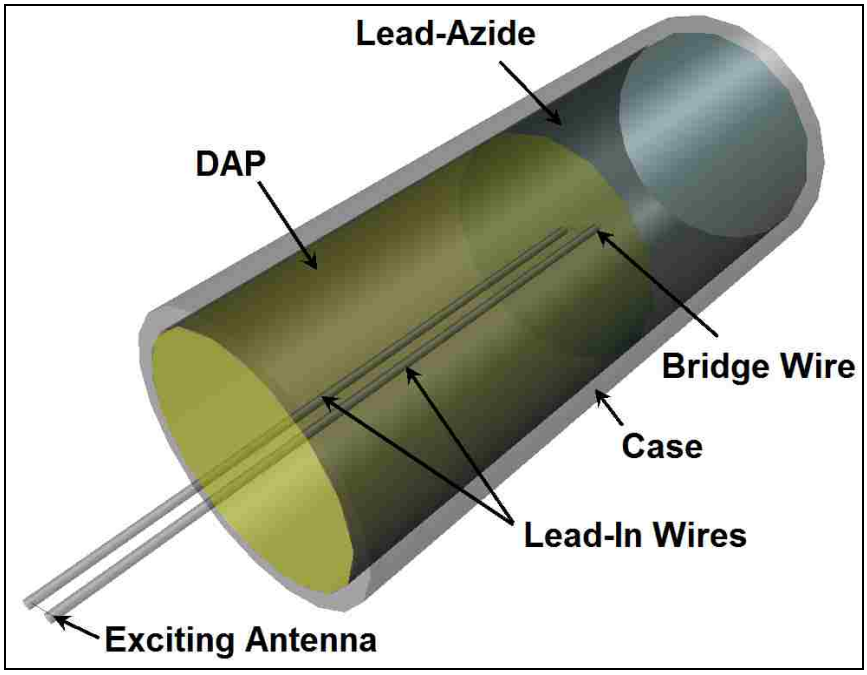

Figure 24: Perspective view of the ICEPIC rendering of the truncated detonator geometry for differential mode excitation indicating detonator components and exciting antenna.

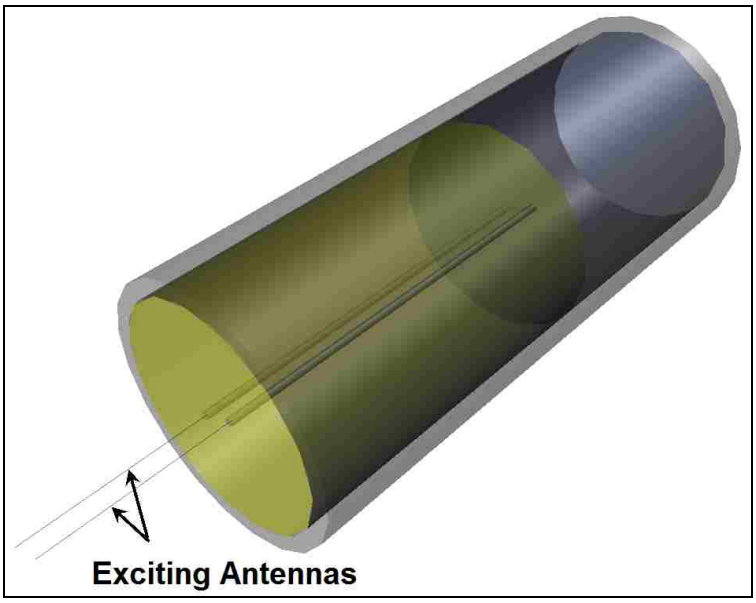

Figure 25: Perspective view of the ICEPIC rendering of the truncated detonator geometry for common mode excitation indicating exciting antenna current sources.

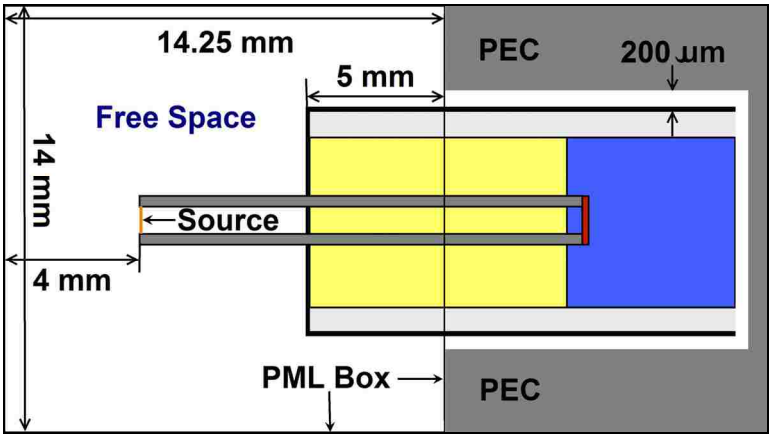

(a)

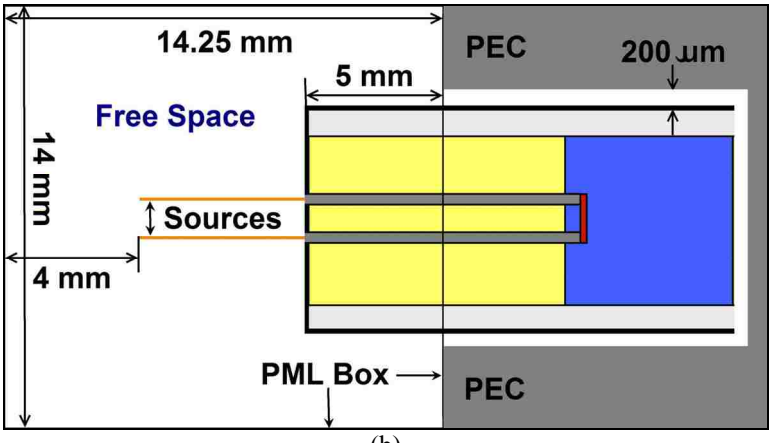

(b)

Figure 26: Illustration of the top view for both the differential mode (a) and common mode (b) simulation space set-up for the truncated detonator geometry indicating regions of PEC and free space, along with the placement and dimensions of the PML box encompassing the excitation source.

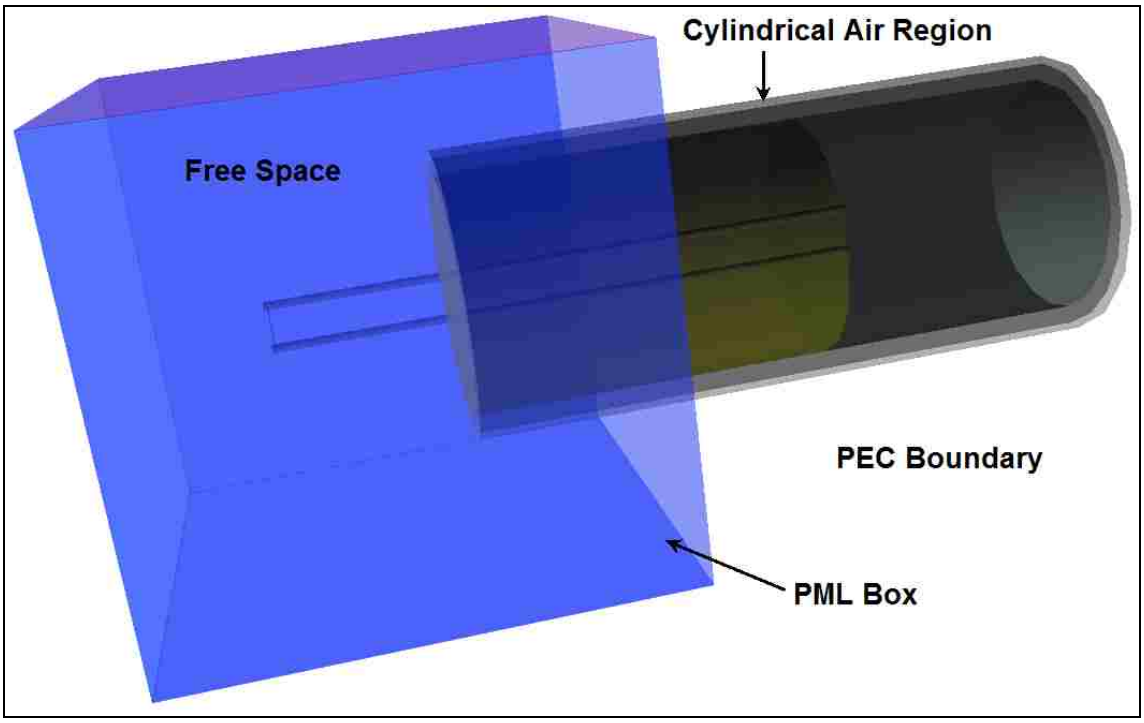

Figure 27: Illustration of the 3-D ICEPIC rendering of the differential mode excitation space from a perspective top-view of the truncated detonator geometry.

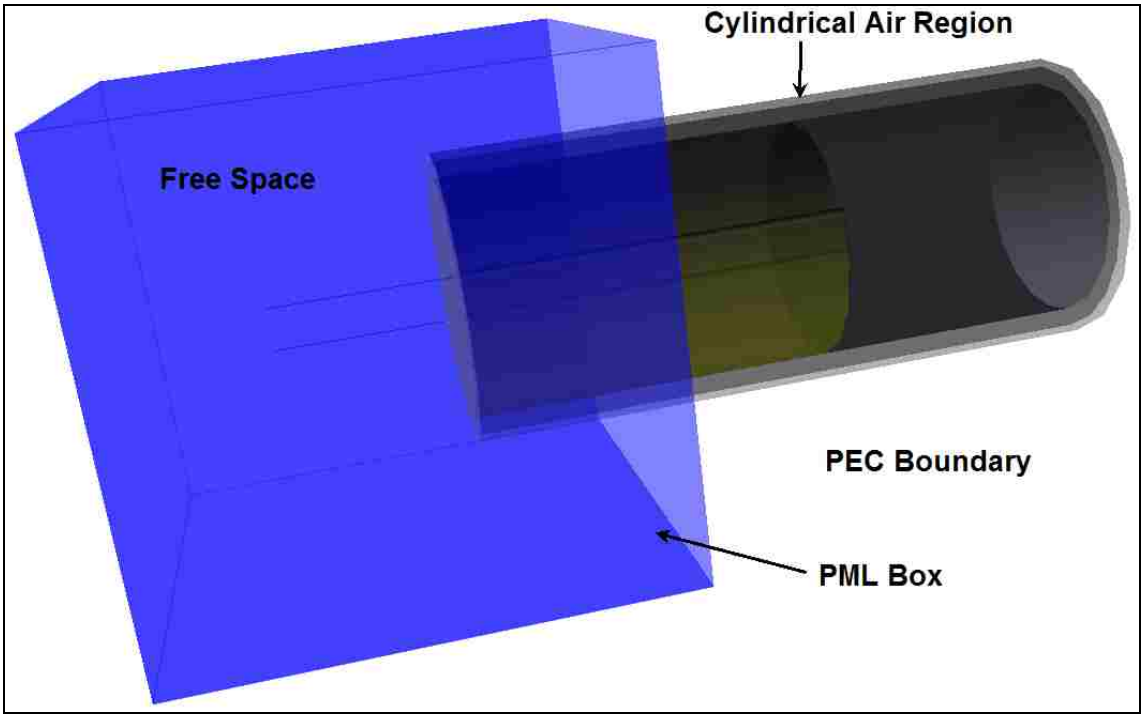

Figure 28: Illustration of the 3-D ICEPIC rendering of the common mode excitation space from a perspective top-view of the truncated detonator geometry.

Truncated Detonator Differential Mode Results

This truncated geometry was then simulated in ICEPIC with the same differential mode excitation conditions used for the full detonator simulations described earlier. Figure 29 is the E_x field distribution in the Y = 0 plane for both 900 MHz and 4 GHz differential mode excitation. Figure 30 is the E_x field distribution for the Y = 0 plane overlaid on the grid for that same plane during both 900 MHz and 4 GHz differential mode excitation.

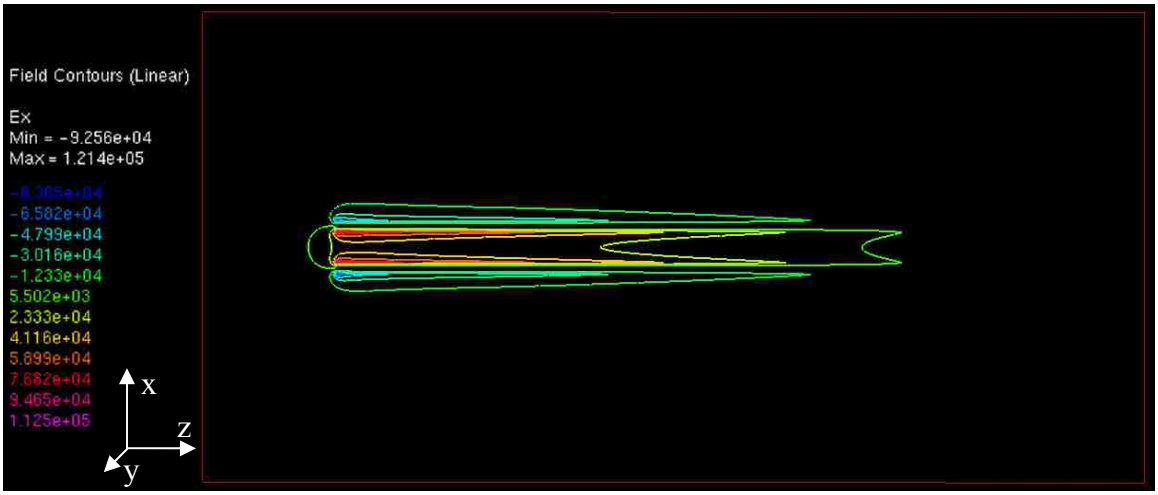

(a)

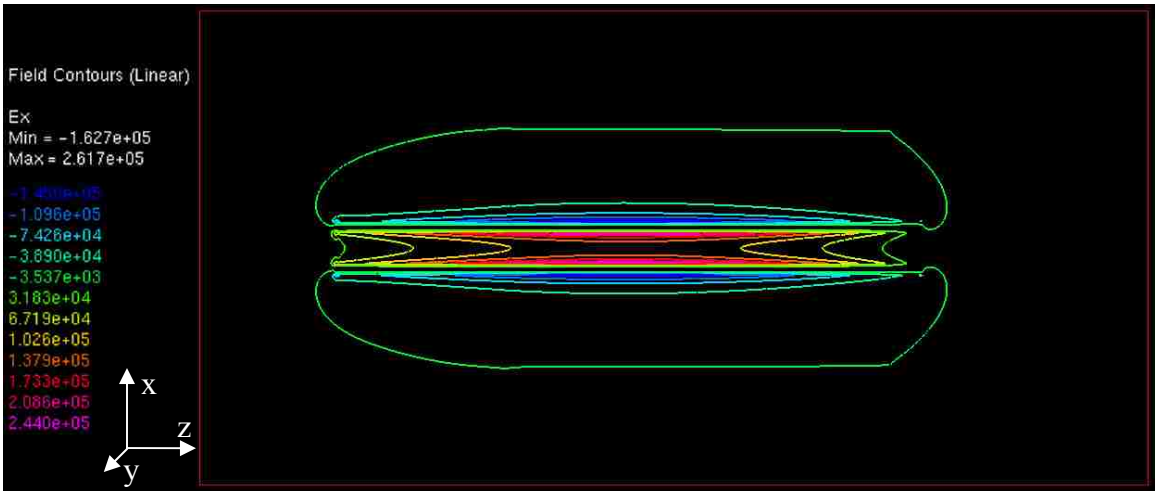

(b)

Figure 29: Contour plot of truncated detonator geometry E_x field distribution in the Y = 0 plane for 900 MHz (a) and 4 GHz (b) differential mode excitation.

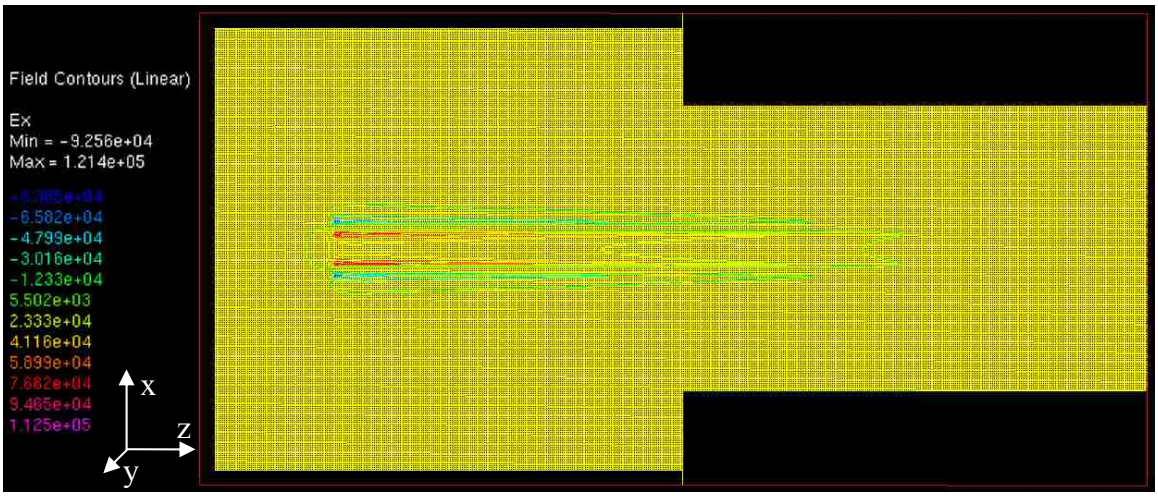

(a)

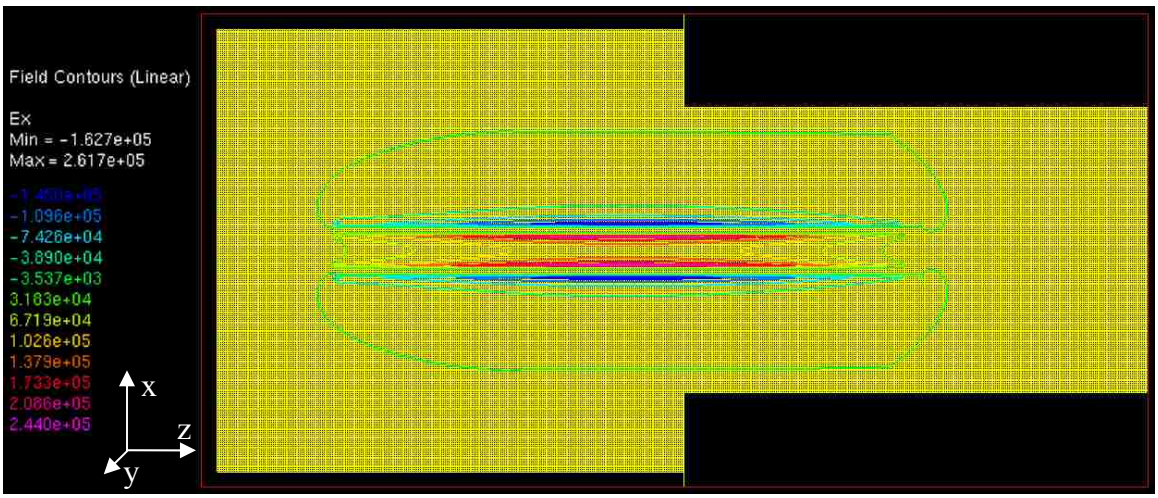

(b)

Figure 30: Contour plot of truncated detonator geometry E_x field distribution in the Y = 0 plane for 900 MHz (a) and 4 GHz (b) differential mode excitation overlaid with the grid of that same plane.

When comparing Figure 29 to Figure 3, the Y = 0 plane E_x field distribution for the full detonator geometry, it can be seen that the two distributions are nearly identical. Close examination of the minimum and maximum values for each of the distributions reveals small variations. For the 900 MHz distributions in Figures 3a and 29a, the minimum E_x field value differs by 2.67% while the maximum differs by 2.71 %. For the 4 GHz distributions in Figures 3b and 29b, the minimum E_x field value differs by 4.18% while the maximum differs by 4.20%. These differences are all less than 5%, and considering the savings in computation time, are not significant. Lastly, examination of Figure 30

indicates that the E_x field distribution is still not approaching the end of the simulation space. This verifies that the truncated geometry is not sufficiently interfering with the formation of the E_x field pattern within the detonator.

However, as discussed earlier, the more important diagnostics for comparison of these two geometries are the voltage EDLs and CUR_CIR. These diagnostics for the input, mid-seal, and bridge wire voltages along with the bridge wire current were analyzed in the same manner as described earlier for the full detonator results. The voltage and current waveforms for all 4 diagnostics at both 900 MHz and 4 GHz are nearly identical to those shown in Figures 5 through 8. Curve-fitting techniques for the 900 MHz data resulted in waveforms similar to those shown in Figures 9 and 10. DFTs of the 4 GHz waveforms are nearly identical to those shown in Figures 11 and 12. The results of these analyses are listed in Tables 5 and 6. The three resonances given in Table 6 were verified by exciting the truncated detonator geometry with a differential mode input at these frequencies. The resulting waveforms are well represented by Figure 13, and will not be repeated. Figure 31 shows comparison charts of the 900 MHz and 4 GHz ICEPIC diagnostic magnitudes for both the full (Table 1) and truncated detonator geometry (Table 5).

Table 5: Truncated detonator geometry differential mode voltage and current magnitudes.

Frequency	Input Voltage	Mid-Seal Voltage	Bridge Wire Voltage	Bridge Wire Current
900 MHz	100.96	40.87	1.21	1.17
4 GHz	38.02	180.70	2.57	1.72

Table 6: Truncated detonator geometry differential mode resonances.

Frequency	First Resonance	Second Resonance	Third Resonance
900 MHz	2.66 GHz	N/A	N/A
4 GHz	2.66 GHz	6.72 GHz	7.67 GHz

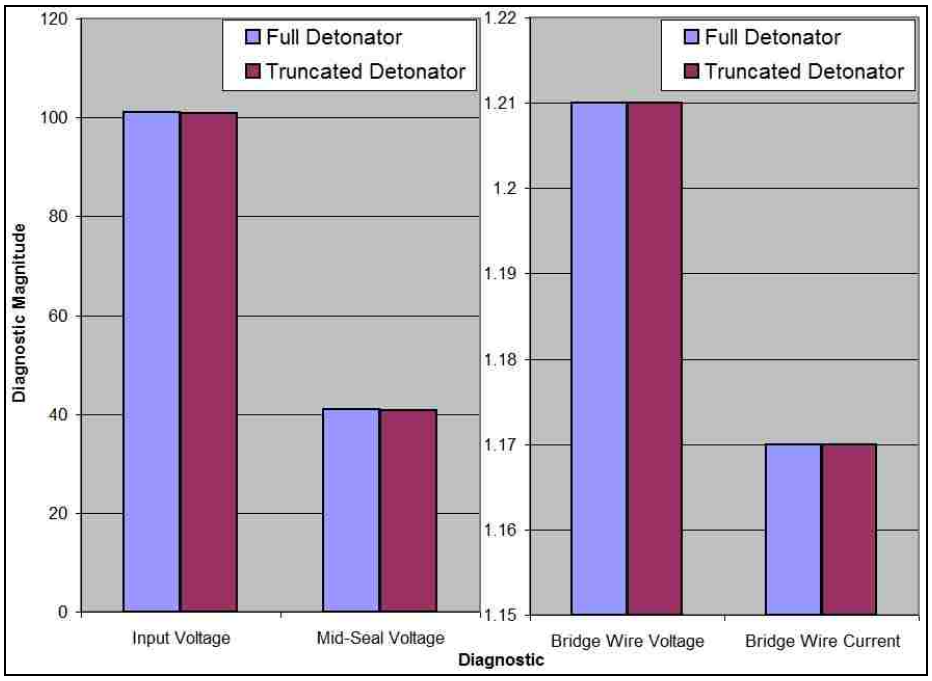

(a)

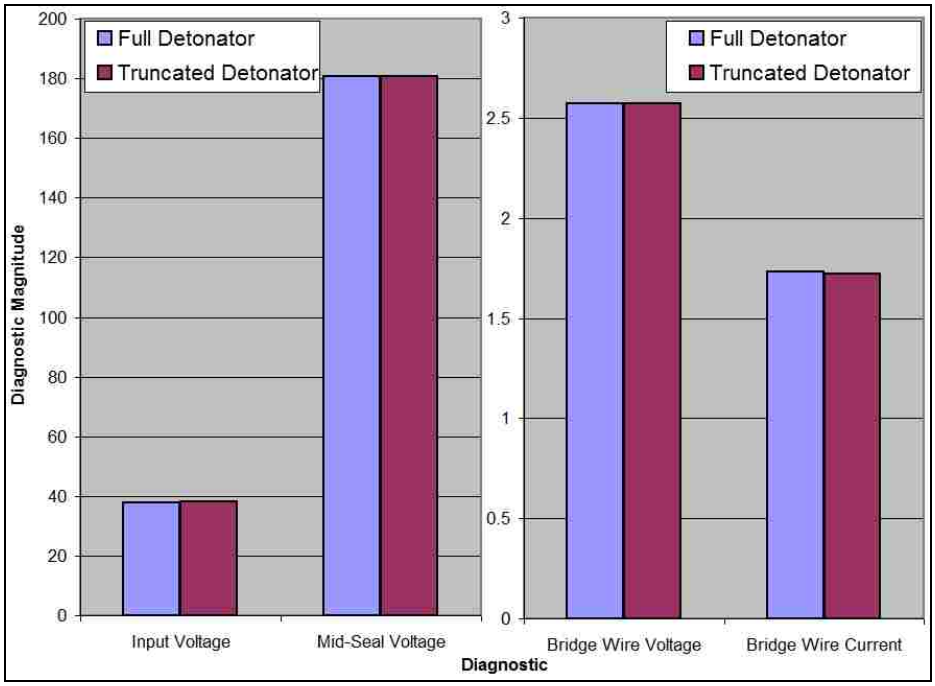

(b)

Figure 31: Comparison charts of ICEPIC diagnostic magnitudes for 900 MHz (a) and 4 GHz (b) differential mode excitation of the full and truncated detonator geometry.

Figure 31 indicates that the voltage and current magnitudes for the full and truncated detonator geometry are nearly identical, with the greatest difference of 0.58% occurring at the 4 GHz bridge wire current. The resonances given in Tables 2 and 6 are also

comparable, with a maximum error of 1.99% for the third resonance. Given the method for determining these resonances from the DFT plots, this error is well within tolerance. The results of both the full detonator and truncated detonator geometries have been nearly identical in all comparisons made for differential mode excitation. Considering the computational and time resources saved, the truncated geometry shall be used for the remaining differential mode simulations, and will be referred to as the "standard" detonator geometry.

Truncated Detonator Common Mode Results

This truncated geometry was also simulated with ICEPIC using the same common mode excitation conditions as for the full detonator simulations described earlier. It is not necessary to show any E_x field distributions for comparison, as very little information can be gathered in this way for means of comparison. As with the differential mode, the common mode voltage diagnostics for the truncated detonator geometry for both 900 MHz and 6 GHz are nearly identical to those shown in Figures 15 through 18. 900 MHz waveforms were again analyzed with curve-fitting, and are represented by Figures 9 and 10. 6 GHz waveforms were analyzed with DFTs, and are represented by Figures 19 and 20. The results of these analyses are listed in Tables 7 and 8. Both resonances given in Table 8 were verified by exciting the truncated detonator geometry with a common mode input at these frequencies. The resulting waveforms are well represented by Figure 22, and will not be repeated. Figure 32 shows comparison charts of the 900 MHz and 6 GHz ICEPIC diagnostic magnitudes for both the full (Table 3) and truncated detonator geometry (Table 7).

Table 7: Truncated detonator geometry common mode voltage magnitudes.

Frequency	Input Voltage	Mid-Seal Voltage	Bridge Wire Voltage
900 MHz	125.04	146.32	164.10
6 GHz	86.66	130.59	60.84

Table 8: Truncated detonator geometry common mode resonances.

Frequency	First Resonance	Second Resonance
900 MHz	N/A	N/A
6 GHz	4.31 GHz	8.76 GHz

Figure 32 indicates that the voltage magnitudes for the full and truncated detonator geometry are nearly identical, with the greatest percent error of 0.58% occurring for the 6 GHz input voltage. The resonances given in Tables 4 and 7 are also comparable, with a maximum error of 1.13% for the second resonance. As mentioned previously, given the method for determining these resonances from the DFT plots, this error is well within tolerance. The results of both the full detonator and truncated detonator geometries have been nearly identical in all comparisons made for common mode excitation. Considering the computational and time resources saved, the truncated geometry shall be used for the remaining common mode simulations, and will again be referred to as the “standard” detonator geometry.

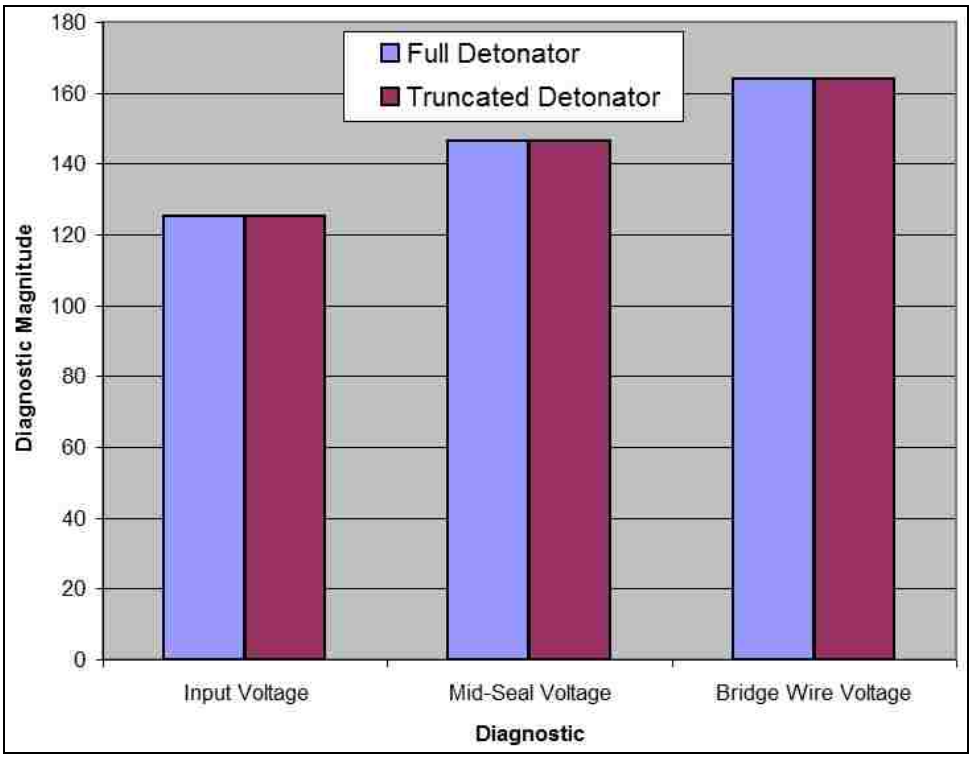

(a)

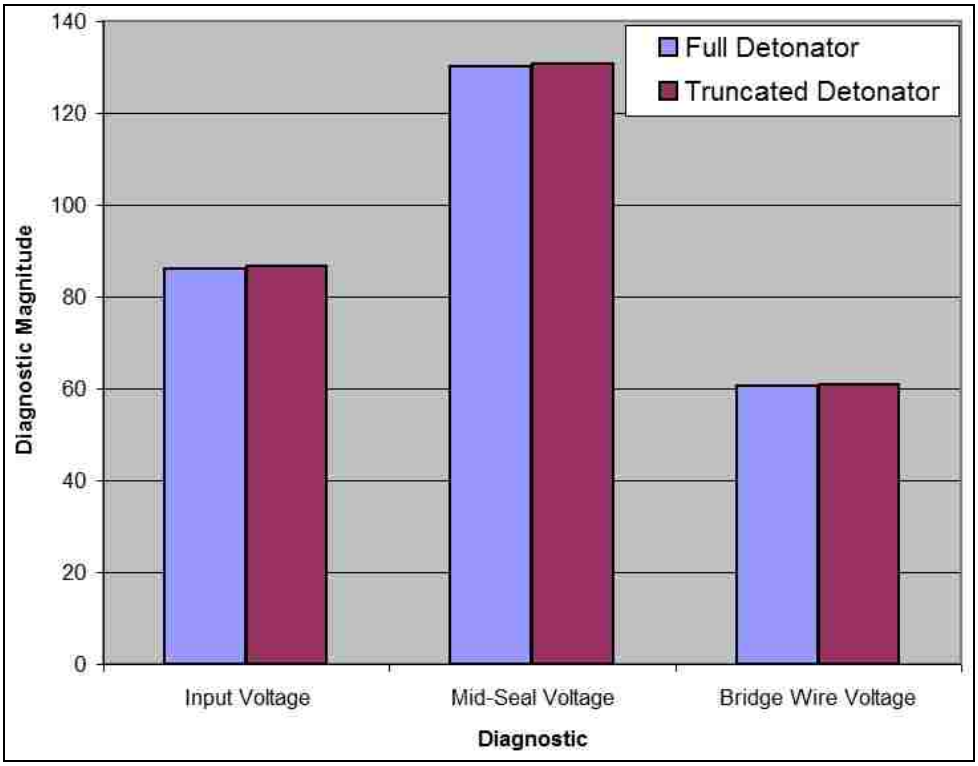

(b)

Figure 32: Comparison charts of ICEPIC diagnostic magnitudes for 900 MHz (a) and 6 GHz (b) common mode excitation of the full and truncated detonator geometry.

Standard Detonator ICEPIC Results Across Frequency

Using the standard detonator geometry established in the previous section, ICEPIC simulations were performed at several frequencies across the frequency range of DC-9 GHz for both differential and common mode excitation. The simulation and excitation parameters were as described in Chapter 4, and the same used in the previous section for detonator geometry comparison.

Standard Detonator Differential Mode Results Across Frequency

Differential mode excitation simulations were performed at 900 MHz, 2, 4, 6, and 8 GHz to find the detonator's EM characteristics across frequency. Diagnostics of the input, mid-seal, and bridge wire voltages along with the bridge wire current were analyzed as described previously. Figures 33 through 35 are overlays of the 2, 4, 6, and 8 GHz DFTs for the input, mid-seal, and bridge wire voltages, respectively. Figure 36 is a similar overlay of the DFTs of the bridge wire current at each frequency. For comparison the magnitude of each of the 900 MHz waveforms, found using curve-fitting techniques, is included on the DFT overlay plots as a single line. Also, Figure 37 is a zoomed view of the input voltage DFT overlay in Figure 33 for the first resonance. Similarly, Figure 38 is a zoomed view of the higher order resonances in Figure 33. Further zoomed views for the other three diagnostics are nearly identical, and are represented by Figures 37 and 38. The magnitudes found using these analyses are then listed in Tables 9 and 10.

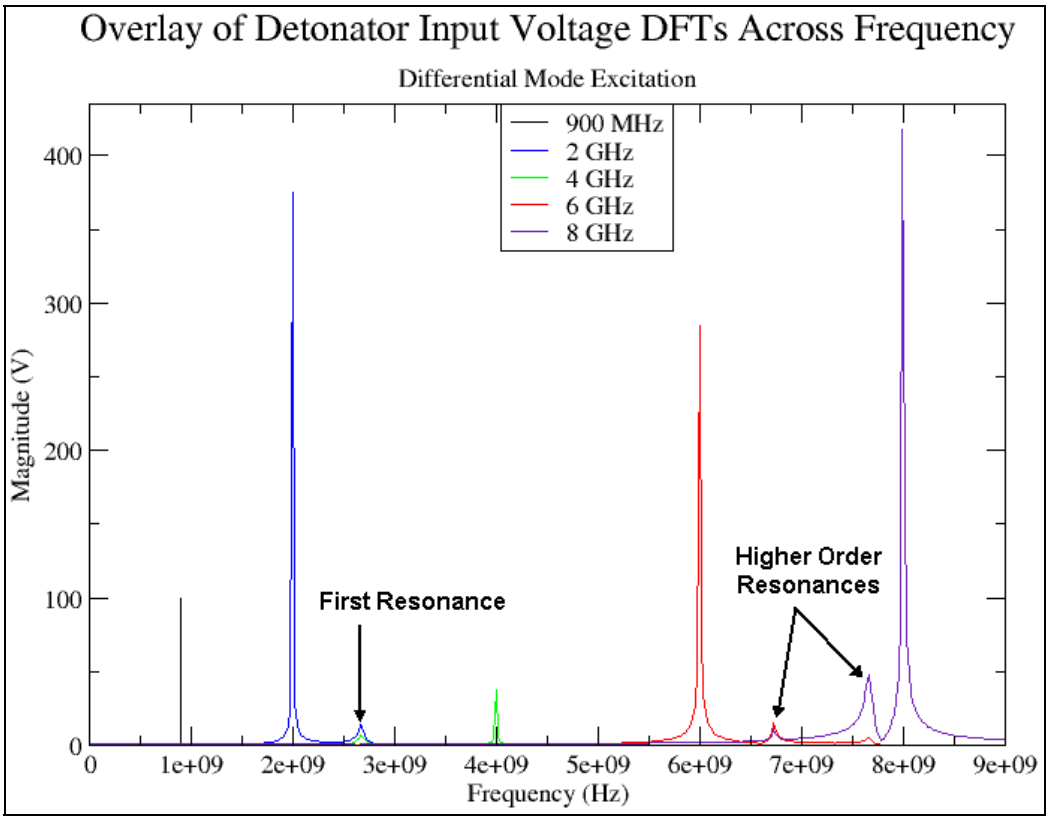

Figure 33: Overlay of standard detonator input voltage differential mode excitation DFTs.

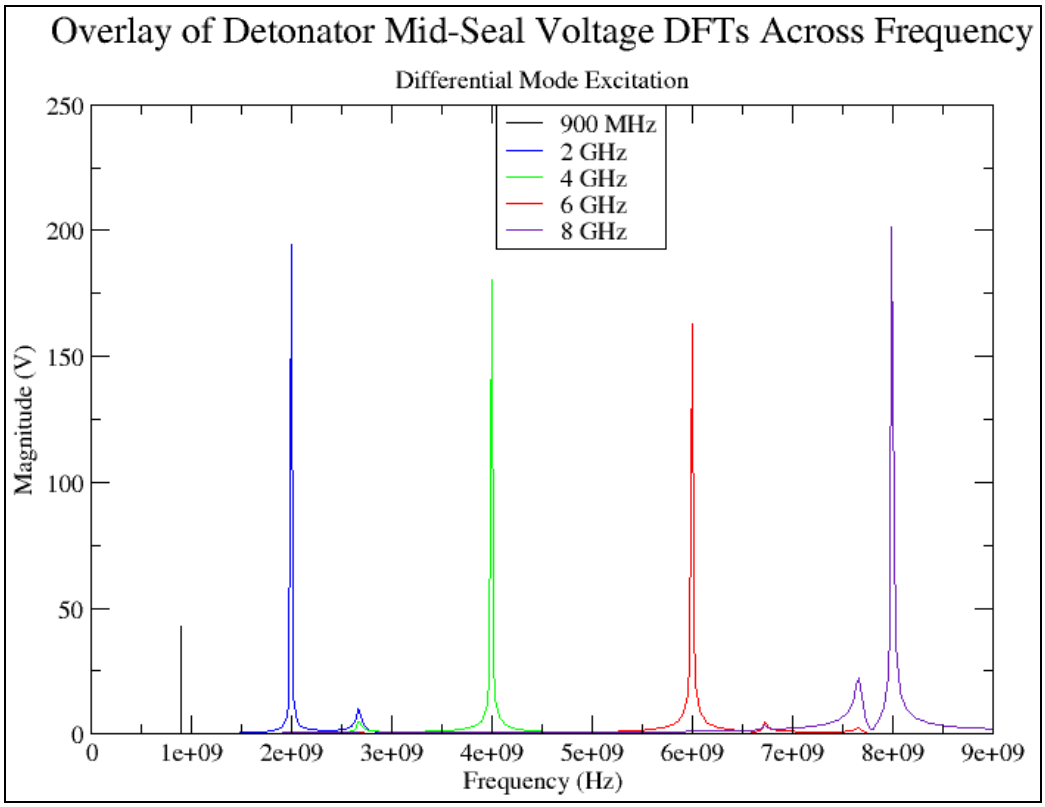

Figure 34: Overlay of standard detonator mid-seal voltage differential mode excitation DFTs.

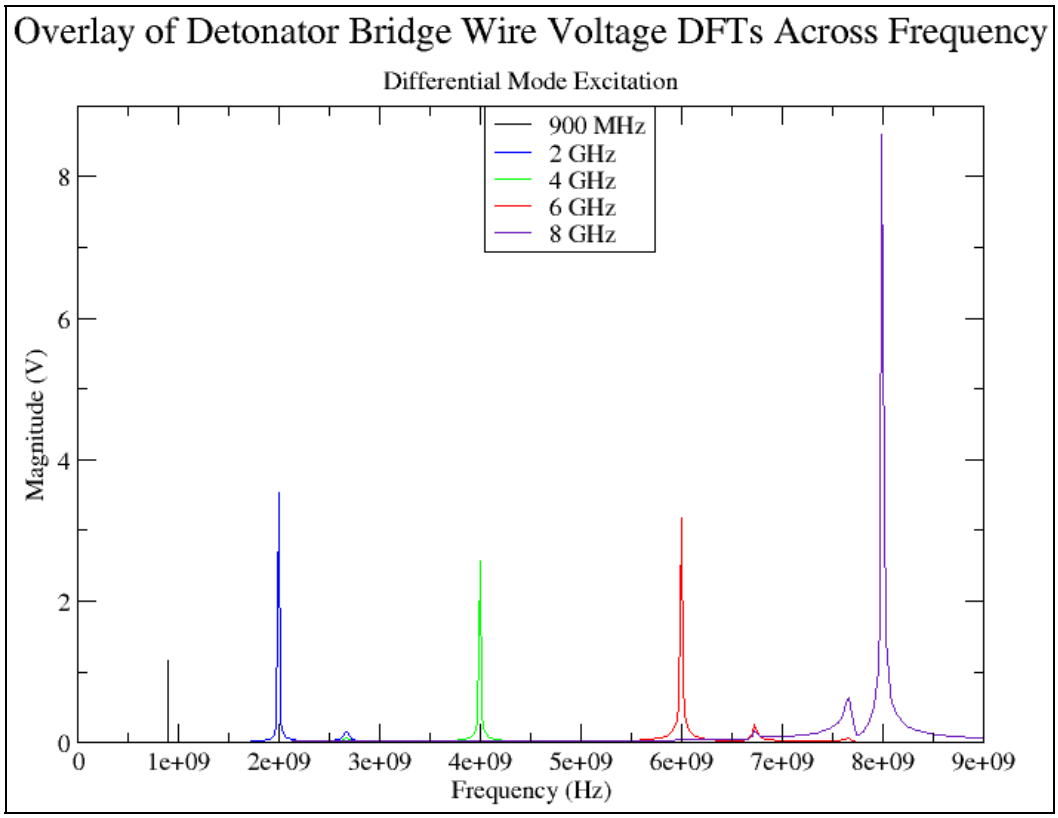

Figure 35: Overlay of standard detonator bridge wire voltage differential mode excitation DFTs.

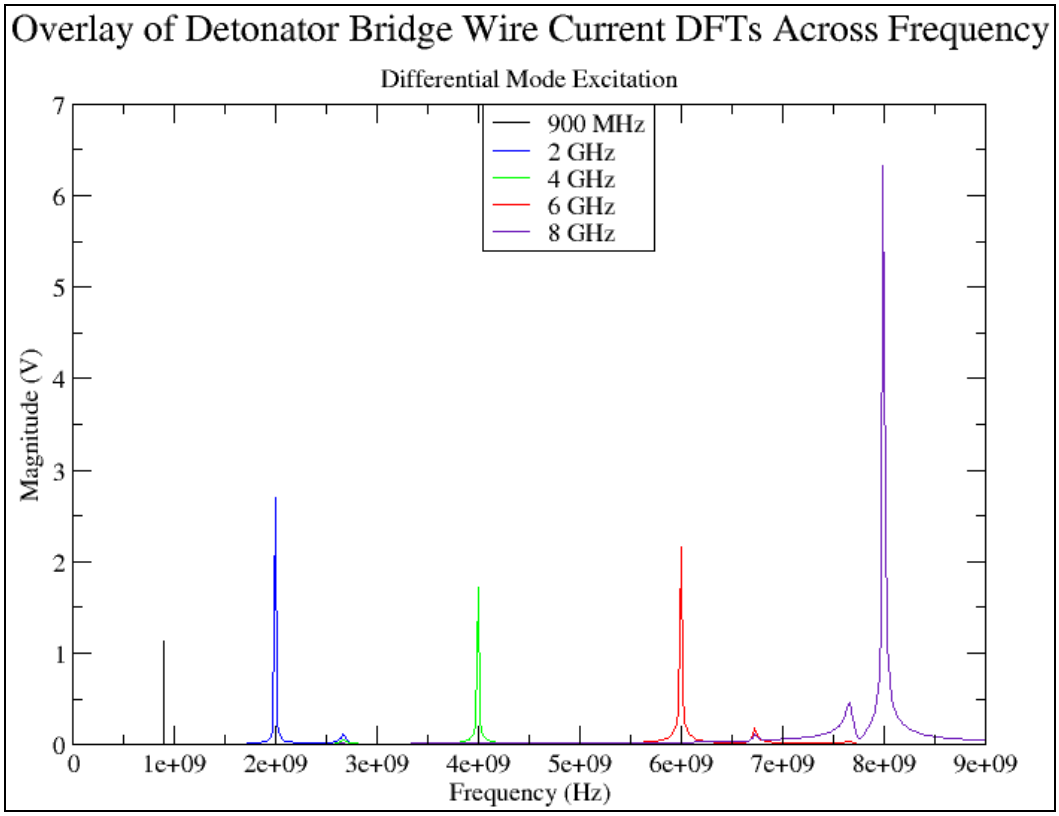

Figure 36: Overlay of standard detonator bridge wire current differential mode excitation DFTs.

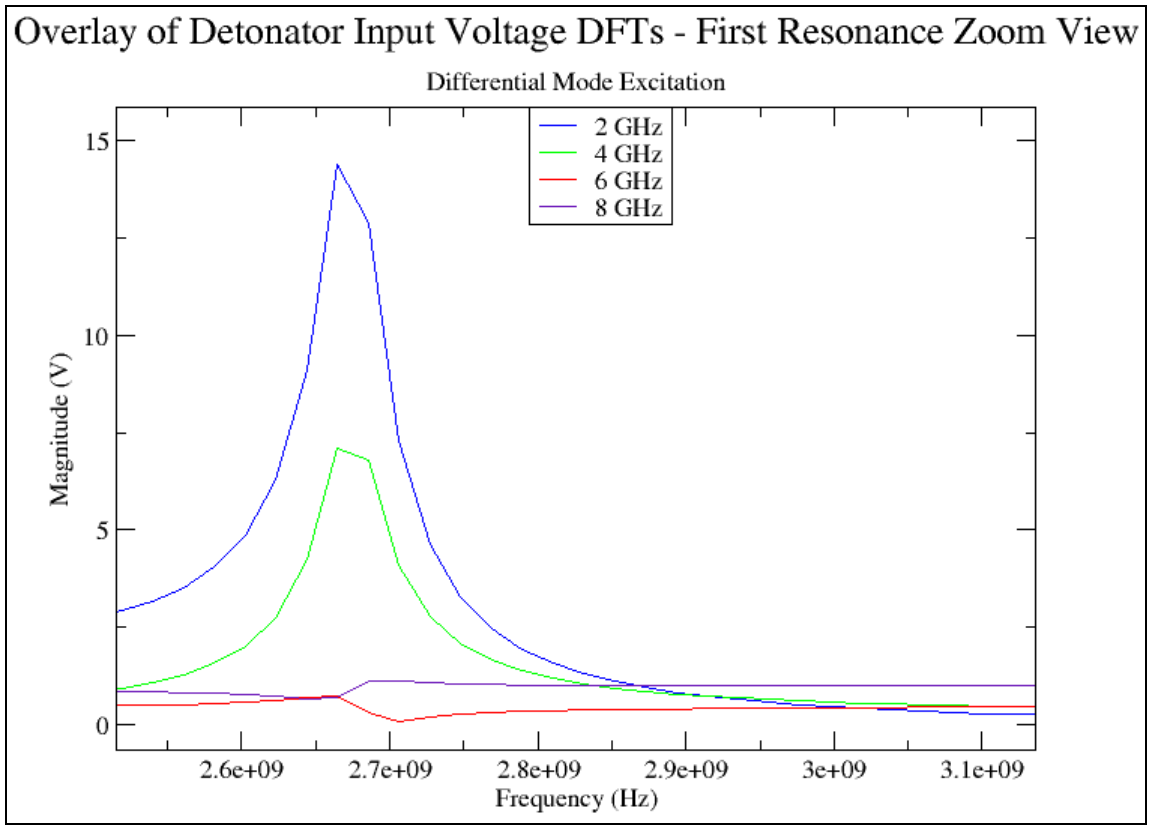

Figure 37: First resonance zoom view of input voltage differential mode excitation DFTs.

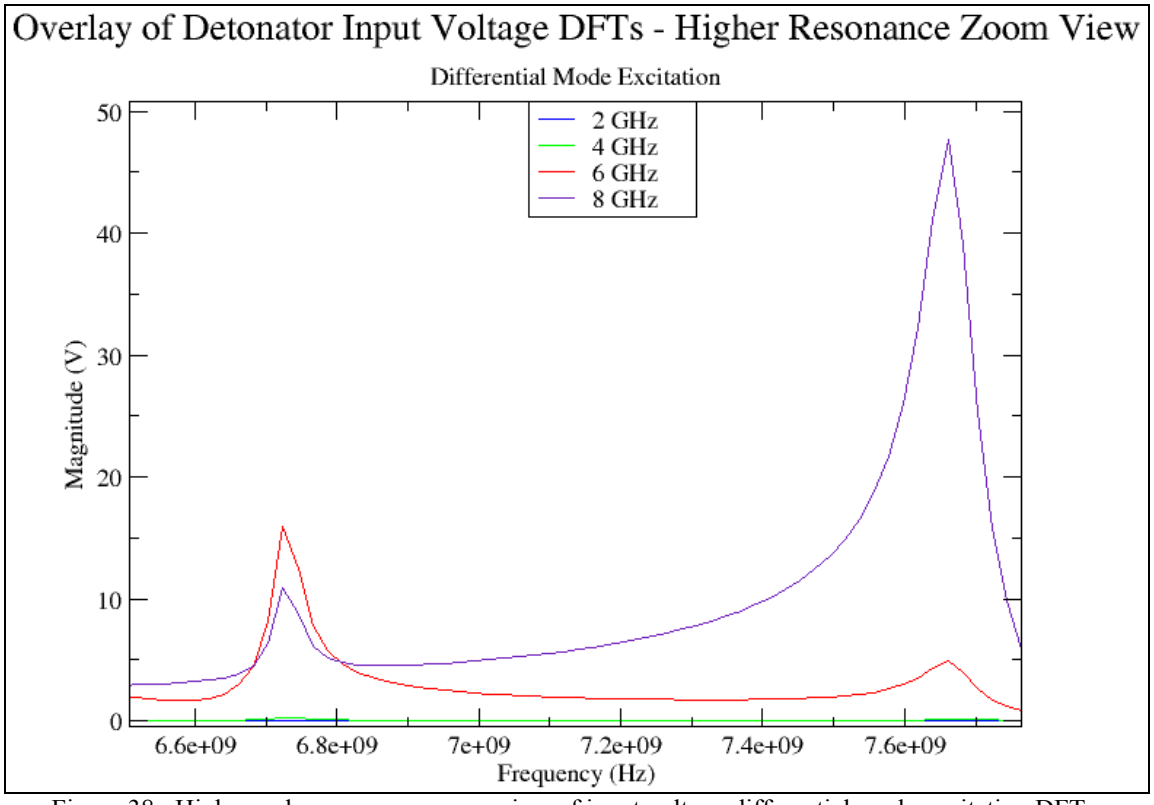

Figure 38: Higher order resonance zoom view of input voltage differential mode excitation DFTs.

Table 9: Standard detonator differential mode voltage and current magnitudes.

Frequency	Input Voltage	Mid-Seal Voltage	Bridge Wire Voltage	Bridge Wire Current
900 MHz	100.96	40.87	1.21	1.17
2 GHz	374.59	194.17	3.53	2.70
4 GHz	38.02	180.70	2.57	1.72
6 GHz	284.19	163.01	3.17	2.17
8 GHz	417.22	201.43	8.60	6.32

Table 10: Standard detonator differential mode resonances.

Frequency	First Resonance	Second Resonance	Third Resonance
900 MHz	2.66 GHz	N/A	N/A
2 GHz	2.66 GHz	6.72 GHz	7.68 GHz
4 GHz	2.66 GHz	6.72 GHz	7.67 GHz
6 GHz	2.66 GHz	6.72 GHz	7.66 GHz
8 GHz	2.66 GHz	6.72 GHz	7.66 GHz

Figures 33 through 36 indicate how the voltages and current vary across frequency, with exact numerical values from these plots given in Table 9. A trend in this data is that the values found at 8 GHz for all four diagnostics are higher than at any other frequency. These high magnitudes are due to the proximity of 8 GHz to the third resonance frequency of 7.66 GHz. Figures 37 and 38 illustrate how all of the DFT plots indicate similar resonant frequencies whose values are given in Table 10. It can also be seen in Figure 37 that the first resonance has a higher magnitude for the lower excitation frequencies (2 and 4 GHz) than for the higher frequencies (6 and 8 GHz). In Figure 38, the converse is true. Here the higher order resonances have high magnitudes for the higher excitation frequencies (6 and 8 GHz) and near 0 magnitudes for the low frequencies (2 and 4 GHz).

Standard Detonator Common Mode Results Across Frequency

Common mode excitation simulations were performed at 900 MHz, 2, 3, 4, 6, and 8 GHz to find the detonator's EM characteristics across frequency. The additional

frequency of 3 GHz was added to the common mode analysis due to the proximity of 4 GHz to the first resonant frequency of 4.31 GHz. Diagnostics of the input, mid-seal, and bridge wire voltage were analyzed as described previously. Overlays of the 2, 3, 4, 6, and 8 GHz DFTs for the input, mid-seal, and bridge wire voltages are redundant, and as such can be simply represented by those shown in Figures 33 through 38. The magnitudes found using these analyses are listed in Tables 11 and 12.

Table 11: Standard detonator common mode voltage magnitudes.

Frequency	Input Voltage	Mid-Seal Voltage	Bridge Wire Voltage
900 MHz	125.04	146.32	164.10
2 GHz	2.69	49.74	99.65
3 GHz	107.54	7.56	113.24
4 GHz	629.71	282.40	373.12
6 GHz	86.66	130.59	60.84
8 GHz	68.78	127.48	39.94

Table 12: Standard detonator common mode resonances.

Frequency	First Resonance	Second Resonance
900 MHz	N/A	N/A
2 GHz	4.31 GHz	8.74 GHz
3 GHz	4.31 GHz	8.74 GHz
4 GHz	4.31 GHz	8.75 GHz
6 GHz	4.31 GHz	8.76 GHz
8 GHz	4.31 GHz	8.74 GHz

A similar trend can be found in the data from Table 11 to what was seen in the differential mode data from Table 9. This trend is that the values found at 4 GHz for all four diagnostics are significantly higher than at any other frequency. These high magnitudes are due to the proximity of 4 GHz to the first resonance frequency of 4.31 GHz. Also, the resonance values given in Table 12 again illustrate how each of the four diagnostics reveal the same resonant frequencies.

Comparison of Standard Detonator ICEPIC Results with Analytical Predictions

In Chapters 3 and 4 a 1-D EM model of the detonator was developed and modified to predict the voltages and current found using ICEPIC simulation. The ICEPIC simulation results shown in the previous section can now be directly compared to these analytical model predictions.

Analytical Bridge Wire Modification

As was discussed in Chapter 4, the bridge wire in the ICEPIC model required an increase in diameter to be successfully modeled with the rest of the detonator geometry. In order to make a direct comparison with the ICEPIC results, the bridge wire diameter in the analytical model must be changed to match that of the scaled bridge wire in ICEPIC. This modification is a simple change in the MatLAB program from a diameter of 25 μm to 150 μm, and will result in changes to the analytical model predictions seen in Chapter 4. Since the purpose of the ICEPIC numerical modeling is to validate the 1-D predictions, a change in bridge wire diameter is justified. Once the analytical model is validated, the bridge wire diameter can then be changed back to its actual size to predict true detonator characteristics. All of the following 1-D predictions, compared to ICEPIC results, have been found using a 150 μm bridge wire.

Differential Mode Predictions Compared to ICEPIC Results

For comparing the MatLAB analytical model predictions to the ICEPIC results, the ICEPIC data points given in Table 9 will be plotted along with the predictions. Figure 39 is the analytical prediction and ICEPIC comparison plot of the detonator input voltage magnitude across the frequency range DC-9 GHz. Also included in Figure 39 are

the three ICEPIC differential mode resonances given in Table 10. These resonances are displayed as simple vertical lines to indicate their position relative to the analytical model predictions of resonant frequencies

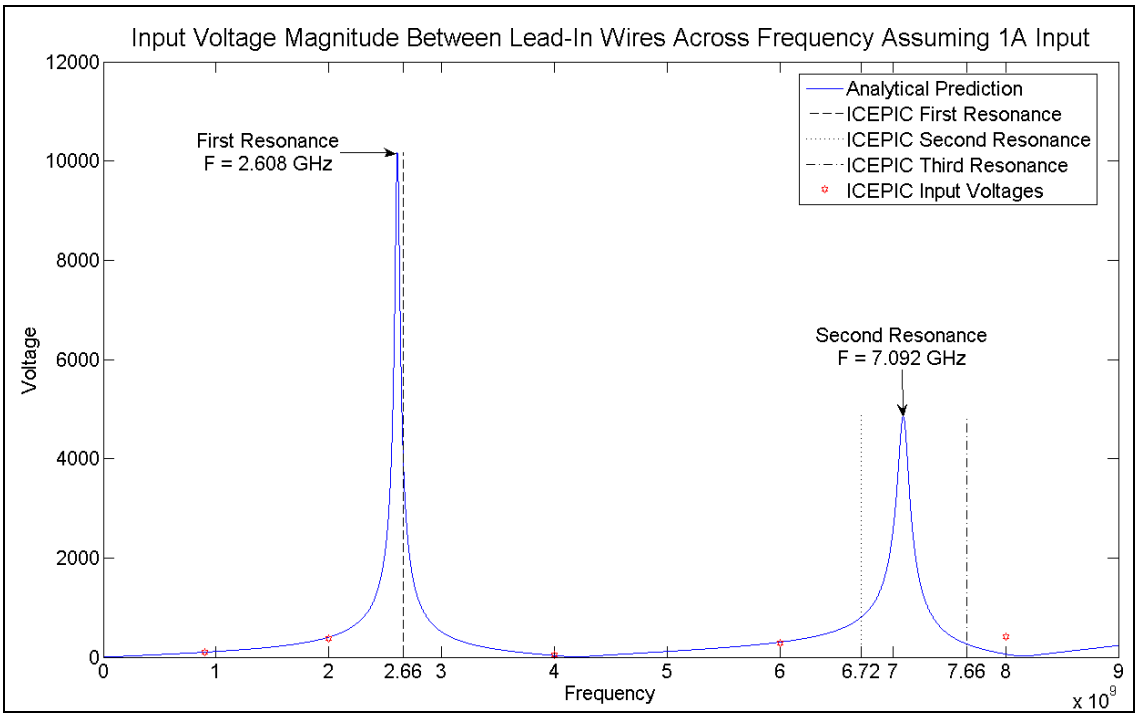

Figure 39: MatLAB analytical prediction and ICEPIC comparison plot of the differential mode detonator input voltage magnitude across the frequency range DC-9 GHz.

Figure 39 indicates good agreement between the first (l.95%) and second (5.54%) resonant frequencies of the analytic and ICEPIC results. However, ICEPIC has determined a third resonant frequency at 7.66 GHz which is not predicted by the analytical model. The magnitudes appear to be in good agreement as well, but due to the magnitude scale possible discrepancies can not easily be discerned. Figure 40 is a reproduction of Figure 39 with the magnitude plotted on a log scale. The ICEPIC resonances are not shown on this plot, as that comparison has already been made. Figure 40 shows very good agreement between the MatLAB predictions and ICEPIC input voltage magnitudes with the exception of the 8 GHz data point.

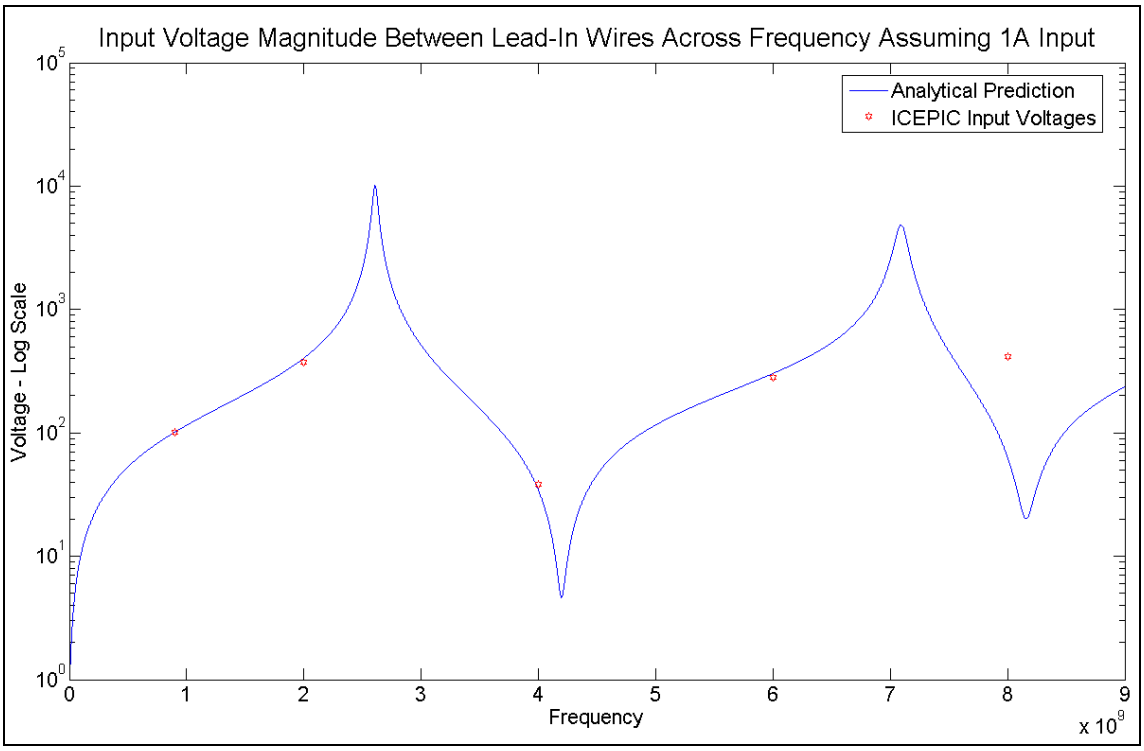

Figure 40: MatLAB analytical prediction and ICEPIC comparison plot of the differential mode detonator input voltage magnitude across the frequency range DC-9 GHz plotted on a log scale.

The reason for the large discrepancy at 8 GHz is due to the data point's proximity to the third resonant frequency of 7.66 GHz. Since ICEPIC predicts this resonance and the analytical model does not, the ICEPIC 8 GHz value is much higher than that of the analytical model, a 555% difference in fact. When the other four frequencies are examined, the average percent difference for all four data points is 5.79%.

Analytic prediction and ICEPIC comparison plots for the detonator mid-seal and bridge wire voltages are shown in Figures 41 and 43, respectively. The corresponding log scale mid-seal and bridge wire voltage comparison plots are shown in Figures 42 and 44, respectively. The comparison and log scale plots of the bridge wire current are then shown in Figures 45 and 46, respectively.

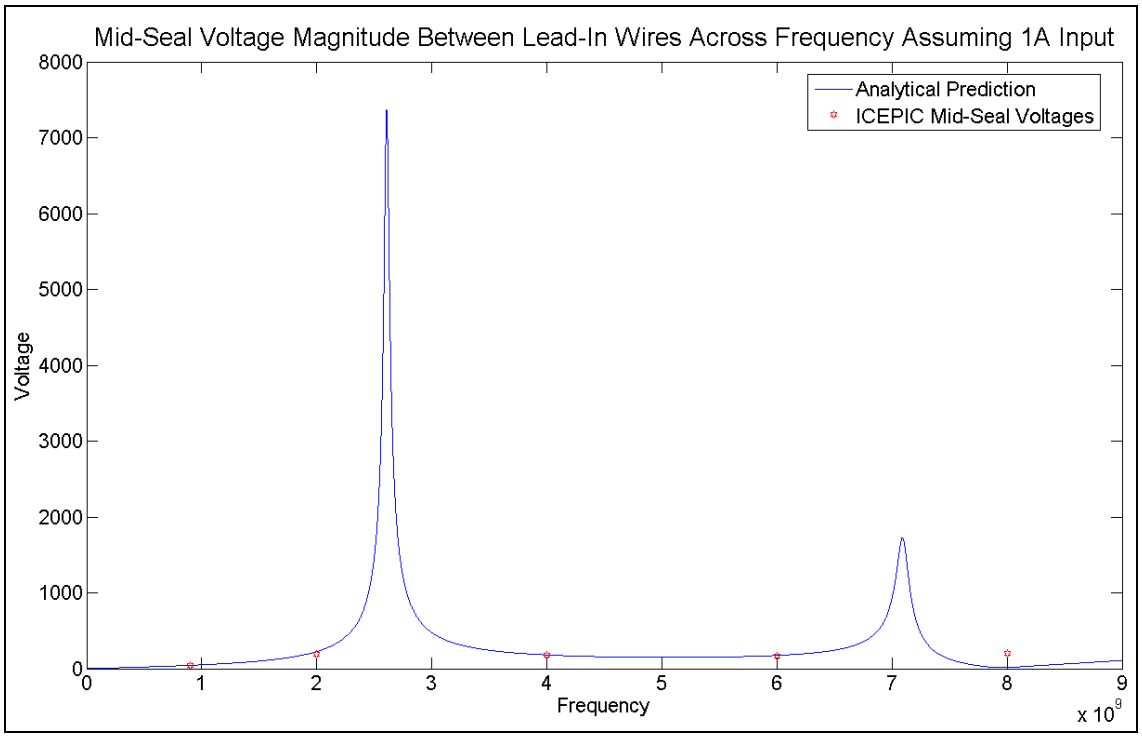

Figure 41: MatLAB analytical prediction and ICEPIC comparison plot of the differential mode detonator mid-seal voltage magnitude across the frequency range DC-9 GHz.

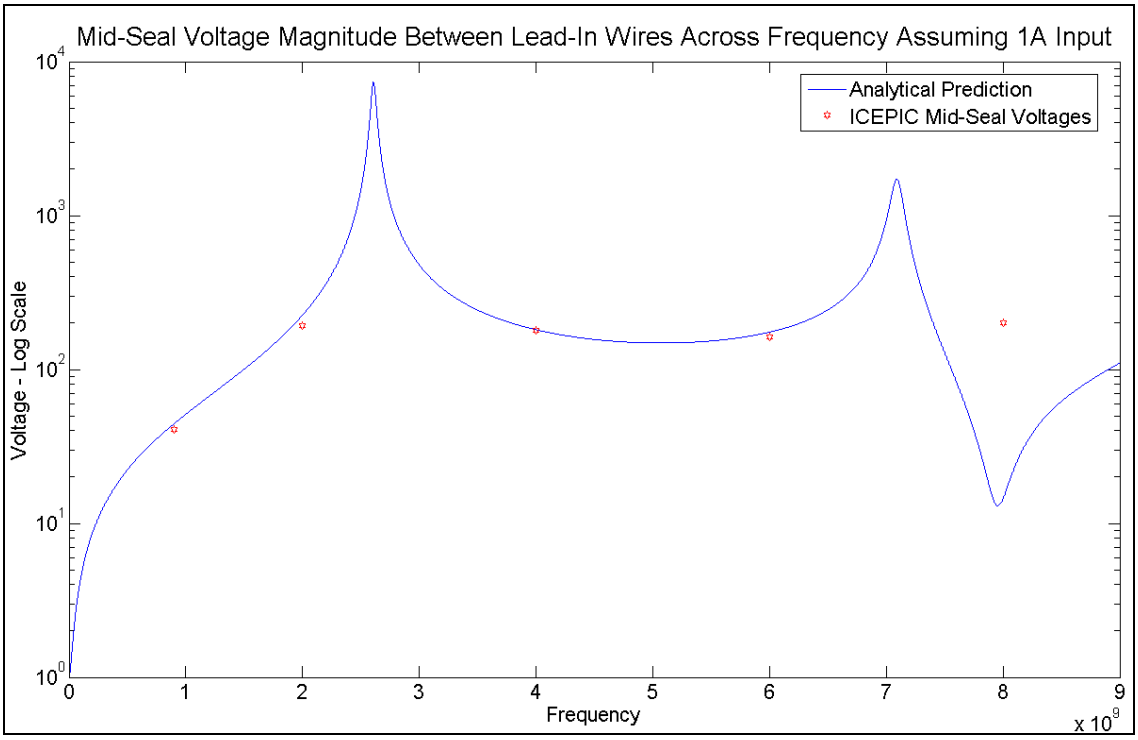

Figure 42: MatLAB analytical prediction and ICEPIC comparison plot of the differential mode detonator mid-seal voltage magnitude across the frequency range DC-9 GHz plotted on a log scale.

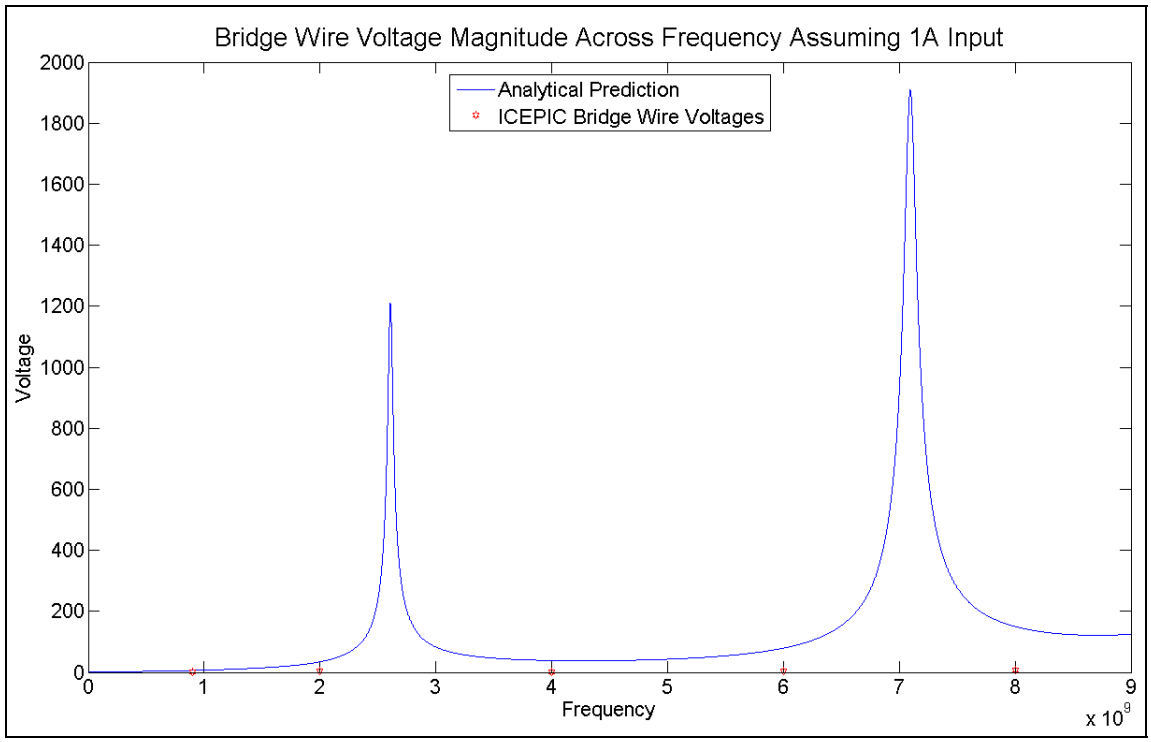

Figure 43: MatLAB analytical prediction and ICEPIC comparison plot of the differential mode detonator bridge wire voltage magnitude across the frequency range DC-9 GHz.

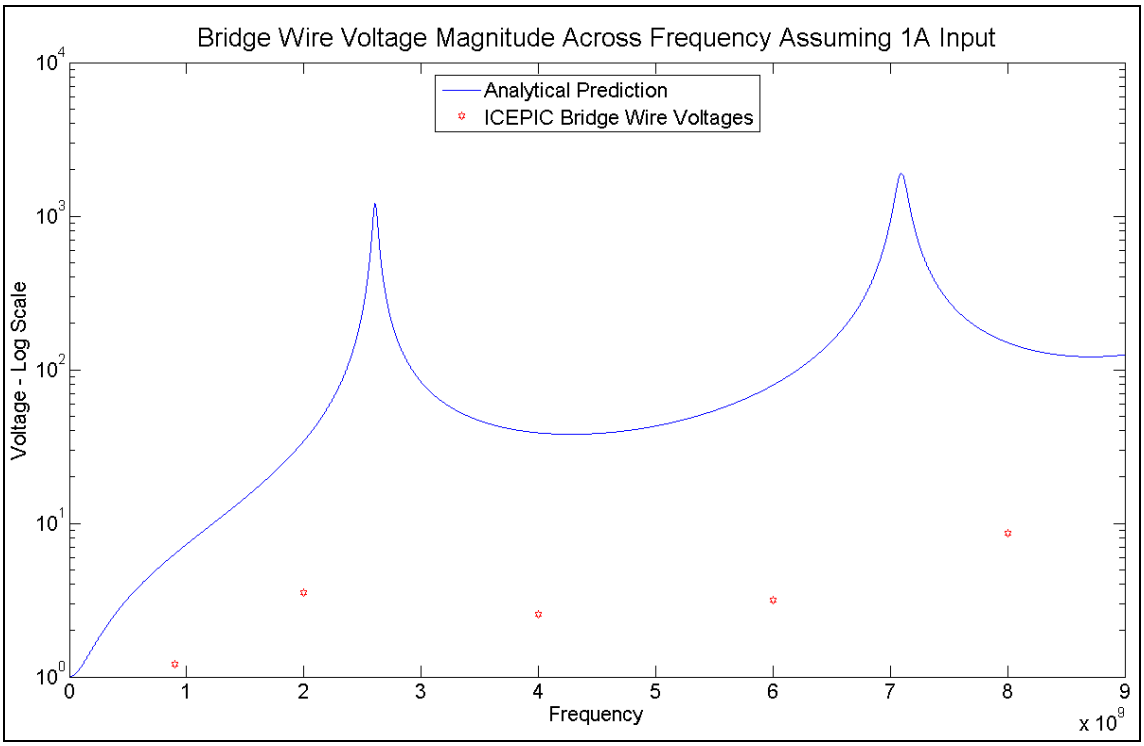

Figure 44: MatLAB analytical prediction and ICEPIC comparison plot of the differential mode detonator bridge wire voltage magnitude across the frequency range DC-9 GHz plotted on a log scale.

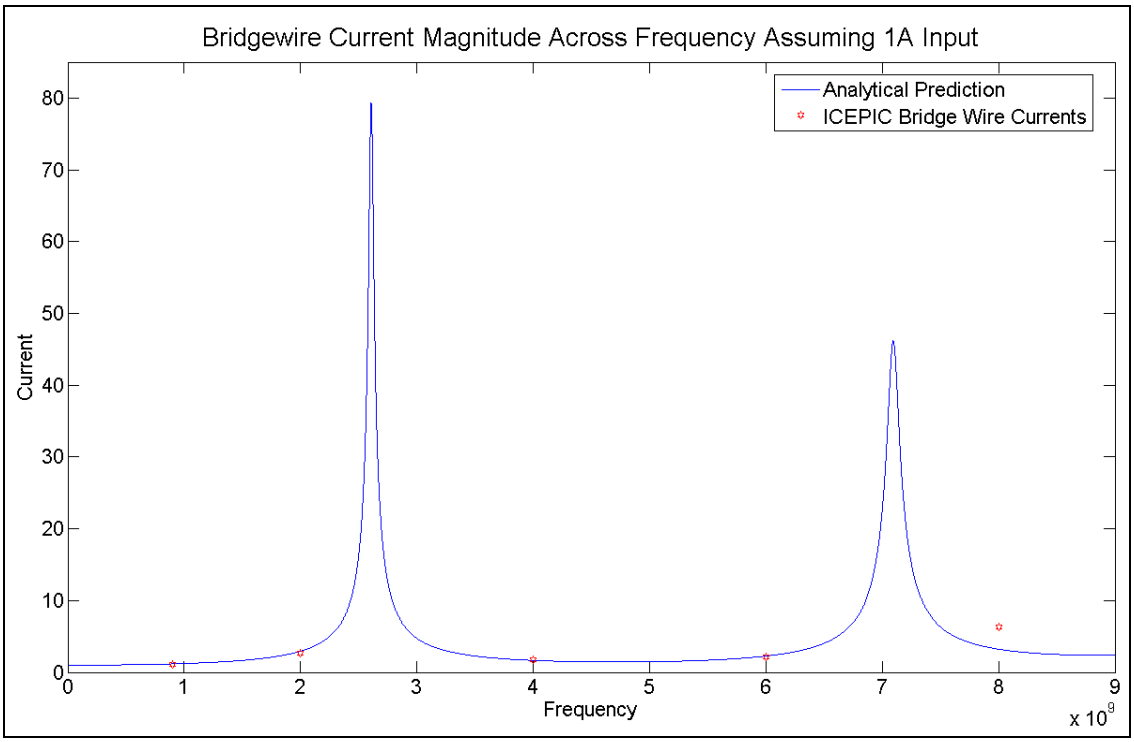

Figure 45: MatLAB analytical prediction and ICEPIC comparison plot of the differential mode detonator bridge wire current magnitude across the frequency range DC-9 GHz.

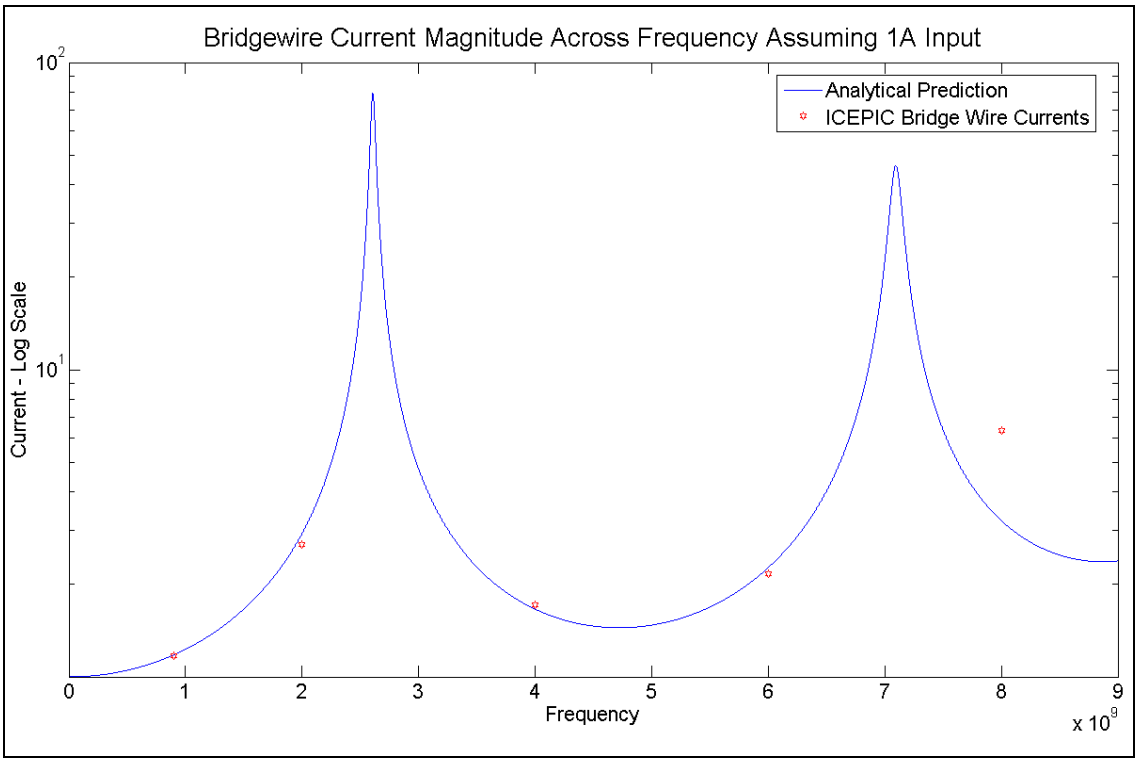

Figure 46: MatLAB analytical prediction and ICEPIC comparison plot of the differential mode detonator bridge wire current magnitude across the frequency range DC-9 GHz plotted on a log scale.

The ICEPIC resonances have not been included on Figures 41, 43, and 45 since they and the resonances predicted by the analytical model in each of these figures are the same as seen in Figure 39 for the input voltage comparison plot. As was observed for the input voltage, the 8 GHz ICEPIC values for the mid-seal voltage and bridge wire current are significantly higher than those predicted analytically. This is again due to the proximity of 8 GHz to the third ICEPIC resonant frequency of 7.66 GHz. The 8 GHz values have a percent difference of 1298% for the mid-seal voltage magnitude and 95.54% for the bridge wire current. However, the remaining four values show very good agreement, having an average percent difference of 7.83% for the mid seal voltage values and 4.15% for the bridge wire current values. The greatest discrepancies are seen in the bridge wire voltage comparison plots. The ICEPIC values are considerably lower than those predicted analytically at all five frequencies. The average percent difference for the bridge wire voltages, again excluding the 8 GHz value, is 1274%.

Common Mode Predictions Compared to ICEPIC Results

The common mode MatLAB analytical model predictions will be compared to the ICEPIC results given in Table 11, as was done in the previous section for the differential mode results. Figure 47 is the analytical prediction and ICEPIC comparison plot of the detonator input voltage magnitude across the frequency range DC-9 GHz. Also included in Figure 47 are both of the ICEPIC common mode resonances given in Table 12. These resonances are displayed as simple vertical lines to indicate their position relative to the analytical model predictions of resonant frequencies.

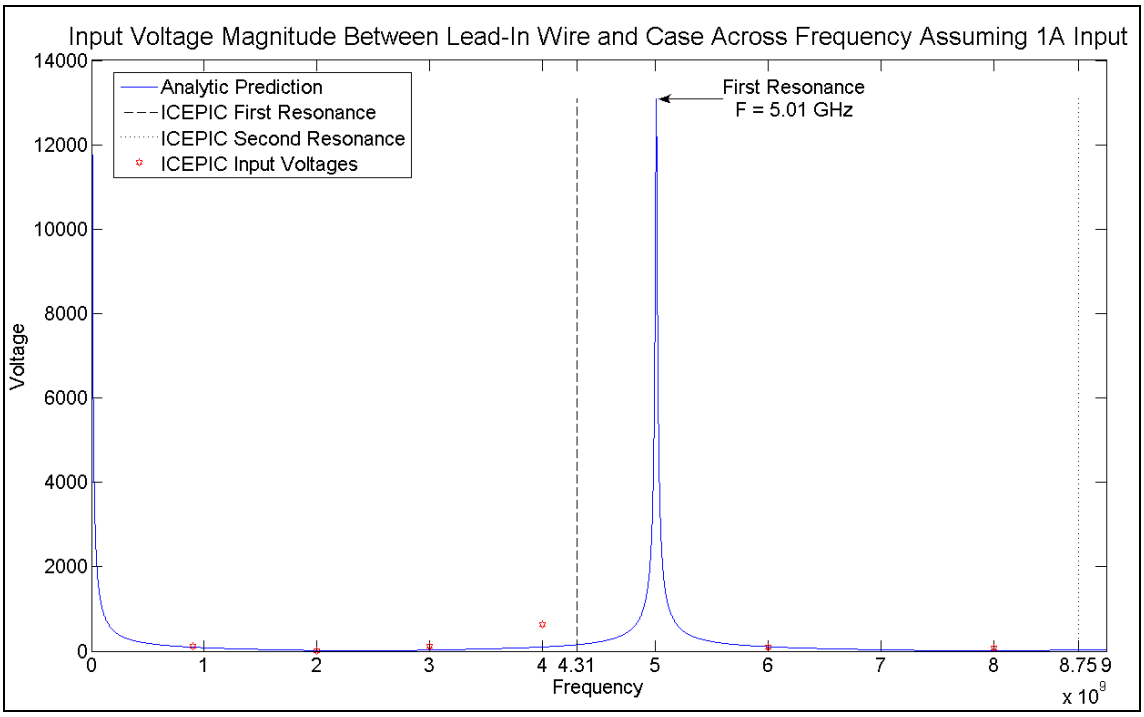

Figure 47: MatLAB analytical prediction and ICEPIC comparison plot of the common mode detonator input voltage magnitude across the frequency range DC-9 GHz.

Figure 47 indicates decent agreement (16.24%) between the first resonant frequency of the analytic and ICEPIC results. However, ICEPIC has determined a second resonant frequency at 8.75 GHz which is not predicted by the analytical model. The magnitudes appear to be in decent agreement as well, but due to the magnitude scale possible discrepancies can not easily be discerned. Figure 48 is a reproduction of Figure 47 with the magnitude plotted on a log scale. The ICEPIC resonances are not shown on this plot, as that comparison has already been made. Figure 48 shows poor agreement between the MatLAB predictions and ICEPIC input voltage magnitudes with the exception of the 900 MHz and 6 GHz data points. Overall, the average percent difference between the ICEPIC and predicted results is 543%. However, the 8 GHz value has the highest percent difference (1857%), the other five values have an average percent difference of 280%.

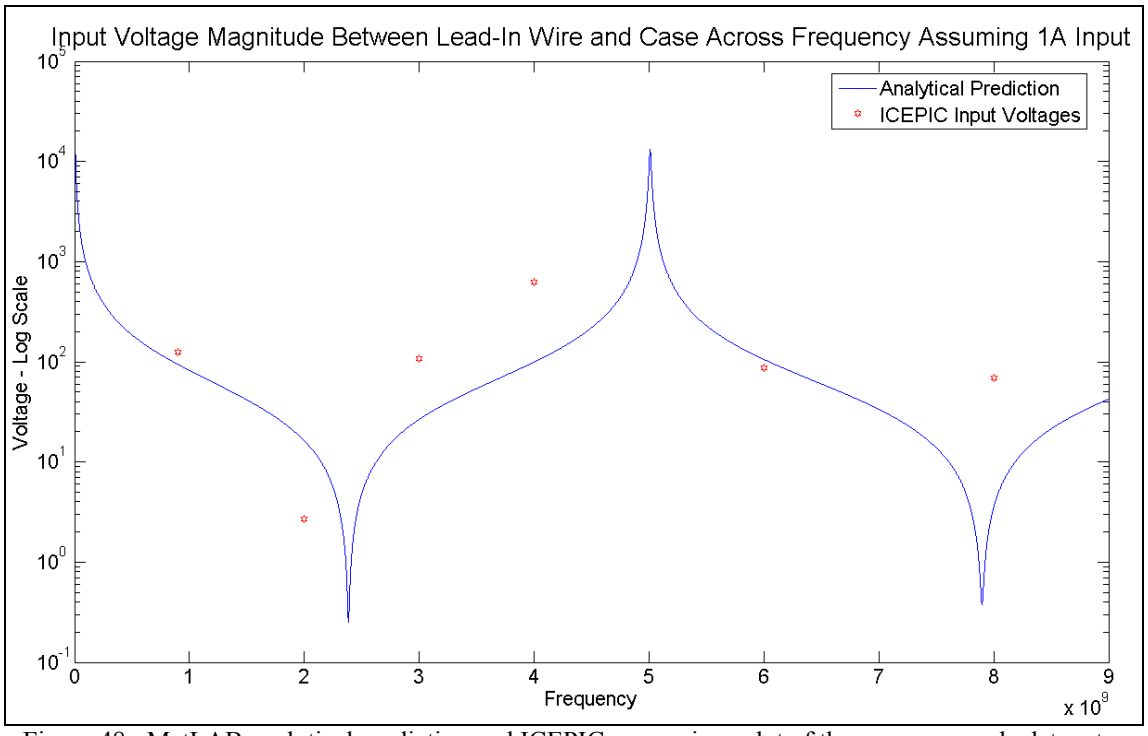

Figure 48: MatLAB analytical prediction and ICEPIC comparison plot of the common mode detonator input voltage magnitude across the frequency range DC-9 GHz plotted on a log scale.

Analytic prediction and ICEPIC comparison plots for the common mode detonator mid-seal and bridge wire voltages are shown in Figures 49 and 50, respectively. These figures are both plotted on a log scale, as standard scale plots corresponding to both of these figures will not be shown since they are well represented by the input voltage plot shown in Figure 47. Overall, the average percent difference between the ICEPIC and predicted results is 466% for the mid-seal voltages and 82% for the bridge wire voltages. However, the 4 GHz values have the highest percent difference for both the mid-seal (2467%) and bridge wire (296%) voltages. The other five values have an average agreement of 67% for the mid-seal voltages and 39% for the bridge wire voltages. This is due to the proximity of the 4 GHz signal to the ICEPIC resonance of 4.31 GHz. Since the analytical model predicts a resonance closer to 5 GHz, the predicted 4 GHz values are not as high as those found using ICEPIC. This trend is also seen in the

input voltage prediction as well, even though the 8 GHz value has the largest percent difference.

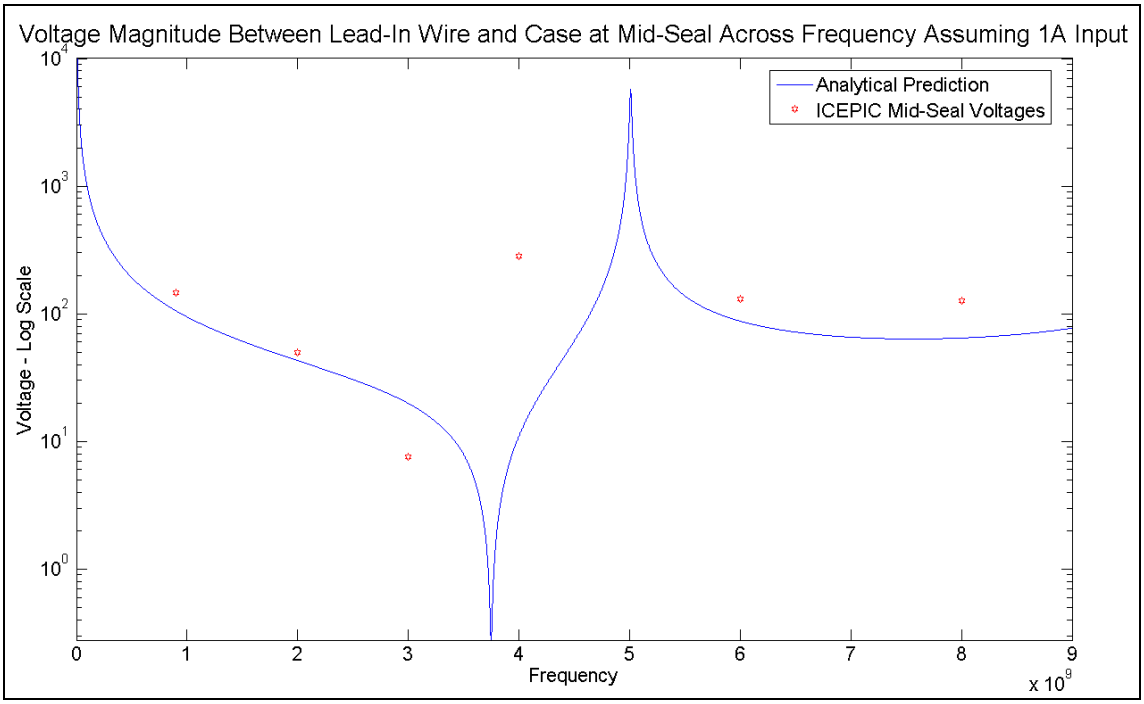

Figure 49: MatLAB analytical prediction and ICEPIC comparison plot of the common mode detonator mid-seal voltage magnitude across the frequency range DC-9 GHz plotted on a log scale.

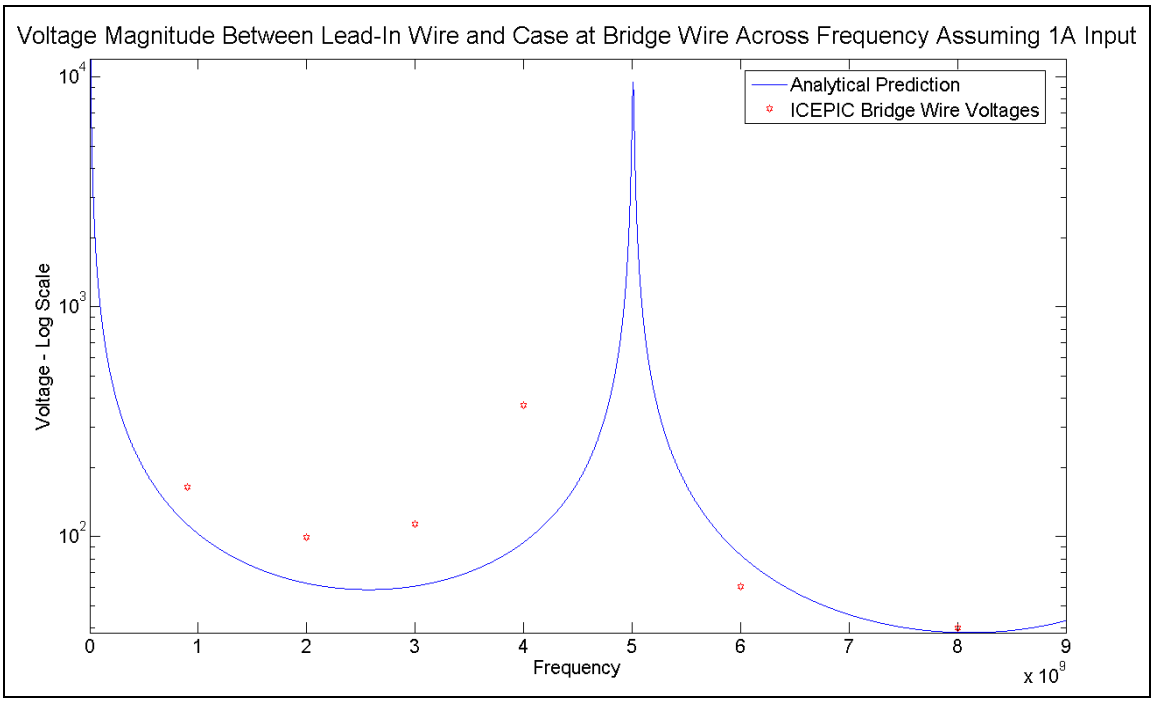

Figure 50: MatLAB analytical prediction and ICEPIC comparison plot of the common mode detonator bridge wire voltage magnitude across the frequency range DC-9 GHz plotted on a log scale.

Chapter Summary

In this chapter, initial full detonator ICEPIC simulation results have been analyzed, resulting in a reduction of detonator geometry to conserve computational resources and time while obtaining the same results. This reduced standard geometry was simulated using both differential and common mode excitations at several frequencies to determine the detonator EM characteristics in the range of DC-9 GHz. The results of these ICEPIC simulations were then directly compared to 1-D predictions made using the MatLAB analytical model. While differential mode results compared favorably, common mode results indicate poor agreement at all points along the detonator.

Chapter 6 – Investigations into Model Improvement

The results reported in Chapter 5 indicate several discrepancies between the voltages and current found using ICEPIC 3-D EM simulations and the values predicted using the analytical 1-D detonator model. In an effort to determine the cause of the differences in the data, many investigations were carried out so that the agreement between the 1-D and 3-D models could be improved.

Determining the Scalability of the Detonator Model

The results reported in Chapter 5 for the standard detonator geometry were all from a simulation utilizing a 50 μm grid spacing. This grid spacing was determined to be sufficient based on the 250 μm diameter of the lead-in wires along with the 150 μm diameter of the scaled bridge wire. The first investigation was aimed at determining the scalability of ICEPIC and the simulated detonator geometry to ascertain whether finer grid spacing would produce different results and if these new results could possibly be in better agreement with the analytical predictions.

For this study the standard detonator geometry grid size was reduced by a factor of 2 and set to a value of 25 μm. This resulted in a factor of 8 increase in the number of computed cells within the detonator geometry up to $2.28*10^8$ from $2.84*10^7$. Due to this computational increase, a 900 MHz input frequency was required for excitation. The reason for this requirement is that the 900 MHz waveforms reach steady state very quickly and are analyzed using curve-fitting techniques so the 2x resolution geometry would only need to be simulated for 20 ns instead of 50 ns. Higher frequencies would require 50 ns so that the DFT of the resulting data set would produce accurate results.

Beyond the finer resolution and the reduction in simulation time, nothing else about the ICEPIC simulation and excitation set-up was changed from what has already been described.

The 2x resolution standard detonator geometry was excited with a 900 MHz differential mode input. The resulting waveforms for the input, mid-seal, and bridge wire voltages along with the bridge wire current are nearly identical to those shown in Figures 5a-8a from Chapter 5 and so will not be repeated. The analyses were also similar to those in Figures 9 and 10 of Chapter 5. The results of these analyses are listed in Tables 1 and 2 along with the 900 MHz values from the 50 μm resolution simulation listed in Tables 9 and 10 from Chapter 5. Figure 1 is a comparison chart of the 25 and 50 μm ICEPIC results from Table 1.

Table 1: Standard detonator geometry differential mode voltage and current magnitudes for 25 and 50 μm grid spacing.

Frequency	Input Voltage	Mid-Seal Voltage	Bridge Wire Voltage	Bridge Wire Current
900 MHz – 25 μm	100.96	40.87	1.21	1.17
900 MHz – 50 μm	100.61	40.40	1.04	1.17

Table 2: Standard detonator geometry differential mode resonances for 25 and 50 μm grid spacing.

Frequency	First Resonance	Second Resonance
900 MHz – 25 μm	2.66	N/A
900 MHz – 50 μm	2.66	N/A

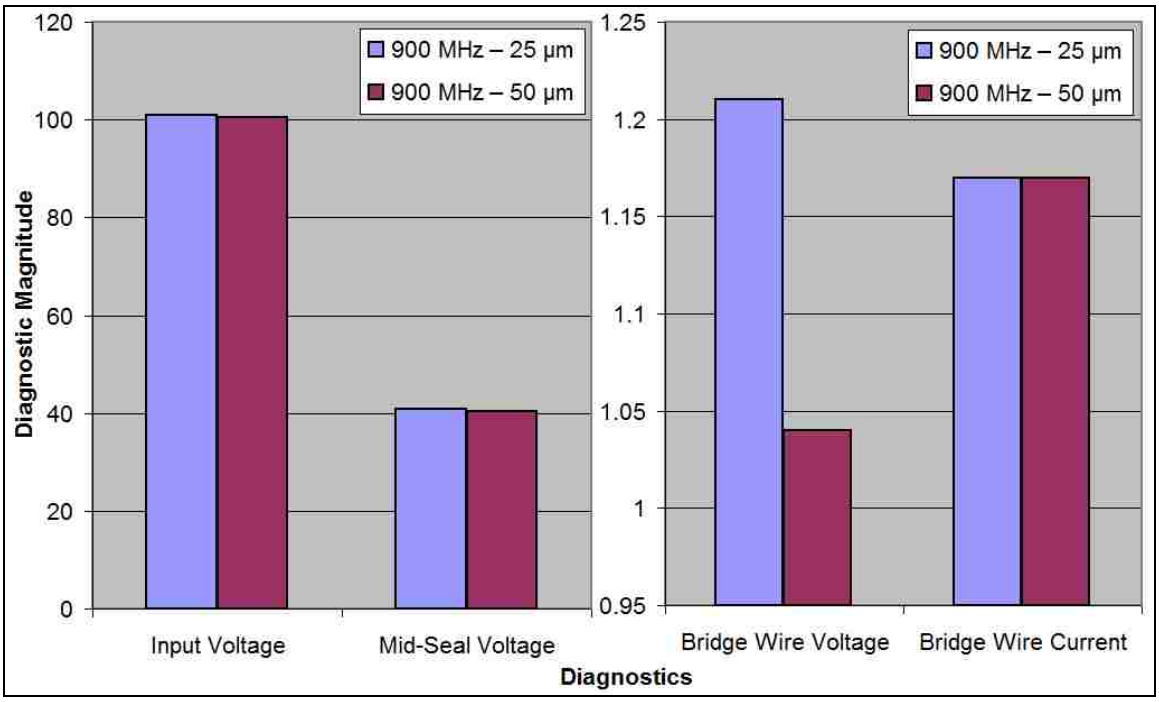

Figure 1: Comparison chart of the ICEPIC diagnostic magnitudes for 900 MHz differential mode excitation of standard detonator geometry using 25 and 50 μm grid spacing.

The data from Figure 1 indicates very good agreement across all four diagnostics. The only diagnostic with a considerable percent difference is the bridge wire voltage at 16.34%. Given the exactness of the other three diagnostics, it is most likely that the bridge wire voltage diagnostics were not in the exact same location for both simulations. While ICEPIC was programmed to put the diagnostic at the same Z position, the re-gridding of the geometry likely caused the bridge wire voltage diagnostic to fall on a grid edge, causing it to be moved to the next grid space. This small difference in Z location, only 25 μm, is enough to cause this 16.34% discrepancy. Also, the resonances found in both cases were identical. These results indicate that a finer mesh size will not provide different or more accurate results compared to predicted values, and that the values obtained using the 50 μm mesh are what can be expected from ICEPIC simulation. Since this scalability investigation yielded conclusive evidence that the geometry is in fact scalable, there is no need to simulate a high resolution geometry at another differential

mode frequency or for any common mode excitation. Any scalability issues with the ICEPIC code with relation to this geometry would be pervasive and would have shown up in the initial investigation.

Investigations into Improving the Differential Mode Model

The comparison of results using ICEPIC simulation of the standard detonator geometry and analytical model prediction for differential mode excitation showed very good agreement overall. However, there were a few exceptions. First, ICEPIC determined a third resonant frequency at 7.66 GHz while the analytical model did not. This affected not only the resonance agreement, but also caused the ICEPIC 8 GHz values to be higher than predicted due to its proximity in frequency to this third resonance. The most glaring discrepancy, however, was that ICEPIC bridge wire voltage values at all frequencies were considerably lower than those predicted analytically. Several investigations were launched into determining the reasons for these discrepancies.

Standard Detonator Geometry Without a Bridge Wire

To assist in understanding the cause of the discrepancy in the bridge wire voltage results, the standard ICEPIC detonator geometry was modified by removing the bridge wire completely, ending the detonator transmission line in an open circuit. The goal of this investigation was to see if the overall transmission line scheme for the analytical detonator model was valid. The bridge wire is treated simply as a load in the analytical model, but is a metal object incurring EM field interactions in the ICEPIC simulation. By removing the bridge wire, the 1-D transmission line model can be compared end to

end with EM simulation. No other part of the standard geometry or simulation space set-up was changed in ICEPIC other than the removal of the bridge wire. This standard geometry without a bridge wire was simulated in ICEPIC using differential mode excitation at the same frequencies used previously with an added frequency of 3 GHz. Also, since there is no bridge wire in the geometry, there is also no bridge wire current to be calculated. The results of these ICEPIC simulations were analyzed using all methods previously described, and are well represented by Figures 33 through 38 in Chapter 5, though individual values have changed. The results are listed in Tables 3 and 4.

The analytical model was also slightly modified. For differential mode predictions, the boundary conditions were as given in (54). Since the model is terminated in an open, the boundary conditions for this differential mode investigation are changed to (66) in the MatLAB program. Figure 2 is the ICEPIC and analytical model comparison plot of the differential mode input voltage across frequency for the standard detonator model without a bridge wire. The corresponding plots of the mid-seal and bridge wire voltage comparisons will not be shown as they are very similar to Figure 2 in that all three predict the same resonant frequency and have a similar shape. In order to discern differences between the ICEPIC and predicted values, the data in Figure 2 is re-plotted on a log scale in Figure 3. Figures 4 and 5 are the log scale plots of the mid-seal and bridge wire voltage comparisons.

Table 3: Standard detonator differential mode voltage magnitudes with the bridge wire removed.

Frequency	Input Voltage	Mid-Seal Voltage	Bridge Wire Voltage
900 MHz	137.49	189.14	204.72
2 GHz	49.48	74.67	119.45
3 GHz	196.66	28.39	141.18
4 GHz	840.43	155.72	495.36
6 GHz	60.49	132.91	98.17
8 GHz	424.62	231.81	118.29

Table 4: Standard detonator differential mode resonances with the bridge wire removed.

Frequency	First Resonance	Second Resonance
900 MHz	N/A	N/A
2 GHz	4.31 GHz	N/A
3 GHz	4.31 GHz	N/A
4 GHz	4.31 GHz	N/A
6 GHz	4.31 GHz	N/A
8 GHz	4.31 GHz	N/A

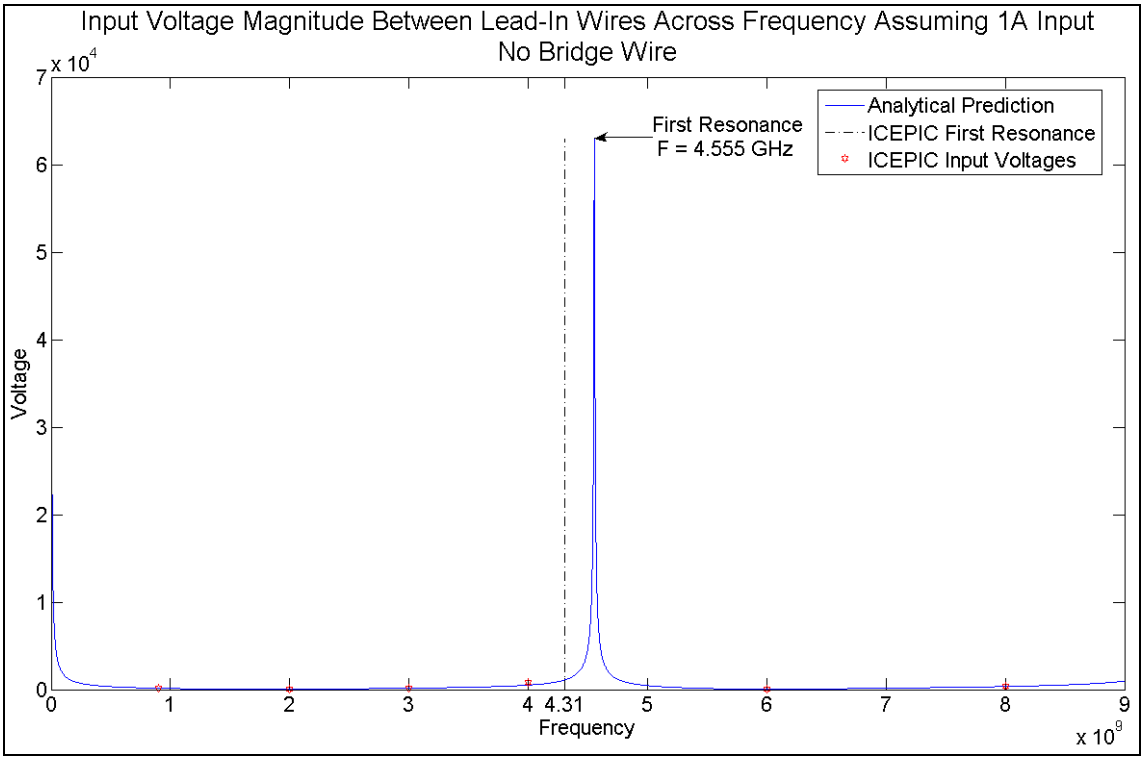

Figure 2: MatLAB analytical prediction and ICEPIC comparison plot of the differential mode detonator input voltage magnitude with no bridge wire across the frequency range DC-9 GHz.

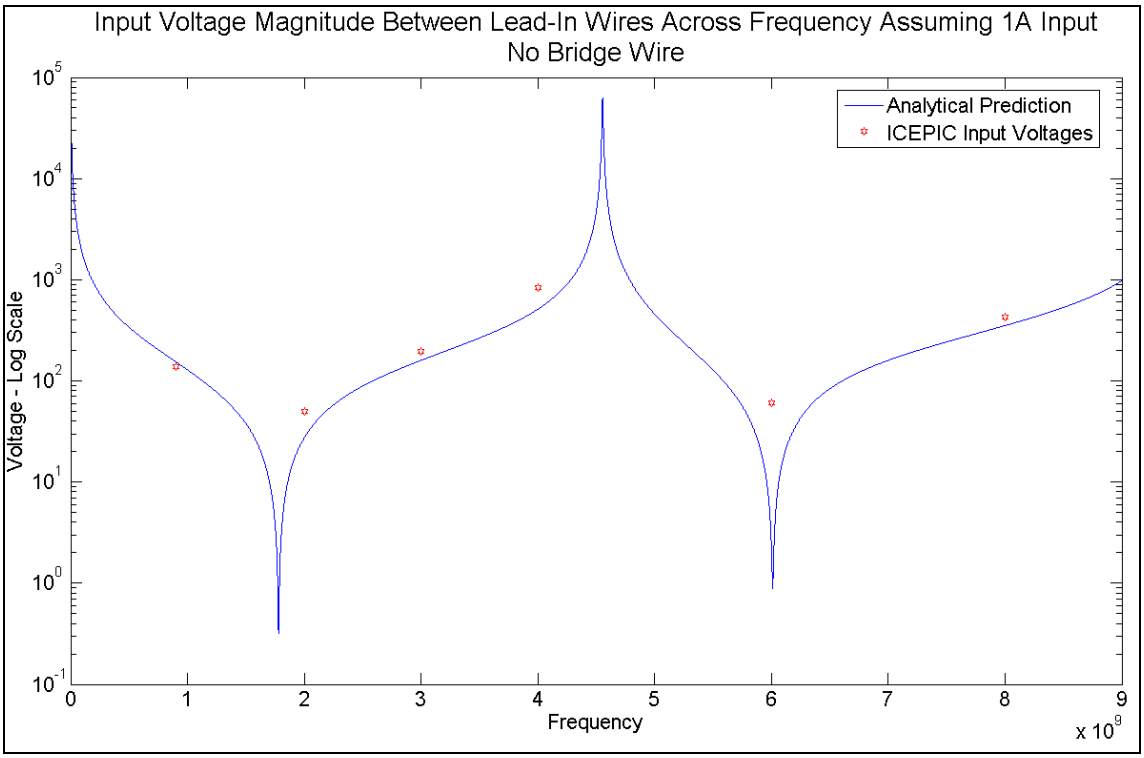

Figure 3: MatLAB analytical prediction and ICEPIC comparison plot of the differential mode detonator input voltage magnitude with no bridge wire across the frequency range DC-9 GHz plotted on a log scale.

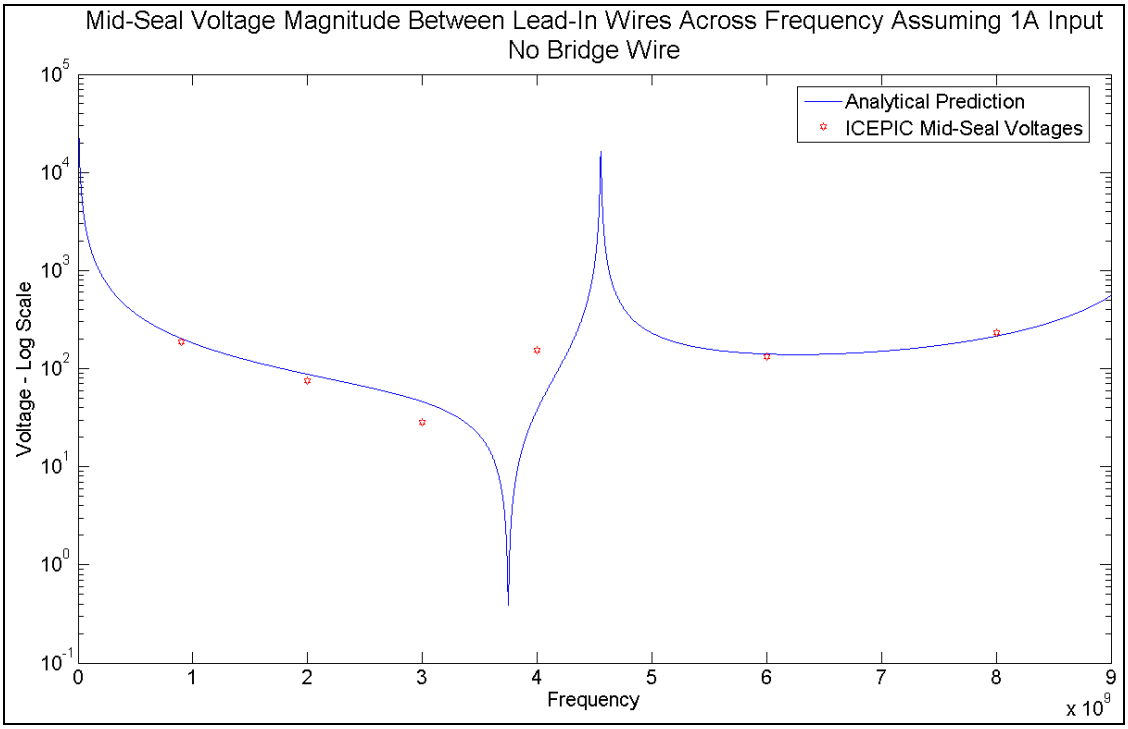

Figure 4: MatLAB analytical prediction and ICEPIC comparison plot of the differential mode detonator mid-seal voltage magnitude with no bridge wire across the frequency range DC-9 GHz plotted on a log scale.

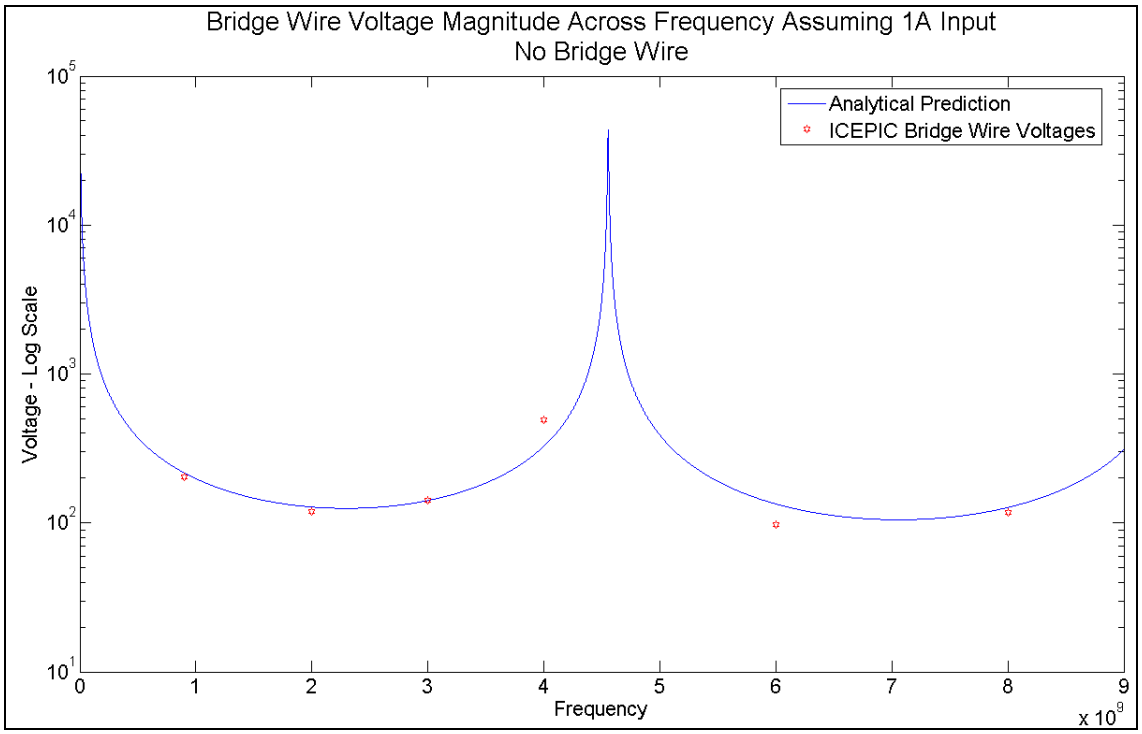

Figure 5: MatLAB analytical prediction and ICEPIC comparison plot of the differential mode detonator bridge wire voltage magnitude with no bridge wire across the frequency range DC-9 GHz plotted on a log scale.

Figure 2 indicates good agreement (5.68%) between the ICEPIC and predicted resonant frequency. Figures 3 through 5 indicate good agreement overall between the ICEPIC and predicted voltages along the detonator, with the exception of the 6 GHz input voltage which indicates a very large discrepancy. However, the percent agreements are not as important as trends seen in the data. First, the data sets now both agree on one resonant frequency, and ICEPIC does not find a higher order resonance that the analytical model does not predict. Second, and due to the first observation, the values at 8 GHz are now in very good agreement for all three diagnostics. Lastly, the bridge wire voltages are now in very close agreement as well. All three of these observations are significant improvements over the standard detonator geometry with the bridge wire included. From these observations, two conclusions can be drawn. First, predictions made by using only the 1-D transmission line model of the detonator can be compared to 3-D simulation

results with a much smaller amount of discrepancy than results obtained when terminating the transmission line in a load impedance and bridge wire. Second, the bridge wire's 90^0 bend connection with the lead-in wire in the ICEPIC model along with the additional EM field interactions which are simulated but not analytically modeled account for a large portion of the discrepancies between the bridge wire voltages in Chapter 5. However, the detonator has a bridge wire and will always have a bridge wire until the device detonates, and so must be included in the model. This investigation has found that the analytical model of the bridge wire requires some modification to take into account the differences seen between the ICEPIC simulation and analytical prediction of the bridge wire voltage.

Modifying the Bridge Wire Inductance

The first step in the investigation for improving the analytical model of the bridge wire is predicated on a simple Ohm's Law [23] analysis of the problem. Figure 44 from Chapter 5 indicates that, at every frequency simulated, the predicted bridge wire voltage is significantly higher than that found using ICEPIC. Since the analytically predicted current through the bridge wire agrees very well with the value found using ICEPIC, the problems with the voltage indicate that the impedance of the bridge wire is significantly different in both models. Specifically, the impedance of the bridge wire in the analytical model is much higher than that of the ICEPIC bridge wire. One other observation is that since the diameter and conductivity of the ICEPIC bridge wire were deliberately chosen to yield a specific resistance, it is unlikely that the real part of the impedance is the problem. Also, from Figure 8 in Chapter 3, the real part of the analytical bridge wire resistance only varies by a factor of approximately 2.4 across the entire frequency range

of DC-9 GHz. This is not enough variation to account for the bridge wire voltage discrepancies, which again indicates that the real part of the impedance is not contributing much to the large error between the two model results. What this means is that the imaginary part of the bridge wire impedance in the analytical model is significantly higher than what is simulated. More specifically, the calculated bridge wire inductance of the analytical model is higher than the amount of inductance present in the wire when simulated.

Recall from Chapter 3 that the inductance calculated for the bridge wire is based on an isolated wire having dimensions equal to that of the bridge wire (26). It now seems that this assumption is incorrect and that due to both the bridge wire's connection to the lead-in wires and its EM field interactions within the detonator geometry, the inductance of the bridge wire is actually much less. To quantify this reduction is extremely difficult, so simply adding a correction factor to account for the environmental differences is not a viable option. Instead, since the transmission line model by itself was appropriately verified in the previous investigation, several values of bridge wire inductance were inputted into the analytical model. These inductances were all significantly less than that of an isolated wire (0.882 nH a for 150 μm diameter bridge wire). Each small change in inductance resulted in a different bridge wire voltage plot, and the agreement between the predicted and ICEPIC bridge wire voltages was examined for each case. At the conclusion of the investigation, an extremely small inductance of 5 pH was chosen for the inductance of the bridge wire. This value of inductance represented a breaking point in the bridge wire voltage predictions compared to ICEPIC simulation, where a lower inductance value did not improve the agreement significantly but a slightly higher value

caused a fairly large increase in the percent difference between the two results. Figure 6 is the ICEPIC and analytical model comparison plot of the differential mode bridge wire voltage across frequency for the standard detonator model with a 5 pH bridge wire. In order to discern differences between the ICEPIC and predicted values, the data in Figure 6 is re-plotted on a log scale in Figure 7.

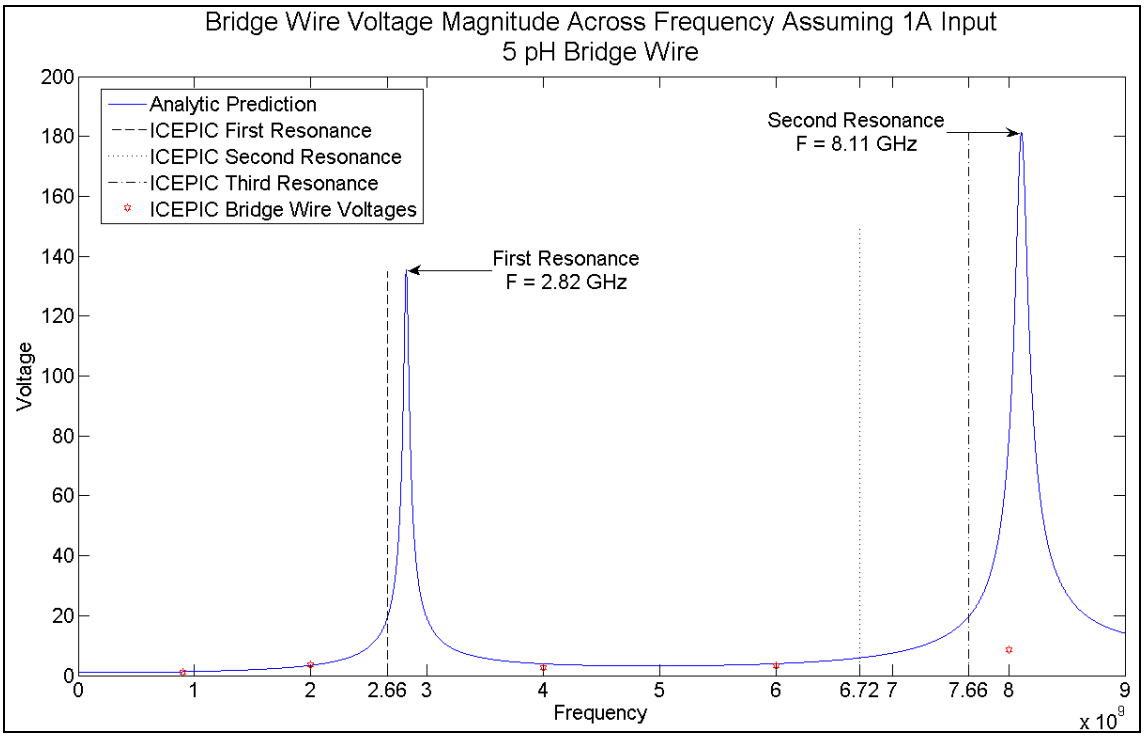

Figure 6: MatLAB analytical prediction and ICEPIC comparison plot of the differential mode detonator bridge wire voltage magnitude with a 5 pH bridge wire across the frequency range DC-9 GHz.

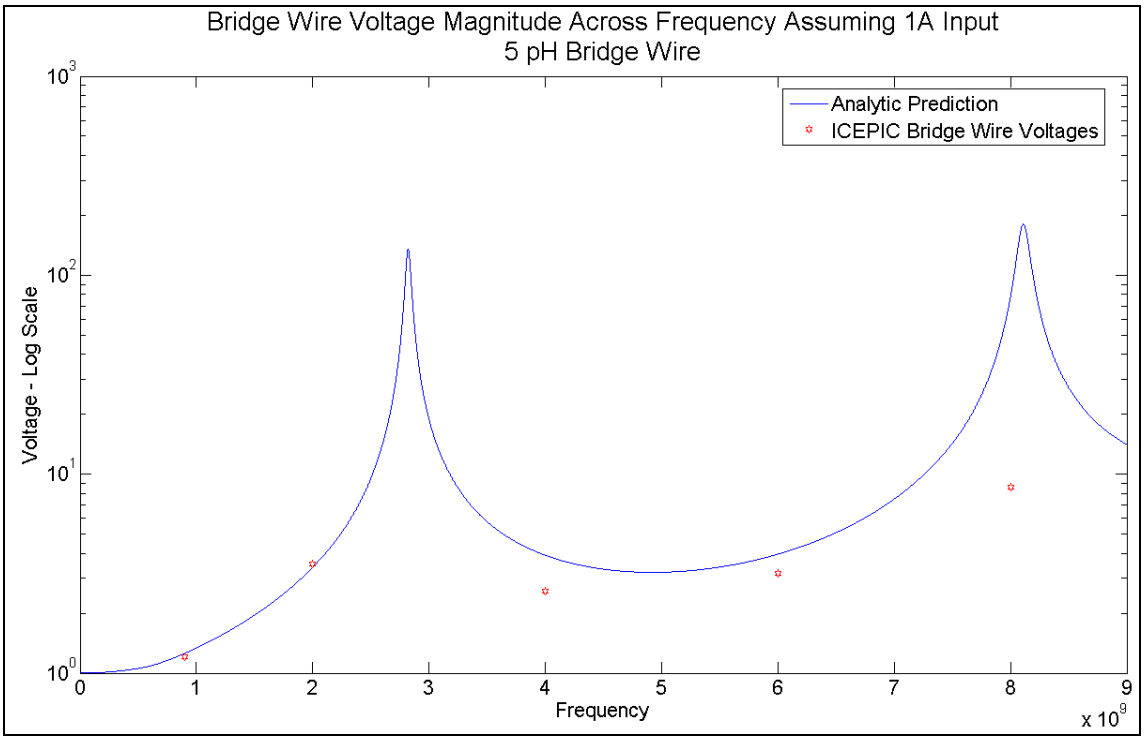

Figure 7: MatLAB analytical prediction and ICEPIC comparison plot of the differential mode detonator bridge wire voltage magnitude with a 5 pH bridge wire across the frequency range DC-9 GHz plotted on a log scale.

Figure 6 indicates a shift in both of the predicted resonant frequencies with the altered bridge wire inductance, as compared to Figure 35 in Chapter 4. Despite this shift, the resonances are still in good agreement with a difference of 6.02% for the first resonance and 5.87% for the second. The change in bridge wire inductance did not facilitate the inclusion of a third resonance, as was found using ICEPIC, so that particular discrepancy remains. However, the agreement between the predicted and ICEPIC simulated values of bridge wire voltage have significantly improved, with the exception of the 8 GHz point whose ICEPIC value is now significantly lower than that predicted due to the analytical resonance shift to 8.11 GHz. Using the isolated wire inductance, the average percent difference between the two sets of values, excluding the 8 GHz value, was 1274% as reported in Chapter 5 and whose corresponding comparison plot can be seen in Figure 44 of Chapter 5. Using the significantly reduced bridge wire inductance,

and again excluding the 8 GHz value, the average percent difference is now 21.30 %. This represents an improvement by a factor of 60.

While the significant improvement in the bridge wire voltage indicated that the modified inductance in the analytical model was more accurately representative of the simulated inductance of the wire, this change did have an affect on the other voltages and current in the system. Figures 8 and 9 are the log scale comparison plots of the input and mid-seal voltages, respectively, while Figure 10 is the log scale comparison plot of the bridge wire current. Standard scale plots indicating predicted resonances for these three diagnostics are not shown since they are similar in appearance to Figure 5.

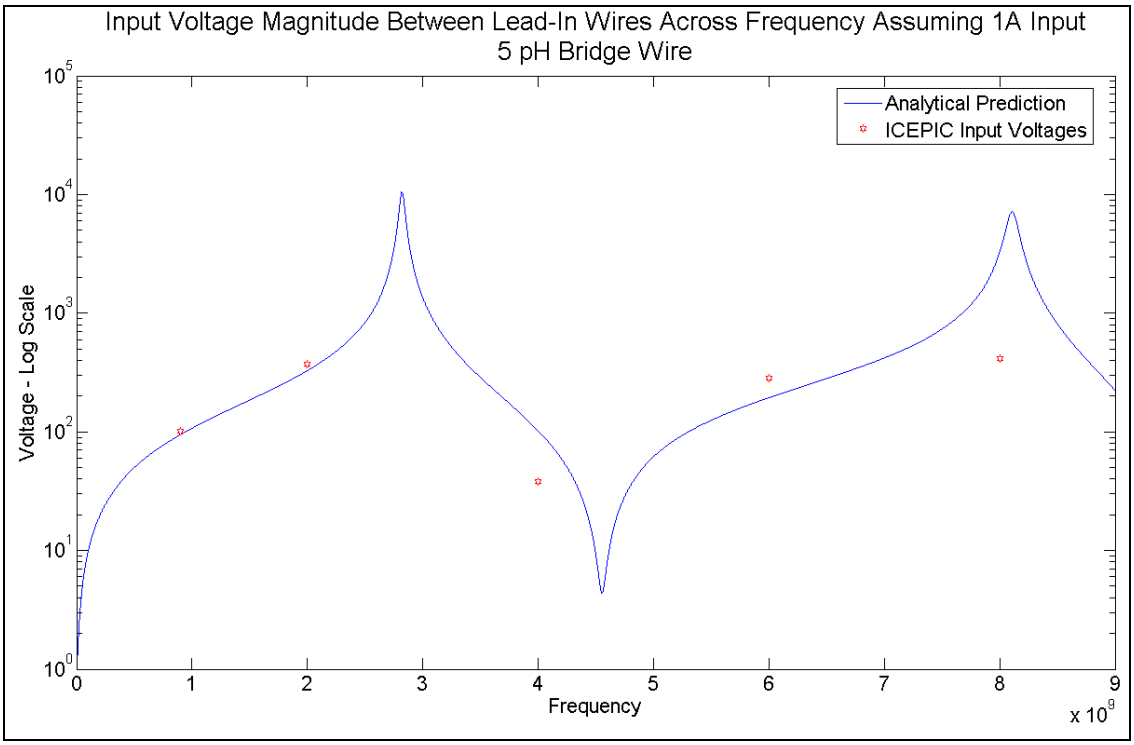

Figure 8: MatLAB analytical prediction and ICEPIC comparison plot of the differential mode detonator input voltage magnitude with a 5 pH bridge wire across the frequency range DC-9 GHz plotted on a log scale.

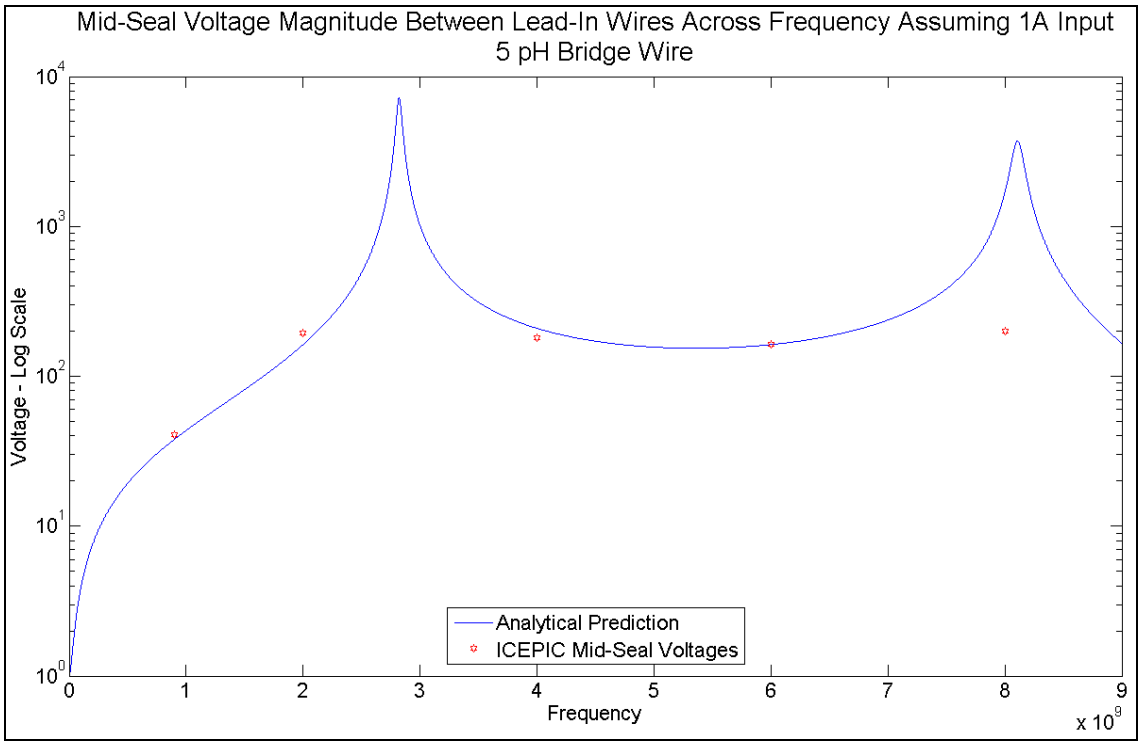

Figure 9: MatLAB analytical prediction and ICEPIC comparison plot of the differential mode detonator mid-seal voltage magnitude with a 5 pH bridge wire across the frequency range DC-9 GHz plotted on a log scale.

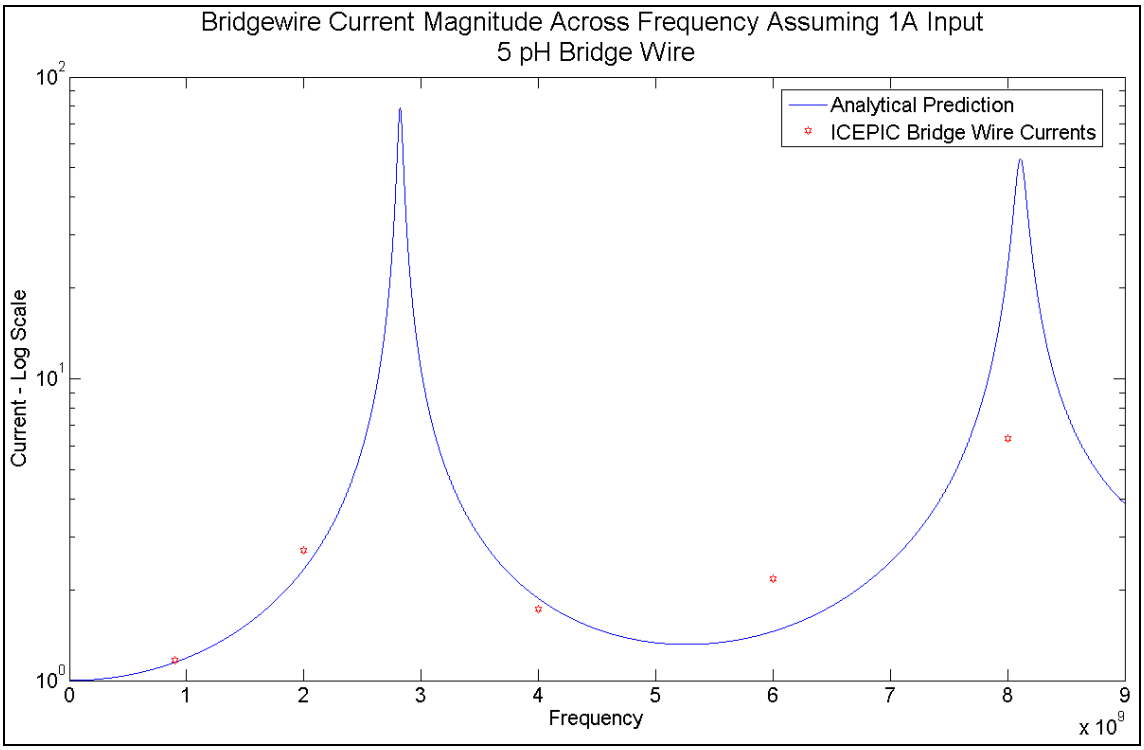

Figure 10: MatLAB analytical prediction and ICEPIC comparison plot of the differential mode detonator bridge wire current magnitude with a 5 pH bridge wire across the frequency range DC-9 GHz plotted on a log scale.

A general observation from Figures 8 through 10 (when compared to Figures 40, 42, and 46 from Chapter 5) is that the predicted and simulated voltages and current have diverged somewhat from the agreement seen using the higher isolated wire inductance for the bridge wire. Excluding the 8 GHz values, the average percent difference for the input voltages is 55.46%, up from 5.79%. The average percent difference for the mid-seal voltage was less affected by the bridge wire inductance change and is calculated at 10.08 %, up from 7.83%. The average percent difference for the bridge wire currents is 14.35 %, up from 4.15%.

While the increase in discrepancy of both the mid-seal voltage and bridge wire current is within an acceptable range, the 55.46% difference for the input voltage is not. Not only is this a significant increase but the input voltage is the most important of all four diagnostics. Recall from Chapter 4 that the input voltage is calculated directly using the input impedance of the detonator. It is this impedance that a radiating RF/MW source will encounter when coupling EM energy into the detonator. Due to the importance of the input voltage, the analytical model must again be modified.

Including an Additonal Inductance Section in the Analytical Model

It is reasonable to assume that since the initial input voltage agreement using the large bridge wire inductance value was favorable, and the removal of much of this inductance caused nearly a factor of 10 increase in the percent difference between the two data sets, the detonator being simulated in ICEPIC has additional inductance that is not being included in analytical model. The most likely source of this additional inductance is the 90^0 bend in the connection between the bridge wire and the lead-in wires. As was shown in Figure 4 in Chapter 5, this bend causes a large amount of radiated $\vec{E}$ field from

each connection point. The additional associated magnetic flux created by this bend gives rise to an inductance at the end of the detonator transmission line. This high concentration of magnetic flux at each end of the bridge wire can also help explain the large reduction in the self-inductance of the bridge wire along its axis.

In order to include the additional inductance, the analytical model must be modified to take into account an additional section. The new differential mode detonator model is illustrated in Figure 11. This set-up includes an additional section connected in series at the end of the detonator transmission line and before the bridge wire load termination. This added section is simply an inductance, not another section of twinaxial transmission line, and represents the additional inductance seen between the end of the transmission line and the load due to the magnetic flux caused by the 90^0 bend connection between the bridge wire and the lead-in wires.

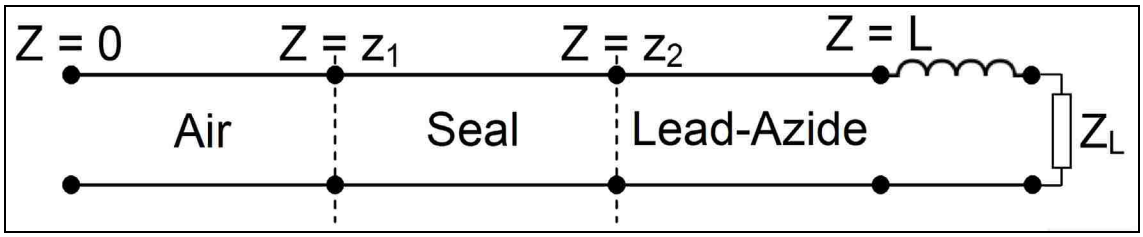

Figure 11: Illustration of dividing the detonator into sections including an additional inductance.

To implement this additonal inductance in the MatLAB analytical model requires two modifications. First, the additional inductance must be included in the determination of the detonator input impedance. Second, the calculation of the bridge wire voltage must be modified to include this additional section.

Referring back to Chapter 3, the input impedance is found through the matrix multiplication of three cascaded transmission line sections with a load termination (107), followed by the division of the resulting voltage by the resulting current (108):

$$\begin{bmatrix} V(0) \\ I(0) \end{bmatrix} = \left[\prod_{z_1}^{0} e^{\Gamma_a dz'} \right] \cdot \left[\prod_{z_2}^{z_1} e^{\Gamma_s dz'} \right] \cdot \left[\prod_{L}^{z_2} e^{\Gamma_l dz'} \right] \cdot \begin{bmatrix} Z_L \\ 1 \end{bmatrix} I(L) \text{, and} \tag{107}$$

$$Z_{in} = \frac{V(0)}{I(0)} . \tag{108}$$

To add the additional inductance section, its representative telegrapher's equations [17] must be solved to find its corresponding 2x2 matrix to be included in the cascaded transmission line multiplication. This will be done in the same manner as was used to determine the matrix representation of the three transmission line sections in Chapter 3. First, the telegrapher's equations are set up as

$$\frac{d}{dz} \begin{bmatrix} V(z) \\ I(z) \end{bmatrix} = -\begin{bmatrix} 0 & j\omega L \\ 0 & 0 \end{bmatrix} \cdot \begin{bmatrix} V(z) \\ I(z) \end{bmatrix} . \tag{109}$$

The primary difference between this calculation and the ones performed in Chapter 3 is that this is just an inductance, not an inductance per-unit length. As such, its solution using the product integral method [21] will not utilize a definite integral. To remain consistent with the calculations performed in Chapter 3, the telegrapher's equation matrix (110) will be multiplied by -1. The reason for this is that the matrix for each transmission line section in Chapter 3 was multiplied by a negative number due to the nature of the limits of integration. This resulted in a positive matrix in the exponent for the solution of the telegrapher's equations. For consistency, the additional inductance matrix will also be positive. This is equivalent to choosing a per-unit length inductance L' along with corresponding integration limits whose resulting negative difference multiplied by L'

yield the actual inductance L, along with a telegrapher's equation matrix with positive values:

$$\Gamma = -\begin{bmatrix} 0 & j\omega L \\ 0 & 0 \end{bmatrix} \cdot (-1) \text{ , and} \tag{110}$$

$$\begin{bmatrix} V(z) \\ I(z) \end{bmatrix} = \left[\prod e^{\Gamma dz'} \right] \cdot \begin{bmatrix} V(z) \\ I(z) \end{bmatrix} \tag{111}$$

$$= \left[e^{\int \Gamma dz'} \right] \cdot \begin{bmatrix} V(z) \\ I(z) \end{bmatrix} \tag{112}$$

$$= [M_I] \cdot \begin{bmatrix} V(z) \\ I(z) \end{bmatrix} . \tag{113}$$

Once the value of $[M_I]$ is determined it can be multiplied in series with the other three sections of the detonator transmission line, and the input impedance to the detonator can be found using (114) and (108).

$$\begin{bmatrix} V(0) \\ I(0) \end{bmatrix} = [M_a] \cdot [M_s] \cdot [M_l] \cdot [M_I] \cdot \begin{bmatrix} Z_L \\ 1 \end{bmatrix} I(L) . \tag{114}$$

This procedure was implemented in the MatLAB analytical model program, where L can be any specified value. This new method finds the detonator input impedance, which is in turn used as described in Chapter 4 to find the input and mid-seal voltages as well as the bridge wire current.

The calculation of the bridge wire voltage will also make use of the new detonator input impedance calculation described above. Referring to Chapter 4, the bridge wire voltage calculation uses not only the detonator input impedance, but also a modified lead-

azide section due to the placement of the bridge wire EDL 50 μm from the end of the transmission line. To facilitate this new calculation, the additional inductance section will pre-multiply the transmission matrix for the truncated lead-azide section given in Chapter 4 (95). Recall that due to the method for calculating the voltage along the detonator, Chapter 4 described how the limits of integration were reversed for the transmission line sections, and that this was equivalent to inverting the original matrix found in Chapter 3. This new bridge wire voltage calculation is similar since the additional inductance section is now pre-multiplying the transmission matrix (as opposed to being post-multiplied in (114)), the matrix for the additional inductance must also be inverted. The transmission matrix is referred to as $U[(z_3,0)]$ in Chapter 4 and Figure 21 in Chapter 4 illustrates how this matrix is defined relative to the bridge wire voltage diagnostic. The transmission matrix for the new detonator model including the additional inductance can be found as:

$$\left[U(z_3,0)\right]=\left[M_I\right]^{-1}\cdot\left[M_{l-trunc}\right]\cdot\left[M_{s-rev}\right]\cdot\left[M_{a-rev}\right]. \quad (115)$$

The remainder of the bridge wire voltage calculation is the same as described in Chapter 4.

Since this additional inductance is not easily quantifiable, the modified MatLAB program was used with several values of L for the additional section. Each value of L resulted in different input and bridge wire voltage plots. The agreement between each of these plots and the ICEPIC values was evaluated. At the conclusion of the investigation, a value of 0.7 nH was chosen for the inductance of the additional section. This value of inductance represented a point where a lower value would improve the bridge wire voltage agreement and detriment the input voltage agreement, while a higher value would

cause the opposite effect. Figure 12 is the ICEPIC and analytical model comparison plot of the differential mode input voltage across frequency for the standard detonator model with a 5 pH bridge wire and a 0.7 nH additional inductance section. In order to discern differences between the ICEPIC and predicted values, the data in Figure 12 is re-plotted on a log scale in Figure 13. Also, Figures 14 and 15 are log scale comparison plots of the mid-seal and bridge wire voltages, respectively, while Figure 16 is a log scale comparison plot of the bridge wire current. Standard scale plots indicating predicted resonances for these three diagnostics are not shown since they are similar in appearance to Figure 12.

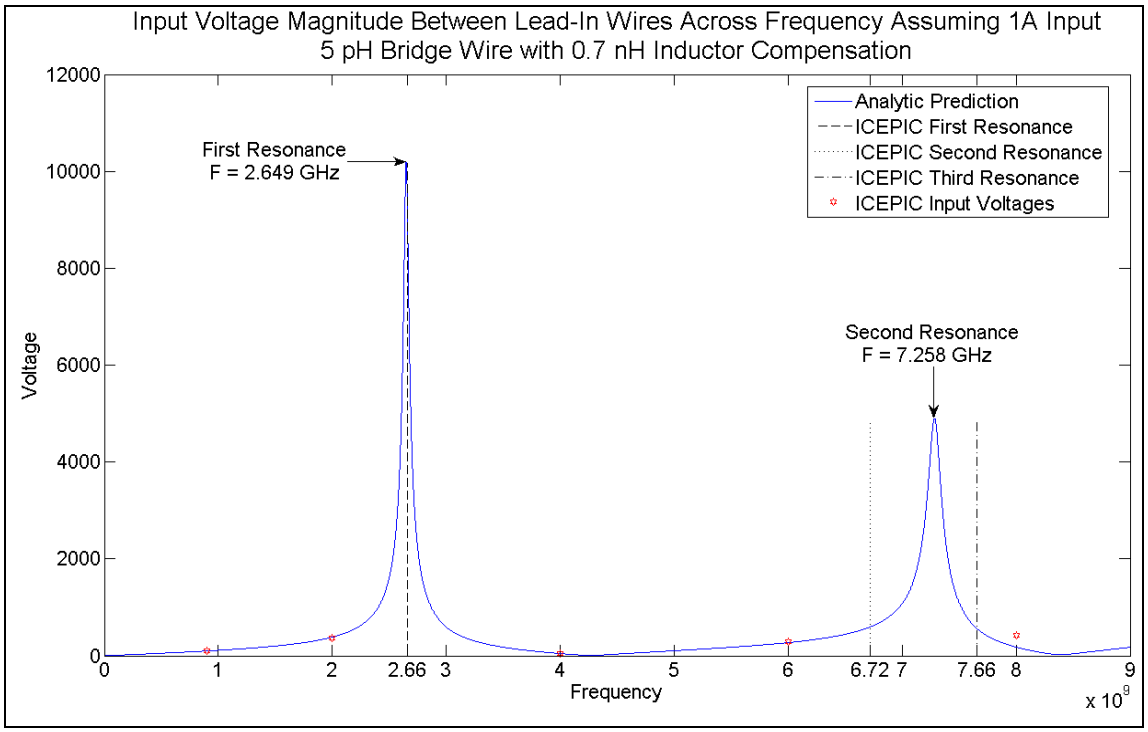

Figure 12: MatLAB analytical prediction and ICEPIC comparison plot of the differential mode detonator input voltage magnitude with a 5 pH bridge wire and 0.7 nH additional inductance section across the frequency range DC-9 GHz.

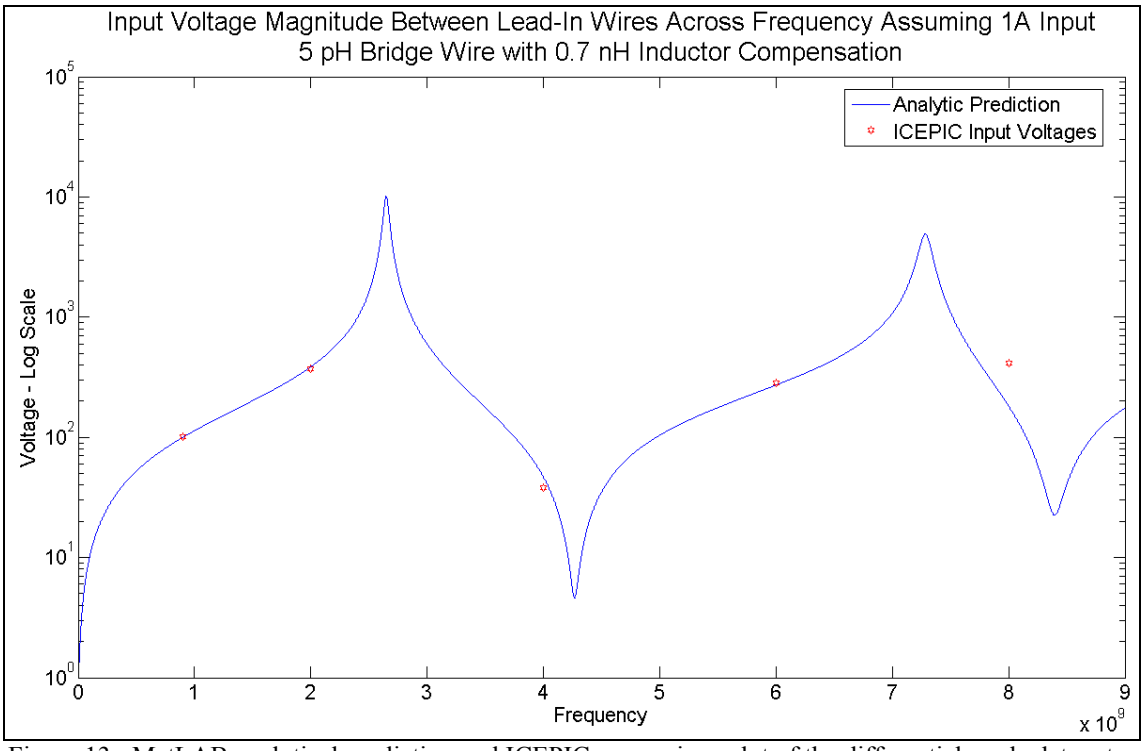

Figure 13: MatLAB analytical prediction and ICEPIC comparison plot of the differential mode detonator input voltage magnitude with a 5 pH bridge wire and 0.7 nH additional inductance section across the frequency range DC-9 GHz plotted on a log scale.

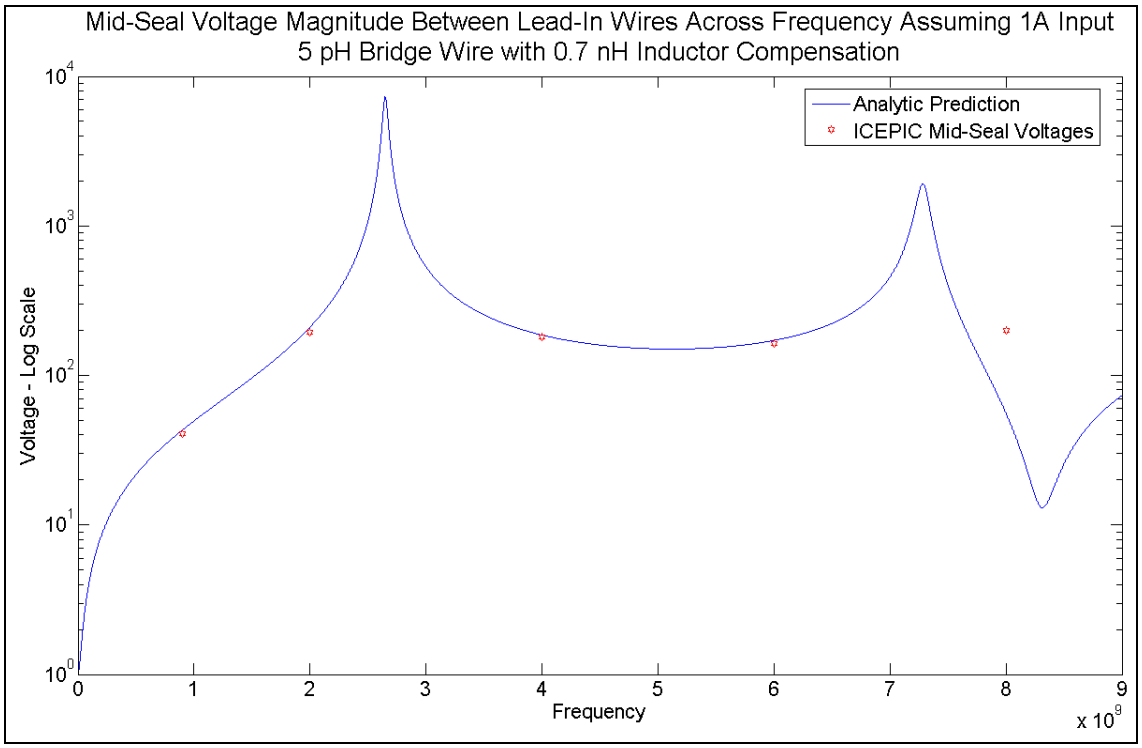

Figure 14: MatLAB analytical prediction and ICEPIC comparison plot of the differential mode detonator mid-seal voltage magnitude with a 5 pH bridge wire and 0.7 nH additional inductance section across the frequency range DC-9 GHz plotted on a log scale.

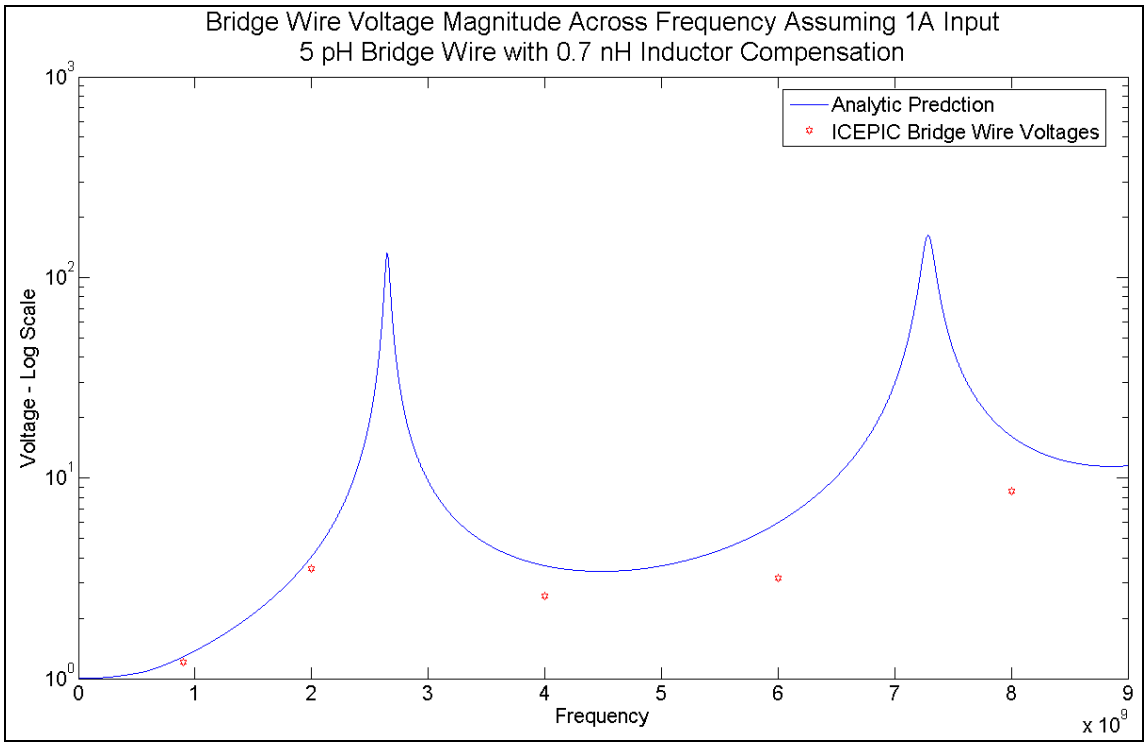

Figure 15: MatLAB analytical prediction and ICEPIC comparison plot of the differential mode detonator bridge wire voltage magnitude with a 5 pH bridge wire and 0.7 nH additional inductance section across the frequency range DC-9 GHz plotted on a log scale.

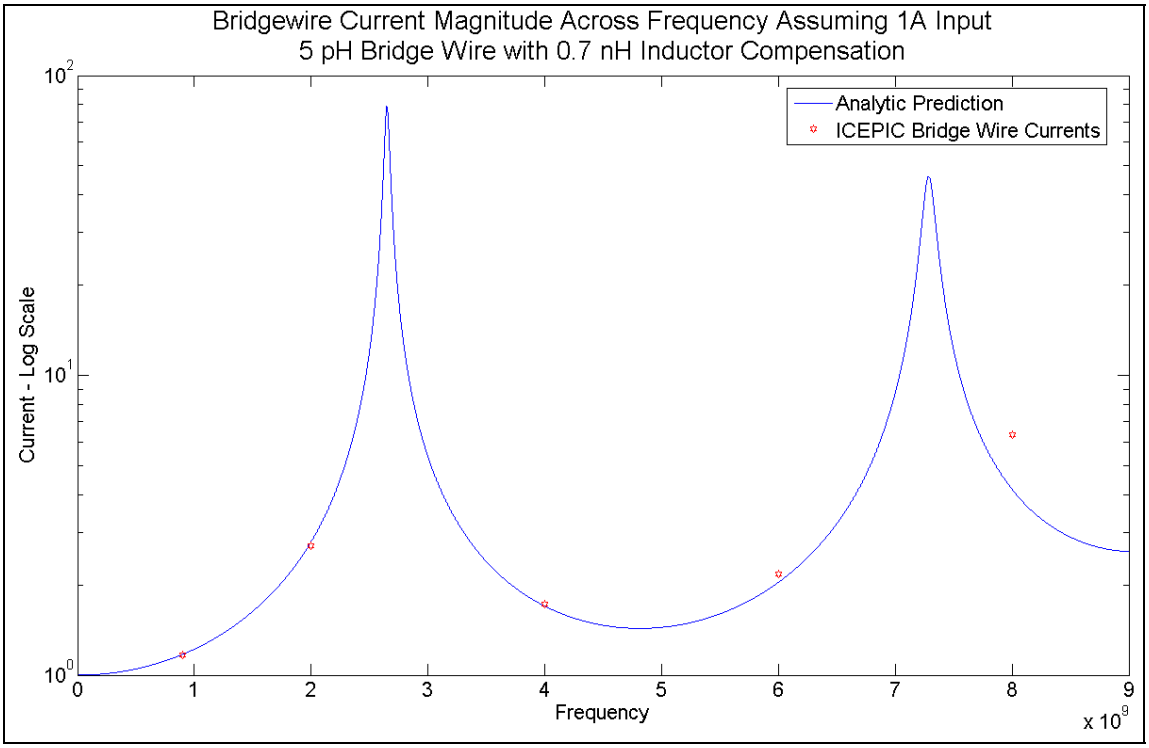

Figure 16: MatLAB analytical prediction and ICEPIC comparison plot of the differential mode detonator bridge wire current magnitude with a 5 pH bridge wire and 0.7 nH additional inductance section across the frequency range DC-9 GHz plotted on a log scale.

Figure 12 indicates a slight shift in both of the predicted resonant frequencies. This frequency shift is in the opposite direction of that seen with the reduced bridge wire inductance alone, and brings the resonances back in the vicinity of where they were before the model modification, as compared to Figure 35 in Chapter 4. Both resonances are in very good agreement with a difference of 0.41% for the first resonance and 5.24% for the second. The combination of the reduced bridge wire inductance along with the additional inductance section did not facilitate the inclusion of a third resonance, as was found using ICEPIC, so that discrepancy remains. However, the agreement between the predicted and ICEPIC simulated values of input voltage have improved. The agreement, excluding the 8 GHz value, has been reduced to 7.8%. If the 8 GHz value is included, with a difference of 129%, is the average percent difference increases to 32.04%. Excluding the 8 GHz values, the mid-seal voltages are to within 5.30% and the bridge wire currents to within 2.64%. Also, the bridge wire voltages are to within 37.89%, which is an increase from the 21.30% calculated without the additional inductance section. While an average agreement of 37.89% is higher than the other three diagnostics, it is still a significant improvement over the 1274% seen when no modifications to the model are made. Table 5 is a summary of the average percent differences for all four diagnostics excluding the 8 GHz values during each of the three model variations: standard model, standard model with 5 pH bridge wire, and standard model with 5 pH bridge wire and 0.7 nH additional inductance section. Table 6 is a summary of average percent differences for all four diagnostics including the 8 GHz values during each of the three model variations, and Table 7 is a summary of percent differences for both resonances during each of the three model variations.

Table 5: Average percent differences for all four diagnostics of the standard detonator for three model variations not including 8 GHz values.

Detonator Property	Standard Model	5 pH Bridge Wire	5 pH Bridge Wire and 0.7 nH Inductance
Input Voltage	5.79	55.46	7.80
Mid-Seal Voltage	7.83	10.08	5.30
Bridge Wire Voltage	1274	21.30	37.89
Bridge Wire Current	4.15	14.35	2.64

Table 6: Average percent differences for all four diagnostics of the standard detonator for three model variations including 8 GHz values.

Detonator Property	Standard Model	5 pH Bridge Wire	5 pH Bridge Wire and 0.7 nH Inductance
Input Voltage	115.61	180.69	32.04
Mid-Seal Voltage	265.84	154.47	56.26
Bridge Wire Voltage	1349.44	177.46	48.06
Bridge Wire Current	22.43	64.89	8.89

Table 7: Percent differences for both resonances of standard detonator for three model variations.

Detonator Property	Standard Model	5 pH Bridge Wire	5 pH Bridge Wire and 0.7 nH Inductance
First Resonance	1.95	6.02	0.41
Second Resonance	5.54	5.87	5.24

Tables 5 through 7 indicate the progression of the average percent differences between ICEPIC simulated values and predicted values for all four diagnostics. As the model transitions from the initial formulation through one utilizing two improvements, the average percent differences decrease in every case with the exception of the input voltage excluding the 8 GHz value which increases from 5.79% to 7.80%. Beyond this minor exception, every other detonator property shows better agreement between the ICEPIC and predicted values as the model becomes more refined. In some cases, this improvement is minor, like a reduction from 5.54% to 5.24% for the second resonance. In other cases, the improvement is significant, as with the bridge voltages with a reduction from 1274% to 37.89%. Taken as a whole, these two modifications of the initial analytical model have made it more representative of the detonator undergoing differential mode excitation in the frequency range of DC-9 GHz by incorporating a more

complicated inductance model at the connection point between the lead-in wires and bridge wire than was initially assumed.

Determining a Cause for the Third ICEPIC Resonance

While the analytical model modifications improved the bridge wire voltages, and to a lesser extent the agreement between the ICEPIC and predicted values at 8 GHz, the third resonant frequency found using ICEPIC was still not present in the prediction. One important conclusion after the investigation of the detonator geometry without a bridge wire was that there was only one resonance found using both methods. This indicates that the bridge wire termination is the likely cause of the additional resonant frequency problem. However, in the previous investigation, the bridge wire was meticulously re-modeled and optimized with no effect on this additional resonance.

The goal of this next investigation was to determine what additional detonator properties are not being taken into account that could possibly be affected by the fringing EM fields at the lead-in wire connection to the bridge wire. When examining the analytic and ICEPIC models, there is a difference between what each of them are modeling. The analytical model takes into account the detonator transmission line and the connection to the bridge wire load. Physically then, the analytical model terminates at the end of the bridge wire. In ICEPIC, however, the entire lead-azide section is being simulated physically. It was discovered in Chapter 4 that extending the detonator geometry past the lead-azide section had a minimal effect on the results, but that is where the detonator geometry optimization stopped. Referring to Figure 30 in Chapter 5, it can be noted the E_x field distribution does extend past the bridge wire. This extra section of the detonator coupled with the fringing EM fields at the ends of the bridge wire which are included in

the simulations but are not included in the analytical model could be the potential cause of the additional resonant frequency seen in ICEPIC. This added section of the detonator will be called the "extra sheath," referring to the outer aluminum case of the detonator

To ascertain the effect of the extra sheath on ICEPIC simulations, the standard detonator geometry was modified to remove the extra sheath and terminate at the bridge wire. With this modification to the geometry, the boundary condition for the bridge wire end of the detonator was re-evaluated. Because of the radiating $\vec{E}$ fields from the bridge wire, it is possible that truncating the new geometry in a PEC could allow reflection of these fields back into the detonator. To prevent this, the bridge wire end of the geometry required a PML boundary. Since the PML box encompassing the excitation source was already present, it was more practical to extend this box to enclose the entire detonator then to add a second box for the bridge wire end of the detonator. To remain consistent, the end of the PML box was extended 4 mm past the end of the detonator geometry, and an illustration of this simulation space set-up is shown in Figure 17. A picture of the ICEPIC-rendered differential mode standard geometry without the extra sheath is shown in Figure 18. Figure 19 is a 3-D picture indicating how this geometry will be enclosed in a PML box. For comparison, this geometry will also be simulated using a PEC boundary near the bridge wire to determine if these two different boundary conditions produce dissimilar results. Figure 20 is a 3-D picture indicating how this geometry will be truncated with a PEC boundary, and Figure 21 is an illustration of the PEC simulation space set-up.

Other than the geometry and boundary condition changes described, no other simulation or excitation parameters were changed from what has been thoroughly

described in Chapter 4. These two geometries were both simulated at 6 GHz. Since this geometry is not physically plausible, a complete frequency scan is not necessary. Also, 6 GHz was chosen since this frequency is sufficiently high enough to excite the higher order resonances previously observed at 6.72 and 7.66 GHz. The results from these simulations were analyzed as described in Chapter 5 using DFTs. The input voltage waveform for the PML geometry is shown in Figure 22, and its corresponding DFT is shown in Figure 23. Figure 24 is a zoomed in view of the first resonance of the DFT plot, while Figure 25 is a zoomed in view of the higher order resonance. The waveforms and DFTs for the PML simulation mid-seal and bridge wire voltages as well as the bridge wire current are well represented by Figures 22 through 25, and will not be shown. Similarly, Figures 22 through 25 are also well representative of the PEC waveforms and DFTs, though amplitudes and magnitudes are slightly different. The results from these analyses are listed in Tables 8 and 9. Figure 26 is a comparison chart of the PEC and PML ICEPIC results from Table 8.

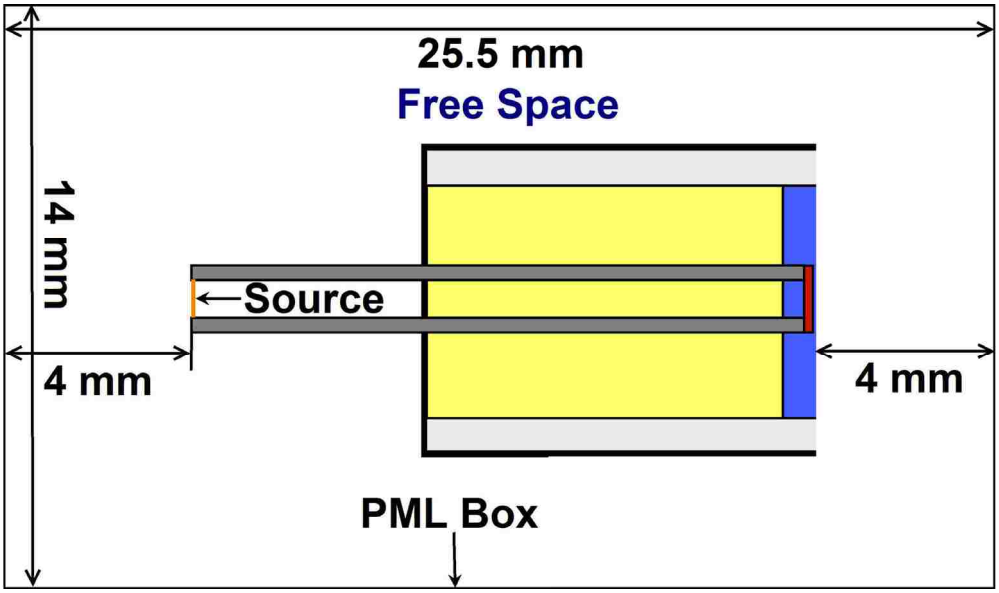

Figure 17: Illustration of the top view for the differential mode simulation space set-up for the standard detonator geometry with the extra sheath removed indicating the free space region along with the placement and dimensions of the PML box encompassing the detonator.

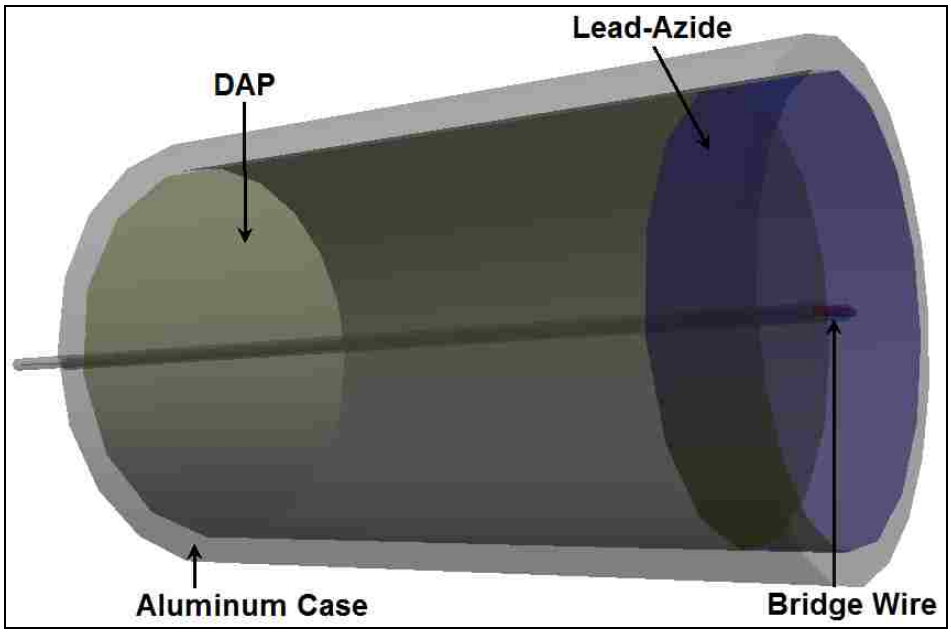

Figure 18: Perspective view of the ICEPIC rendering of the standard detonator geometry with the extra sheath removed for differential mode excitation indicating detonator components.

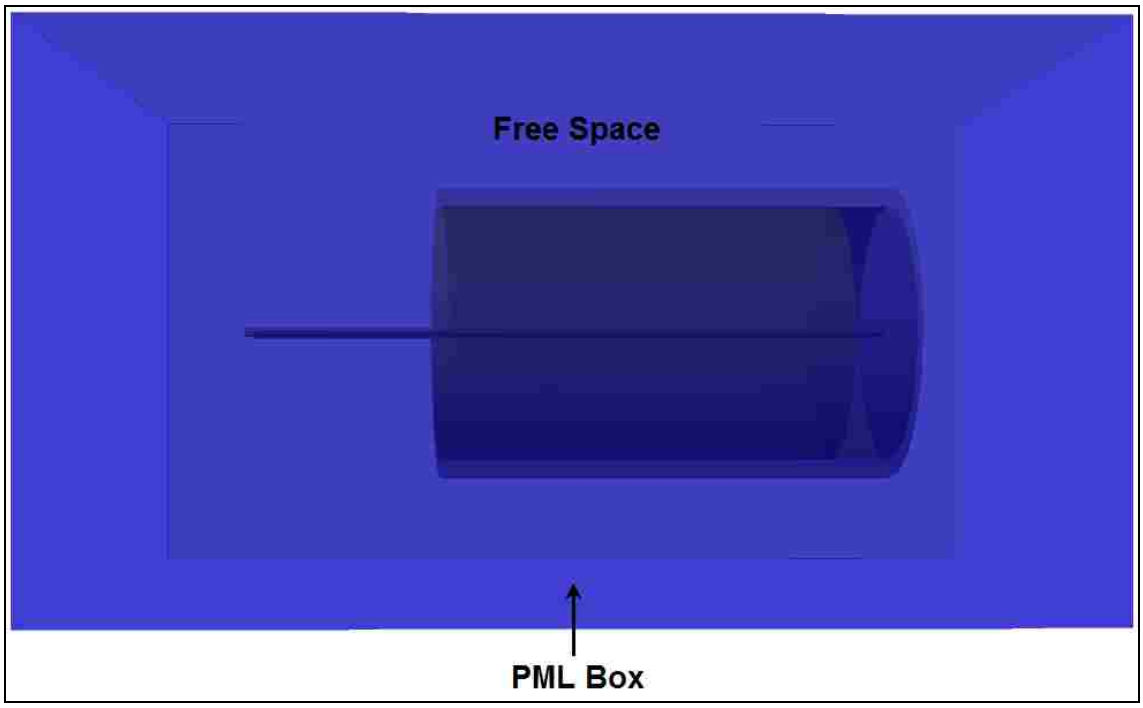

Figure 19: Illustration of the 3-D ICEPIC rendering of the differential mode PML simulation space from a side-view of the standard detonator geometry with the extra sheath removed.

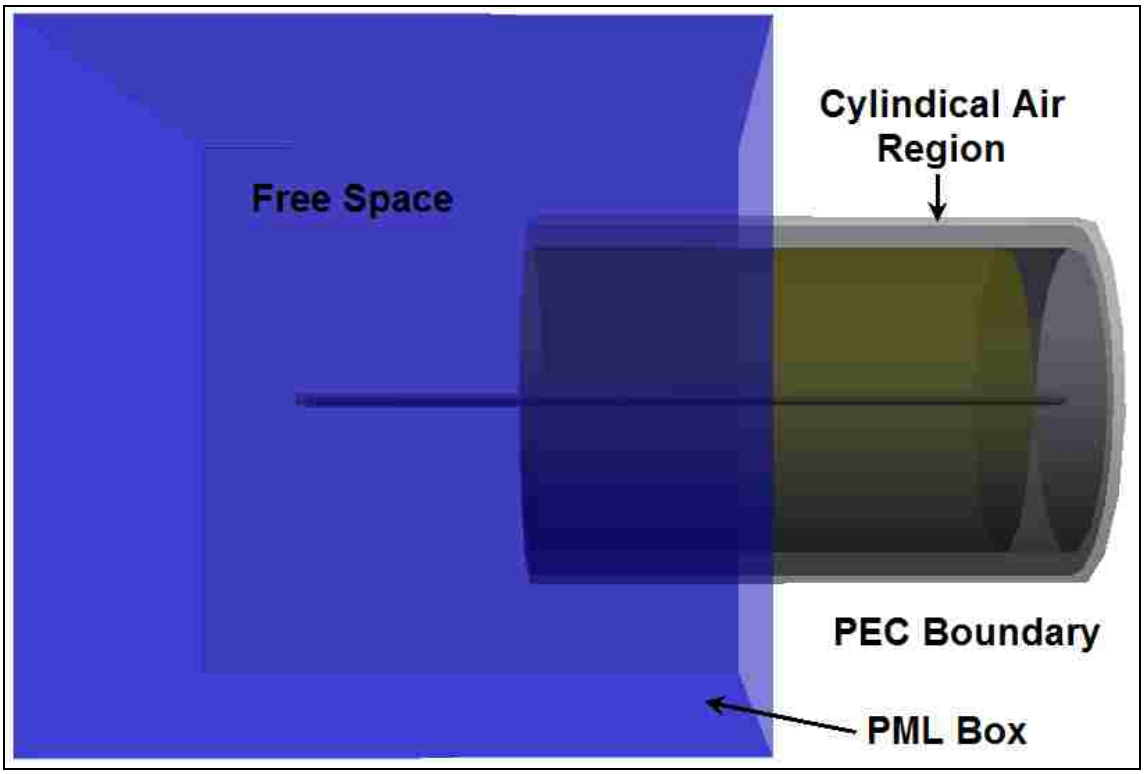

Figure 20: Illustration of the 3-D ICEPIC rendering of the differential mode PEC simulation space from a side-view of the standard detonator geometry with the extra sheath removed.

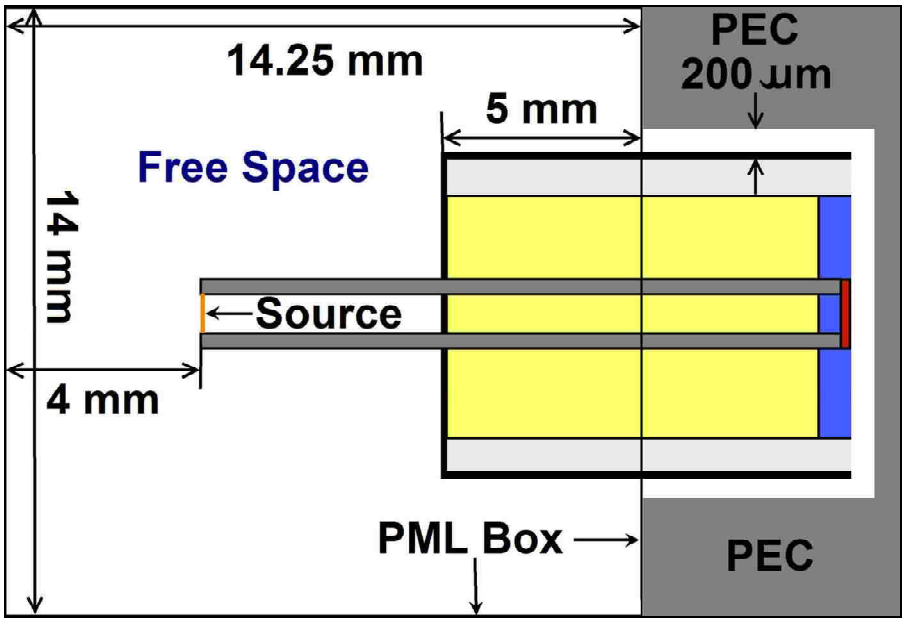

Figure 21: Illustration of the top view for the differential mode simulation space set-up for the standard detonator geometry with the extra sheath removed indicating regions of PEC and free space, along with the placement and dimensions of the PML box encompassing the excitation source.

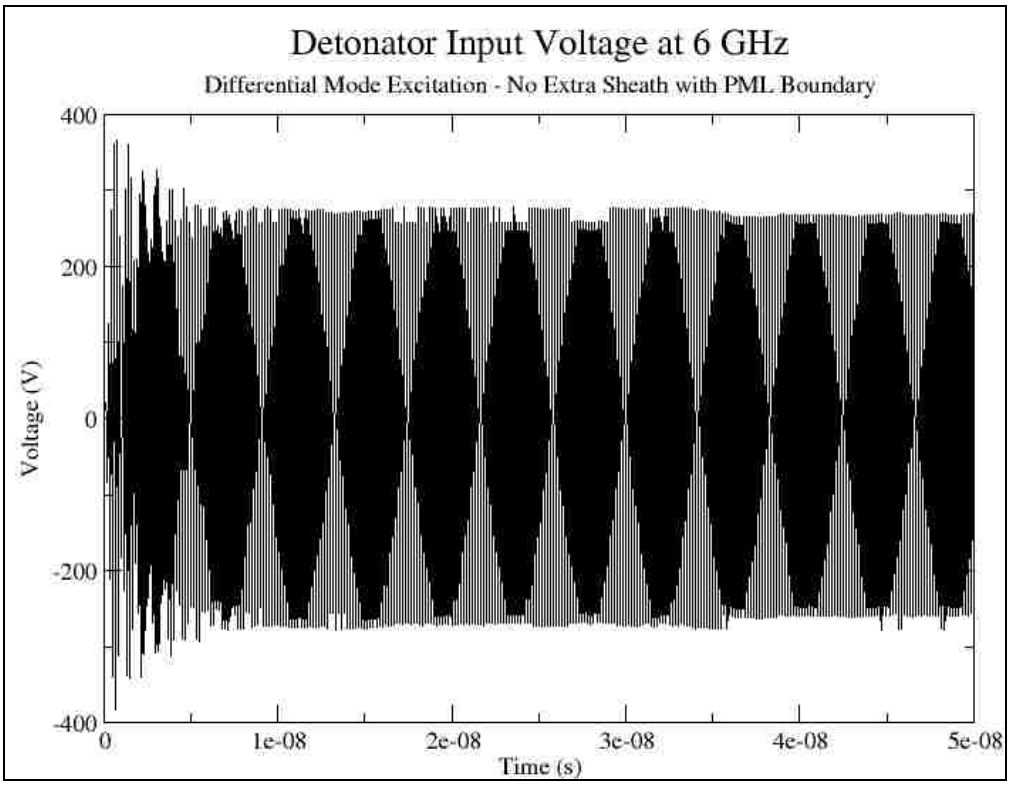

Figure 22: Standard detonator input voltage with 6 GHz differential mode excitation and the extra sheath removed while utilizing the PML boundary.

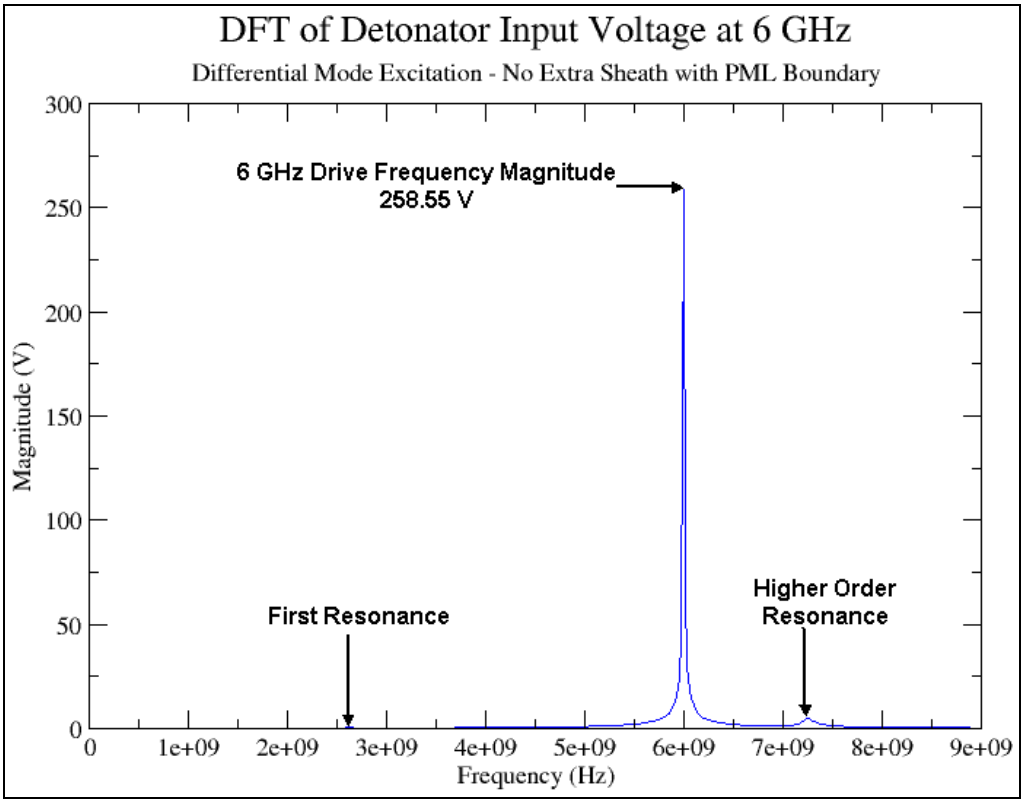

Figure 23: DFT of standard detonator input voltage with 6 GHz differential mode excitation and the extra sheath removed while utilizing the PML boundary.

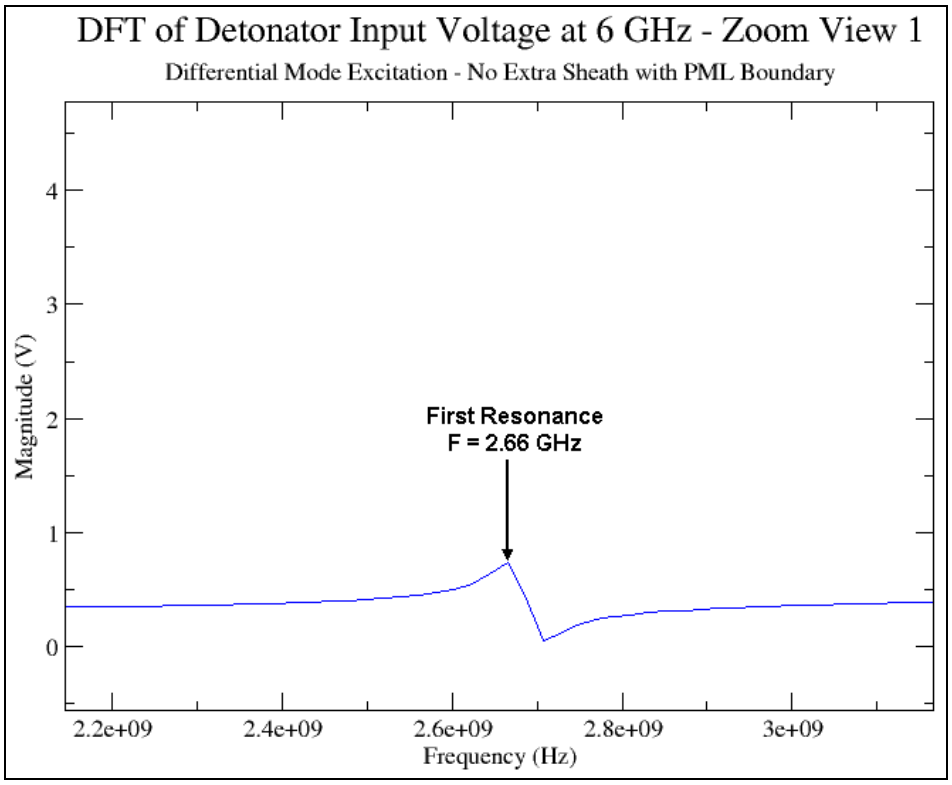

Figure 24: First resonance zoom view of DFT of standard detonator input voltage with 6 GHz differential mode excitation and the extra sheath removed while utilizing the PML boundary.

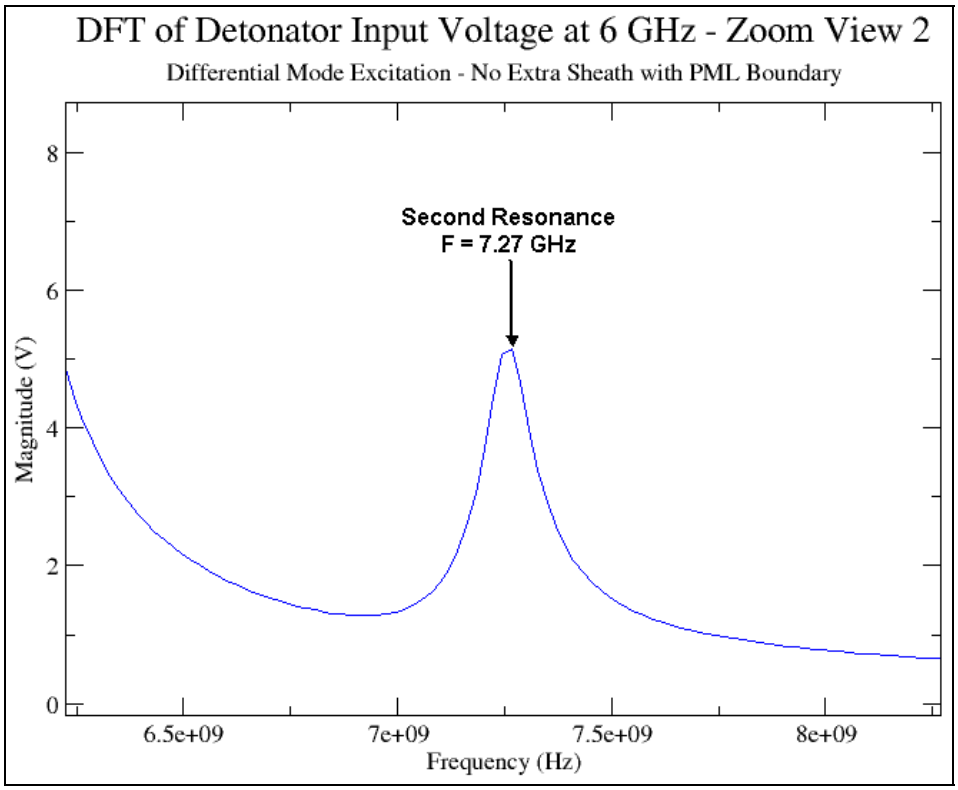

Figure 25: Second resonance zoom view of DFT of standard detonator input voltage with 6 GHz differential mode excitation and the extra sheath removed while utilizing the PML boundary.

Table 8: Voltage and current magnitude values for standard detonator geometry with no extra sheath and 6 GHz differential mode excitation using both PML and PEC boundary conditions.

Boundary Condition	Input Voltage	Mid-Seal Voltage	Bridge Wire Voltage	Bridge Wire Current
PEC	249.61	159.07	2.53	1.77
PML	258.55	162.28	4.86	1.93

Table 9: Resonance values for standard detonator geometry with no extra sheath and 6 GHz differential mode excitation using both PML and PEC boundary conditions.

Boundary Condition	First Resonance	Second Resonance	Third Resonance
PEC	2.66	7.52	N/A
PML	2.66	7.27	N/A

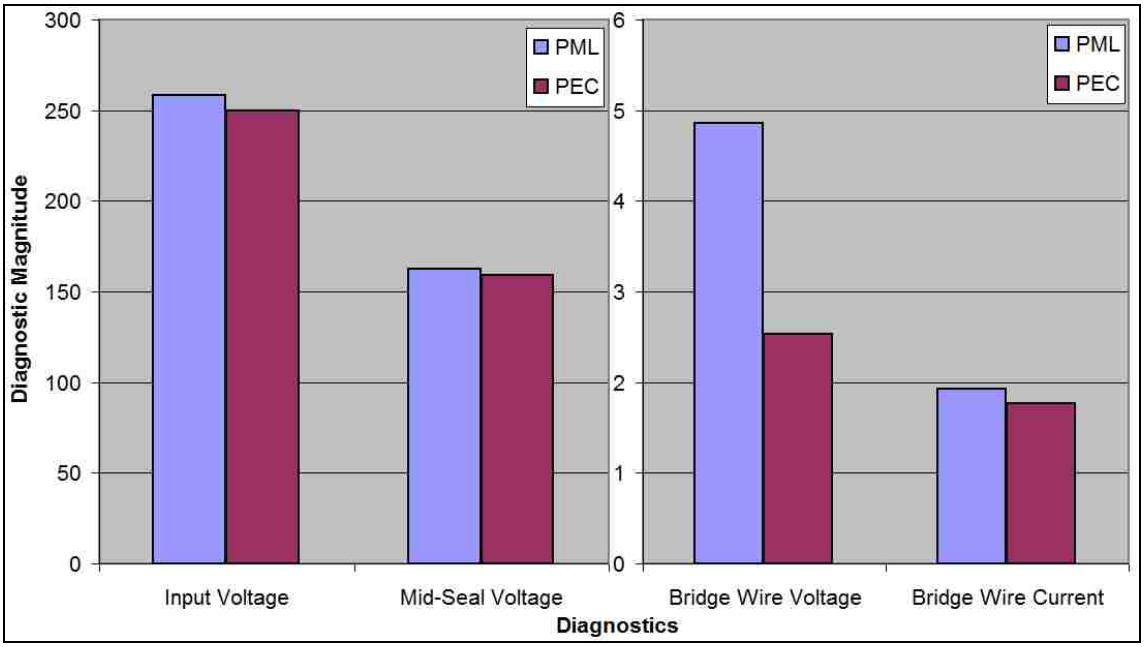

Figure 26: Comparison chart of the PML and PEC ICEPIC diagnostic magnitudes for 6 GHz differential mode excitation of the standard detonator geometry with the extra sheath removed.

Figures 23 through 25 indicate that while the first resonance is unchanged at 2.66 GHz, the second resonance has shifted from 6.72 GHz to 7.52 GHz for the PEC simulation and to 7.27 GHz for the PML simulation. Also, the third resonance has shifted beyond 9 GHz, and past the frequency range of interest. In comparison to the second resonant frequency predicted using the analytical model (7.258 GHz) the PEC second resonance is within 3.48% the PML second resonance is within 0.16%. This is an improvement over the ICEPIC model that included the extra sheath. Not only is the

agreement between the second resonant frequency of both models improved, but the ICEPIC model with the extra sheath removed does not yield a third resonant frequency. This result is important because it indicates that the additional sheath along with the bridge wire's fringing EM fields cause a shift in the higher order resonant frequencies and that this shift brings about the discrepancy with the analytical model. Figure 26 and Table 8 indicate that the ICEPIC values found using the PEC and PML boundary conditions are very similar, though the PML values are consistently higher. The bridge wire voltage has the largest variance, and this is explained by the proximity of the EDL to the end of the detonator geometry and the two different boundary conditions. The voltage and current values in Table 8 do not agree as well with those predicted using the analytical model as do the ICEPIC values found using the standard detonator model shown in Table 9 of Chapter 5. The conclusion is that while this investigation was useful for determining the reason for the discrepancy in the resonances, the detonator model with the extra sheath removed is not a viable representation for the prediction of detonator EM properties.

Although this investigation has revealed that the additional sheath beyond the bridge wire is the reason for the discrepancy between the ICEPIC and predicted resonant frequencies, it has not yet been determined how to implement a modification in the analytical model to take this additional section into account. This modification, whatever it may be, need only change the resonant behavior of the prediction plots while leaving the magnitudes of the predicted values largely intact. Since the additional section extends beyond the bridge wire termination of the detonator transmission line, adding a section or

modification to the transmission line model is not a feasible option. This modeling challenge will be discussed further in Chapter 8.

Investigations into Improving the Common Mode Model

The comparison of results using ICEPIC simulation of the standard detonator geometry and analytical model prediction for common mode excitation showed very poor agreement overall for all three voltage diagnostics with the exception of only a few data points. In addition, ICEPIC determined a second resonant frequency at 8.75 GHz while the analytical model did not. Several investigations were launched into determining the reasons for these discrepancies in an effort to improve the agreement between the two models.

Determining a Cause for the Second ICEPIC Resonance

The goal of the first investigation was to determine what additional detonator properties are not being taken into account that could possibly cause an additional higher order resonance in EM simulation but not in the analytical prediction. As was described in the analogous differential mode investigation, there is a difference between what is represented by the analytic and ICEPIC models. The analytical model takes into account the detonator transmission line up until the bridge wire, where the common mode model ends in an open. In the standard ICEPIC detonator geometry the entire lead-azide section is included in the simulation. As was seen with differential mode excitation, this extra section of the detonator could be the potential cause of the additional resonant frequency seen in ICEPIC for common mode excitation. This added section of the detonator will

continue being referred to as the “extra sheath,” which is the outer aluminum case of the detonator

To ascertain the effect of the extra sheath on the ICEPIC simulation for common mode excitation, the standard detonator geometry was modified to remove the extra sheath and terminate at the bridge wire. This modification to the geometry was previously described for the analogous differential mode investigation, along with a concern about truncating the detonator geometry in a PEC boundary. For the differential mode investigation both PEC and PML boundaries were evaluated to ascertain whether the two different boundary conditions produced different results. When the results for each of these two simulations were evaluated it was discovered that each boundary condition produced comparable results (Figure 26). Since the PML simulation and its detonator-encompassing free space box requires a significantly larger amount of computational resources, only the PEC boundary condition will be pursued for the common mode investigation. A picture of the ICEPIC-rendered common mode standard geometry without the extra sheath is shown in Figure 27. Figure 28 is a 3-D picture indicating how this geometry will be truncated with a PEC boundary with a PML box encompassing the excitation source, and Figure 29 is an illustration of the simulation space set-up.

Other than the geometry change described, no other simulation or excitation parameters were changed from what has been thoroughly described in Chapter 4. Due to the large discrepancy between the standard detonator ICEPIC results and predicted values, this modified geometry with the extra sheath removed was simulated at all frequencies used previously. This was done to get an indication of not only the extra

sheath's effect on the ICEPIC resonance values, but also to determine whether voltages found by ICEPIC for this modified geometry are in better agreement with analytically predicted values. The results from these simulations were analyzed as described in Chapter 5 using curve-fitting and DFTs. The input voltage waveform for a 6 GHz common mode input is shown in Figure 30, and its corresponding DFT is shown in Figure 31. Figure 32 is a zoomed in view of the DFT plot indicating the absence of a higher order resonance. The waveforms and DFTs for the mid-seal and bridge wire voltages are well represented by Figures 30 through 32, and will not be shown. The results from these analyses are summarized in Tables 10 and 11.

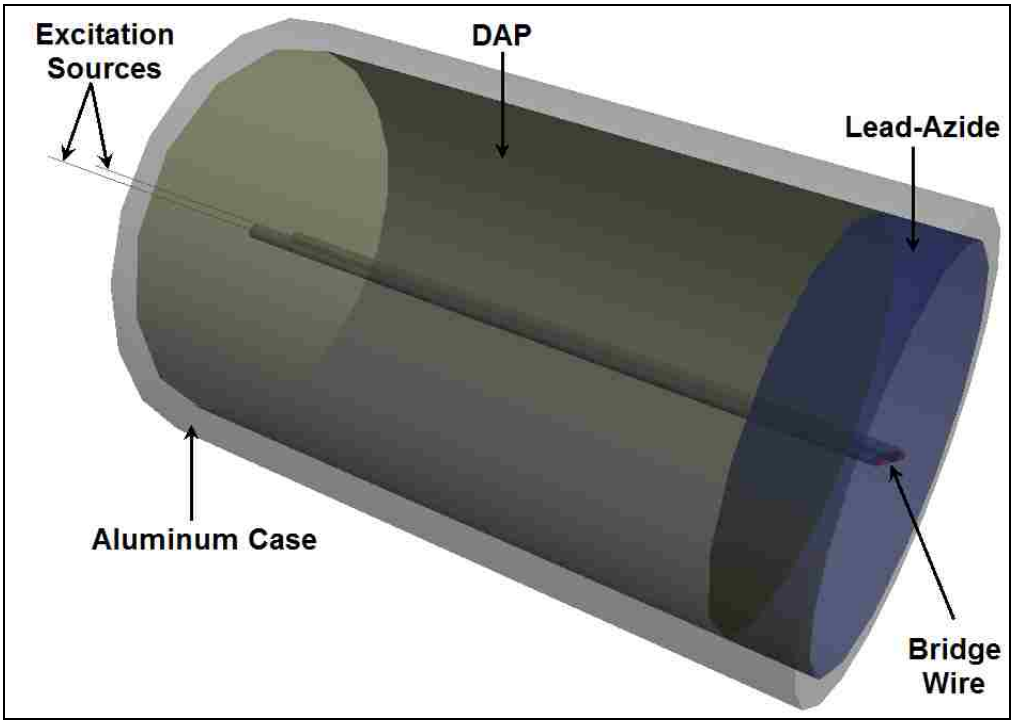

Figure 27: Perspective view of the ICEPIC rendering of the standard detonator geometry with the extra sheath removed for common mode excitation indicating detonator components.

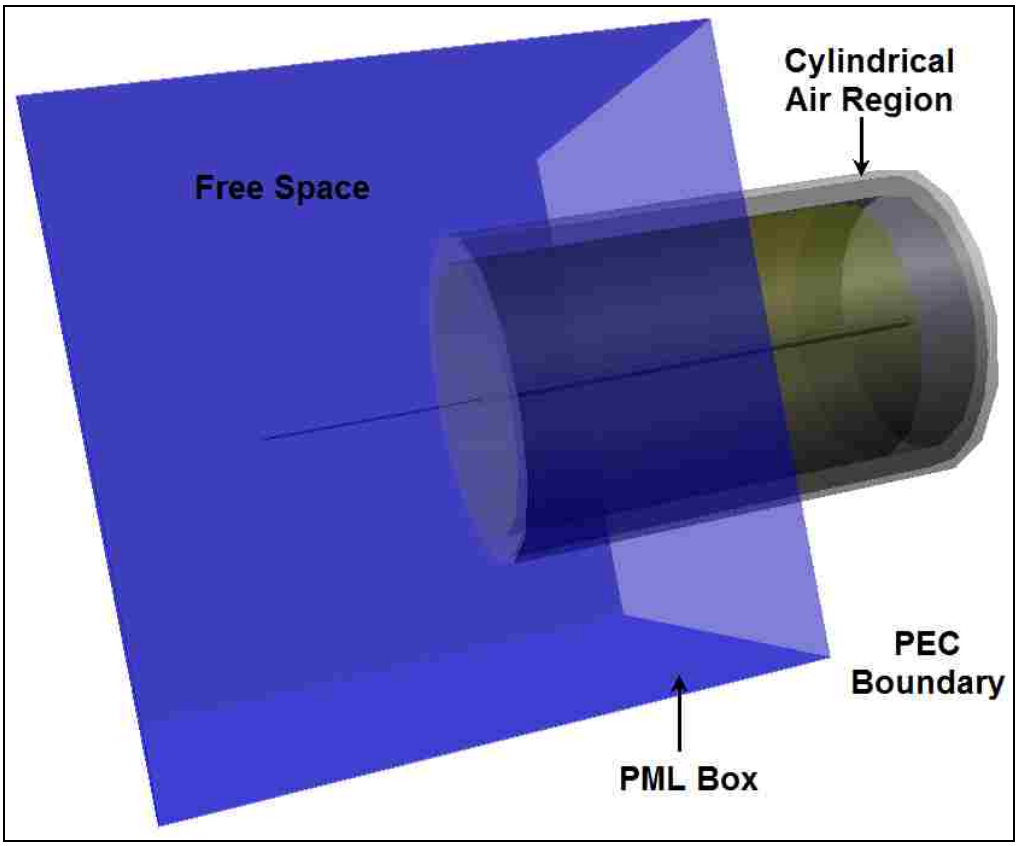

Figure 28: Illustration of the 3-D ICEPIC rendering of the common mode PEC simulation space for the standard detonator geometry with the extra sheath removed.

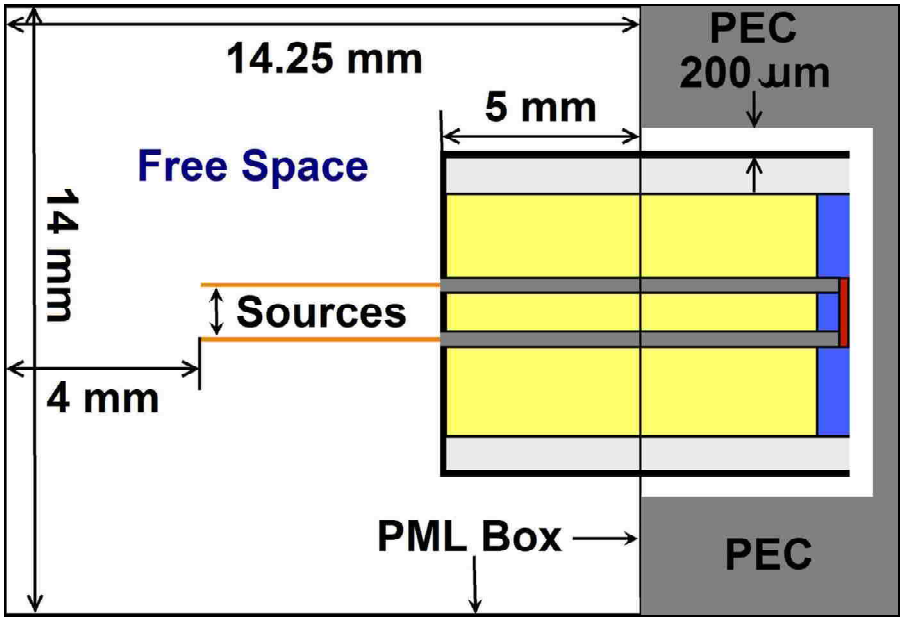

Figure 29: Illustration of the top view for the common mode simulation space set-up for the standard detonator geometry with the extra sheath removed indicating regions of PEC and free space, along with the placement and dimensions of the PML box encompassing the excitation sources.

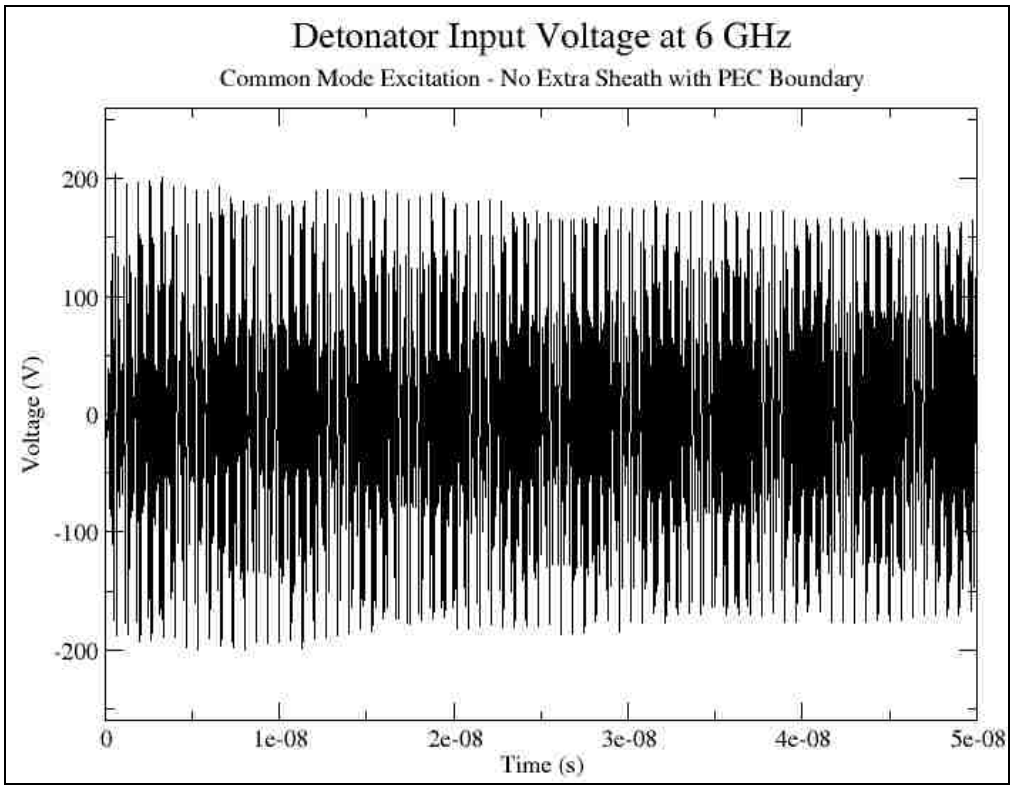

Figure 30: Standard detonator input voltage with 6 GHz common mode excitation and the extra sheath removed while utilizing the PEC boundary.

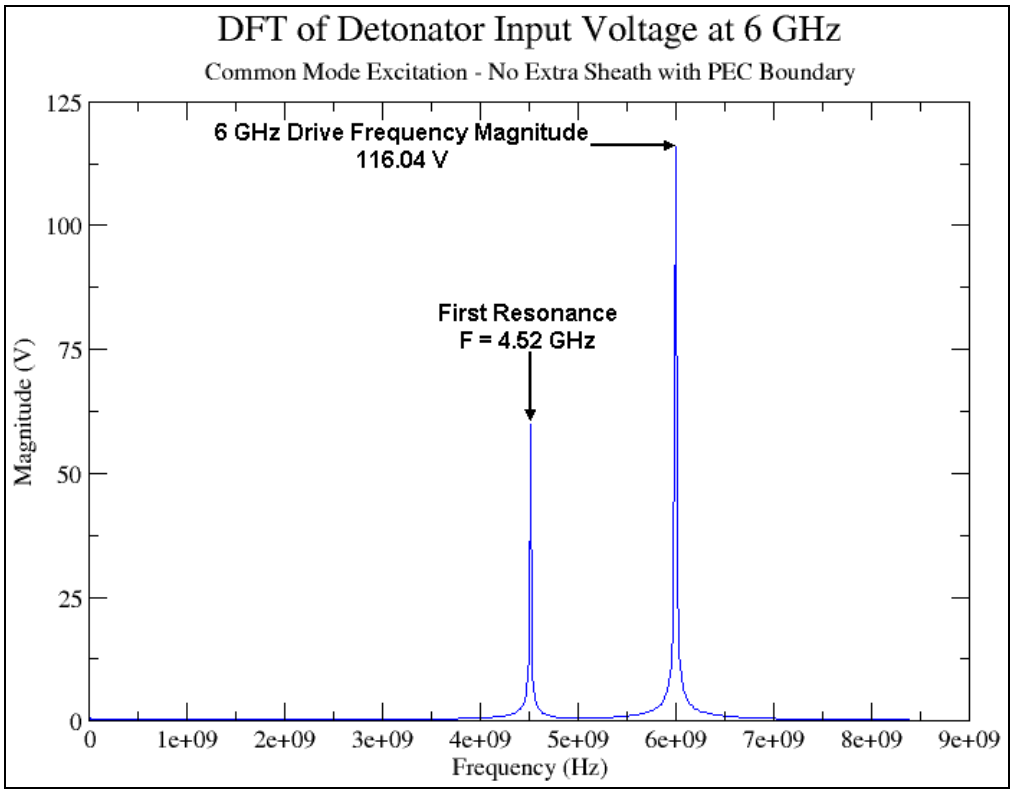

Figure 31: DFT of standard detonator input voltage with 6 GHz common mode excitation and the extra sheath removed while utilizing the PEC boundary.

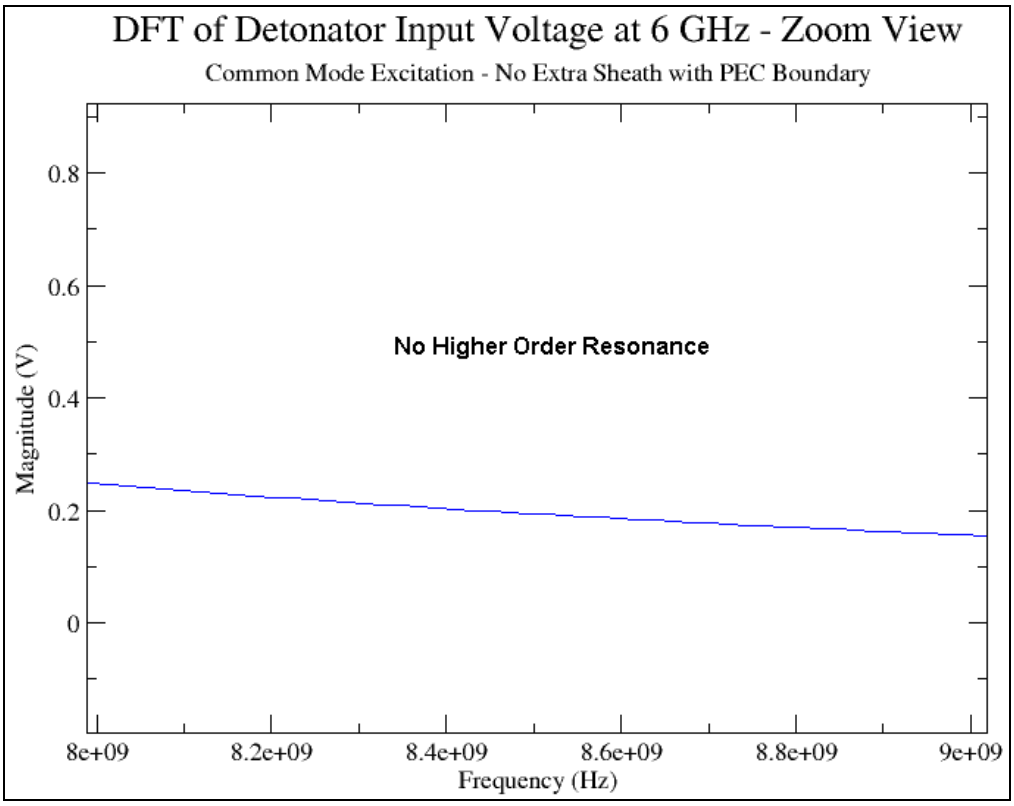

Figure 32: Higher order resonance zoom view of the DFT for standard detonator input voltage with 6 GHz common mode excitation and the extra sheath removed while utilizing the PEC boundary.

Table 10: Common mode voltage magnitudes for standard detonator geometry with extra sheath removed utilizing PEC boundary.

Frequency	Input Voltage	Mid-Seal Voltage	Bridge Wire Voltage
900 MHz	136.86	157.89	174.67
2 GHz	7.32	58.68	104.75
3 GHz	86.78	8.35	113.94
4 GHz	379.22	132.92	265.09
6 GHz	116.04	135.37	85.43
8 GHz	30.33	117.39	54.17

Table 11: Common mode resonances for standard detonator geometry with extra sheath removed utilizing PEC boundary.

Frequency	First Resonance	Second Resonance
900 MHz	N/A	N/A
2 GHz	4.52	N/A
3 GHz	4.52	N/A
4 GHz	4.52	N/A
6 GHz	4.52	N/A
8 GHz	4.52	N/A

The effect of the extra sheath on the agreement between the analytic prediction and ICEPIC simulation must also be determined. This will be displayed visually by plotting the values given in Tables 10 and 11 with the standard analytical model predictions seen in Figures 47-50 of Chapter 5. Figure 33 is the comparison plot of the common mode input voltage across frequency for the analytical standard detonator model and the ICEPIC detonator simulation without the extra sheath. The corresponding plots of the mid-seal and bridge wire voltage comparisons will not be shown as they are very similar to Figure 33 in that all three predict the same resonant frequency and have a similar shape. In order to discern differences between the ICEPIC and predicted values, the data in Figure 33 is re-plotted on a log scale in Figure 34. Figures 35 and 36 are the log scale plots of the mid-seal and bridge wire voltage comparisons.

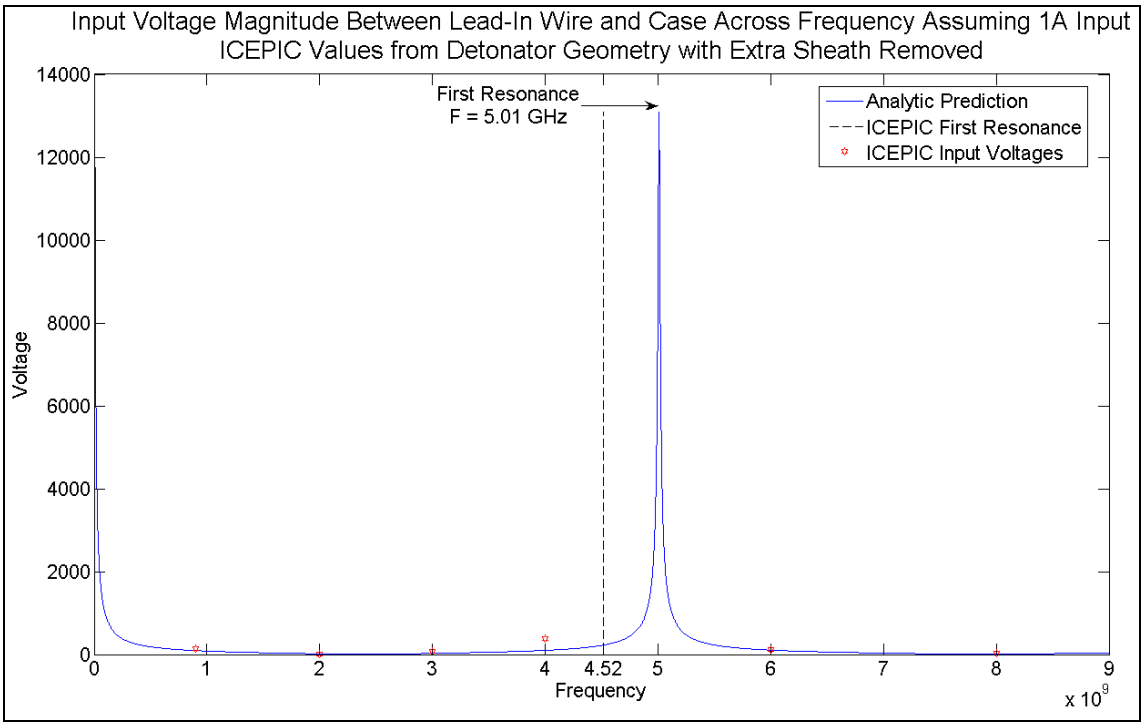

Figure 33: MatLAB analytical prediction and ICEPIC comparison plot of the common mode detonator input voltage magnitude with the extra sheath removed across the frequency range DC-9 GHz.

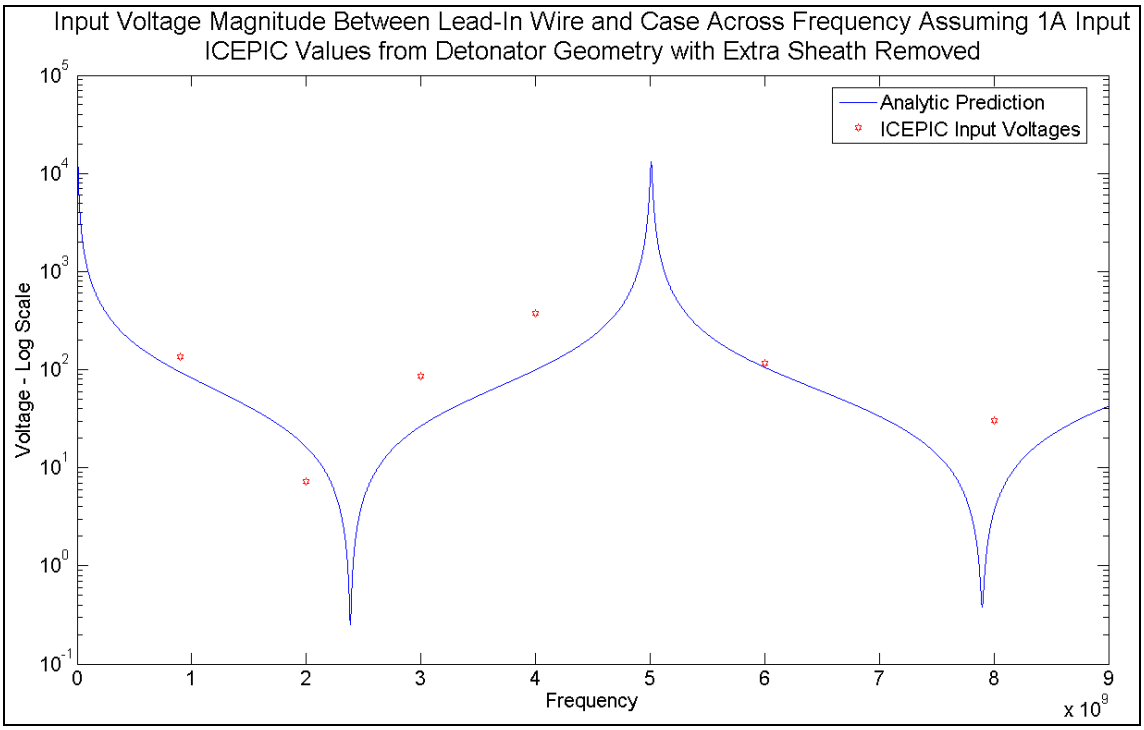

Figure 34: MatLAB analytical prediction and ICEPIC comparison plot of the common mode detonator input voltage magnitude with the extra sheath removed across the frequency range DC-9 GHz plotted on a log scale.

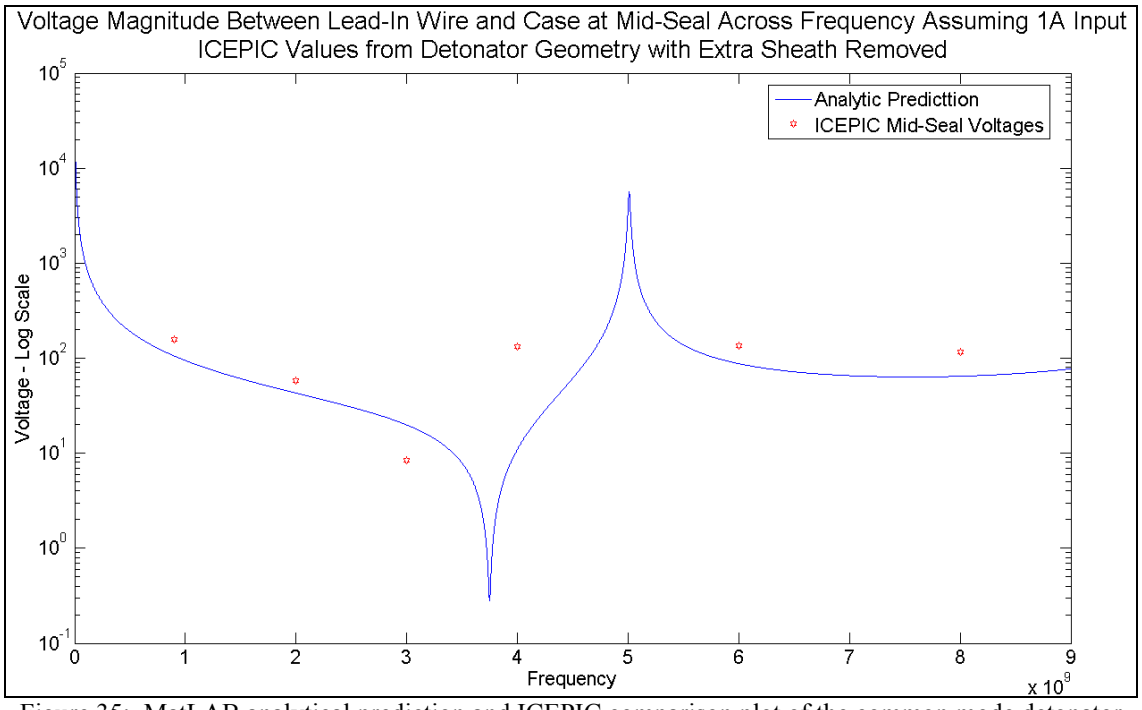

Figure 35: MatLAB analytical prediction and ICEPIC comparison plot of the common mode detonator mid-seal voltage magnitude with the extra sheath removed across the frequency range DC-9 GHz plotted on a log scale.

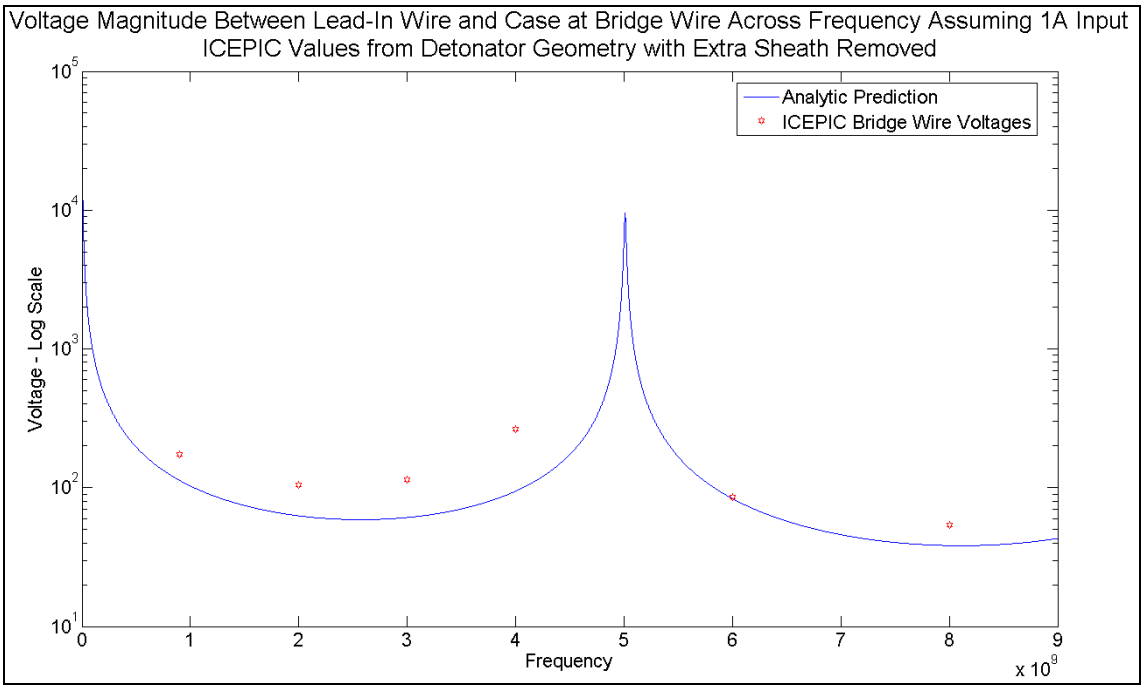

Figure 36: MatLAB analytical prediction and ICEPIC comparison plot of the common mode detonator bridge wire voltage magnitude with the extra sheath removed across the frequency range DC-9 GHz plotted on a log scale.

Figure 33 illustrates the shift from 4.31 to 4.52 GHz in the ICEPIC first resonant frequency due to the extra sheath being removed. This shift improved the agreement between the predicted and ICEPIC resonances from 16.24% to 10.84%. Also, the ICEPIC common mode simulation without the extra sheath does not predict a second resonance at 8.7 GHz, as was seen using the standard detonator geometry. This is an improvement since the analytical model does not predict a second resonance either.

A general observation from Figures 34 through 36 (when compared to Figures 47 through 50 from Chapter 5) is that the agreement between the predicted and simulated voltages has improved. The average percent difference for the input voltages is 240%, down from 543%. The 8 GHz value still shows the largest discrepancy, but it too has improved with a difference of 763%, down from 1857%. If this value is not included, the remaining five values have an average percent difference of 134%, down from 280%. The average percent difference between the ICEPIC and predicted results is 237% for the

mid-seal voltages and 62% for the bridge wire voltages, again an improvement over the 466% and 82% seen for the standard detonator geometry. The 4 GHz values have the highest percent difference for both the mid-seal (1108%) and bridge wire (181%) voltages. The other five values have an average agreement of 63% for the mid-seal voltages and 39% for the bridge wire voltages, which is not a significant improvement from the 67% and 39% found using the standard detonator geometry.

This investigation has revealed that the additional sheath beyond the bridge wire is the reason for the discrepancy between the second resonance found using ICEPIC and the absence of a second resonance in the analytical model. The removal of the additional sheath also improved the agreement for the first resonant frequency and the voltage values at all three positions along the detonator. While this is an important finding, the detonator without the additional sheath is not physically plausible. Therefore, an effort to determine what modifications to the analytical model can be made to account for this additional sheath during common mode excitation is required.

Finding the Additonal Capacitance of the Extra Sheath

Unlike differential mode excitation, common mode excitation involves current flow and voltage potential on the aluminum case of the detonator. Because of this method of excitation, it may be possible to account for the additional sheath even though the lead-in wires, and thus the transmission line, end at the bridge wire. The reason for this is that current continues to flow in the aluminum sheath of the detonator past the point where the transmission line ends. This current flow is being accounted for in the ICEPIC standard detonator geometry, but is not accounted for in the analytical model. The additional potential on the extra sheath introduces a stray capacitance at the end of

the detonator transmission line. This goal of this next investigation is to use ICEPIC to determine the value of this capacitance.

The method for determining this stray capacitance will be to first find the capacitance in the standard detonator model and then determine the capacitance present when the extra sheath is removed. The difference between these two capacitance values will be the stray capacitance introduced into the system by the extra sheath. To find these values in ICEPIC both the standard detonator geometry and the geometry with the extra sheath removed, previously described using the PEC boundary, will undergo common mode excitation. This excitation, however, will be very different from what has been used up to this point. To find the capacitance in the system, a DC voltage excitation must be used. The DC excitation will then produce a voltage charge in the system which can be measured using the bridge wire EDL. If the DC input is given very specific parameters, the amount of charge input into the detonator can be calculated. Using this charge along with the voltage measured by the EDL, the capacitance in the system can be found using $C = Q/V$ [23].

To control the amount of charge input into the system requires a DC excitation with a very specific profile. The amount of simulated time can be very short since a long simulation time only increases the amount of charge input into the system, which will produce a larger voltage, and the ratio of these two will produce the same capacitance value as a short simulation time. The most important factor in determining the simulation time was to make it longer than the amount of time the DC source was exciting the detonator. The reason for this is so that it will be clear that the voltage increases to some value while charge is being introduced into the system, and that it remains at that value

once the excitation ends. For simplicity, the magnitude of the current is kept at 1 A, and will excite the system for a short but arbitrary duration of 4.5 ns. The simulation time will be 7 ns to ensure the voltage value remains constant after the excitation ends at 4.5 ns. To ensure that instantaneous rise and fall times do not introduce spurious results into the system, the voltage will be ramped up to 1 A from 0 over 1.5 ns, remain constant for 1.5 ns, and then ramp down from 1 A to 0 over the remaining 1.5 ns. An illustration of the DC excitation profile is shown in Figure 37.

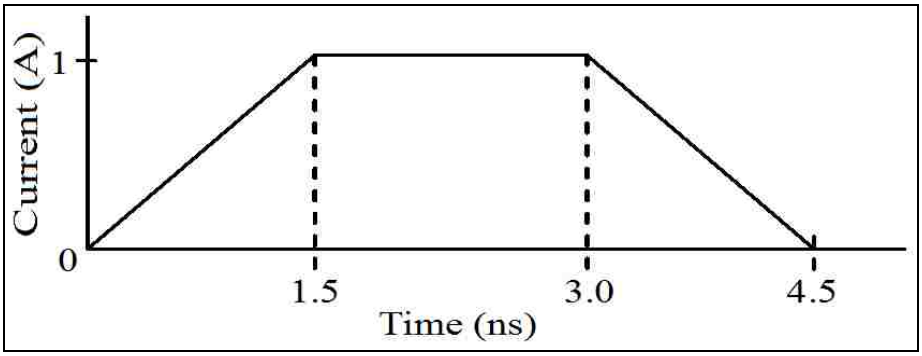

Figure 37: DC common mode excitation profile for determining detonator capacitance.

The amount of energy input into the detonator using this excitation can be calculated by finding the area under the input current curve:

$$Q = 1\left(\frac{C}{s}\right)\cdot\left[1.5*10^{-9} + 2\cdot\left(\frac{1}{2}\cdot 1.5*10^{-9}\right)\right]s \qquad (116)$$

$$= 3*10^{-9}C$$

This profile was input into the ICEPIC common mode excitation sources, and simulated for 7 ns. The resulting voltage waveforms for both the standard and removed extra sheath geometry are shown in Figures 38 and 39, respectively.

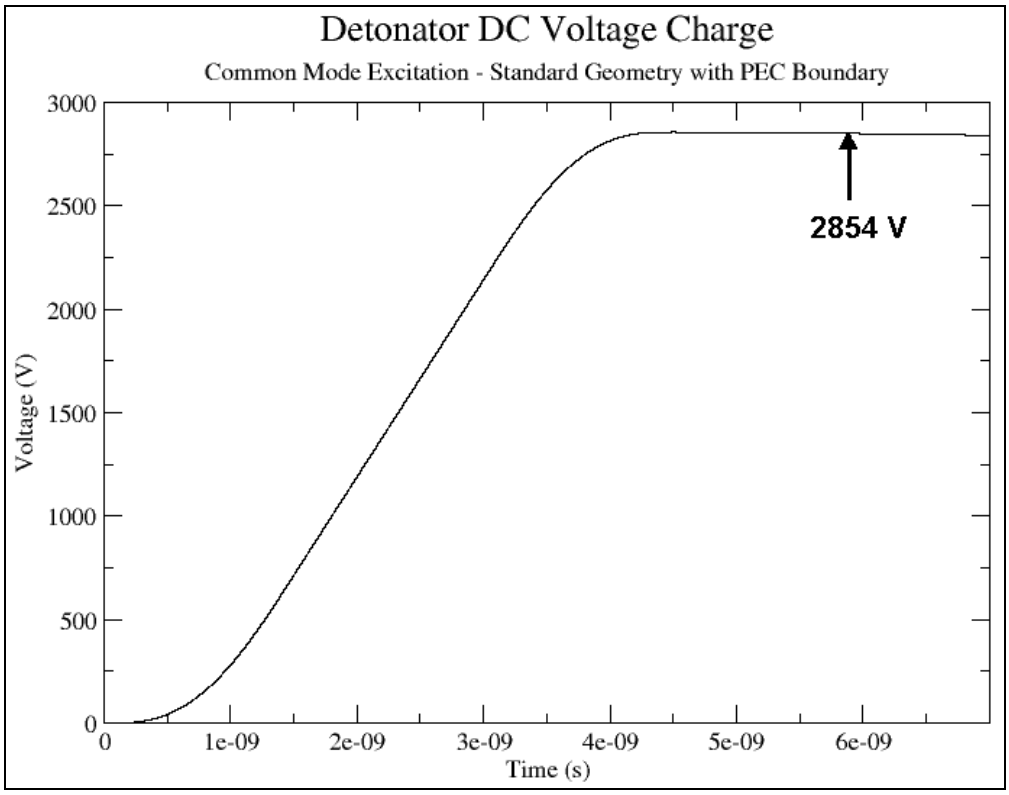

Figure 38: Voltage charge for common mode 4.5 ns DC excitation for determining standard detonator capacitance.

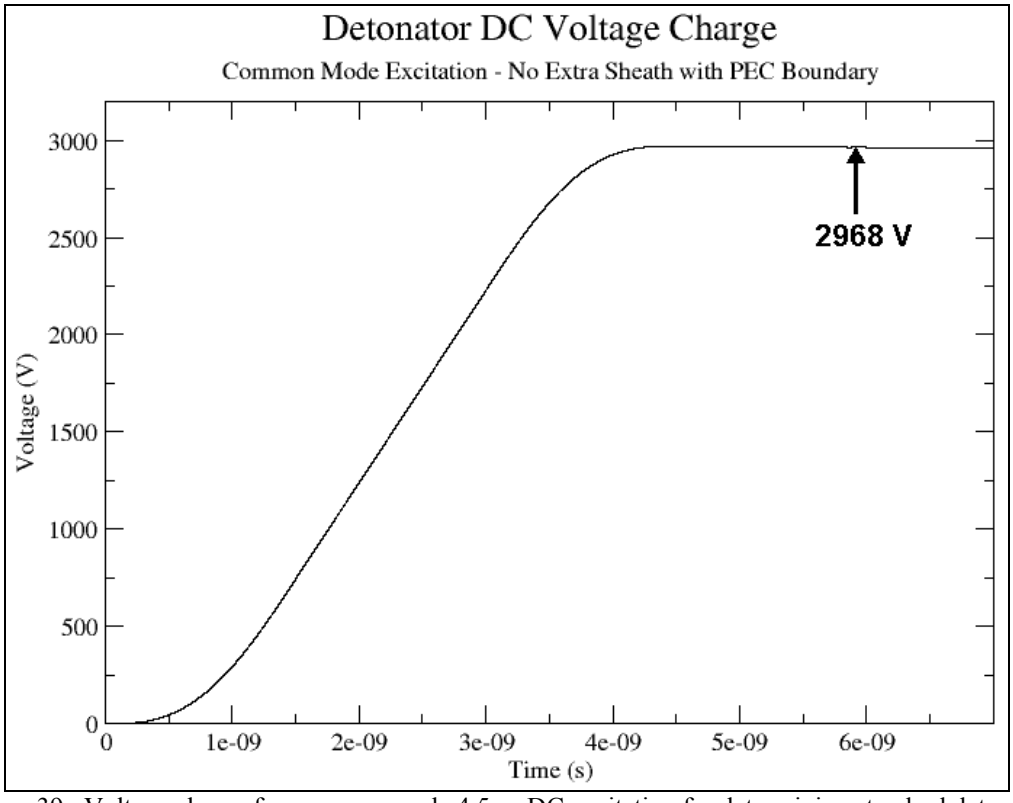

Figure 39: Voltage charge for common mode 4.5 ns DC excitation for determining standard detonator capacitance with the extra sheath removed.

Using the results from Figures 38 and 39 the capacitances for both geometries, as well as the difference between them, can be found:

$$C = \frac{Q}{V}, \tag{117}$$

$$C_s = \frac{3*10^{-9}}{2854} = 1.051 \text{ pF},$$

$$C_{s\text{-}r} = \frac{3*10^{-9}}{2968} = 1.011 \text{ pF}, \text{ and}$$

$$\Delta = 1.051 - 1.011 = 0.0404 \text{ pF}.$$

Based on the calculations above, the extra sheath creates an additional 0.0404 pF capacitance in the detonator.

Including the Additional Capacitance in the Common Mode Analytical Model

The additional capacitance can be included in the analytical model in a similar manner as described previously for adding the additional inductance section into the differential mode model. The new common mode detonator model is illustrated in Figure 40. This set-up includes an additional section connected in series at the end of the detonator transmission line and before the open termination. This added section is only a capacitance, not another section of twinaxial transmission line, and represents the additional capacitance due to the extra sheath. To implement this added capacitance in the MatLAB analytical model requires that it be included in the determination of the detonator input impedance.

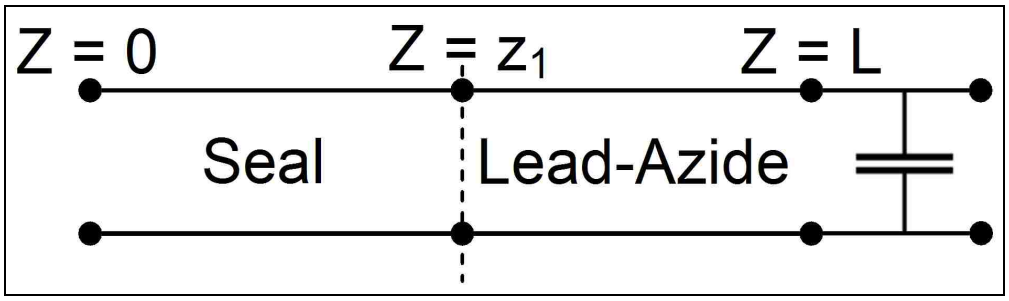

Figure 40: Illustration of dividing the detonator into sections including an additional capacitance.

Referring back to Chapter 3, the input impedance is found through the matrix multiplication of two cascaded transmission line sections with an open termination (118), followed by the division of the resulting voltage by the resulting current (108):

$$\begin{bmatrix} V(0) \\ I(0) \end{bmatrix} = \left[\prod_{z_1}^{0} e^{\Gamma_s dz'} \right] \cdot \left[\prod_{L}^{z_1} e^{\Gamma_l dz'} \right] \cdot \begin{bmatrix} 2 \\ 0 \end{bmatrix} V(L) \,. \tag{118}$$

To add the additional capacitance section, its representative telegrapher's equations [17] must be solved to find its corresponding 2x2 matrix to be included in the cascaded transmission line multiplication. This will be done in the same manner as was used to include the additional inductance section in the differential mode model. First, the telegrapher's equations are set up as

$$\frac{d}{dz}\begin{bmatrix} V(z) \\ I(z) \end{bmatrix} = -\begin{bmatrix} 0 & 0 \\ j\omega C & 0 \end{bmatrix} \cdot \begin{bmatrix} V(z) \\ I(z) \end{bmatrix} . \tag{119}$$

As has previously been described, the telegrapher equation matrix will be multiplied by -1 to remain consistent with transmission line matrices calculated in Chapter 3:

$$\Gamma = -\begin{bmatrix} 0 & 0 \\ j\omega C & 0 \end{bmatrix} \cdot (-1) \text{ , and} \tag{120}$$

$$\begin{bmatrix} V(z) \\ I(z) \end{bmatrix} = \left[\prod e^{\Gamma dz'} \right] \cdot \begin{bmatrix} V(z) \\ I(z) \end{bmatrix} \tag{121}$$

$$= \left[e^{\int \Gamma dz'} \right] \cdot \begin{bmatrix} V(z) \\ I(z) \end{bmatrix} \tag{122}$$

$$= \left[M_C \right] \cdot \begin{bmatrix} V(z) \\ I(z) \end{bmatrix} . \tag{123}$$

Once the value of $[M_C]$ is determined it can be multiplied in series with the other two sections of the detonator transmission line, and the input impedance to the detonator can be found using (124) and (108):

$$\begin{bmatrix} V(0) \\ I(0) \end{bmatrix} = \left[M_s \right] \cdot \left[M_l \right] \cdot \left[M_C \right] \cdot \begin{bmatrix} 2 \\ 0 \end{bmatrix} V\left(L\right) . \tag{124}$$

This procedure was implemented in the MatLAB analytical model program, where C can be any specified value. This new method finds the detonator input impedance, which is in turn used as described in Chapter 4 to find the input, mid-seal, and bridge wire voltages.

Modified Common Mode Model Comparison to Standard Detonator ICEPIC Simulations

The additional capacitance introduced into the system due to the additional sheath is 0.0404 pF. This capacitance is in addition to that already computed for the lead-azide section of common mode transmission line, which is 0.0552 pF. The total capacitance of the additional section is then 0.5916 pF. When this value is input into the MatLAB model with the modifications described above the resulting input voltage magnitude

prediction plot is shown in Figure 41 along with the standard detonator input voltage magnitudes found using ICEPIC (Table 11, Chapter 5). Again the mid-seal and bridge wire voltage magnitude comparison plots are not shown as they are both of a similar shape and predict the same resonant frequency as Figure 41. To better discern the differences between the ICEPIC simulation magnitudes and the predicted values, the data from Figure 41 is re-plotted on a log scale in Figure 42. Figures 43 and 44 are the log scale comparison plots of the mid-seal and bridge wire voltages, respectively.

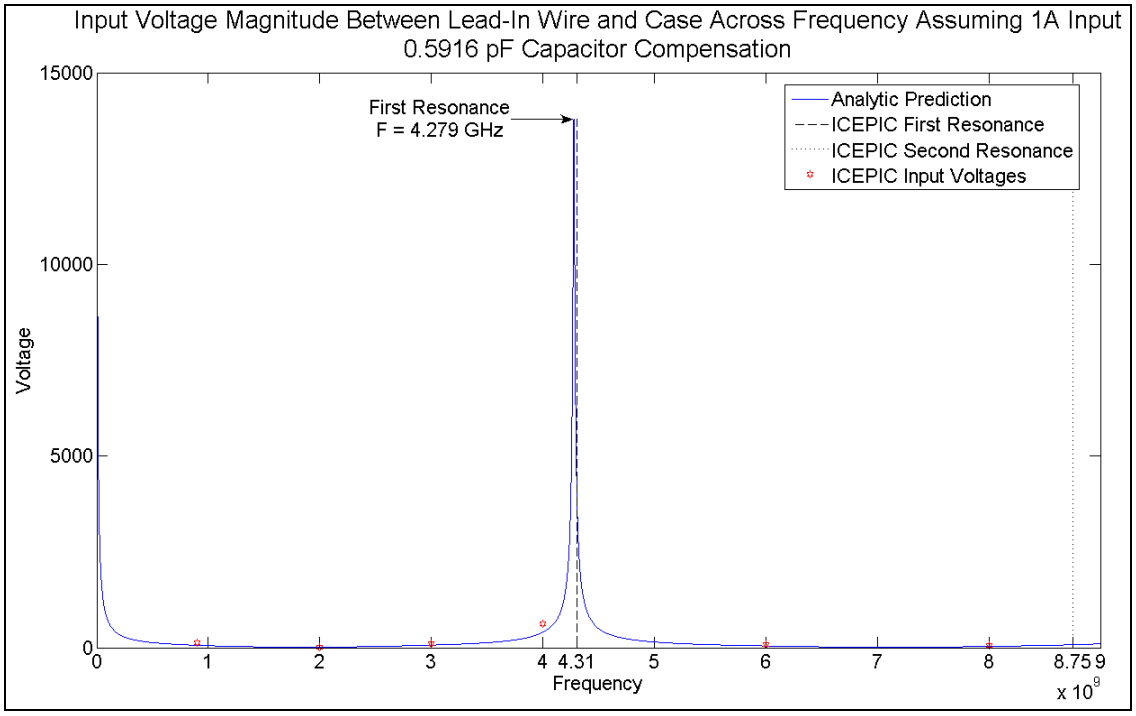

Figure 41: MatLAB analytical prediction and ICEPIC comparison plot of the common mode detonator input voltage magnitude with a 0.5916 pF additional capacitance section across the frequency range DC-9 GHz.

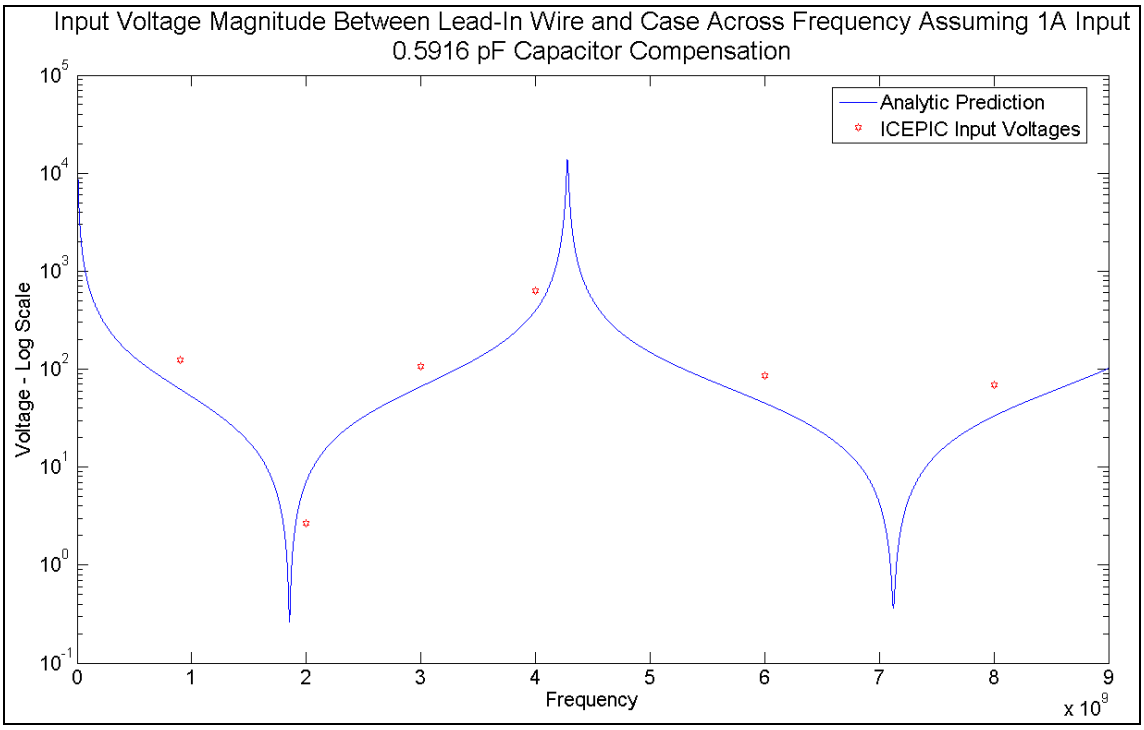

Figure 42: MatLAB analytical prediction and ICEPIC comparison plot of the common mode detonator input voltage magnitude with a 0.5916 pF additional capacitance section across the frequency range DC-9 GHz plotted on a log scale.

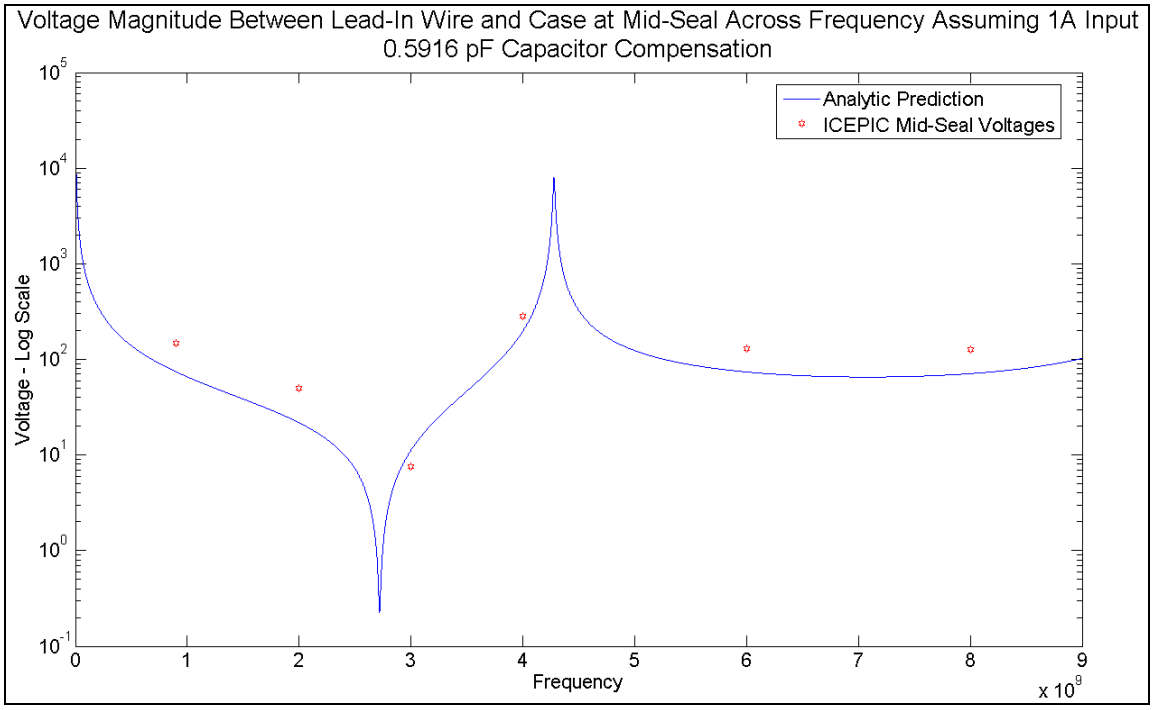

Figure 43: MatLAB analytical prediction and ICEPIC comparison plot of the common mode detonator mid-seal voltage magnitude with a 0.5916 pF additional capacitance section across the frequency range DC-9 GHz plotted on a log scale.

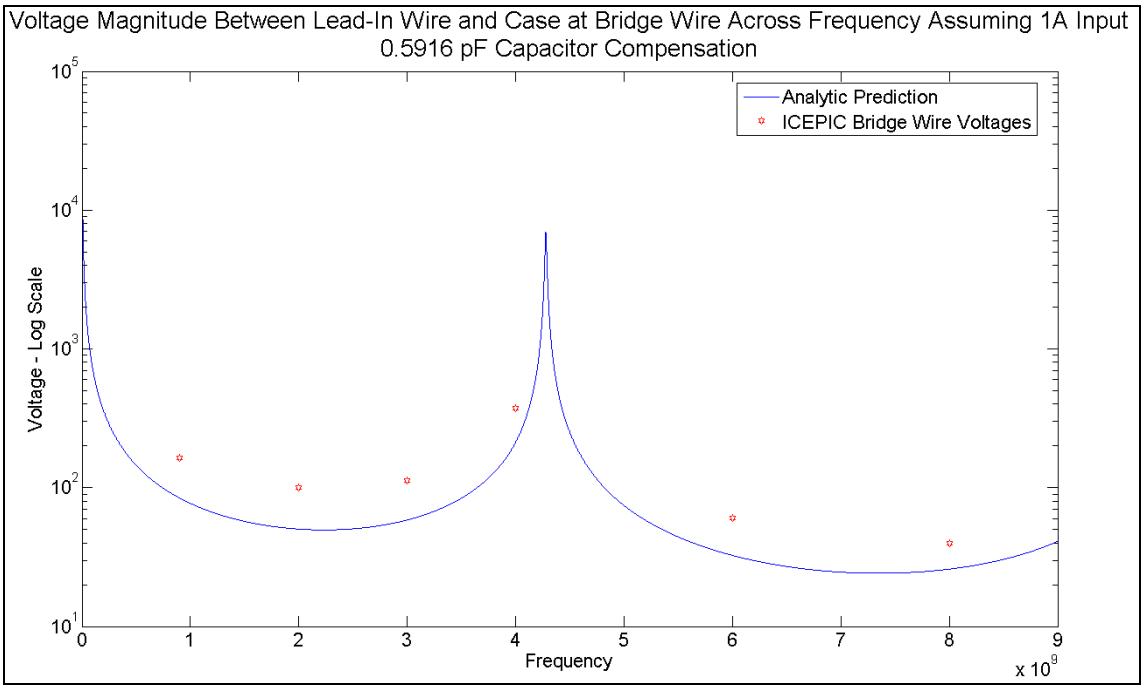

Figure 44: MatLAB analytical prediction and ICEPIC comparison plot of the common mode detonator bridge wire voltage magnitude with a 0.5916 pF additional capacitance section across the frequency range DC-9 GHz plotted on a log scale.

Figure 41 indicates a shift in the predicted first resonant frequency. This frequency shift results in an improved agreement with the analytical model at 0.72%, down from 16.24%. The additional capacitance section did not facilitate the inclusion of a second resonance, as was found using ICEPIC, so that discrepancy remains. However, the agreement between the predicted and ICEPIC simulated values of all three voltage diagnostics have improved. Table 12 is a summary of the average percent differences for all three diagnostics excluding the single highest discrepancy value during each of the three model variations: standard model, standard model with sheath removed, and standard model with 0.5916 additional capacitance section. Table 13 is a summary of average percent differences for the three diagnostics including all values during each of the model variations, and Table 14 is a summary of percent differences for the first resonance during each of the three model variations.

Table 12: Average percent differences for all three diagnostics of the standard detonator for three model variations not including the single highest discrepancy value.

Detonator Property	Standard Model	Removed Sheath	0.5916 pF Additional Capacitance
Input Voltage	280	134	66
Mid-Seal Voltage	67	63	52
Bridge Wire Voltage	39	39	54

Table 13: Average percent differences for all three diagnostics of the standard detonator for three model variations including all values.

Detonator Property	Standard Model	Removed Sheath	0.5916 pF Additional Capacitance
Input Voltage	543	240	82
Mid-Seal Voltage	466	240	65
Bridge Wire Voltage	82	62	60

Table 14: Percent differences for the first resonance of standard detonator for three model variations.

Detonator Property	Standard Model	Removed Sheath	0.5916 pF Additional Capacitance
First Resonance	16.24	10.84	0.72

Tables 12 through 14 indicate the progression of the average percent differences between ICEPIC simulated values and predicted values for all three diagnostics. As the model transitions from the initial formulation through to the inclusion of the additional capacitance, the average percent differences decrease in every case with the exception of the bridge wire voltage excluding the largest discrepancy value which increases from 39% to 54%. Beyond this exception, every other detonator property shows better agreement between the ICEPIC and predicted values when the model includes the capacitive adjustment for the additional sheath. In nearly every case, the improvement is significant, indicating that the inclusion of the additional capacitance makes the analytical model more representative of the detonator undergoing common mode excitation in the frequency range of DC-9 GHz.

This investigation has revealed that the additional sheath beyond the bridge wire accounts for a large portion of the discrepancy between the ICEPIC and predicted

voltages. However, while an average agreement of 82% for the input voltage is a significant improvement over the initial agreement of 543%, it is still a high value, especially compared to the 7.80% percent agreement for the differential mode input voltage. The extra sheath was also found to be the cause for the second resonance found using ICEPIC that was not predicted analytically. Adding the additional capacitance to the analytical model to account for the extra sheath did not bring about the prediction of a second resonance. There is yet another EM property of the detonator in ICEPIC that is not accounted for analytically, and so the common mode aspect of the analytical model still requires additional refinement. This modeling challenge will be discussed further in Chapter 8.

Chapter Summary

In this chapter, several investigations were carried out in an effort to improve the agreement between the 1-D analytical model and 3-D ICEPIC EM simulation. Through these investigations it was found that the ICEPIC results are scalable and that the physical representation of the bridge wire and extra sheath in 3-D simulation, not completely accounted for in the analytical model, were primary reasons for the discrepancies seen in both the differential and common mode results. The differential mode excitation analytical model was successfully modified to account for bridge wire inductance differences found between the two models, resulting in an improvement in the agreement between the analytical and ICEPIC models, most notably for the bridge wire voltage. An additional capacitance was added to the common mode excitation model to help account for the extra sheath in the ICEPIC model, again resulting in better agreement between the two models. An additional higher order resonance in both the differential and common

mode simulations found using ICEPIC have not been successfully accounted for analytically, though the reason for the discrepancy is known to be the extra sheath. Further improvements accounting for this additional resonance in both excitation modes as well as for improving the common mode voltage agreements are still possible and will be discussed in Chapter 8.

Chapter 7 – Modeling the State-of-the-Art Blasting Cap and Comparison to Experimental Measurements

The SABC discussed in Chapter 2 will now be modeled and simulated using ICEPIC and the analytical model to determine its EM properties across a frequency range of DC-6 GHz. The analytical model results will be compared to experimental impedance measurements taken on a set of SABCs in the frequency range of 10 MHz to 6 GHz. The change in the upper limit of the frequency range (9 to 6 GHz) was made to remain consistent throughout all comparisons in this chapter, since the experimental measurements were made through 6 GHz. Similarly, only differential mode excitation of the SABC will be investigated since differential mode measurements are all that is available for comparison to predicted and simulated results.

Modeling the SABC

SABC Simulation in ICEPIC

The physical model of the SABC from Chapter 2 is repeated here for reference as Figure 1. Recall from Chapter 2 that the dimensions of this model came in part from the SABC specification sheet [10], but many were given reasonable approximations based on general detonator knowledge and some observations of the experimental procedure outlined later in this chapter.

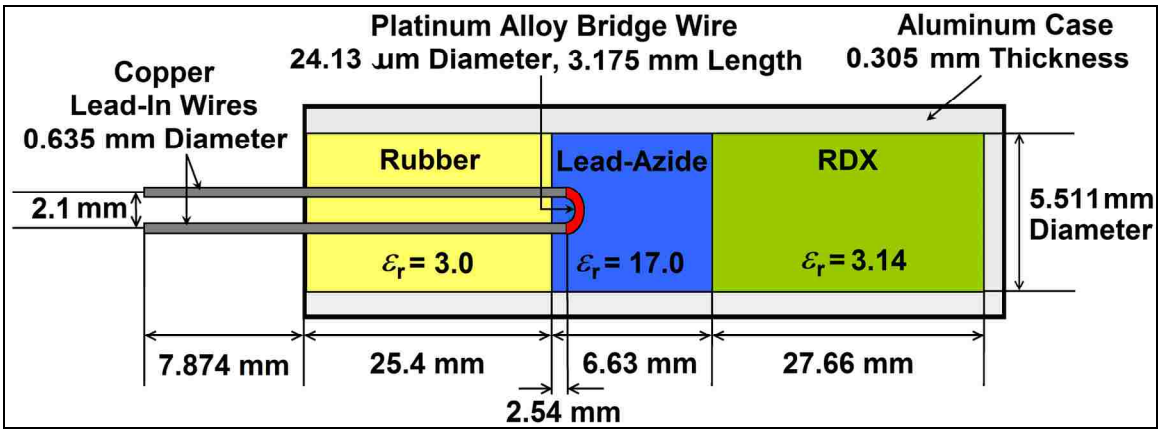

Figure 1: Illustration of the SABC geometry dimensions and EM properties.

The above model of the SABC was created in ICEPIC in the same way as the standard detonator geometry that has been investigated to this point. A change of the dimensions and dielectric properties for the detonator features in the ICEPIC model is a relatively simple procedure. Using previous observations for optimizing the generic detonator model, the SABC model was terminated at the end of the lead-azide section. As before, a PML box was used to encompass the exciting source placed at the beginning of the lead-in wires, the SABC geometry was truncated in PEC with a 200 μm cylindrical air region, and the bridge wire was extended partially into the lead-in wires to ensure connection. To remain consistent, a 50 μm grid spacing was used, and the system was simulated for 50 ns. The courant condition [22] was used to determine a time step of $9.536*10^{-14}$ s, resulting in 524,303 time steps for each ICEPIC simulation, and $3.37*10^{7}$ cells were updated each time step. Also, the same voltage EDLs and CUR_CIR were used for determining the EM properties of the SABC as were illustrated in Figure 11 in Chapter 4 for the generic detonator, with the only difference being that the mid-seal voltage EDL was placed 12.7 mm from the beginning of the detonator case reflecting the increased length of the seal section. From these properties, it can be observed that every effort was made to keep the SABC simulation space and excitation conditions similar to

what has been previously used, and this simulation space set-up is illustrated in Figure 2. The ICEPIC rendering of the SABC geometry is shown in Figure 3, and a 3-D illustration of the simulation space is shown in Figure 4.

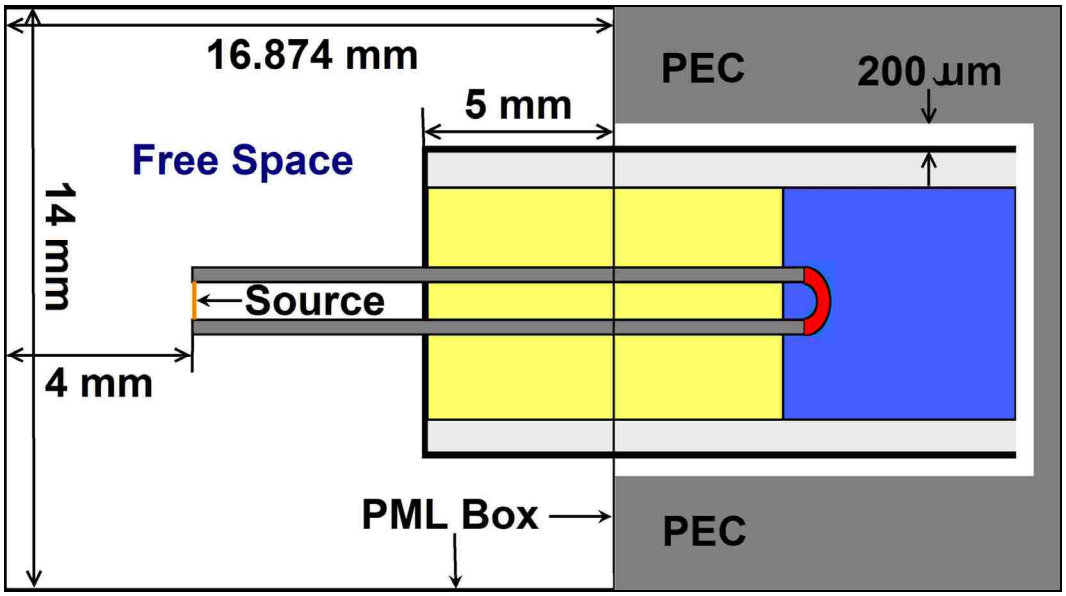

Figure 2: Illustration of the top view for the differential mode simulation space set-up for the SABC geometry indicating the free space region along with the placement and dimensions of the PML box encompassing the excitation source.

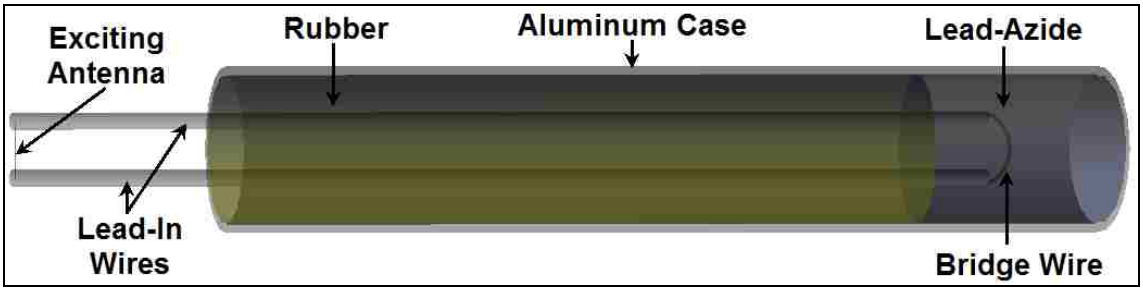

Figure 3: Side view of the ICEPIC rendering of the SABC geometry for differential mode excitation indicating detonator components.

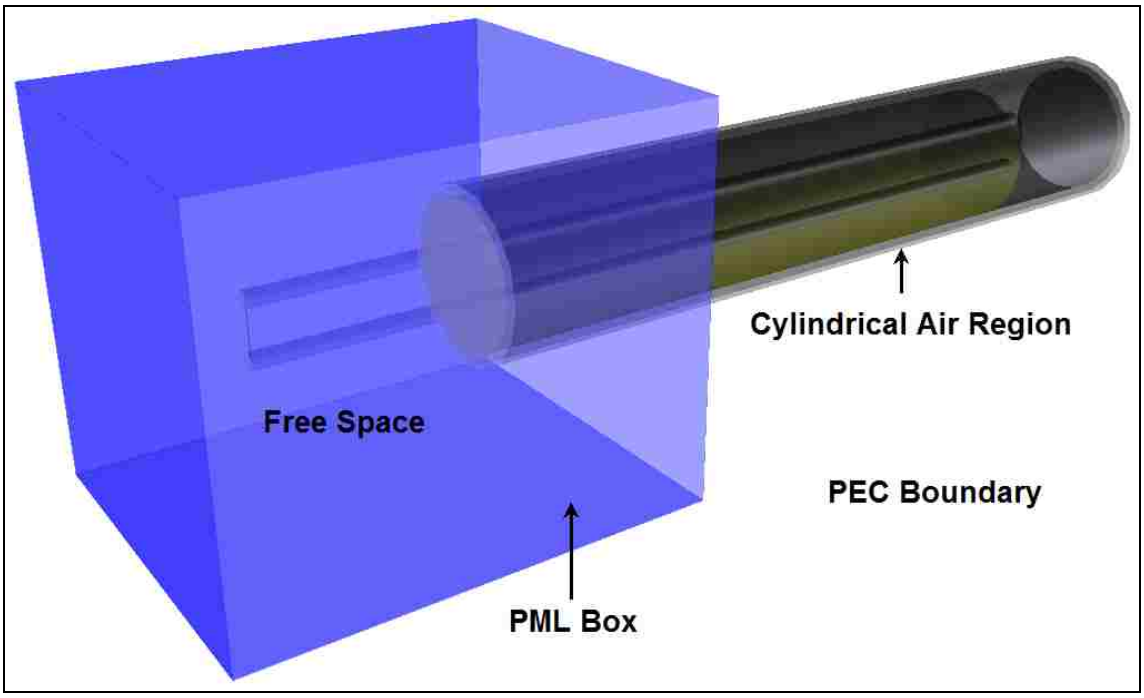

Figure 4: Illustration of the 3-D ICEPIC rendering of the differential mode simulation space from a perspective view of the SABC geometry.

There are two primary differences between the SABC and generic detonator ICEPIC geometries beyond the dimensional values. First, the bridge wire has a higher DC resistance (1.6 Ω), and so requires a re-calculation of the effective conductivity and diameter for use in simulation. Recall from Chapter 4 that the extremely small diameter of the bridge wire is not feasible in simulation, and that its conductivity and diameter must be scaled appropriately so that it can be resolved in ICEPIC and still have the same DC conductivity. The process described in (68) and (69) in Chapter 4 was repeated for the SABC bridge wire, resulting in a diameter of 168.9 μm, and a conductivity of 88,571.4 S/m. Second, the bridge wire's increased length and arching connection to the lead-in wires facilitated a new modeling effort in ICEPIC. Due to the 3.175 mm length of the bridge wire and the 2.1 mm spacing of the lead-in wires, the bridge wire can not have a semi-circular shape and connect properly to the lead-in wires. ICEPIC was used to create many spheres of 168.9 μm diameter, placed extremely close together, along the

arc of cycloid to create the correct length and connection for the bridge wire. A close-up view of the ICEPIC rendering of the SABC bridge wire is shown in Figure 5.

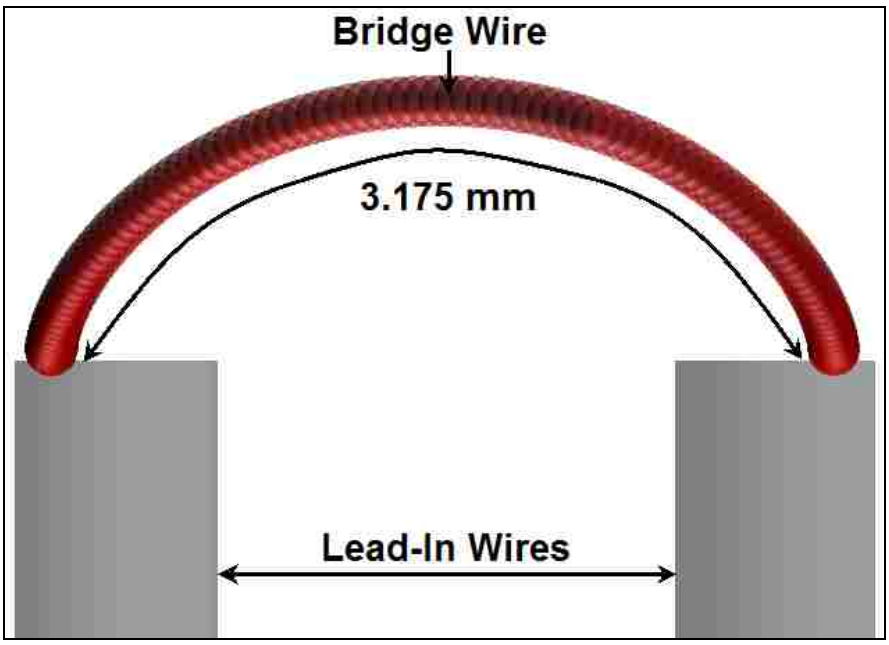

Figure 5: Close-up view of the bridge wire and its connection to the lead-in wires.

For this study the SABC geometry was excited using a differential mode input at 900 MHz, 2, 4, and 6 GHz, with all simulation properties and diagnostics described. The results were analyzed using curve-fitting and DFTs, as described in detail in Chapter 5. Figure 6 is the input voltage for the differential mode 4 GHz excitation. Figure 7 is the corresponding DFT of the 4 GHz input voltage waveform, and Figure 8 is the zoomed view of the DFT plot indicating the first resonance. As with the generic detonator results, additional SABC input voltage and DFT waveforms at other frequencies do not offer any additional insight into SABC behavior and will not be shown. Similarly, Figures 6 and 7 are representative of results obtained from the mid-seal and bridge wire voltage along with the bridge wire current diagnostics, and will also not be shown. The results of these analyses are listed in Tables 1 and 2.

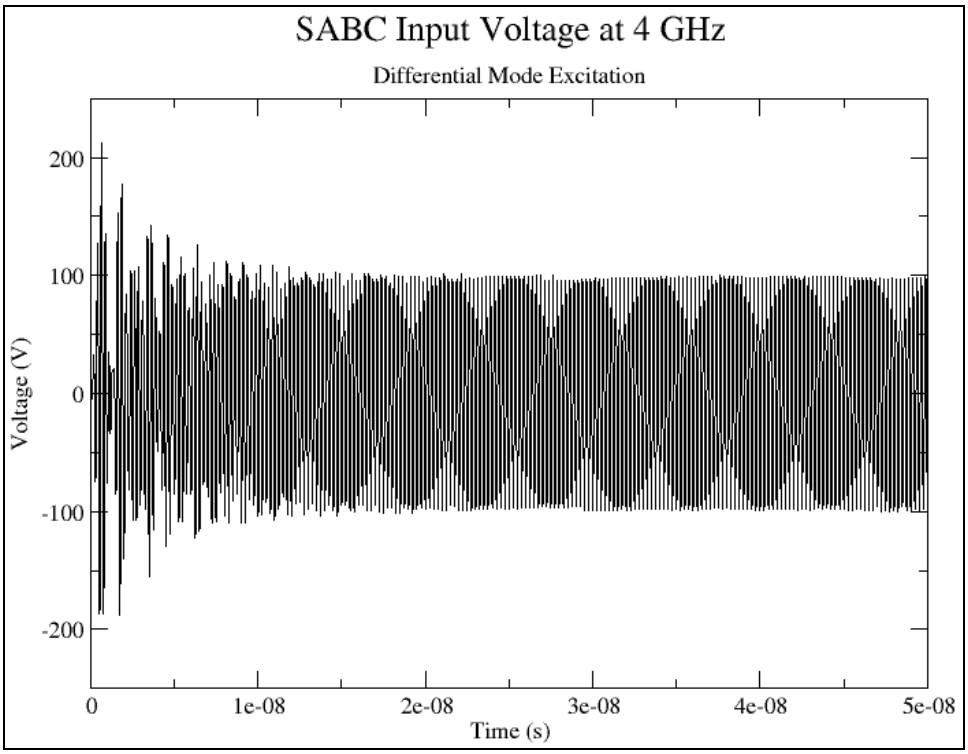

Figure 6: SABC input voltage with 4 GHz differential mode excitation.

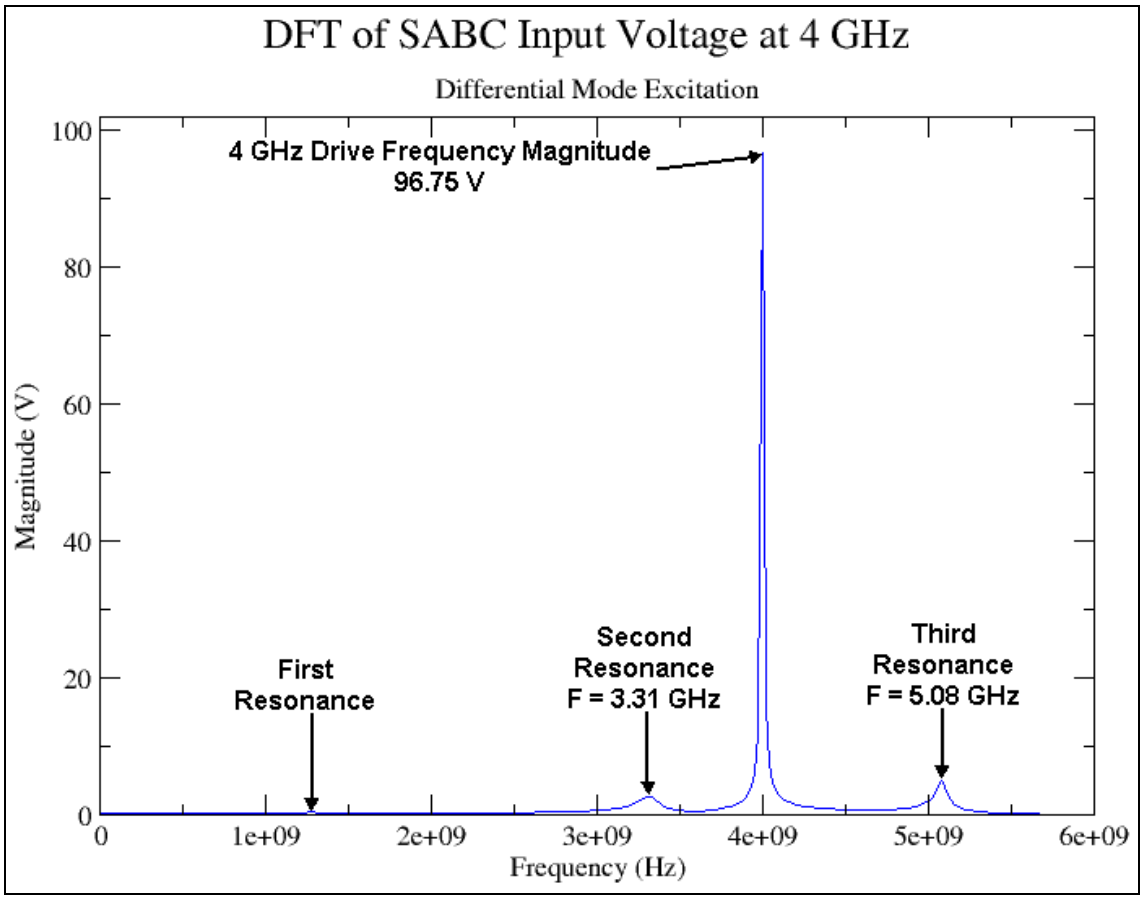

Figure 7: DFT of SABC input voltage with 4 GHz differential mode excitation.

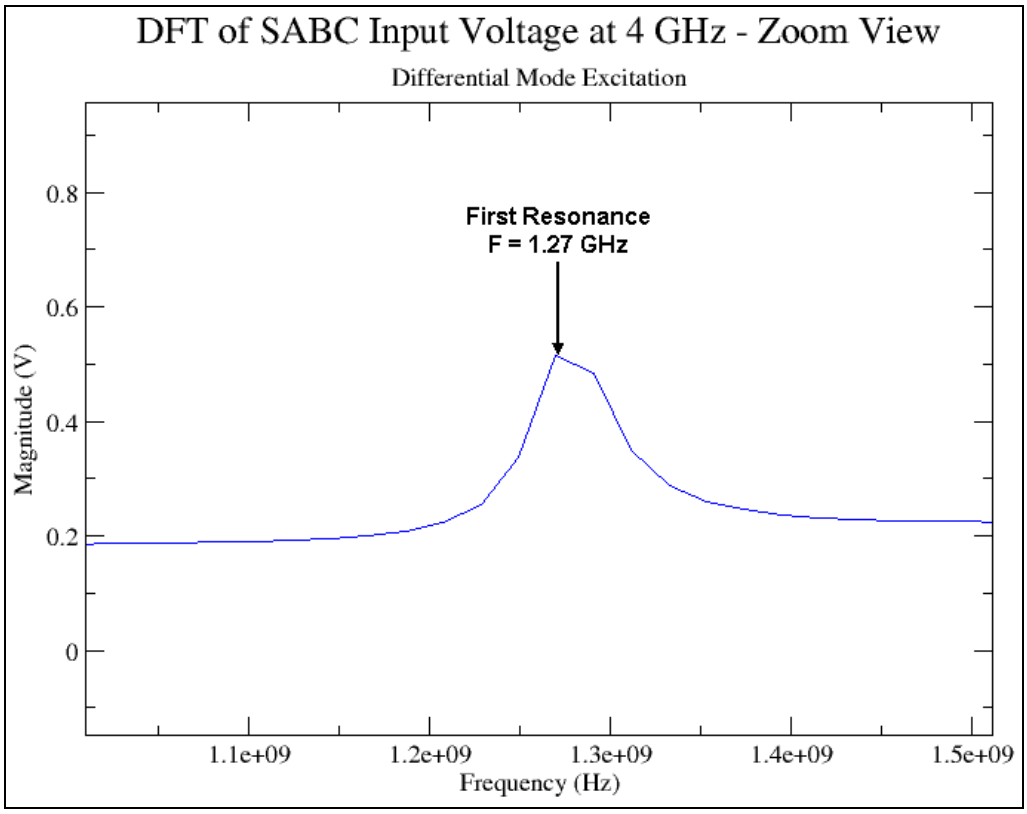

Figure 8: First resonance zoom view of DFT of the SABC input voltage with 4 GHz differential mode excitation.

Table 1: SABC geometry differential mode voltage and current magnitudes.

Frequency	Input Voltage	Mid-Seal Voltage	Bridge Wire Voltage	Bridge Wire Current
900 MHz	246.34	136.88	21.72	2.35
2 GHz	20.34	137.84	33.2	1.71
4 GHz	96.75	82.30	78.51	2.22
6 GHz	101.39	102.11	57.53	1.23

Table 2: SABC geometry differential mode resonances.

Frequency	First Resonance	Second Resonance	Third Resonance
900 MHz	1.27	N/A	N/A
2 GHz	1.27	3.31	N/A
4 GHz	1.27	3.31	5.08
6 GHz	1.27	3.31	5.08

Table 1 indicates that the input and mid-seal voltages as well as the bridge wire current values are comparable to those found using the standard detonator geometry (Table 9, Chapter 5). The bridge wire voltages, however, are much larger. This result is

suggesting that a smoother bridge wire connection to the lead-in wires, compared to a 90^0 bend, helps eliminate the inductance problem discussed in Chapter 6. Figure 7 and Table 2 show that only a handful of detonator geometry changes can result in a large change in resonance pattern. The SABC geometry contains three resonance frequencies in the same frequency space (DC-6 GHz) that the standard detonator geometry had only one. In a similar manner as discussed in Chapter 5, all of the resonances were verified with additional simulations using differential mode excitations at the frequencies listed in Table 2. All three frequencies did indeed exhibit resonant behavior, similar to what was shown in Figure 13 of Chapter 5.

SABC Analytical Model Predictions Compared to ICEPIC Simulations

Modifying the analytical model to predict the EM properties of the SABC required changing the physical dimensions and bridge wire DC resistance input into the MatLAB program. Note that the program being modified for SABC analysis is the original program using the bridge wire self-inductance formula (26) without any additional inductance section, not the version of the program optimized for the generic detonator in Chapter 6. So that the analytical model predictions can be directly compared to ICEPIC results, the bridge wire diameter must be 168.9 μm instead of the prescribed 24.13 μm in Figure 1. Figure 9 is the ICEPIC and analytical model comparison plot of the differential mode input voltage across frequency for the SABC. In order to discern differences between the ICEPIC and predicted values, the data in Figure 9 is re-plotted on a log scale in Figure 10. Also, Figures 11 and 12 are log scale comparison plots of the mid-seal and bridge wire voltages, respectively, while Figure 13 is a log scale comparison plot of the bridge wire current. Standard scale plots indicating predicted

resonances for these three diagnostics are not shown since they are similar in appearance to Figure 9.

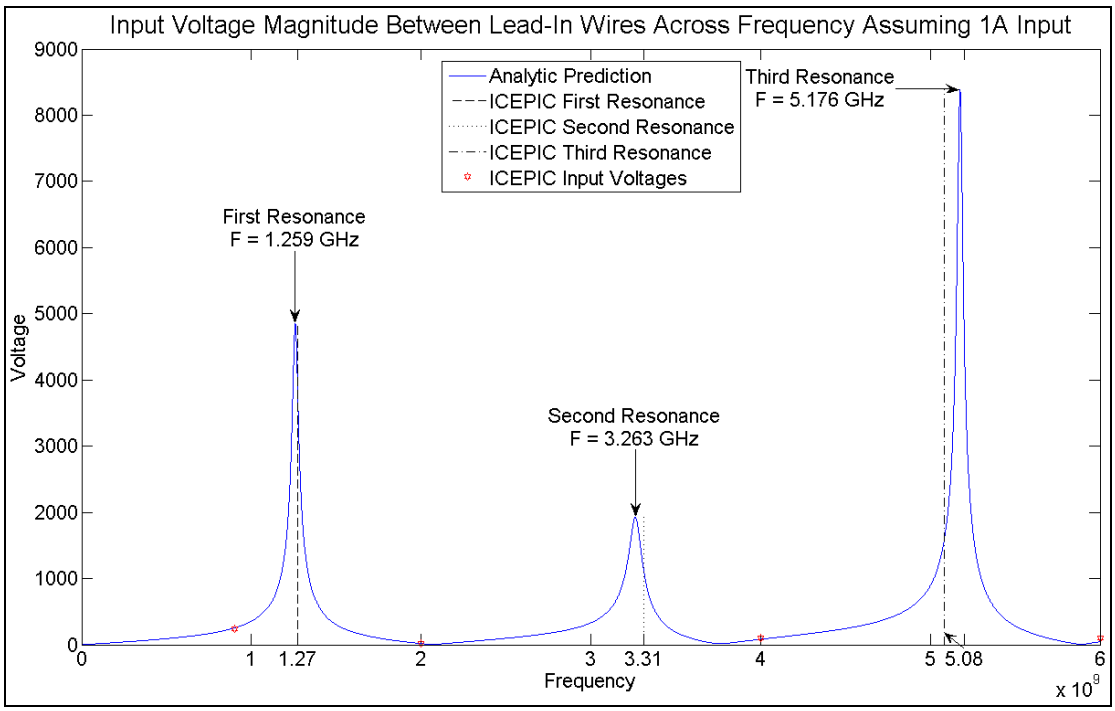

Figure 9: MatLAB analytical prediction and ICEPIC comparison plot of the differential mode SABC input voltage magnitude across the frequency range DC-6 GHz.

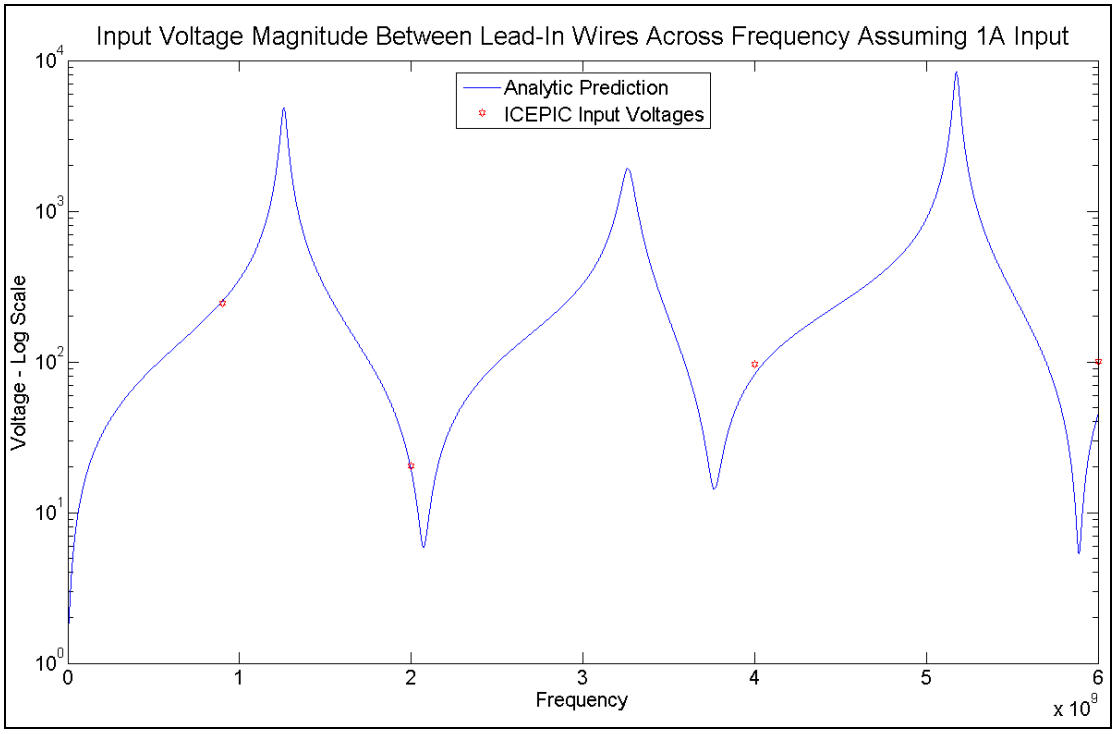

Figure 10: MatLAB analytical prediction and ICEPIC comparison plot of the differential mode SABC input voltage magnitude across the frequency range DC-6 GHz plotted on a log scale.

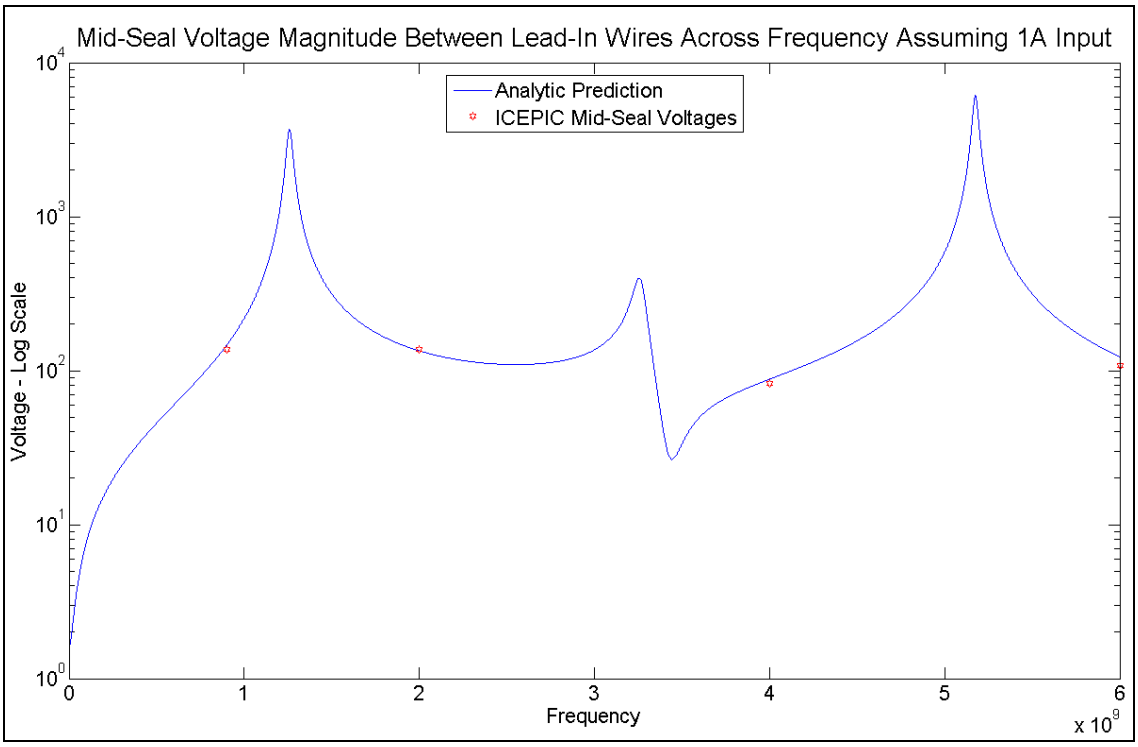

Figure 11: MatLAB analytical prediction and ICEPIC comparison plot of the differential mode SABC mid-seal voltage magnitude across the frequency range DC-6 GHz plotted on a log scale.

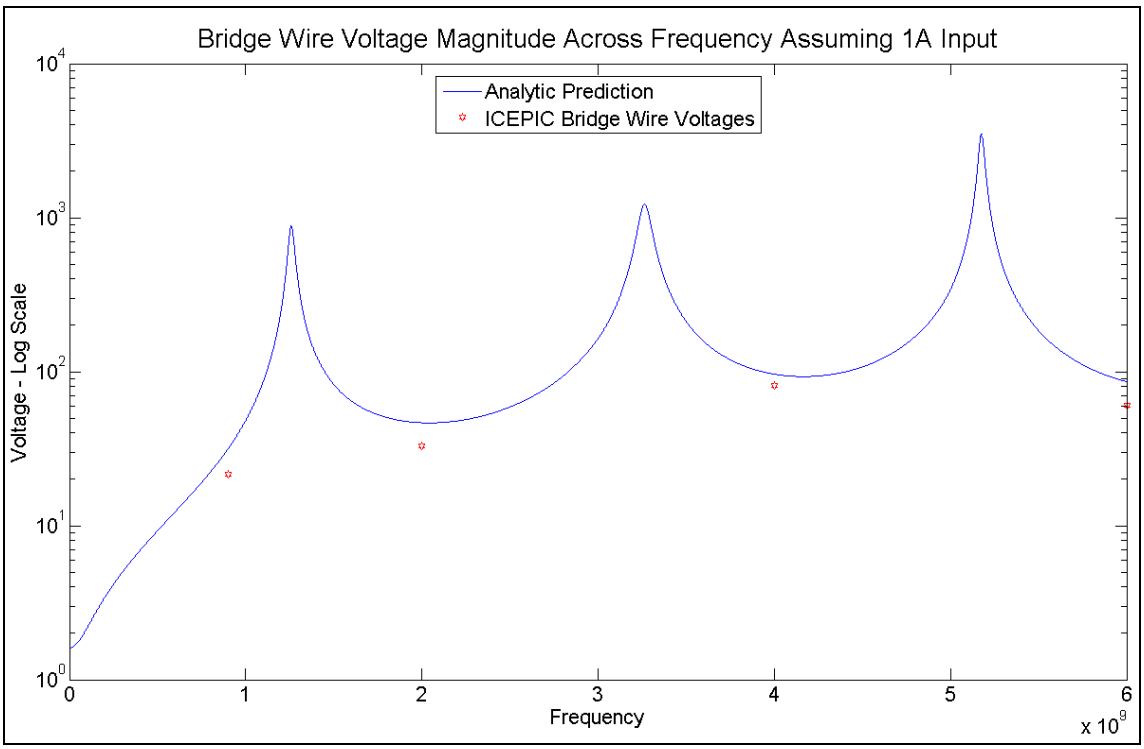

Figure 12: MatLAB analytical prediction and ICEPIC comparison plot of the differential mode SABC bridge wire voltage magnitude across the frequency range DC-6 GHz plotted on a log scale.

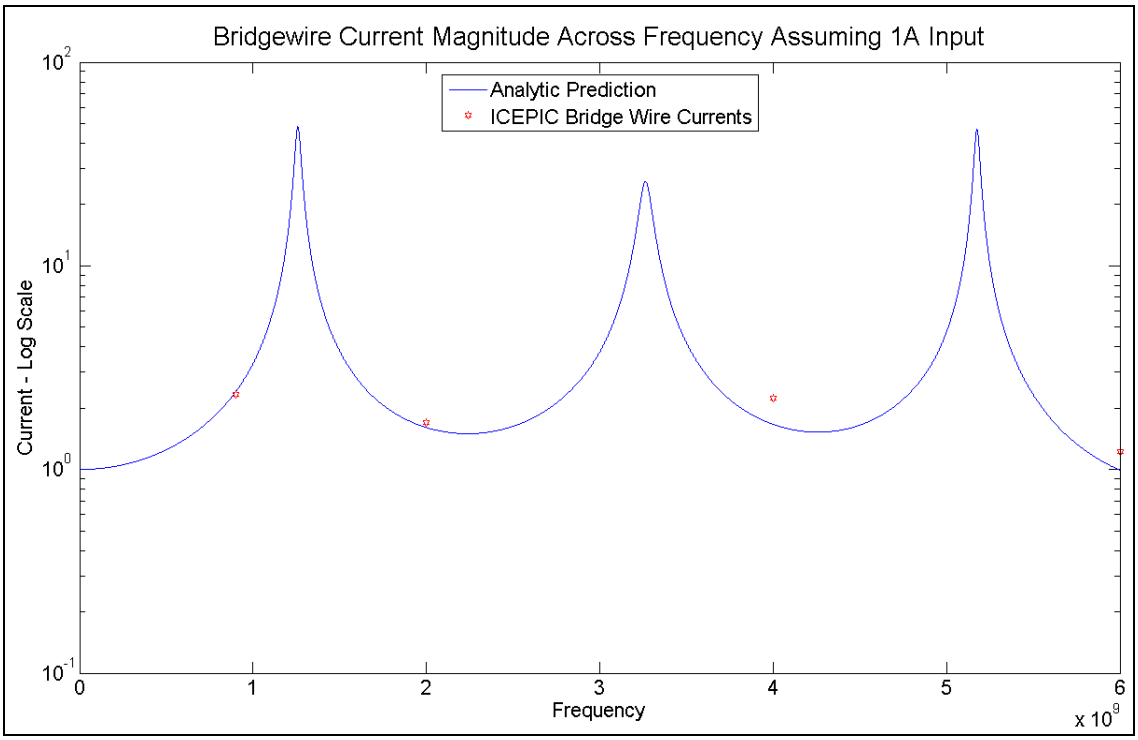

Figure 13: MatLAB analytical prediction and ICEPIC comparison plot of the differential mode SABC bridge wire current magnitude across the frequency range DC-6 GHz plotted on a log scale.

The comparison of results using ICEPIC simulation of the SABC geometry and analytical model prediction for differential mode excitation in Figures 9 through 13 showed very good agreement overall. The predicted and simulated resonances are within 0.86% for the first resonance, 1.42% for the second, and 1.89% for the third. The average agreement for each of the four diagnostics is 19.71% for the input voltages, 9.04% for the mid-seal voltages, 36.62% for the bridge wire voltages, and 13.06% for the bridge wire currents. These percentages represent good agreement between the two models, especially considering that the analytical model has not undergone any modifications to account for discrepancies. This exercise has shown that the ICEPIC and analytic models for a different detonator geometry can still produce similar results, again validating 1-D predictions with 3-D EM simulation.

SABC Analytical Model Predictions Compared to Experimental Results

To this point, the 1-D analytical model predictions have been compared to 3-D EM simulation solely for the purposes of validating the 1-D model. The validation has been sufficient for the SABC to now use the analytical model to compare these predictions to experimental measurements made on live SABCs. To do this, the only geometry change required in the analytical model is that of the bridge wire diameter from the scaled value of 168.9 μm to the true value 24.13 μm. For comparison to the measurements, the analytical model will again be used to find input impedance, not voltages and current.

An experimental setup at Ktech Inc. used an HP 8753C network analyzer along with an HP 85047A S-parameter test set to measure the S_{11} parameters of live SABCs in air from 10 MHz to 6 GHz. The SABCs were kept in an isolated and experimentally safe environment, and the network analyzer was calibrated using an HP 85033D calibration kit. Differential mode measurements were performed on 108 detonators, and the measured S_{11} parameters were converted to impedances [17]. The real part of the measured impedance of all 108 SABCs is shown in Figure 14 which indicates that the SABC measurements were all very similar across the frequency range investigated. Also, several high impedance areas were found at 730 MHz and 2, 3.3, and 5.4 GHz, suggesting resonances at these frequencies.

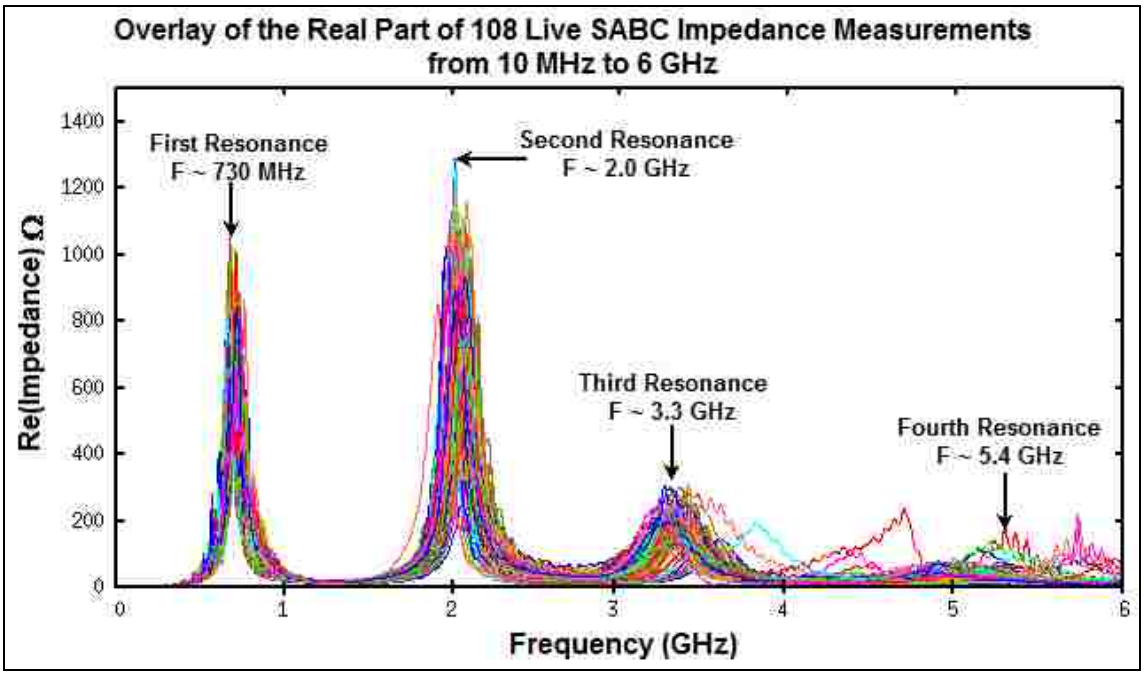

Figure 14: Overlay of the real part of impedance measurements on 108 live SABCs.

Due to the nature of this data, it is more prudent to compare the resonant frequencies found during experiment to those predicted by the analytical model, rather than trying to compare impedance values at different frequencies. Figure 15 is a plot of the SABC analytical model impedance prediction with all predicted resonances indicated. Also on this plot, included as single vertical lines, are the measured resonance frequencies. The magnitudes of these vertical lines are not in scale with the measured values at these frequencies, they are set so that they may be easily compared to predicted resonance frequencies nearby. The resonance comparison plot in Figure 15 indicates that the experimental measurements found an additional resonance at 3.3 GHz that has not been predicted analytically. Of the three resonances that do correspond to measured values, the first resonance differs by 27.95%, the second by 28.5%, and the third by 8.7%. While these agreements are a decent first attempt at comparing the analytical model to measurements, differences of over 25% and the absence of a resonant frequency requires that the model be modified.

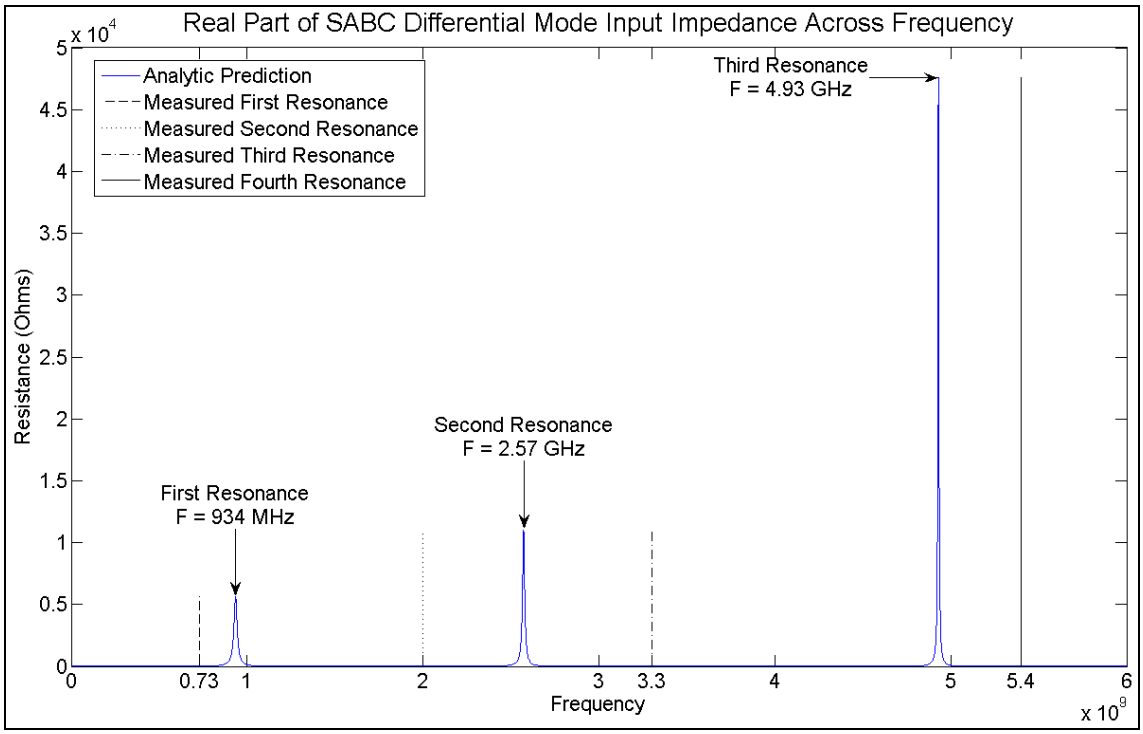

Figure 15: Comparison plot of measured and predicted SABC resonances across the frequency range 10 MHz to 6 GHz.

Recall that the dimensions given in Figure 1 of the SABC contain estimated values based on educated guesses. These initial guesses are likely in error due to the discrepancies seen in the resonance pattern agreement in Figure 15. More specifically, it is the individual lengths of the seal and lead-azide sections (up to the bridge wire) that are conjecture and have the largest impact on the input impedance of the SABC. These two values were optimized in the SABC MatLAB detonator program for agreement with experimental measurements. It was found that increasing the seal length to 37 mm and the lead-azide length to 3.3 mm resulted in an improvement between measured and predicted resonant frequencies. Since the total length of the SABC has been specified to be 59.7 mm (including the RDX section), these values are certainly reasonable. A comparison plot of the optimized SABC analytical predictions and experimentally measured resonances is shown in Figure 16.

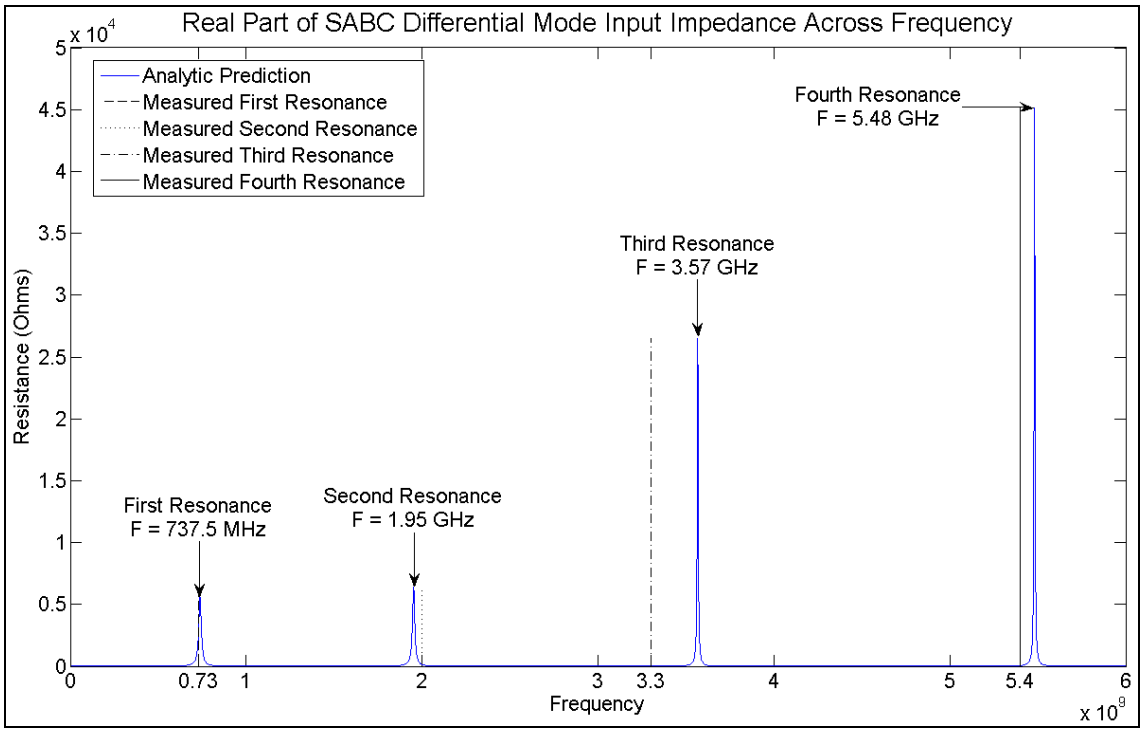

Figure 16: Comparison plot of measured and predicted SABC resonances across the frequency range 10 MHz to 6 GHz for modified SABC seal and lead-azide section lengths.

Figure 16 shows a significant improvement in the agreement between the predicted and measured SABC resonant frequencies as compared to Figure 15. Not only is the analytical model now predicting all four resonances, but the agreements for the three predicted earlier have vastly improved. A summary of the percent difference between the measured and predicted resonance frequencies for both the original SABC model and the modified SABC model with lengthened seal and lead-azide sections is given in Table 3. The results in Table 3 show a less than 9% error in the prediction of all four resonant frequencies. This result suggests that the inner dimensions of the SABC are closer to those used in the modified model than were used in the initial model.

Table 3: Percent differences between predicted and measured resonant frequencies for two SABC model variations.

Detonator Property	Initial SABC Model	Modified SABC Model
First Resonance	27.95	1.03
Second Resonance	28.50	2.50
Third Resonance	N/A	8.18
Fourth Resonance	8.70	1.48

While the resonance agreement is well within tolerance, a comparison of the amplitudes of the resonances in Figures 14 and 16 reveals that they are significantly different. Not only are the amplitudes predicted by MatLAB much larger (5 times higher for the first resonance), but the resonances in general follow opposite patterns. Experimentally, as the frequency increases, the magnitude of the input impedance at each resonance decreases (Figure 14), while the MatLAB predictions behave oppositely, with the magnitudes increasing with increasing frequency (Figure 16). These two amplitude discrepancies are linked to one common problem with the analytical model, which is the exclusion of a finite conductivity for lead-azide. A value for the conductivity of lead-azide has not been published in the literature, and so the analytical model assumed a value of 0 S, and the assumption of G = 0 S/m was inputted in the telegrapher's equations from (31) onward. This was thought to be a valid assumption based on the very short section of lead-azide in the detonator transmission line. However, since lead-azide is composed of lead and nitrogen [7], it has some finite conductivity due to the presence of lead.

While the assumption of G = 0 S/m was acceptable with regards to the resonance characteristics, the absence of a finite conductivity does affect the impedance values due to the additional loss it adds to the system. Since lead-azide is a compound, it is difficult to speculate as to its conductivity. Certainly, it is significantly lower than that of lead,

and is likely to be frequency-dependent due to the chemical bonds within it. Until the conductivity of lead-azide is carefully measured it is difficult to speculate what value to use in this model. However, as a test, a finite conductivity was added to the model for verification purposes by including an arbitrary value of G = 50 S/m to the telegrapher's equation of the lead-azide section. A plot of the impedance using this G value is shown in Figure 17. This addition had the desired effect on the amplitudes, significantly lowering them overall, and producing the decreasing resonance amplitude pattern observed in the experimental measurements. Including this finite conductivity also had a negative effect of the resonance pattern. However, since the value of 50 S/m is not only incorrect, but not frequency-dependent, this result is not completely unexpected. Adding this finite conductivity was done simply as an exercise to show that adding some additional loss into the analytical model would reduce the overall amplitude of the resonance peaks, and also force them to decrease with increasing frequency.

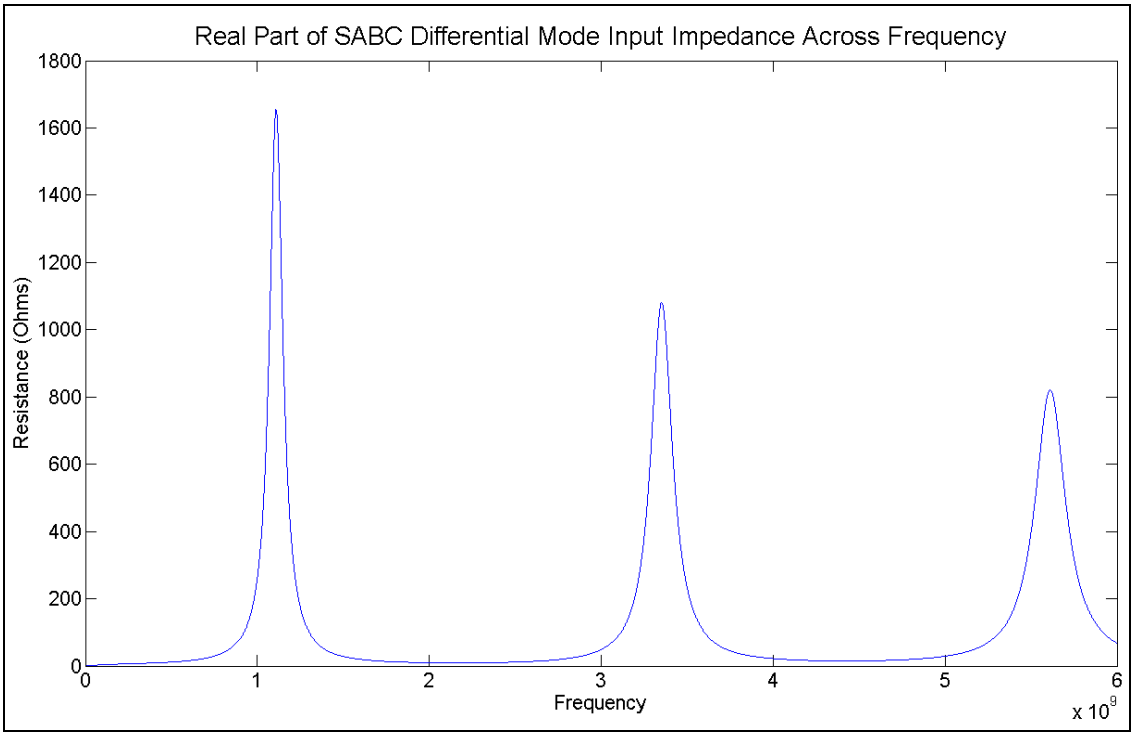

Figure 17: Predicted SABC input impedance using a finite conductivity for the lead-azide section.

Chapter Summary

In this chapter, EM properties of the SABC were predicted analytically and compared to simulated values using ICEPIC, with good agreement overall for all four diagnostics without any additional 1-D model modifications. The analytical model predictions of SABC impedance were then compared to experimental measurements taken on 108 live devices, and discrepancies were found between the resonances of each method. Since the model included speculative dimensional values, the agreement between the 1-D predictions and measurement was optimized by varying these dimensions. The end result showed vast improvement in the resonance agreement and the optimized dimensions were physically plausible. Amplitude discrepancies remained, however, and it was discovered that the absence of a finite conductivity term for the lead-azide section was a contributing factor, and that the properties of lead-azide are needed to make the model more accurate.

Chapter 8 – Conclusions and Future Work

Through the course of this dissertation, the physical characteristics of a generic hot-wire detonator have been thoroughly described, and these characteristics have been used to model the detonator using both analytical and numerical methods. These models were used to determine the detonator's EM characteristics across a frequency range of DC-9 GHz, and the results compared. Modifications have been made to the analytical model based on findings using 3-D EM simulation to improve the 1-D detonator representation and its ability to predict EM properties.

For the generic detonator undergoing differential mode excitation, the analytical model was successfully modified to account for the decreased inductance of the bridge wire and additional inductance near the bridge wire due to the effect of fringing EM fields at the 90^0 bend connection between the bridge wire and lead-in wires. These modifications produced an accurate agreement between analytic predictions and ICEPIC simulation. A discrepancy remains between the two models with regards to a third higher order resonance frequency found in simulation but not predicted by the 1-D model. The extra sheath is known to be the cause for this discrepancy, but accounting for this additional sheath using differential mode excitation is problematic since the transmission line ends at the bridge wire. Work is ongoing to solve this problem. A process for determining the additional capacitance of this extra sheath using DC differential mode excitation, as was done for common mode excitation, did not produce a capacitance difference of discernible value. The EM mechanism which will account for this sheath can be found by running several more ICEPIC simulations with varying sheath diameters and lead-in wire lengths. This process will help ascertain how these geometry changes

affect the standard detonator model's resonance frequencies, and perhaps lead to the discovery of the EM property which must be added to the analytical model.

The analytical model for the generic detonator undergoing common mode excitation was successfully modified to account for the extra sheath extending past the open termination of the transmission line. The additional capacitance introduced by the extra sheath was added into the analytical model and produced a significant accuracy improvement between analytic predictions and ICEPIC simulation. However, the average percent differences between the two models are still much larger than those calculated for differential mode excitation. A discrepancy also remains between the two models with regards to a second higher order resonance frequency found in simulation but not predicted by the 1-D model. The extra sheath is known to be the cause for this discrepancy, but the additional capacitance added to the analytical model accounting for this sheath does not bring about the prediction of a second resonance to match simulation. These modeling challenges remain for common mode excitation, and they are continuing to be investigated. While small changes in outer sheath diameter and lead-in wire length will also bring insight into this problem, the assumptions made for this common mode excitation must also be examined. It was assumed for the formulation of the analytical model that current flowed through the lead-in wires are returned by the sheath. However, in the ICEPIC simulation, it is possible that the excitation conditions being used do not reproduce this assumption. In other words, the 1 A of current input into the lead in wires does not all return by the sheath. This can be investigated by placing additional CUR_CIR diagnostics with different radii around the aluminum sheath to measure how much current is flowing through it. This process may determine if the initial assumption

of all current returning by the sheath is the underlying cause for the common mode discrepancies. The results of the sheath current investigation may lead the way for a new method of common mode excitation in ICEPIC, or an adjustment in the current calculation performed in the analytical model, or both.

Analytical model predictions were successfully compared to SABC measurements by optimizing two unknown parameters within the SABC. Investigations will continue into the SABC to include obtaining the exact dimensions, if possible. Common mode SABC impedance measurements could also be performed and compared to analytical predictions. Also, the effect of small dimensional variations on the SABC EM characteristics can be ascertained to help determine EM safety limits due to manufacturing variation.

In addition to the SABC, differential and common mode impedance measurements of other types and brands of detonator need to be performed and compared to the analytical model. This will help the model's development, and to show that it can accurately predict EM behavior for any similarly constructed hot-wire detonator with different dimensions.

Finally, work must be done to determine the exact dielectric and conductivity properties of lead-azide across a large frequency spectrum. The result of not including the lead-azide's conductivity in the model was seen in Chapter 7 for the SABC. It would help the analytical model accuracy considerably to include frequency-dependent permittivity and conductivity values for the lead-azide section.

References

[1] F. Sonnemann. "Susceptibility of bridgewire EED (inert) against HPEM," *2007 International Conference on Electromagnetics in Advanced Applications*, pp. 205-208, September 2007.

[2] G. K. Deb and M. Mukherjee. "EM Susceptibility Studies and Measurements on Electro Explosive Devices," *IEEE International Symposium of Electromagnetic Compatibility*, pp. 552-559, 1985.

[3] L. A. Rosenthal. "New Method for Assessing EED Susceptibility to Electromagnetic Radiation," *IEEE Transactions on Electromagnetic Compatibility*, Vol. 33, No. 4, pp. 328-333, November 1991.

[4] "Blasting Cap," Wikipedia, May 2008.

[5] Tucker, T. J. "Explosive Initiators," Sandia National Laboratories, Kirtland Air Force Base, Albuquerque, NM, 1972.

[6] J. Scaturro. "Survey of Electroexplosive Devices," Air Force Weapons Laboratory, Kirtland Air Force Base, NM, ARWL-TR-76-122, 1977.

[7] Cooper, Paul W. Explosive Engineering. New York: Wiley, 1996.

[8] "N 388 Electric Detonators," DaveyFire, Inc. 2006.

[9] "Igniters." Schaffler & Co., 2005.

[10] "PRF 14000030." Stresau Laboratory, Inc. 2007.

[11] "ElectricMS." Orica Inc., 2004.

[12] Diallyl Phthalate – DAP Short Glass Fibre Reinforced. The A to Z of Materials and AZojomo, 2007. http://www.azom.com/details.asp?ArticleID=251.

[13] The Design Guide for Bonding Plastics, Volume 3. Loctite, January 2005.

[14] B.M. Dobratz and P.C. Crawford. "LINL Explosives Handbook: Properties of Chemical Explosives and Explosive Stimulants," Lawrence Livermore National Laboratory, Livermore, CA, UCRL-52997, 1985.

[15] M.F. Iskander, "Electromagnetic Fields and Waves," Prospect Heights, IL: Waveland Press, Inc., 2000.

[16] Military Specification: Caps, Blasting, Special. MIL-C-45468E, 2005.

[17] Pozar, David M. Microwave Engineering. Third Ed. New Jersey: John Wiley and Sons, Inc., 2005.

[18] Jordan, Edward C. Reference Data for Engineers: Radio, Electronic, Computer, and Communications. Seventh Ed., 1988.

[19] Fjetland, L. "Design Considerations for a Special Twinaxial Cable", Sensor and Simulation Notes 14, Air Force Weapons Laboratory. Mar 17, 1965.

[20] Grover, Frederick W. Inductance Calculations: Working Formulas and Tables. New York: Dover Publications, Inc., 1962.

[21] Baum, Carl. E. "Nonuniform Multiconductor Transmission Lines," Interaction Notes 516, Air Force Weapons Laboratory. February 2, 1996.

[22] Sadiku, Mathew N. O. Numerical Techniques in Electromagnetics. Second Ed. Boca Raton: CRC Press LLC, 2000.

[23] Sadiku, Mathew N. O. Elements of Electromagnetics. Third Ed. New York: Oxford University Press, 2001.